Reduced basis method applied to large non-linear multi-physics problems : application to high field magnets design

Cécile Daversin - Catty

Thèse

INSTITUT DE RECHERCHE MATHÉMATIQUE AVANCÉE

UMR 7501

Strasbourg

présentée pour obtenir le grade de docteur de
l'Université de Strasbourg
Spécialité MATHÉMATIQUES APPLIQUÉES

Cécile Daversin - Catty

Reduced basis method applied to large non-linear multi-physics problems. Application to high field magnets design.

Soutenue le 19 septembre 2016
devant la commission d'examen

Clémentine Prieur, rapporteur
Christophe Geuzaine, rapporteur
Frédéric Hecht, examinateur
Philippe Helluy, examinateur
Emmanuel Frénod, examinateur
Christophe Prud'homme, directeur de thèse
Eric Beaugnon, co-directeur de thèse
Christophe Trophime, co-encadrant de thèse

www-irma.u-strasbg.fr

cnrs dépasser les frontières

IRMA Institut de Recherche Mathématique Avancée

UNIVERSITÉ DE STRASBOURG

UNIVERSITÉ DE STRASBOURG

École Doctorale Mathématiques, Sciences de l'Information et de l'Ingénieur

Institut de Recherche Mathématique Avancée, UMR 7501

THÈSE présentée par

Cécile DAVERSIN - CATTY

soutenue le 19 septembre 2016

pour obtenir le grade de Docteur de l'Université de Strasbourg

Spécialité : Mathématiques Appliquées

Reduced basis method applied to large non-linear multi-physics problems.

Application to high field magnets design.

THÈSE DIRIGÉE PAR :

Christophe PRUD'HOMME	Directeur de thèse, Université de Strasbourg
Eric BEAUGNON	Co-directeur de thèse, Université Grenoble Alpes
Christophe TROPHIME	Co-encadrant de thèse, CNRS Grenoble

RAPPORTEURS :

Clémentine PRIEUR	Université Grenoble Alpes
Christophe GEUZAINE	Université de Liège

JURY :

Frédéric HECHT	Université Pierre et Marie Curie
Philippe HELLUY	Université de Strasbourg
Emmanuel FRÉNOD	Université Bretagne Sud

J'ai appris que le courage n'est pas l'absence de peur,
mais la capacité de la vaincre.

Nelson Mandela

À mon papa,

Remerciements

Mes premiers mots vont tout naturellement à Christophe Prud'homme, mon directeur de thèse. Tout d'abord merci pour m'avoir offert l'opportunité de travailler sur ce sujet et m'avoir convaincu que j'en étais capable. Je suis très reconnaissante de la confiance qui m'a été accordée tout au long de ce projet, et je sais la chance que j'ai eu de pouvoir travailler avec quelqu'un de si passionné.

Je tiens également à adresser mes remerciements à Eric Beaugnon pour avoir accepté de co-diriger cette thèse. Merci pour m'avoir fait découvrir le monde de l'expérimentation et pour m'avoir fait confiance malgré mon manque d'expérience(s) dans ce domaine.

Un grand merci à Christophe Trophime pour son implication, et pour son aide précieuse au quotidien. Tes conseils avisés ont largement contribué à la qualité de ce travail. Je remercie aussi François Debray pour s'être risqué à miser sur ce projet, et pour m'avoir fait une place dans son équipe.

Je tiens à remercier Clémentine Prieur et Christophe Geuzaine de me faire l'honneur d'être les rapporteurs de ma thèse. Je remercie également Frédéric Hecht, Philippe Helluy et Emmanuel Frenod pour avoir accepté de faire partie de mon jury, et de contribuer ainsi à l'évaluation de mon travail. J'adresse aussi mes remerciements au labex IRMIA qui à financé l'ensemble de ma thèse, et à la direction du LNCMI pour avoir accepté de m'accueillir.

Je remercie tout le personnel du LNCMI, et en particulier merci à toute l'équipe du bâtiment U pour votre accueil. J'ai beaucoup appris en étant parmis vous.

Et je remercie bien sur toute l'équipe qui travaille autour de Feel++. Un grand merci à Stéphane pour m'avoir patiemment guidé dans mon apprentissage de la méthode des bases réduites. Merci aussi à Vincent C., je garde un super souvenir de l'équipe qu'on a formé à la SEME. Et merci à Abdoulaye pour ta bonne humeur communicative. Sans oublier les Strasbourgeois de l'équipe : Ranine, Guillaume, Vincent H., Alexandre, Jean-Baptiste et Romain. Merci pour votre très bon accueil à chacun de mes séjours en Alsace, et pour les bons moments passés à l'occasion des FUD ou en conférences. Un merci spécial à Vincent H. pour l'aide apportée dans le développement du modèle de magnéto.

J'adresse un grand merci à tous mes amis, qui m'ont encouragé et soutenu de près ou de loin. Un petit clin d'oeil à Mathilde, mon fidèle binome. Et à Jerem' qui m'a "for"-mé à la programmation. Sans vous mon parcours n'aurait surement pas été le même. Un grand merci à Sheetal de s'être courageusement attelé à la relecture, pour corriger mon anglais maladroit. Merci à Etienne mon fournisseur officiel d'histoires drôles, et à Raj' mon fournisseur officiel de cheese nan!

Je remercie également Tara et Isabelle (dignes représentantes de la gente féminime du LNCMI !), pour tous les bons moments passés ensemble au labo ou ailleurs.

Un immense merci à tous mes amis danseurs et en particulier à Marion et Sébastien #DreamSellers, à Aurélie et Loïc, et bien sûr à Béné et Jérôme. Je savais qu'il me serait primordial de faire des breaks. Maintenant je sais aussi qu'on peut les entendre et les interpreter. Merci pour tous ces bons moments rythmés par votre bonne humeur qui m'ont été si précieux.

Je remercie bien évidemment toute ma famille pour son soutien inconditionel et sans faille dans tous mes projets. Un merci spécial à Patrice pour le temps que tu as consacré à la relecture de ce manuscrit, malgré un emploi du temps chargé.

Et j'adresse un merci tout particulier à ma maman, sans qui rien de tout cela n'aurait été possible. Quelque soient les épreuves que l'on a traversé, tu as toujours fait en sorte que je ne manque de rien. Merci d'avoir cru en moi, et de m'avoir donner les moyens de réaliser mes ambitions.

Enfin, ces remerciements ne seraient pas complets sans un immense merci à celui qui partage ma vie et qui est devenu mon mari. Merci infiniment pour tout l'amour que tu me portes et qui me porte chaque jour depuis maintenant dix ans. Ta présence, ton soutien et toutes tes petites attentions au quotidien sont autant d'éléments indispensables à l'accomplissement de cette thèse, qui est aussi la tienne.

Résumé

Introduction

Le champ magnétique, qui s'exprime en Tesla dans le système international, est présent partout dans notre environnement. Si les magnétars sont caractérisés par l'intensité de leur champ magnétique pouvant atteindre 10^{11} T, il se limite à 10^{-12} T pour le cerveau humain. Le champ magnétique terrestre atteint quant à lui 4.7×10^{-5} T.

Certains matériaux ont la propriété de produire naturellement du champ magnétique. On parle alors d'aimantation permanente, que l'on distingue de l'aimantation induite par la circulation d'un courant électrique à travers un matériau conducteur. La description mathématique de l'électromagnétisme, établie par James Clerk Maxwell en 1864 a donné naissance aux équations de Maxwell, que l'on utilise encore aujourd'hui. Elle a notamment permis de comprendre et de contrôler la production de champ magnétique.

Les aimants à haut champ

Les premiers développements d'aimants capables de générer un champ magnétique "fort" datent du début des années 1900. Un solenoïde produisant 5 T a été développé par Deslandres et Perot en 1914, suivi par le grand électro-aimant de l'Académie des sciences [Cotton, 1928], qui a fonctionné de 1920 à 1970 à Bellevue, France. Son grand volume a permis la réalisation de nombreuses expériences sous champ magnétique, avant qu'il devienne une pièce de musée. Les techniques modernes d'aimants pour champ intense sont apparues dans les années 1940, avec les travaux de Francis Bitter.

Découverts à la fin des années 1960, les matériaux supraconducteurs permettent de conduire le courant sans résistance électrique à basse température, typiquement pour des température inférieures à 4 K. Les aimants supraconducteurs utilisant ce type de matériaux sont maintenant produits et utilisés couramment, pouvant atteindre jusqu'à 23.5 T – record mondial obtenu au Centre de Résonance Magnétique Nucléaire à très haut champs, à Lyon. Au delà de cette valeur, on parle de champ magnétique intense. Les recherches actuelles sur les supraconducteurs à haute température (HTS) – qui conservent leurs propriétés à des températures supérieures à 4 K – laissent entrevoir la possibilité de dépasser ce record.

Les champs magnétiques intenses sont produits par des aimants résistifs, composés de matériaux résistifs comme les alliages de cuivre, et refroidis par circulation d'eau. Utilisés par exemple en imaginerie médicale, ce type d'aimants constitue plus généralement un

outil puissant permettant de sonder la matière pour mieux déterminer ses propriétés.

Seulement quelques aimants dans le monde permettent d'atteindre des champs magnétiques intenses. On les trouve dans des infrastructures de recherche dédiées, permettant à l'ensemble de la communauté scientifique d'en bénéficier.

En France, le Laboratoire National des Champs Magnétiques Intenses (LNCMI) est présent à Grenoble et à Toulouse. Il fait partie de l'EMFL (European Magnetic Field Laboratory) regroupant l'ensemble des laboratoires Européens produisant des champs magnétiques intenses. Les électroaimants développés à Grenoble peuvent atteindre jusqu'à 36 T pendant plusieurs heures.

Au LNCMI, le design de ces aimants est basé sur plusieurs technologies. Les aimants Bitter – du nom de leur inventeur, Francis Bitter en 1933 – consistent en un empilage de disques de cuivre formant un solenoïde. Ils sont refroidis par circulation d'eau – à travers des trous répartis régulièrement dans les disques – permettant de contrôler leur montée en température. Ce type d'électroaimants est le plus utilisé pour la production de champ magnétique intense, et permet d'atteindre 38 T – record récemment établi par Hefei, en Chine.

Les aimants dits polyhélices – développés exclusivement au LNCMI – sont une alternative aux précédents aimants Bitter. Ils sont formés de tubes composés d'alliages de cuivre, découpés en hélice et empilés de manière concentrique. On en compte deux types, qui se distinguent par la méthode de refroidissement utilisée.

Pour les polyhélices dites à refroidissement longitudinal, l'eau circule uniquement entre les tubes. La découpe hélicoïdale réalisée par électroérosion est comblée par un mélange de colle époxy et de billes de verre, garantissant ainsi l'isolation électrique entre les tours. Les polyhélices à refroidissement radial autorisent quant à elles la circulation d'eau entre les spires, augmentant ainsi la surface refroidie. Dans ce cas, l'isolation électrique est assurée des isolants disposés régulièrement le long de la découpe. Plus d'informations sur ces technologies sont disponibles dans [Debray et al., 2012].

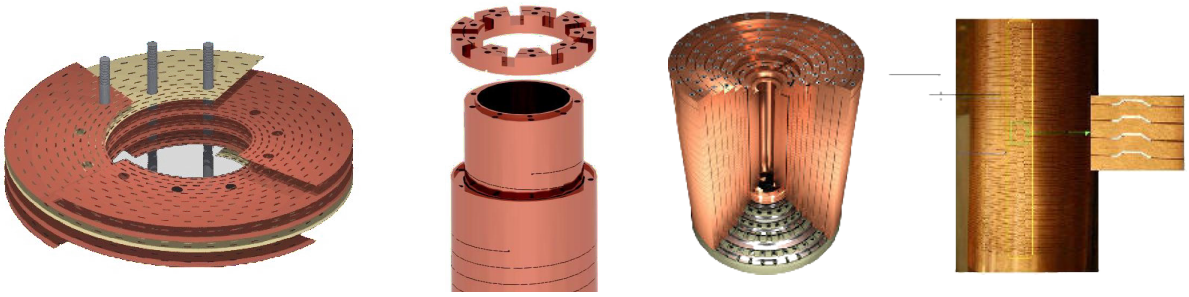

(a) Aimant Bitter (jusqu'à 1m de diamètre)

(b) Aimants polyhélices (jusqu'à 400m de diamètre)

Figure 1 – Plusieurs technologies d'aimants résistifs sont utilisées pour produire des champs magnétiques intenses

Pour garder son rang dans la compétition entre les différentes infrastructures mondiales pour le record de champ magnétique, le LNCMI doit sans cesse améliorer la capacité de ses aimants. Cependant, le dévelopement d'aimants capables de générer des champs

magnétiques de plus en plus intenses représente un challenge en termes de matériaux et de design. La simulation numérique s'avère être un élément essentiel dans le procédé d'optimisation.

Un outil pour la modélisation

Basé sur une collaboration entre l'université de Strasbourg et le LNCMI, le projet HiFi-Magnet vise à mettre en place un outil complet pour la modélisation des aimants à haut champ. Cette thèse s'inscrit dans le cadre de ce projet, avec comme objectif principal le développement d'une gamme de modèles dédiés. Leur couplage doit former un **modèle multi-physiques 3D** qui puisse être *(i)* **générique** pour être facilement applicable aux différents design, *(ii)* **efficace** au vu de la complexité des géométries et *(iii)* **fiable** compte tenu des incertitudes sur les données d'entrée.

Les développements réalisés dans cette thèse donnent la possibilité de réaliser des simulations numériques sur des **géométries d'aimants réels**, en utilisant le **calcul haute performance**. Pour réduire le coût calcul associé dans un but de quantification d'incertitude sur les paramètres d'entrée – propriétés des matériaux, conditions de fonctionnement – , nous proposons l'utilisation de **méthodes de réduction de modèle**.

Les différentes physiques mises en jeu dans l'étude des aimants à haut champ sont décrites par des équations aux dérivées partielles (EDP) sur lesquelles est basé notre modèle multi-physiques. Au vu de la complexité des géométries, nous avons choisi d'utiliser la méthode des éléments finis pour résoudre ces EDPs. La librairie élément finis `Feel++` [Prud'Homme et al., 2012] – dont le nom signifie *Finite Element Embedded Language in C++* – a été choisie dans ce contexte. Elle fournit une interface C++ dédiée à la résolution des EDPs, offrant un syntaxe proche de leur formulation mathématique.

En particulier, ses capacités de calcul haute performance sont particulièrement intéressantes pour gérer la complexité des problèmes non concernant. Cette librairie fournit également une interface pour l'utilisation de la méthode des bases réduites.

Plan de la thèse

La thèse s'organise en 4 parties.

La première partie concerne les outils mathématiques nécessaires aux développements réalisés. Un premier chapitre est dédié à la description de la méthode des **éléments finis** d'un point de vue théorique, et en particulier aux éléments vectoriels H_{div} et H_{curl} intervenant dans la résolution des équations de Maxwell. L'implémentation des éléments de **Raviart-Thomas** et de **Nédélec** dans la librairie `Feel++` est une contribution de la thèse. Le deuxième chapitre est axé sur les méthodes de réduction de modèle. La **méthode des bases réduites** (RB) est décrite pour les problèmes non-linéaires et non affines nous concernant, utilisant la méthode d'interpolation empirique (EIM). Enfin, le dernier chapitre introduit la **méthode SER** – signifiant *Simultaneous Empirical interpolation and Reduced basis method* – développée dans cette thèse. Combinant les méthodes EIM et RB, la méthode SER [Daversin and Prud'Homme, 2016, Daversin and Prud'Homme, 2015a] offre un gain considérable en coût calcul, tout en conservant une qualité d'approximation raisonnable. Ses performances sont illustrées sur un cas test 2D, puis sur une géométrie

d'aimant dans la dernière partie.

La seconde partie est centrée sur le développement du **modèle 3D multi-physiques** dédié à la modélisation des aimants à haut champ. On s'intéresse tout d'abord au modèle éléments finis dont les composantes sont *(i)* un **modèle thermo-électrique** permettant de modéliser le courant électrique circulant dans l'aimant et la montée en température associée, *(ii)* un **modèle magnétostatique** donnant le champ magnétique produit, et *(iii)* un **modèle d'élasticité linéaire** couplé aux deux modèles précédents permettant d'évaluer les déplacements et contraintes mécaniques induites par les forces magnétiques et la dilatation thermique. L'application de la méthode des bases réduites est décrite dans un second temps.

La troisième partie liste les **contributions apportées à la librairie** `Feel++` dans le cadre de cette thèse, à savoir *(i)* l'implémentation des éléments finis de Raviart-Thomas et de Nédélec, *(ii)* le développement et l'implémentation d'un algorithme parallèle pour la loi de Biot & Savart permettant de calculer le champ magnétique et *(iii)* l'ajout de la méthode SER dans le framework bases réduites de `Feel++`, rendant son utilisation disponible pour l'ensemble des utilisateurs de la librairie.

La dernière partie de la thèse illustre l'ensemble des développements présentés, sur des **applications numériques concrètes** répondant aux besoins formulés par le LNCMI. Ces exemples démontrent la capacité des modèles à être utilisés sur des géométries réelles, et permettent leur validation à partir de mesures expérimentales. Cette partie regroupe entre autres, *(i)* des exemples d'applications du modèle réduit pour la **quantification d'incertitude**, *(ii)* la mise en place d'une **campagne de mesures** de champ magnétique visant à valider les modèles de magnétostatique ou *(iii)* des simulations réalisées pour la **future génération d'aimants hybride** visant 43 T.

Outils mathématiques

La plupart des phénomènes physiques peuvent être décrits par des équations aux dérivées partielles. De nombreuses méthodes peuvent être utilisées pour les résoudre, parmi lesquelles les différences finies, les éléments finis ou encore les volumes finis. Particulièrement adaptée à la complexité des géométries des aimants à haut champ, la méthode des éléments finis est au coeur des développements réalisés.

Méthode des éléments finis

On considère que les équations aux dérivées partielles (EDPs) admettent une formulation variationnelle, dont la solution u définie sur le domaine Ω est la solution du problème variationnel consistant à trouver $u \in X(\Omega)$ telle que

$$a(u, v) = f(v) \ \forall v \in X(\Omega) \tag{1}$$

avec $X(\Omega)$ un espace de Hilbert, $a : X(\Omega) \times X(\Omega) \longrightarrow \mathbb{R}$ une forme bilinéaire coercive et $f : X(\Omega) \longrightarrow \mathbb{R}$ une forme linéaire continue.

D'un point de vue numérique, on résout (1.1) sous sa forme discrète, dans un sous espace $X_{\mathcal{N}}(\Omega)$ de $X(\Omega)$, de dimension finie $\mathcal{N}$. Basée sur la méthode d'approximation interne de Galerkin, la solution discrète $u_{\mathcal{N}}$ provient de la résolution du système $\mathcal{N} \times \mathcal{N}$ donnant ses coefficients dans une base de $X_{\mathcal{N}}(\Omega)$.

$$u_{\mathcal{N}} = \sum_{j=1}^{\mathcal{N}} u_{\mathcal{N}}^j \phi_j \quad \text{avec} \quad X_{\mathcal{N}}(\Omega) = span\{\phi_1, \ldots, \phi_{\mathcal{N}}\} \tag{2}$$

La méthode des éléments finis est utilisée pour définir le sous espace $X_{\mathcal{N}}(\Omega)$ de $X(\Omega)$ en déterminant ses fonctions de base.

D'après le formalisme de Ciarlet, un élément fini se définit comme un triplet (K, P_K, Σ_K) composé *(i)* d'un élément géométrique K, *(ii)* d'un espace polynomial P_K dans lequel sont définies les fonctions de bases ϕ_i de $X_{\mathcal{N}}(\Omega)$, et *(iii)* d'un ensemble de fonctionnelles linéaires $\Sigma_K = \{\sigma_i\}$ définissant ses degrés de liberté.

Les coefficients des fonctions de bases locales ϕ_i (1.3) dans la base de l'espace polynomial P_K sont déterminés à partir des degrés de liberté de l'élément K.

En pratique, pour des raisons d'efficacité, on considère chaque élément K comme l'image d'un élément de référence $\hat{K}$ par une transformation géométrique ϕ_K^{geo}. Cela permet notamment de limiter le calcul des fonctions de bases à l'élément de référence.

Enfin, le choix de l'espace $X(\Omega)$ associé au problème (1.1) doit garantir la conservation des propriétés attendues pour la solution u. Le diagramme de De-Rham (1.10) établit un lien entre les espaces vectoriels

$$\begin{aligned}
&L_2(\Omega) = \{f \mid \textstyle\int f^2 < \infty\}) \\
&H_1(\Omega) = \{f \in L_2(\Omega) \mid \nabla f \in L_2(\Omega)\} \\
&H_{\text{div}}(\Omega) = \{\boldsymbol{f} \in [L_2(\Omega)]^d \mid \nabla \cdot \boldsymbol{f} \in L_2(\Omega)\} \\
&H_{\text{curl}}(\Omega) = \{\boldsymbol{f} \in [L_2(\Omega)]^d \mid \nabla \times \boldsymbol{f} \in L_2(\Omega)\}
\end{aligned} \tag{3}$$

avec d la dimension du domaine Ω.

$$H_1(\Omega) \xrightarrow{grad} H_{\text{curl}}(\Omega) \xrightarrow{curl} H_{\text{div}}(\Omega) \xrightarrow{div} L_2(\Omega) \xrightarrow{0} \{0\} \tag{4}$$

Cette relation reste vraie dans le cas discret.

Les éléments finis de Lagrange sont les plus couramment utilisés. Ces éléments nodaux sont adaptés à la plupart des problèmes variationnels, dont la solution réside dans l'espace H_1 (1.9). C'est le cas pour les modèles électro-thermique et élastique dédiés à l'étude des aimants. Ils sont définis comme les triplets $\left(K, \mathcal{L}_k, \Sigma_K^L\right)$ avec k l'ordre polynomial, et $\mathcal{L}_k$ l'ensemble des polynômes de degré inférieur à k. Les degrés de liberté de ces éléments correspondent à l'évaluation des polynômes $p \in \Sigma_K^L$ aux points d'interpolation de K.

D'après les équations de Maxwell, le champ magnétique produit par les aimants est dans $H_{\text{div}}(\Omega)$. Le potentiel magnétique dont il dérive, solution de l'équation résolue dans le modèle de magnétostatique, vit quant à lui dans $H_{\text{curl}}(\Omega)$. Le développement de ce modèle requiert un espace $X_{\mathcal{N}}(\Omega)$ dont les fonctions de base satisfont les propriétés associées. Dans ce but, nous définissons les éléments finis de Raviart-Thomas pour $H_{\text{div}}(\Omega)$ et de Nédélec pour $H_{\text{curl}}(\Omega)$, dont l'implémentation dans `Feel++` est une contribution de la thèse.

Élément finis de Raviart-Thomas

Les éléments finis de Raviart-Thomas sont définis par les triplets $\left(K, \mathcal{D}_k, \Sigma_K^{RT}\right)$, où k est l'ordre polynomial. L'espace polynomial $\mathcal{D}_k$ est un sous ensemble de l'espace vectoriel $[\mathbb{P}_{k+1}]^d$ des polynômes de degré inférieur à $k+1$, avec d la dimension du domaine Ω.

$$\mathcal{D}_k = [\mathbb{P}_k]^d \oplus \mathbf{x}\mathbb{P}_k \subset [\mathbb{P}_{k+1}]^d \tag{5}$$

On distingue deux types de fonctionnelles dans l'ensemble Σ_K^{RT} des degrés de liberté. Au plus bas ordre – dit ordre 0 –, Σ_K^{RT} se limite aux degrés de liberté σ_f localisés sur les faces, définis comme l'intégrale sur les faces de la composante normale. Les degrés de liberté internes σ_K viennent s'ajouter à ces derniers à partir de l'ordre 1.

$$\begin{aligned} \sigma_f(\mathbf{u}) &= \int_f \mathbf{u}\cdot\mathbf{n}p \quad \forall p \in \mathbb{P}_k(f) \\ \sigma_K(\mathbf{u}) &= \int_K \mathbf{u}\cdot\mathbf{q} \quad \forall \mathbf{q} \in [\mathbb{P}_{k-1}(K)]^d \end{aligned} \tag{6}$$

La normale associée à chaque face des éléments du maillage joue un rôle important dans la définition des degrés de liberté. Pour une face partagée par deux éléments, l'orientation de la normale dépend de l'élément dans lequel on se place. Une attention particulière doit donc être apportée pour assurer l'unicité des normales et ainsi de chaque degré de liberté.

La transformation géométrique ϕ_K^{geo} évoquée précédemment ne permet pas de conserver les propriétés des éléments de Raviart-Thomas. La transformation de Piola (1.41) définie à partir de ϕ_K^{geo} et de sa Jacobienne J_K^{geo} est utilisée pour garantir les propriétés attendues sur tous les éléments réels $K \in \mathcal{T}_h$.

$$\mathbf{u}(\mathbf{x})|_K = \frac{1}{det(J_K^{\text{geo}})} J_K^{\text{geo}} \hat{\mathbf{u}}(\hat{\mathbf{x}}) \;\Leftrightarrow\; \mathbf{u}(\mathbf{x})|_K = \frac{1}{det(J_K^{\text{geo}})} J_K^{\text{geo}} \hat{\mathbf{u}} \circ \phi_K^{\text{geo}\,-1}(\mathbf{x}) \tag{7}$$

Élément finis de Nédélec

Il existe plusieurs types d'éléments de Nédélec. En ce qui nous concerne, on se limite aux éléments de Nédélec de type 1 définis par les triplets $(K, \mathcal{R}^{k,1}, \Sigma_k^{Ned,1})$. Comme pour les éléments de Raviart-Thomas, l'espace polynomial $\mathcal{R}^{k,1}$ est un sous espace de $[\mathbb{P}_{k+1}]^d$ défini par la somme

$$\mathcal{R}^{k,1} = [\mathbb{P}_k]^d \oplus \mathcal{S}^k \subset [\mathbb{P}_{k+1}]^d \tag{8}$$

où $\mathcal{S}^k$ est défini comme

$$\mathcal{S}^k = \{\mathbf{p} \in [\mathbb{P}_k]^d \mid \mathbf{p} \cdot \hat{\mathbf{x}} = 0\} \tag{9}$$

L'ensemble $\Sigma_k^{Ned,1}$ se compose de plusieurs types de fonctionnelles. En 2D, les degrés de libertés σ_e sont localisés sur les arêtes, et complétés par des degrés de liberté internes σ_K à partir de l'ordre 1.

$$\begin{aligned} \sigma_e(\mathbf{u}) &= \int_e (\mathbf{u} \cdot \mathbf{t}) p \quad \forall p \in \mathbb{P}_k(e) \\ \sigma_K(\mathbf{u}) &= \int_K \mathbf{u} \cdot \mathbf{q} \quad \forall q \in [\mathbb{P}_{k-1}(K)]^2 \end{aligned} \tag{10}$$

En 3D, les arêtes se distinguent des faces contrairement au cas 2D, et on a *(i)* des degrés de liberté σ_e localisés sur les arêtes, *(ii)* des degrés de liberté σ_f localisés sur les faces à partir de l'ordre 1, et *(iii)* des degrés de liberté internes σ_K à partir de l'ordre 2.

$$\begin{aligned} \sigma_e(\mathbf{u}) &= \int_e (\mathbf{u} \cdot \mathbf{t}) p \quad \forall p \in \mathbb{P}_k(e) \\ \sigma_f(\mathbf{u}) &= \int_f (\mathbf{u} \times \mathbf{n}) \cdot \mathbf{q} \quad \forall q \in [\mathbb{P}_{k-1}(f)]^2 \\ \sigma_K(\mathbf{u}) &= \int_K \mathbf{u} \cdot \mathbf{q} \quad \forall q \in [\mathbb{P}_{k-2}(K)]^2 \end{aligned} \tag{11}$$

En plus de l'orientation des normales comme dans le cas des éléments de Raviart-Thomas, on doit s'assurer de l'unicité des tangentes associées aux arêtes communes. Si les faces ne peuvent être partagées que par deux éléments, il y a beaucoup plus de possibilités à considérer dans le cas des arêtes en 3D.

Là aussi, la transformation géométrique ϕ_K^{geo} ne permet pas de conserver les propriétés des éléments de Nédélec. On utilise la transformation de Piola adaptée (1.71).

$$\mathbf{u}(\mathbf{x})|_K = J_K^{\text{geo}-T} \hat{\mathbf{u}}(\hat{\mathbf{x}}) \;\Leftrightarrow\; \mathbf{u}(\mathbf{x})|_K = J_K^{\text{geo}-T} \hat{\mathbf{u}} \circ \phi_K^{\text{geo}-1}(\mathbf{x}) \tag{12}$$

Dans la thèse, on décrit précisément ces deux familles d'éléments finis. En particulier, l'expression des fonctions de base sur l'élément de référence est détaillée pour les cas 2D et 3D, illustrées par leur calcul dans `Feel++`.

Méthode des bases réduites

L'optimisation du design ou encore le choix du matériau peuvent être guidés par l'évaluation de quantités d'intérêt dans différentes configurations, modélisées par des EDPs dites paramétrées. L'ensemble des configurations considérées peut également tenir compte des incertitudes sur les données d'entrée du problème. Les besoins actuels en ingénierie vont ainsi au delà de la simple prédiction d'une quantité physique, c'est le cas des aimants à haut champ nécessitant une optimisation très fine.

Suivant la taille du problème, le temps de calcul associé à une seule configuration peut

être important, rendant ainsi le coût d'une telle étude prohibitif. Les méthodes de réduction d'ordre transforment le problème paramétré initial en un problème de dimension réduite, permettant une résolution nettement plus efficace. Développée dans ce contexte, la méthode des bases réduites [Patera and Rozza, 2007] consiste en une projection de Galerkin sur un espace d'approximation de taille réduite, composé de solutions éléments finis.

Chaque configuration étudiée faisant intervenir p paramètres est définie comme un vecteur $\boldsymbol{\mu} = (\mu_1, \ldots, \mu_p) \in \mathcal{D} \subset \mathbb{R}^p$. L'équivalent paramétré du problème (1.1) consiste à trouver $u \in X(\Omega)$ tel que

$$a(u(\boldsymbol{\mu}), v; \boldsymbol{\mu}) = f(v : \boldsymbol{\mu}) \ \forall v \in X(\Omega) \tag{13}$$

Les quantités d'intérêt $s(\boldsymbol{\mu})$ sont des fonctions linéaires de la solution.

La méthode des bases réduites est basée sur une stratégie hors-ligne/en-ligne. On introduit l'espace d'approximation W_N engendré par N solutions éléments finis calculées à l'étape hors-ligne, avec $N \ll \mathcal{N}$. L'approximation bases réduites $u_N \in W_N$ est définie par ses coefficients dans la base de l'espace d'approximation. L'étape en-ligne désigne la résolution du système $N \times N$ associé permettant de déduire u_N et $s_N(\boldsymbol{\mu}) = \ell(u_N(\boldsymbol{\mu}))$.

L'efficacité de cette méthode réside également dans l'écriture d'une décomposition affine (2.6) du problème paramétré (2.3), permettant de pré-calculer – une seule fois lors de l'étape hors-ligne – les termes indépendants du paramètre $\boldsymbol{\mu}$. Elle permet en particulier de s'affranchir de la dimension éléments finis à l'étape en-ligne.

$$\begin{aligned} a(u, v; \boldsymbol{\mu}) &= \sum_{q=1}^{Q_a} \theta_a^q(\boldsymbol{\mu}) a^q(u, v) \quad \forall u, v \in X, \ \forall \boldsymbol{\mu} \in \mathcal{D} \ , \\ f(v; \boldsymbol{\mu}) &= \sum_{q=1}^{Q_f} \theta_f^q(\boldsymbol{\mu}) f^q(v) \quad \forall v \in X, \ \forall \boldsymbol{\mu} \in \mathcal{D} \end{aligned} \tag{14}$$

Méthode d'interpolation empirique (EIM)

Lorsque le problème considéré présente une dépendance non-affine en paramètres, la décomposition (2.6) n'existe pas. C'est le cas pour le modèle multi-physiques dédié aux aimants à haut champ.

La méthode d'interpolation empirique (EIM) est couramment utilisée pour construire une approximation affine w_M (2.8) des termes concernés w.

$$w_M(u(\boldsymbol{\mu}), \mathbf{x}; \boldsymbol{\mu}) = \sum_{m=1}^{M} \beta_m^M(u(\boldsymbol{\mu}); \boldsymbol{\mu}) \boldsymbol{q}_m(\mathbf{x}) \tag{15}$$

Comme la méthode des bases réduites, cette méthode s'appuie sur une stratégie hors-ligne/en-ligne. L'espace d'approximation associé se compose d'évaluations $w(u(\boldsymbol{\mu}), \mathbf{x}; \boldsymbol{\mu})$, pour des valeurs de $\boldsymbol{\mu}$ sélectionnées à l'aide d'un algorithme glouton (2.11).

La première fonction de base est construite à partir d'un paramètre choisi aléatoirement dans l'espace des paramètres. Ensuite, l'algorithme glouton (2.11) sélectionne le

paramètre qui maximise l'erreur d'approximation.

$$\bar{\boldsymbol{\mu}}_M = arg \max_{\boldsymbol{\mu}\in\Xi} \inf_{z\in W_{M-1}} ||w(.;.;\boldsymbol{\mu}) - z||_{L^\infty(\Omega)} \tag{16}$$

Les fonctions de base $\boldsymbol{q}_M$ formant l'espace d'approximation sont basées sur le résidu

$$\mathbf{r}_M(\mathbf{x}) = w(u(\boldsymbol{\mu}), \mathbf{x}; \bar{\boldsymbol{\mu}}_M) - w_{M-1}(u(\boldsymbol{\mu}), \mathbf{x}; \bar{\boldsymbol{\mu}}_M) \tag{17}$$

et sur la définition de points d'interpolation $\boldsymbol{t}_M$

$$\boldsymbol{t}_M = arg \sup_{\mathbf{x}\in\Omega} |\mathbf{r}_M(\mathbf{x})|, \quad \boldsymbol{q}_M(\mathbf{x}) = \frac{\mathbf{r}_M(\mathbf{x})}{\mathbf{r}_M(\boldsymbol{t}_M)} \tag{18}$$

La partie en-ligne consiste à évaluer les coefficient β_m^M de w_M (2.8) à l'aide d'un système de taille $M \times M$, assurant que l'approximation w_M soit exacte aux points d'interpolation.

En plus d'être non affine, le problème considéré dans le cas des aimants est non-linéaire. Cette non-linéarité est gérée par une méthode de point fixe de type Picard ou Newton, à la fois à l'étape hors-ligne et à l'étape en-ligne.

Méthode EIM bases réduites simultanée

Nécessaires pour écrire la décomposition affine, les approximations EIM sont construites avant l'application de la méthode bases réduites. L'algorithme glouton (2.11) nécessite un grand nombre d'approximations éléments finis, pouvant rendre le coût de l'étape hors-ligne prohibitif suivant la taille du problème.

En effet, le nombre de solution éléments finis $u_{\mathcal{N}}(\boldsymbol{\mu})$ à calculer est proportionnel à la taille de l'espace de paramètres $\Xi \subset \mathcal{D}$. Suivant l'expression w considérée, la taille de cet ensemble de paramètres joue un rôle important dans la qualité de l'approximation.

La méthode EIM bases réduites simultanée (SER pour *Simultaneous Empirical Interpolation and Reduced Basis Method*) propose de réduire le coût hors-ligne en utilisant l'approximation bases réduites disponible. Pour se faire, les espaces d'approximation EIM et bases réduites sont construits simultanément.

En l'absence d'approximation bases réduites, la première fonction de base EIM est construite de façon standard à partir d'un paramètre choisi aléatoirement. L'évaluation de w pour ce paramètre ne nécessite qu'une seule approximation éléments finis, permettant d'obtenir un premier espace d'approximation EIM. Bien que formées d'un seul terme, les approximations EIM engendrées permettent d'avoir une première décomposition affine et d'appliquer la méthodologie bases réduites. L'ajout d'une première fonction de base à W_N permet de construire une approximation bases réduite u_1.

A partir de là, l'algorithme glouton (2.11) est utilisé pour enrichir l'espace d'approximation EIM. Contrairement à la méthode standard, il utilise l'approximation réduite u_{M-1} obtenue

à l'étape précédente plutôt qu'une approximation éléments finis.

$$\bar{\boldsymbol{\mu}}_M = arg \max_{\boldsymbol{\mu} \in \Xi} \inf_{z \in W_{M-1}} ||w(u_{M-1}(\boldsymbol{\mu}); .; \boldsymbol{\mu}) - z||_{L^\infty(\Omega)} \tag{19}$$

L'évaluation du résidu (2.13) permettant de déduire la fonction de base et le point d'interpolation suivants, est également basée sur u_{M-1}. Les espaces d'approximation EIM et RB sont ainsi enrichis de manière alternative, avec une mise à jour de la décomposition affine à chaque étape.

Le nombre de résolutions éléments finis requis pour EIM se résume à la seule évaluation nécessaire pour la première base, et ne dépend plus de la taille de l'espace des paramètres. Avec $N + 1$ résolutions éléments finis au total – où N désigne la taille de l'espace d'approximation RB –, la méthode SER prévoit un gain de temps considérable pour la partie hors-ligne.

Plusieurs variantes de la méthode SER initiale sont proposées dans la thèse, principalement basées sur l'utilisation d'un indicateur d'erreur inspiré des récents travaux réalisés quant au développement d'estimateurs d'erreur pour les problèmes affines non-linéaires. S'il ne constitue pas une borne d'erreur, l'indicateur d'erreur proposé permet de guider la construction de l'espace d'approximation bases réduites.

La première variante propose l'enrichissement des espaces d'approximations EIM et RB par groupes de bases, dont la taille est adaptée en fonction de l'erreur d'approximation estimée. La deuxième vise à trier les évaluations bases réduites de l'algorithme glouton (2.11) selon leur précision, éliminant celles qui seraient jugées non significatives. Nous n'avons pas constaté d'amélioration notable en termes d'erreur d'approximation par rapport à la méthode SER initiale pour ces deux premières variantes.

La troisième variante propose de combiner plusieurs applications de la méthode SER. Le premier niveau correspond à la méthode SER initiale. Les suivants utilisent l'approximation bases réduites provenant du niveau précédent dans l'algorithme EIM. Obtenue à partir d'une décomposition affine plus précise, cet approximation est plus proche de la solution éléments finis, comparée au premier niveau. Les résultats obtenus montrent une nette amélioration de la convergence EIM à partir du second niveau, permettant de réduire l'erreur d'approximation.

L'implémentation de la méthode SER et de ses variantes dans la librairie `Feel++` est détaillée dans la thèse, et illustrée par des applications sur un benchmark 2D et sur le problème électro-thermique dédié aux aimants à haut champ. Ayant déjà fait l'objet de deux publications [Daversin and Prud'Homme, 2016, Daversin and Prud'Homme, 2015a], c'est une avancée importante dans l'utilisation de la méthode bases réduites pour les problème non-linéaires et non affines. De nombreuses variantes restent à étudier, et la question de la convergence *a priori* de cette méthode est quant à elle toujours ouverte.

Modèle multi-physiques pour les aimants à haut champ

La plupart des installations fournissant du champ magnétique intense utilisent des aimants de type Bitter. L'utilisation d'un modèle 2D axisymmétrique est satisfaisante pour ce type de géométries, et est pour le moment à la base de l'optimisation du design des aimants polyhélices. Des résultats expérimentaux tendent à montrer que le champ magnétique produit par ce type d'aimants est 3D, et que ces hypothèses ne sont pas adaptées. Dans la thèse, nous proposons un modèle multi-physiques 3D complet pour l'étude de ces aimants.

Produire un champ magnétique intense suppose de fournir un courant électrique dont l'intensité peut atteindre plusieurs dizaines de kA. Les pertes Joules induites provoquent une montée en température, pouvant être critique pour les matériaux. Le modèle électro-thermique basé sur l'équation de la chaleur dont le terme source correspond aux pertes Joule est la première composante de notre modèle.

La densité de courant qui en découle est une donnée d'entrée pour les équations de Maxwell, permettant d'évaluer le champ magnétique produit. Deux modèles sont proposés dans ce contexte. Le premier utilisant les éléments finis de Raviart-Thomas et de Nédélec, le deuxième basé sur la loi de Biot & Savart.

La dilatation thermique provenant de la montée en température, ainsi que les forces engendrées par le champ magnétique produit, créent des déformations dans l'aimant. Les déplacements et contraintes induits doivent êtres soigneusement pris en compte dans le design des aimants. Pour cela, nous proposons un modèle d'élasticité linéaire couplé aux modèles précédents, permettant d'évaluer ces quantités.

Les équations et les formulations variationnelles associées à chacun de ces modèles sont détaillées dans la thèse. La vérification des modèles est illustrée par des études de convergence 2D et 3D, ainsi qu'à l'ordre élevé lorsque c'est possible.

Le modèle multi-physiques éléments finis

Le modèle électro-thermique

Le potentiel électrique V est solution d'une équation de diffusion, dont le coefficient est la conductivité électrique σ. Les pertes Joules provenant de la circulation du courant dans l'aimant s'expriment comme le produit de la densité de courant $\mathbf{j} = \sigma \nabla V$ par le champ électrique induit ∇V. L'équation de la chaleur faisant intervenir la conductivité thermique k du matériau, est couplée au modèle précédent pour déduire la température T dans l'aimant.

Dans la gamme de température considérée – typiquement entre $20°C$ et $200°C$ –, la résistance des métaux augmente linéairement avec la température. De plus, les conductivités électrique et thermique sont liées par une relation de proportionnalité faisant intervenir T. Ces propriétés dépendent donc de la température, ce qui introduit une non-linéarité dans le modèle (3.18).

$$
\begin{aligned}
-\nabla \cdot (\sigma(T) \nabla V) &= 0 \text{ dans } \Omega \\
-\nabla \cdot (k(T) \nabla T) &= \sigma(T) \nabla V \cdot \nabla V \text{ dans } \Omega
\end{aligned}
\tag{20}
$$

Des conditions aux limites sont nécessaires pour que le problème soit bien posé. La circulation du courant est modélisée par une différence de potentiel entre l'entrée V_{in} et la sortie V_{out} du courant. Et l'environnement – air ou eau de refroidissement – est supposé électriquement isolant, se traduisant par un flux nul.

$$V = 0 \text{ sur } V_{in}, \quad V = V_D \text{ sur } V_{out} \quad \text{et} \quad -\sigma(T)\nabla V \cdot \mathbf{n} = 0 \text{ sur } \partial\Omega \backslash (V_{in} \cup V_{out}) \tag{21}$$

On considère que les échanges thermiques sont limités aux zones $\partial\Omega_{\text{cooled}}$ refroidies par circulation d'eau. La condition de Robin associée s'appuie sur un coefficient de transfert thermique h et la température de l'eau T_w.

$$-k(T)\nabla T \cdot \mathbf{n} = h(T - T_w) \text{ sur } \partial\Omega_{\text{cooled}} \quad \text{et} \quad -k(T)\nabla T \cdot \mathbf{n} = 0 \text{ on } \partial\Omega \backslash \partial\Omega_{\text{cooled}} \tag{22}$$

La non linéarité est prise en charge par des méthodes itératives de point fixe, de type Picard ou Newton.

Une première étude de convergence est présentée sur une version linéaire du modèle – avec $\sigma(T)$ et $k(T)$ constants –, basée sur une solution analytique. La vérification du modèle non-linéaire utilise quant à elle des estimateurs d'erreur à posteriori. L'implémentation de ces estimateurs est préalablement validée par comparaison avec l'erreur réelle, obtenue avec le modèle linéaire.

Le modèle magnétostatique

L'induction magnétique $\mathbf{B}$ – parfois abusivement appelée champ magnétique – est liée au champ magnétique $\mathbf{H}$ par la perméabilité magnétique μ, d'après la loi $\mathbf{B} = \mu\mathbf{H}$. L'équation de Maxwell-Thomson décrit $\mathbf{B}$ comme un champ à divergence nulle. L'induction magnétique dérive ainsi d'un champ $\mathbf{A}$, défini comme le potentiel vecteur magnétique.

$$\nabla \cdot \mathbf{B} = 0 \quad \Rightarrow \quad \exists A \mid \mathbf{B} = \nabla \times \mathbf{A} \tag{23}$$

L'équation de la magnétostatique est basée sur le théorème d'Ampère $\nabla \times \mathbf{B} = \mu\mathbf{j}$, donnant

$$\nabla \times \left(\frac{1}{\mu} \nabla \times \mathbf{A} \right) = \mathbf{j} \tag{24}$$

Dans notre cas, la perméabilité magnétique μ est une constante égale à la perméabilité du vide μ_0. Pour des matériaux dont l'aimantation n'est pas négligeable, ce coefficient peut dépendre du champ magnétique ce qui rend le modèle non-linéaire.

Le diagramme de De Rham (1.10) donne $\mathbf{A}$ dans H_{curl}, et $\mathbf{B}$ dans H_{div}. C'est pourquoi les éléments de Raviart-Thomas et de Nédélec introduits dans la première partie sont essentiels.

En supposant que la circulation du courant est limitée à un domaine fini, le champ magnétique est considéré comme nul à l'infini. Bien que cette condition aux bords soit nécessaire pour que le problème soit bien posé, le domaine de calcul est de dimension finie en pratique. Pour se faire, le domaine Ω comprend une boite enveloppant le conducteur,

dont les bords $\partial\Omega$ sont le plus loin possible.

$$\mathbf{A} \times \mathbf{n} = 0 \text{ sur } \partial\Omega \tag{25}$$

Cependant, l'équation (3.40) n'admet pas de solution unique. Deux formulations sont étudiées dans la thèse pour faire face à cette situation.

La formulation régularisée s'appuie sur les équations de Maxwell décrites dans le domaine fréquentiel. L'unicité de la solution est assurée par l'ajout d'un terme de régularisation à l'équation (3.40).

$$\nabla \times \left(\frac{1}{\mu} \nabla \times \mathbf{A}_\epsilon \right) + \epsilon \mathbf{A}_\epsilon = \mathbf{j} \tag{26}$$

La solution $\mathbf{A}_\epsilon$ du problème (3.47) tend vers $\mathbf{A}$ lorsque ϵ tend vers 0.

La formulation point-selle utilise la jauge de Coulomb imposant une condition de divergence nulle sur $\mathbf{A}$. Cette condition supplémentaire est imposée à l'aide d'un multiplicateur de Lagrange p.

$$\begin{aligned} \nabla \times \left(\frac{1}{\mu} \nabla \times \mathbf{A} \right) + \nabla p &= \mathbf{j} \text{ on } \Omega \\ \nabla \cdot \mathbf{A} &= 0 \end{aligned} \tag{27}$$

Le conditionnement des matrices associées aux problèmes (3.47) et (3.48) joue un rôle important dans la convergence des solveurs itératifs utilisés pour la résolution. L'utilisation des éléments finis de Nédélec dont les degrés de liberté sont localisés sur les arêtes peuvent détériorer ce conditionnement, et ainsi compromettre la convergence du modèle. Dans la thèse, nous décrivons une méthode de préconditionnement dédiée à ce type de problème, que nous testons avec les deux formulations.

La loi de Biot & Savart

La loi de Biot & Savart est couramment utilisée pour calculer le champ magnétique produit par un courant de densité de courant $\mathbf{j}$. Pour la décrire, on introduit Ω_{cond} le domaine associé au conducteur électrique, et Ω_{mgn} la région dans laquelle on souhaite calculer le champ. La loi de Biot & Savart donne l'expression du potentiel magnétique $\mathbf{A}$ et de l'induction magnétique $\mathbf{B}$ en tout point $\mathbf{r}$ de Ω_{mgn}

$$\mathbf{A}(\mathbf{r}) = \frac{\mu_0}{4\pi} \int_{\Omega_{cond}} \frac{\mathbf{j}(\mathbf{r}')}{\mid \mathbf{r} - \mathbf{r}' \mid} d\mathbf{r}' \quad \mathbf{r} \in \Omega_{mgn} \tag{28}$$

$$\mathbf{B}(\mathbf{r}) = \frac{\mu_0}{4\pi} \int_{\Omega_{cond}} \frac{\mathbf{j}(\mathbf{r}') \times (\mathbf{r} - \mathbf{r}')}{\mid \mathbf{r} - \mathbf{r}' \mid^3} d\mathbf{r}' \quad \mathbf{r} \in \Omega_{mgn} \tag{29}$$

La distance $\mid \mathbf{r} - \mathbf{r}' \mid$ apparaissant au dénominateur de (3.81) et (3.82) induit une singularité pour les points situés dans le conducteur. Plus précise que le modèle magnétostatique précédent, on privilégiera la loi de Biot & Savart pour les régions où sont placés les échantillons lors des expériences.

Au vu de la complexité des géométries, le calcul haute performance est un outil indispensable pour nos modèles. Si son implémentation en séquentiel ne représente pas de difficultés particulières, la loi de Biot & Savart n'est pas naturellement parallélisable.

Dans la thèse, nous proposons un algorithme original basé sur une gestion efficace des communications entre processeurs, dont les performances sont illustrées par des calculs sur des géométries d'aimants réels. Cet algorithme se révèle pertinent pour ce type de géométries, pour un coût calcul raisonnable. De plus, la comparaison des performances réalisée sur un supercalculateur – jusqu'à 192 processeurs – montre une scalabilité linéaire de l'algorithme.

Le modèle d'élasticité linéaire

Le modèle d'élasticité linéaire est couplé aux modèles élecro-thermique et magnétostatique pour évaluer les déplacements et contraintes générés par les forces magnétiques et par la dilatation thermique. Il repose sur l'équation d'équilibre

$$div(\bar{\bar{\sigma}}) + \mathbf{f} = 0 \tag{30}$$

où $\bar{\bar{\sigma}}$ est le tenseur des contraintes, et $\mathbf{f}$ les forces volumiques qui s'appliquent.

Défini à partir du tenseur des petites déformations $\bar{\bar{\varepsilon}} = \frac{1}{2}(\nabla\mathbf{u} + \nabla\mathbf{u}^T)$ où le déplacement $\mathbf{u}$ est l'inconnue de notre problème, le tenseur des contraintes $\bar{\bar{\sigma}}$ fait intervenir la température T, pour prendre en compte la dilatation thermique.

$$\bar{\bar{\sigma}}(\bar{\bar{\varepsilon}}) = \bar{\bar{\sigma}}^E(\bar{\bar{\varepsilon}}) + \bar{\bar{\sigma}}^T \quad \text{avec} \quad \bar{\bar{\sigma}}^T = -\frac{E}{1-2\nu}\alpha_T(T - T_0)I \tag{31}$$

où E et ν désignent respectivement le module Young et le coefficient de Poisson, α_T est le coefficient de dilatation thermique et T_0 la température de référence.

Les forces magnétiques sont les forces volumiques $\mathbf{f} = \mathbf{j} \times \mathbf{B}$.

Les conditions aux limites sont de deux types. On peut soit fixer les déplacements dans certaines régions $\partial\Omega_D$ avec de des conditions de Dirichlet, soit imposer des forces de pression sur $\partial\Omega_P$.

$$\mathbf{u} = \mathbf{u}_D \text{ sur } \partial\Omega_D \quad \text{ou} \quad \bar{\bar{\sigma}} \cdot \mathbf{n} = \mathbf{g} \text{ sur } \partial\Omega_P \tag{32}$$

Dans la thèse, nous détaillons l'étude de convergence réalisée jusqu'à l'ordre polynomial 3, en 2D et en 3D. Elle permet de vérifier que ce modèle satisfait les propriétés mathématiques attendues.

Les contraintes mécaniques subies par l'aimant sont évaluées à partir du tenseur des contraintes diagonalisé $\bar{\bar{\sigma}}^d$. Les critères de Tresca (3.95) et de Von-Mises (3.97) servent à

déterminer la nature de la déformation, *i.e.* élastique ou plastique.

$$tr_{\bar{\bar{\sigma}}^d} = \max_{1 \leqslant i < j \leqslant Dim} (\mid \bar{\bar{\sigma}}^d_{ii} - \bar{\bar{\sigma}}^d_{jj} \mid) \tag{33}$$

$$vm_{\bar{\bar{\sigma}}^d} = \sqrt{\sum_{1 \leqslant i < j \leqslant Dim} \frac{1}{2} \left(\bar{\bar{\sigma}}^d_{ii} - \bar{\bar{\sigma}}^d_{jj}\right)^2} \tag{34}$$

Le modèle d'élasticité linéaire précédemment décrit n'est valable que dans le domaine élastique. Pour des déformations plastiques, le tenseur des contraintes ne s'exprime plus comme une fonction linéaire de $\bar{\bar{\varepsilon}}$.

Le modèle réduit électro-thermique

Le modèle électro-thermique décrit précédemment est un élément clé dans la modélisation des aimants, dont la température peut atteindre des valeurs critiques pour les matériaux. Cependant, les données d'entrée nécessaires à ce modèle ne sont pas toujours connues de manière exacte.

Les propriétés des matériaux sont mesurées par le fournisseur, qui nous donne seulement un intervalle de définition pour ces valeurs. Les paramètres de fonctionnement des aimants – intensité du courant, conditions de refroidissement – sont également entachés d'incertitudes car ils sont difficiles à mesurer précisément.

La réalisation d'études paramétriques ainsi que l'application de méthodes de quantification d'incertitude sont essentielles dans ce contexte. Cependant, elles nécessitent un grand nombre d'évaluations du modèle, impliquant un coût calcul important. La méthode des bases réduites est donc tout à fait indiquée dans ce type d'applications.

Rappelons que la méthode des bases réduites permet de résoudre efficacement les EDPs paramétrées, pour un grand nombre de configurations. Dans notre cas, le paramètre $\boldsymbol{\mu}$ considéré regroupe les propriétés des matériaux – conductivité électrique σ_0, coefficient de température α et nombre de Lorentz L – et les conditions de fonctionnement de l'aimant – voltage V_D, coefficient de transfert h et température de l'eau de refroidissement T_w –.

$$\boldsymbol{\mu} = (\sigma_0, \alpha, L, V_D, h, T_w) \tag{35}$$

D'après l'expression des conductivités électrique $\sigma(T)$ et thermique $k(T)$,

$$\sigma(T) = \frac{\sigma_0}{1 + \alpha(T - T_0)} \quad \text{et} \quad k(T) = \sigma(T) L T \tag{36}$$

le problème couplé électro-thermique (3.18) présente une dépendance non affine en paramètres.

L'écriture d'une décomposition affine de (3.18) pour appliquer la méthodologie bases réduites requiert ainsi l'utilisation de la méthode d'interpolation empirique (EIM) introduite dans la première partie. Les termes concernés sont $\sigma(T)$, $k(T)$, ainsi que le terme source de l'équation de la chaleur qui dépend de $\sigma(T)$.

La non-linéarité du problème est gérée – comme pour le modèle éléments finis sous-jacent – par des méthodes de point fixe de type Picard ou Newton.

Les quantités d'intérêt considérées pour ce modèle sont nombreuses. On peut citer la température moyenne dans l'aimant, sa puissance, sa résistance ou encore le champ magnétique en un point.

Pour valider l'implémentation de ce modèle réduit, on s'interesse aux erreurs d'approximation EIM et RB commises par rapport au modèle éléments finis. L'étude de convergence consiste à vérifier que cette erreur décroît avec l'enrichissement de l'espace d'approximation associé. Dans la thèse, on détaille les études de convergence réalisées sur des géométries réelles d'aimants allant d'un secteur d'aimant Bitter à une hélice à refroidissement radial complète. Toutes ont montré la possibilité d'obtenir une erreur d'approximation satisfaisante pour un nombre de fonctions de base raisonnable.

Le gain en temps de calcul est démontré par son application sur une hélice à refroidissement radial, dont le maillage est formé de 500 000 noeuds. Si la résolution éléments finis prend 16 minutes, l'approximation bases réduites est 150 fois plus rapide (6.7 secondes).

Applications numériques

La dernière partie de la thèse expose différentes applications numériques reposant sur les modèles développés, participant ainsi à leur validation. Dans ce résumé, nous introduisons seulement une partie de ces applications, illustrées par une sélection de résultats.

Analyse de sensibilité

L'analyse de sensibilité consiste à évaluer l'influence de l'incertitude que l'on a sur les paramètres d'entrée, sur une quantité d'intérêt spécifique. Ce type d'étude nécessitant un grand nombre d'évaluations du modèle, la méthode des bases réduites est parfaitement adaptée pour le calcul des quantités d'intérêt en question.

Pour cet exemple, nous appliquons le modèle électro-thermique réduit à l'hélice à refroidissement radial (figure 8.1), dont le maillage est formé de 500 000 noeuds.

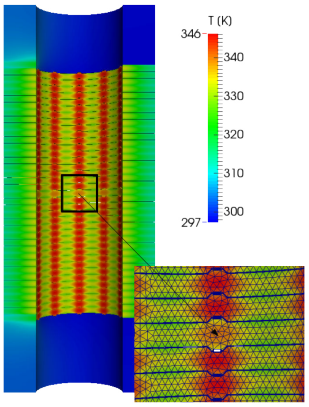

Figure 2 – Approximation RB de la température

Les isolants insérés le long de la découpe des hélices induisent localement des points chauds, ce qui renforce les besoins d'études précises de la température. On se focalise ici sur la température moyenne comme quantité d'intérêt.

Les propriétés des matériaux sont données par le fournisseur ou mesurées en interne. La température de l'eau est une moyenne entre les mesures à l'entrée et à la sortie de l'aimant. Le coefficient de transfert thermique est estimé à partir de corrélations hydrauliques. Enfin, on fait varier l'intensité du courant injectée dans l'aimant pour des valeurs correspondant à une utilisation "standard".

σ_0	$[50; 50.2] \quad MS.m^{-1}$
α	$[3.3 \times 10^{-3}; 3.5 \times 10^{-3}] \quad K^{-1}$
L	$[2.5 \times 10^{-8}; 2.9 \times 10^{-8}]$
I	$[25000; 35000] \quad A$
h	$[70000; 90000] \quad W.m^{-2}.K^{-1}$
T_w	$T_w \in [293, 313] \quad K$

Table 1 – Paramètres d'entrée pour l'analyse de sensibilité

L'étude suivante est basée sur 300 évaluations, réalisées sur un ensemble de paramètres répartis selon une loi de probabilité uniforme. Le modèle électro-thermique réduit nous permet de calculer efficacement la température moyenne pour chacun de ces paramètres. Notre modèle est ensuite couplé à la librairie `OpenTurns` dédiée à la quantification d'incertitude, pour en déduire la moyenne des quantités d'intérêt, l'écart type, ou encore les quantiles que nous ne détaillons pas ici.

En particulier, on s'intéresse aux indices de Sobol, qui nous permettent de quantifier l'influence des paramètres (table 8.5) sur la température moyenne. Dans cette étude, on se limite aux indices d'ordre 1 supposant les paramètres d'entrée comme indépendants.

σ_0	1.9×10^{-5}
α	2.3×10^{-4}
L	0.0028
I	0.75
h	0.069
T_w	0.16

Table 2 – Indices de Sobol pour la température moyenne

Sans compter l'influence évidente de l'intensité du courant, ce sont les paramètres de refroidissement qui ont le plus d'impact sur la température moyenne.

SER appliquée au modèle électro-thermique

La seconde application introduit l'utilisation de la méthode SER sur le modèle réduit électro-thermique précédent. Cette étude s'appuie sur la géométrie d'un secteur d'aimant Bitter, et compare les performances obtenues par rapport à la méthode bases réduites

standard.

Pour cela, on étudie l'erreur entre le modèle réduit – basé sur M fonctions de bases EIM, et un espace d'approximation RB de taille N –, et le modèle éléments finis sous jacent. La table 11.2 donne les erreurs maximales et moyennes $max(\epsilon^u_{M,N})$ et $mean(\epsilon^u_{M,N})$ (resp. $max(\epsilon^s_{M,N})$ et $mean(\epsilon^s_{M,N})$) sur la solution (resp. sur la quantité d'intérêt considérée, à savoir la température moyenne), obtenues avec la méthode standard. Ces résultats s'appuient sur un ensemble de 1000 paramètres utilisé pour l'ensemble de l'étude.

N	M	$max(\epsilon^u_{M,N})$	$max(\epsilon^s_{M,N})$	$mean(\epsilon^u_{M,N})$	$mean(\epsilon^s_{M,N})$
5	5	1.64e+1	1.94e-1	1.51e+0	1.69e-2
10	10	6.84e+0	8.24e-2	4.90e-1	5.96e-3
15	15	6.30e-2	4.90e-4	5.33e-3	3.16e-5
20	20	1.31e-2	1.65e-4	1.28e-3	1.33e-5
25	25	9.80e-3	6.74e-5	6.88e-4	5.77e-6

Table 3 – Méthode RB standard

La table 11.3 donne les erreurs obtenues en utilisant la méthode SER, pour la même configuration.

N	M	$max(\epsilon^u_{M,N})$	$max(\epsilon^s_{M,N})$	$mean(\epsilon^u_{M,N})$	$mean(\epsilon^s_{M,N})$
5	5	1.05e+1	2.09e-2	1.26e+0	3.27e-3
10	10	5.07e-1	3.42e-3	1.05e-1	4.69e-4
15	15	5.24e-1	1.05e-3	3.95e-2	1.18e-4
20	20	9.23e-2	1.89e-4	8.78e-3	2.79e-5
25	25	3.26e-2	1.90e-4	3.59e-3	2.72e-5

Table 4 – Méthode SER

Au vu des erreurs obtenues, on note que la qualité de l'approximation est peu détériorée par rapport à l'approche standard. Ces résultats confirment la pertinence de la méthode SER, montrant que l'on peut espérer de bons résultats pour un coût calcul hors-ligne moindre.

Les tables 11.2 et 11.3 s'appuient sur une sélection aléatoire des paramètres utilisés pour la construction de l'espace d'approximation RB. Les résultats obtenus en combinant SER avec l'utilisation d'un algorithme glouton – via l'indicateur d'erreur proposé – montrent une amélioration significative pour la qualité de l'approximation.

Ces comparaisons, ainsi que l'étude des variantes proposées pour SER sont détaillées dans la thèse. La variante la plus prometteuse s'avère être la méthode multi-niveaux combinant plusieurs applications de l'algorithme SER. La figure 11.5 montre les courbes de convergence EIM associées aux approximations de $\sigma(T)$ et de $k(T)$. On peut voir que la qualité des approximations EIM est nettement meilleure dès le deuxième niveau.

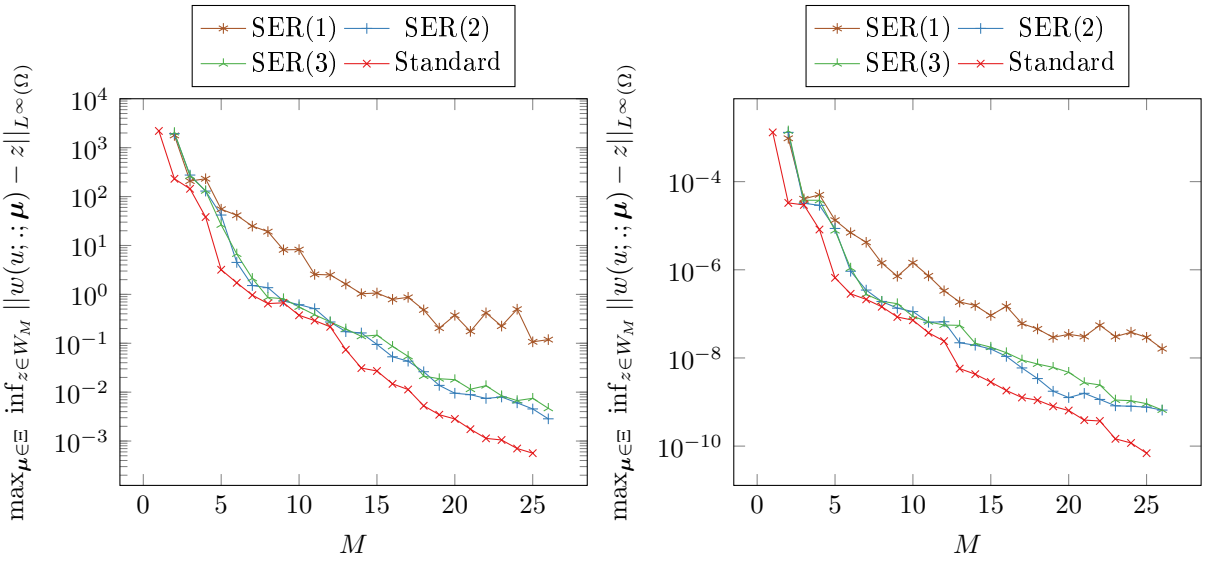

(a) EIM $\sigma(T)$ (b) EIM $k(T)$

Figure 3 – Méthode SER multi-niveaux - convergence EIM

Enfin, nous détaillons dans la thèse l'étude des performances de la méthode SER en termes de temps de calcul pour l'hélice à refroidissement radial déjà évoquée précédemment. Le facteur de gain observé sur l'algorithme glouton EIM atteint deux ordres de magnitude, pour une approximation bases réduites très peu détériorée.

Validation du modèle magnétostatique

Initialement, les modèles utilisés au LNCMI pour calculer le champ magnétique produit par les aimants sont basés sur des hypothèses 2D axisymmétriques. Des expériences de magnétoscience réalisées au laboratoire – en Résonance Magnétique Nucléaire (RMN), ou en lévitation magnétique – semblent pourtant indiquer que le champ magnétique mesuré peut être très différent de l'approximation axisymmétrique.

Pour confirmer ces observations, nous avons mené une campagne de mesures du champ magnétique de ce type d'aimants. Dans cet exemple, on propose d'utiliser l'algorithme parallèle de Biot & Savart développé dans la thèse pour calculer le champ magnétique et tenter de reproduire ces résultats. Cette comparaison sert également à valider notre implémentation.

Pour les mesures expérimentales, nous utilisons une sonde à effet Hall tri-axe (figure 9.3c) mesurant les composantes B_x, B_y et B_z du champ magnétique (figure 9.3d). Le porte-sonde développé pour cette expérience permet de déplacer la sonde hors de l'axe de l'aimant – où l'effet 3D sera le plus visible –, le long d'un cercle de rayon constant $r = 17.5\ mm$ (figure 9.8b).

(a) Sonde à effet Hall dans son porte-sonde

(b) Gaussmètre (LakeShore Model 460)

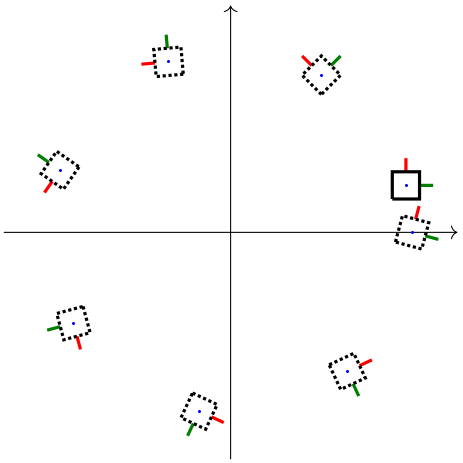

(c) Rotation de la sonde

Figure 4 – On mesure le champ sur un cercle de rayon constant à l'aide d'une sonde à effet Hall

Les mesures ont été réalisées sur un aimant polyhélices formé de 14 hélices à refroidissement longitudinal, dans lequel nous avons injecté un courant de 500 A pour un champ maximum de 0.361 T. Pour être comparés aux résultats obtenus avec le modèle axisymmétrique, nous étudions les variations des composantes B_r et B_θ du champ magnétique le long du cercle.

Les figures 9.16 et 9.17 comparent les résultats obtenus à une hauteur $z = 100\ mm$ au-dessus du centre magnétique. Elles comparent les résultats obtenus *(i)* lors de deux expériences, *(ii)* avec le modèle axisymmétrique, et *(iii)* avec notre modèle de Biot & Savart appliquée sur des maillages plus ou moins fins.

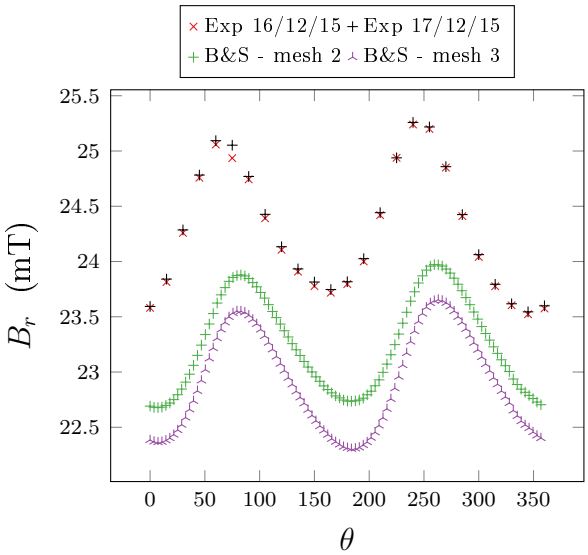

Figure 5 – Comparaison de B_r le long du cercle de rayon $r = 17.5\ mm$ à $z = 100\ mm$

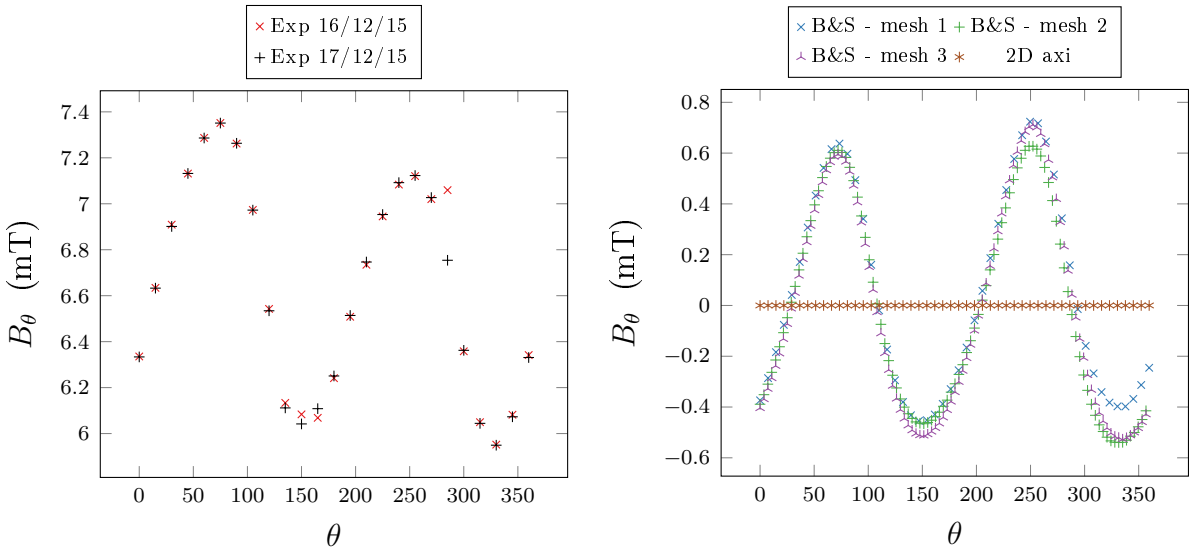

(a) Experimental (b) Numérique

Figure 6 – Comparaison de B_θ le long du cercle de rayon $r = 17.5\ mm$ à $z = 100\ mm$

Les mesures expérimentales réalisées sont reproductibles, et permettent tout d'abord de confirmer les observations préliminaires, attestant que le champ magnétique produit par les polyhélices est effectivement 3D. Les variations observées le long du cercle de rayon $r = 17.5\ mm$ à $z = 100\ mm$ sont bien captées par notre modèle basé sur la formulation de Biot & Savart, validant son implémentation parallèle. D'autres comparaisons sont détaillées dans la thèse, notamment à $z = -100\ mm$ pour lesquelles les résultats sont moins satisfaisants, possiblement dûs à l'usure de l'aimant ou à l'environnement magnétique. De nouvelles campagnes de mesures sont actuellement en cours pour étayer cette étude préliminaire.

Simulations pour l'aimant hybride

Les aimants hybrides visent à produire des champs magnétiques continus supérieurs à 40 T en combinant un aimant résistif et un aimant supraconducteur. Actuellement, le seul aimant de ce type en fonctionnement se trouve en Floride, et permet d'atteindre 45 T. Le développement d'un aimant hybride est en cours à Grenoble, s'appuyant à la fois sur des aimants polyhélices et Bitter pour la partie résistive.

Pour cette application numérique, on se limite à l'insert polyhélices composé de 14 hélices à refroidissement longitudinal. Son design est d'autant plus critique du fait du champ de fond produit par les aimants Bitter (9.2 T) et supraconducteur (8.5 T) qui l'entourent. Cette étude vise à anticiper le comportement de cet aimant dans son environnement de fonctionnement, à partir du modèle multi-physiques éléments finis proposé.

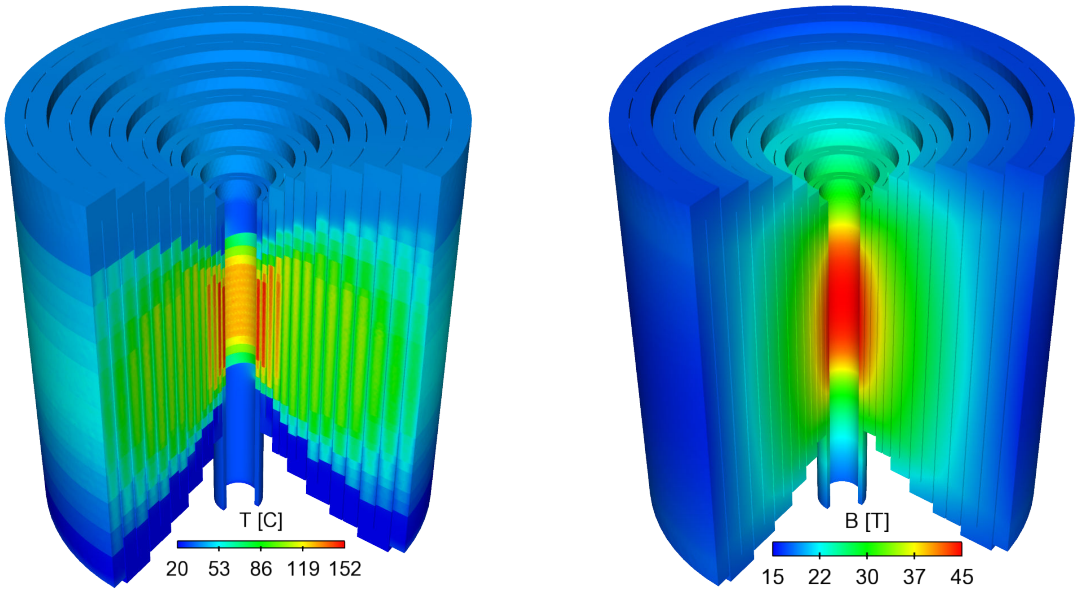

(a) Température (b) Champ magnétique

Figure 7 – Température et champ magnétique

Dans la thèse, ces résultats sont comparés au comportement obtenu pour le même type d'aimant, mais avec un design prévu pour fonctionner dans un environnement standard, *i.e.* sans champ de fond supraconducteur. En plus de prévoir la répartition de la température et des contraintes dans l'ensemble de l'insert – ce qui n'était pas réalisable avec les anciens modèles –, cette analyse prédictive permet de donner des spécifications plus précises notamment en termes de matériaux.

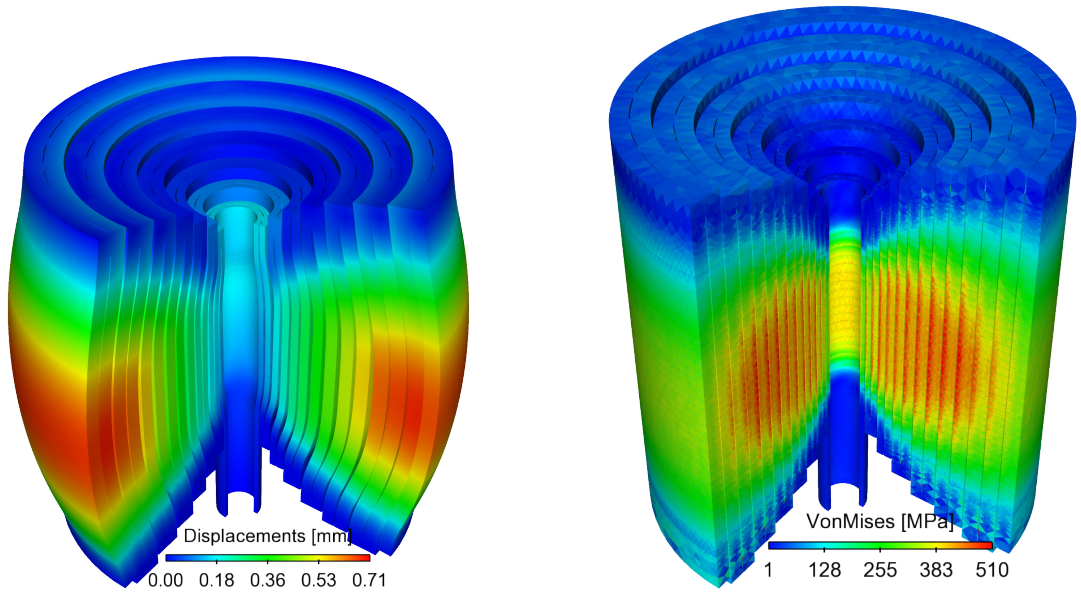

(a) Déplacements (b) Contraintes (Von-Mises)

Figure 8 – Déplacements et contraintes

D'un point de vue numérique, cette étude démontre la faisabilité de notre modèle multi-physiques sur ce type de problème. Le temps d'une simulation complète est

d'environ 1 heure sur 32 processeurs, pour un maillage comptant environ 1 million de degrés de liberté.

Conclusion

Nous avons introduit à travers cette thèse un ensemble d'outils dédiés à la modélisation des aimants à haut champ. Ces développements sont basés sur la méthode éléments finis et son implémentation dans la librairie `Feel++`.

Nous proposons un modèle multi-physiques non-linéaire 3D couplant un modèle électro-thermique, un modèle de magnétostatique et un modèle d'élasticité linéaire. Chacun d'eux est vérifié à travers des études de convergence, et validé par comparaison avec des mesures expérimentales lorsque c'est possible.

Les équations de Maxwell à la base du modèle de magnétostatique impliquent l'utilisation d'éléments finis spécifiques. L'implémentation des éléments H_{div}-conforme de Raviart-Thomas et H_{curl}-conforme de Nédélec dans `Feel++` est une contribution de la thèse. Le champ magnétique produit par les aimants peut également être calculé d'après la loi de Biot & Savart pour laquelle nous proposons un algorithme parallèle original.

Au vu de la taille des problèmes à résoudre, le coût calcul peut être un frein pour la réalisation d'études paramétriques ou la quantification d'incertitude. Dans ce contexte, nous proposons l'application de la méthode des bases réduites pour le modèle électro-thermique, dont les performances sont illustrées par plusieurs applications concrètes. Les pré-calculs associés restent néanmoins coûteux, du fait de la non-linéarité et de la dépendance non affine. L'algorithme SER – Simultaneous EIM and RB – est un apport original de cette thèse, dédié à ce type d'équations. Cette méthode permet un gain de temps considérable, tout en conservant une approximation bases réduites de qualité. Plusieurs variantes pour SER sont également proposées et testées.

Pour la suite du projet, l'un des objectifs premier est l'enrichissement du modèle multi-physiques, notamment avec un modèle hydraulique plus avancé permettant de mieux prendre en compte le refroidissement. On pourrait aussi envisager un modèle d'élasticité non-linéaire pour les déformations plastiques. Un modèle instationnaire peut également être considéré, pour mieux comprendre ce qu'il se passe lors d'une coupure de courant par exemple.

Les méthodes numériques sous jacentes présentent également des perspectives d'évolution. L'implémentation des éléments H_{div}-conforme et H_{curl}-conforme d'ordre élevé, ainsi que l'application de méthodes HDG – Hybrid Discontinuous Galerkin – sont d'ores et déjà prévues. Les méthodes HDG offrent une approximation optimale à la fois pour la variable en question et pour son flux. Dans notre cas, elles permettraient une meilleure approximation de l'intensité et de la densité du courant, aidant en particulier à la convergence du modèle de magnétostatique.

Le modèle électro-thermique réduit pourra être complété pour obtenir une version réduite du modèle multi-physiques complet. Enfin, la méthode SER offre de belles perspectives qui méritent de continuer son exploration.

Contents

Notations

Methods

FE	:	Finite Element
RB	:	Reduced Basis
EIM	:	Empirical Interpolation Method
SER	:	Simultaneous EIM and RB

Mesh

d	:	Geometrical dimension $d = 1$, 2 or 3
(K, P_K, Σ_K)	:	Finite Element tuple
Γ_h	:	Mesh of characteristic size h
K	:	Geometrical element $K \in \Gamma_h$
$\hat{K}$	:	Reference geometrical element
ϕ_K^{geo}	:	Geometrical transformation $\phi_K^{\text{geo}} : \hat{K} \to K$
$\mathbf{n}$	:	Unit outward normal
$\mathbf{t}$	:	Unit outward tangent

Functional spaces

Ω	:	Regular bounded domain $\Omega \subset \mathbb{R}^d$
$X(\Omega)$	:	Continuous functional space
$(\cdot, \cdot)_X$	:	Scalar product associated with function space X
∇f	:	Gradient of scalar function f
$\nabla \cdot \boldsymbol{f}$	:	Divergence of vectorial function $\boldsymbol{f}$
$\nabla \times \boldsymbol{f}$	:	Curl of vectorial function $\boldsymbol{f}$
$L_2(\Omega)$	:	$\{f \mid \int f^2 < \infty\}$
$H_1(\Omega)$	:	$\{f \in L_2(\Omega) \mid \nabla f \in [L_2(\Omega)]^d\}$
$H_{\text{div}}(\Omega)$	:	$\{\boldsymbol{f} \in [L_2(\Omega)]^d \mid \nabla \cdot \boldsymbol{f} \in L_2(\Omega)\}$
$H_{\text{curl}}(\Omega)$	:	$\{\boldsymbol{f} \in [L_2(\Omega)]^d \mid \nabla \times \boldsymbol{f} \in [L_2(\Omega)]^d\}$

Finite Element method

$\mathcal{N}$	:	Global finite element space dimension
$\mathcal{B}$	:	Primal basis $\mathcal{B} = \{\zeta_i\}$
ϕ_i	:	FE basis function
$\hat{\phi}_i$	:	FE basis function on reference element $\hat{K}$
$X_{\mathcal{N}}(\Omega)$	:	FE approximation space $X_{\mathcal{N}}(\Omega) = span\{\phi_i\}_{1 \leqslant i \leqslant \mathcal{N}}$
$u_{\mathcal{N}}$	:	FE approximation

Reduced basis method

N	:	RB space dimension
ξ_i	:	RB function
S_N	:	RB trainset
W_N	:	RB approximation space $W_N = span\{\xi_i\}_{1 \leqslant i \leqslant N}$
u_N	:	RB approximation
M	:	EIM dimension
q_m	:	EIM basis function
$\bar{S}_M$	:	EIM trainset
$\bar{W}_M$	:	EIM approximation space $\bar{W}_M = span\{q_m\}_{1 \leqslant m \leqslant M}$
$\boldsymbol{\mu}$	:	Input parameter
$\mathcal{D}$	:	Parameter space
$\mathcal{Y}g$	:	Riesz representation of the functional g

High field magnets modeling

$\mathbf{E}$	:	Electrical field $[V.m^{-1}]$
$\mathbf{j}$	:	Current density $[A.m^{-2}]$
T_0	:	Reference temperature $[K]$
σ_0	:	Electrical conductivity at reference temperature T_0 $[S.m^{-1}]$
$\sigma(T)$	:	Electrical conductivity $[S.m^{-1}]$
ρ_0	:	Resistivity at reference temperature T_0 $[\Omega.m]$
$\rho(T)$	:	Resistivity $[\Omega.m]$
k_0	:	Thermal conductivity at reference temperature T_0 $[W.m^{-1}.K^{-1}]$
$k(T)$	:	Thermal conductivity $[W.m^{-1}.K^{-1}]$
V	:	Electrical potential $[V]$
T	:	Temperature $[K]$
L	:	Lorentz number
h	:	Heat transfer coefficient $[W.m^{-2}.K^{-1}]$
T_w	:	Water cooling temperature $[K]$

$\mathbf{H}$	:	Magnetic field $[A.m^{-1}]$
$\mathbf{B}$	:	Magnetic induction - often abusively referred as magnetic field $[T]$
$\mathbf{A}$	:	Magnetic potential vector $[V.s.m^{-1}]$
μ_0	:	Vacuum permeability $[T.m.A^{-1}]$
$\bar{\bar{\sigma}}$	:	Stress tensor
$\mathbf{f}$	:	Volumic forces
$\bar{\bar{\epsilon}}$	:	Tensor of small deformations
$\mathbf{u}$	:	Displacement vector $[m]$
ν	:	Poisson's ratio
E	:	Young modulus $[Pa]$
α_T	:	Thermal dilatation coefficient $[K^{-1}]$

Introduction

The magnetic field, given in Tesla in the International System of Units, is present throughout our environment. For instance, the magnetic field in the human brain is about $10^{-12}\ T$ while the magnetars are characterized by their extremely powerful magnetic fields which can reach up to $10^{11}\ T$. We can also quote the Earth's magnetic field whose intensity is $4.7 \times 10^{-5}\ T$.

Magnetic fields can be generated in various ways. There are magnetized materials whose magnetization, either permanent or remanent, naturally produces a magnetic field. The magnetic field can also arise from the circulation of an electrical current within a conductive material, solid or liquid. The complete mathematical description of electromagnetism has been provided by James Clerk Maxwell since 1864 [Maxwell, 1865], resulting in Maxwell's equations. Electromagnetism has hence been perfectly characterized for more than 100 years. From this knowledge, people have understood how to create and control magnetic fields.

The first developments aiming to generate strong magnetic fields date from the early 1900s, based on the theoretical investigations of Fabry in 1898. In 1914, Deslandres and Perot successfully built a solenoid able to generate $5\ T$. At that time, several electromagnets able to produce a magnetic field of similar intensity have been developed. In France, the big electromagnet of Bellevue [Cotton, 1928] operated from 1920 to 1970 offering a larger useful volume, hence giving the possibility to conduct numerous experiments. Nowadays, this 120 tons electromagnet is a museum piece. The modern techniques for the generation of steady magnetic fields had emerged in the 1940s through the works of Francis Bitter. Further historical details can be found in [D.H. Parkinson, 1967].

Since then, various electromagnets have been developed following or improving the technology introduced by F. Bitter (see [Montgomery, 1969]). In the late 1960's, magnets made of superconducting materials which conduct current without electrical resistance at low temperature, namely below $4\ K$, were built. These magnets are now commonly fabricated and are able to produce up to $23.5\ T$. This record magnetic field value represents the current limit for Low Temperature Superconductors (LTS). It is provided by a magnet located at the Ultra-High Field European NMR Center in Lyon, France.

Electromagnets are widely used in a large range of domains. As an example, medical imagery uses electromagnets – generating from $1\ T$ to $3\ T$ – to put in resonance certain atoms of the matter. These magnets enable to obtain a clear picture of the human body.

Note that there also exist High Temperature Superconductors (HTS) which remain superconducting at higher temperature. Research is currently carried out to use this kind of materials, discovered in the 1980s. It is the focus of active developments as they should enable to design magnets breaking the LTS magnetic field limit.

To reach high magnetic fields, *i.e.* higher than 24 T, watercooled resistive magnets made out of resistive materials as copper alloys are used.

More generally, high magnetic fields constitute a powerful tool for researchers to probe and determine the properties of matter. For instance, they can serve to understand the physics of superconducting state in High Temperature Superconductors. They can also provide microgravity conditions. Indeed, the magnetic forces generated in some magnetic materials can locally balance the gravity, allowing to perform on Earth experiments that would otherwise have to be performed in space.

Only few electromagnets in the world allow to reach high magnetic fields. They can be found in laboratories that operate as user facilities. The European laboratories are grouped into the European Magnetic Field Laboratory (EMFL) providing high field magnets to scientists through two annual calls for experiments. Present in Grenoble and Toulouse, the Laboratoire National des Champs Magnétiques Intenses (LNCMI) is the French high field magnet laboratory. The electromagnets developed on the Grenoble site can reach up to 36 T for several hours.

At LNCMI, various electromagnet technologies are used to perform the magnet design. At first, the Bitter electromagnets, which consist of a solenoid made of a stack of conducting disks. These disks are arranged so that the current moves in a helical path through them. To control the increase of temperature due to the electrical current, these magnets are cooled with water going through holes pierced in their disks. This kind of electromagnets, invented by F. Bitter in 1933, is the most commonly used in high magnetic field facilities. At the present time, the record magnetic field obtained with this technology is 38 T reached in Hefei, China.

A second technology consists in the so-called polyhelix magnets made of concentric copper alloy tubes, which are helically cut. Exclusively developed at LNCMI, two types of polyhelix are considered depending on their water cooling process. In the first case, the helical slits performed by spark erosion through Electrical Discharge Machine (EDM) are filled with a mix of epoxy glue and glass marbles to ensure the electrical insulation between turns. The cooling water thus only circulates between the copper tubes, for which we employ the term of longitudinally cooled helices. As to the so-called radially cooled helices, the electrical insulation between turns is ensured by the insertion of insulators regularly arranged over the helix cut. In this context, the cooling water flows also between the turns, allowing a better cooling of the magnet. More details on these technologies can be found in [Debray et al., 2002] and [Debray et al., 2012].

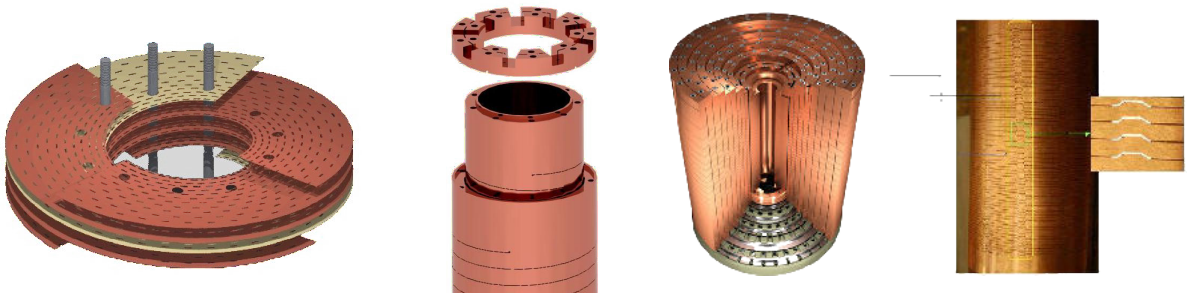

(a) Bitter magnet
(up to 1m in diameter)

(b) Polyhelix magnets
(up to 400mm in diameter)

Figure 9 – Various resistive magnet technologies are used to reach high magnetic fields

High field magnet modeling

In a strong international competition for higher magnetic fields, the LNCMI needs to improve the characteristics of its magnets to remain a major competitor. Nevertheless, the development of magnets able to generate higher and higher and/or more and more homogeneous fields represents a challenge in terms of materials and design. As mentioned in [Trophime et al., 2002], numerical simulation proves to be an essential tool for the optimization process.

Based on a collaboration between the university of Strasbourg and the LNCMI, the HiFiMagnet project aims to develop a software toolchain for high field magnet modeling. As part of this project, the main objective of this thesis is to provide a range of non-linear coupled models that are suitable in this context. Besides the complexity of the geometries, the input data is subject to uncertainty which has to be taken into account in the model. The aimed 3D multi-physics model has hence to be efficient in addition to being generic and reliable.

The developments provided in this thesis allow to efficiently perform numerical simulations on real magnet geometries thanks to High Performance Computing techniques. Moreover, its combination with model order reduction methodology enables to take into account the previously mentioned uncertainties, thus covering the whole input parameter space. The significant gain in terms of computational time especially makes parametric studies and uncertainty quantification feasible, which was unattainable with earlier models.

Feel++ : Finite Element Embedded Library

The physics involved within high field magnets study are described by coupled Partial Differential Equations (PDE), which form the considered model.

Especially adapted for such complex geometries, the Finite Element (FE) method is assessed as being suitable for the numerical resolution of these PDEs. In this context, the FE method is at the basis of all the developments undertaken through this thesis.

The use of the `Feel++` library which stands for *Finite Element Embedded Language in C++* has been selected for this purpose. It offers a language specifically designed to address the resolution of PDEs relying on a domain specific embedded language (DSEL). Embedded into the C++ language, this library helps in the formulation of the considered equations being close to their mathematical synthax.

`Feel++` has already been the subject of various publications, amongst which [Prud'homme, 2006] and [Prud'Homme et al., 2012].

`Feel++` is an open-source library involved in numerous scientific projects which especially benefits from the development of state of the art methods coming from diverse domains. It is combined with various dedicated libraries especially PETSc [Balay et al., 2012] and Hypre [Falgout et al., 2006] which offer a wide range of solvers and preconditionners, and GMSH [Geuzaine and Remacle, 2009] for meshing.

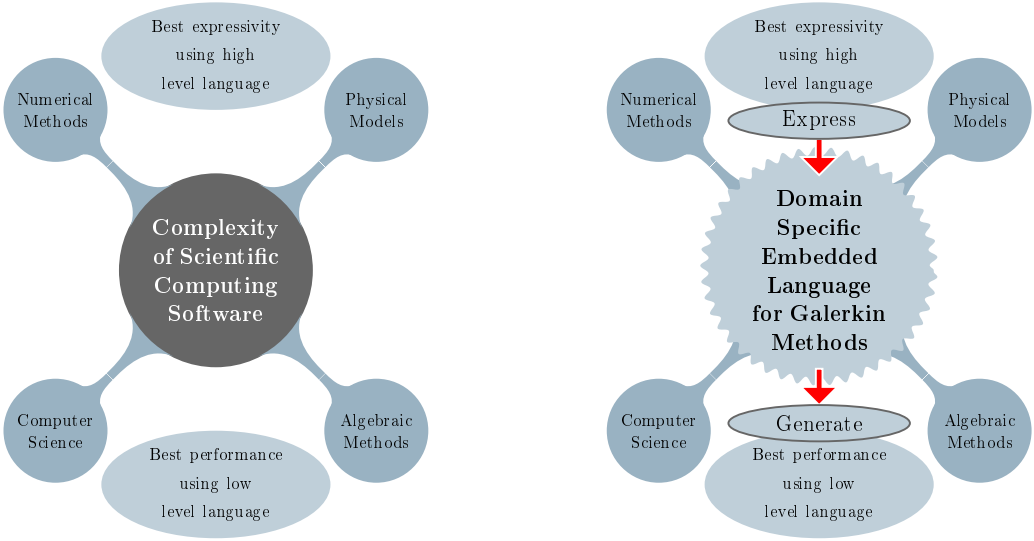

Figure 10 – The DSEL offered by `Feel++` provides high level language to break the complexity of scientific computing software while keeping the performances of a low level language.

Its High Performance Computing capability is also a core feature of the library allowing seamless parallel computing. This is a very important aspect in the context of high field magnet modeling in view of the size and the complexity of the considered problems.

Based on its finite element method implementation, `Feel++` also provides a framework dedicated to the reduced basis method. The use of this model order reduction method is a key point of the developments presented in this thesis in the context of uncertainty quantification previously discussed.

Plan

This manuscript is organized into four parts.

The first part is dedicated to the mathematical tools on which the presented developments are based.

The Chapter 1 focuses on the finite element method in a theoretical point of view. Starting with the description of the standard Lagrange finite elements, this chapter especially deals with the H_{div} and H_{curl} conforming finite elements as basis ingredients in the development of the aimed 3D multi-physics model.

The Chapter 2 is dedicated to the reduced basis methodology specifically applied to the non-linear and non affinely parametrized problems that concern us. To this end, we introduce the so-called Empirical Interpolation Method (EIM) used to recover the core ingredients involved in the reduced basis methodology.

As an original contribution, the Section 2.3 proposes a combination of these two methods allowing a decrease of the resulting computational cost. Named SER for Simultaneous Empirical interpolation and Reduced basis method, this work is the subject of two publications [Daversin and Prud'Homme, 2016] and [Daversin and Prud'Homme, 2015a].

The second part describes the components of the multi-physics model dedicated to high field magnets study based on the previously introduced methods. The Chapter 3 focuses on the finite element multi-physics model, while the Chapter 4 deals with the use of the reduced basis method.

The current flow and the resulting temperature increase are ruled by the non-linear coupled electro-thermal model detailed in the first chapter.

Coupled to the latter, the magnetostatic model secondly described in this chapter allows to determine the magnetic effect of the current flow within the magnet. We distinguish two techniques to compute the magnetic field both based on Maxwell's equations. The 3D magnetostatic model allows to compute the magnetic field both in and around the magnet. The initial problem being ill-posed, we consider several formulations allowing to overcome the resulting numerical issues. This model requires also the H_{curl}-conforming finite elements previously discussed, combined with appropriate preconditioning techniques which are briefly described. The Biot and Savart's law is the second alternative for solving Maxwell's equations. It is especially well suited to determine the magnetic field seen by scientists.

Finally, the last section of this chapter focuses on the linear elasticity model coupled with the two previous ones. It takes into account both the forces induced by the magnetic field and the ones induced by the thermal dilatation, enabling to quantify their mechanical effects.

As mentioned, the Chapter 4 lastly details the characteristics of the reduced version of the electro-thermal model. Already introduced in several contributed talks, this model is illustrated with numerical results in [Daversin et al., 2016b].

The third part of this manuscript deals with the significant contributions made to `Feel++` in the context of this thesis.

Initially not available within the library, the implementation of the Raviart-Thomas and Nédélec finite elements of lowest order are the focus of the Chapter 5. This chapter details their integration into the `Feel++` finite element framework using the theoretical considerations of the first part.

The Chapter 6 is dedicated to the implementation of the Biot and Savart's law offering

an accurate evaluation of the magnetic field. Although trivial in a sequential context, the implementation of this formulation cannot be easily parallelized. We propose an algorithm based on a smart strategy for the communications between processors. The performances of this algorithm which is original to our knowledge are illustrated by numerical experiments performed on a supercomputer.

Finally, the Chapter 7 of this part details the implementation of the previously mentioned SER method as part of the `Feel++` reduced basis framework.

The last part of this thesis is dedicated to numerical experiments illustrating the whole set of methods and models previously introduced. All of these applications address concrete needs of LNCMI in terms of numerical simulations.

The Chapter 8 illustrates the use of the reduced electro-thermal in the context of parametric studies and uncertainty quantification providing essential information for magnet maintenance.

The Chapter 9 is dedicated to the setting up of an experimental measurement campaign especially undertaken as part of this thesis, which first enables to validate our magnetostatic model. These measurements especially highlight the pertinence of considering a full 3D model instead of the existing 2D axisymmetrical ones.

Still on the subject of model validation, the Chapter 10 describes the validation of the linear elasticity model from the comparison to commercial software since only few experimental data are available. Indeed, the magnets are operated in a highly constrained environment due both to high pressure and lack of space which makes the instrumentation difficult.

The Chapter 11 focuses on the application of the proposed SER method within the reduced electro-thermal model. The use of the initial SER method as well as its variants on real magnet geometries proves their relevance for such applications.

Finally, the Chapter 12 emphasizes on the feasability of our multi-physics model on complete magnet inserts in the context of the development of the future Hybrid magnet [Pugnat et al., 2016] aiming to reach 43 T in a 34 mm diameter bore.

Publications

[1] C. Daversin and C. Prud'Homme. Simultaneous empirical interpolation and reduced basis method, application to non-linear multi-physics problem. Submitted, 2016.

[2] C. Daversin, C. Prud'Homme, and C. Trophime. Full three-dimensional multiphysics model of high-field polyhelices magnets. *IEEE transactions on applied superconductivity*, 26(4), January 2016.

[3] C. Daversin and C. Prud'Homme. Simultaneous empirical interpolation and reduced basis method for non-linear problems. *C. R. Acad. Sci. Paris, Ser. I*, 353(12):1105–1109, December 2015.

Oral presentations

[4] C. Daversin and C. Trophime. High field magnets modeling : ongoing developpements at lncmi grenoble, October 2013. *EMFL Days, Netherlands.*

[5] C. Daversin, C. Prud'Homme, and C. Trophime. High field magnets modeling : Towards a full non-linear model for high field magnets, February 2014. *3rd Feel++ User Days, Strasbourg.*

[6] C. Daversin, C. Prud'Homme, S. Veys, and C. Trophime. Reduced order modeling of high field magnets : An application of feel++ reduced basis framework, June 2014. *17th U.S. National Congress on Theoretical & Applied Mechanics, Michigan State.*

[7] C. Daversin. Feel++ finite element framework updates : Vectorial finite element h_{div} - h_{curl}, October 2014. *Feel++ Webinar.*

[8] C. Daversin, C. Prud'Homme, and C. Trophime. High field magnets multi-physics modeling, March 2015. *LNCMI Seminar.*

[9] C. Daversin. A simultaneous empirical interpolation and reduced basis method for non-linear problems, March 2015. *4th Feel++ User Days.*

[10] C. Daversin and V. Huber. Magnetostatic simulation of electro-magnets, March 2015. *4th Feel++ User Days.*

[11] C. Daversin, C. Prud'Homme, and C. Trophime. Numerical modeling of high field magnets, April 2015. *International Technical Design magnet Review, Grenoble.*

[12] C. Daversin and C. Prud'Homme. Simultaneous empirical interpolation and reduced basis method for non-linear problems, October 2015. *Model Reduction of Parametrized Systems, Trieste, Italy.*

[13] C. Daversin, R. Hild, C. Prud'Homme, and C. Trophime. Full 3d non-linear multiphysics model for high field polyhelix magnets, April 2016. *10th International Symposium on Electric and Magnetic Fields, Lyon, France.*

Posters

[14] C. Daversin, C. Prud'Homme, and C. Trophime. Bases réduites certifiées pour des problèmes multi-physiques non-linéaires de grande taille. application au design d'aimants à haut champ, 2014. *Journée Poster de l'école doctorale, Strasbourg.*

[15] C. Daversin, C. Prud'Homme, and C. Trophime. Reduced basis method applied to large scale non linear multiphysics problems, October 2015. *Model Reduction of Parametrized Systems, Trieste, Italy.*

[16] C. Daversin, C. Prud'Homme, and C. Trophime. Full 3d multiphysics model of high field polyhelices magnets, October 2015. *24th International Conference on Magnet Technology, Seoul, South Korea.*

Part I

Mathematical modeling

Chapter 1

Finite Element Method

Most of physical phenomena can be described by Partial Differential Equations (PDE), as for the physics involved in high field magnets we focus on. Many methods have been proven in the domain of engineering analysis for such problems, among which finite differences, finite elements or finite volumes. Especially recognized for its versatile properties, the Finite Element (FE) method is widely used in this context and particularly suitable for complex geometries such as those of high field magnets.

In this chapter, we start with a general description of the finite element method [Ciarlet, 1978], [Brezzi and Fortin, 1991], [Canuto et al., 2006] as the basis of all further developments of this thesis.

The first section is a reminder of the definition and the characteristics of the most standardly used finite elements, namely the H_1 conforming finite elements. A fuller description can be found in [Pena, 2009] or in [Chabannes, 2013]. Even though H_1-conforming Lagrange finite elements are widely used in the considered models, their development doesn't represent a contribution since their use was already fully available. This assessment allows to take the next step, which focuses on other finite element types as essential ingredients of the multi-physics model described in Chapter 3.

Especially needed for the development of the magnetostatic model detailed in Section 3.2, the implementation of the H_{div} and H_{curl} conforming finite elements within the `Feel++` library as well as its validation represents an important contribution.

Contents

We admit that all PDEs read as a variational formulation whose solution u defined on a domain Ω is the solution of a variational problem

$$\text{Find } u \in X(\Omega) \mid a(u,v) = f(v)\ \forall v \in X(\Omega) \tag{1.1}$$

where $X(\Omega)$ is an Hilbert space, $a : X(\Omega) \times X(\Omega) \longrightarrow \mathbb{R}$ is a continuous and coercive bilinear form, and $f : X(\Omega) \longrightarrow \mathbb{R}$ is a continuous linear form.

The numerical computation of the solution u of (1.1) requires to transpose the considered continuous variational problem into a discrete one. To this end, the so-called internal approximation replaces the continuous Hilbert space $X(\Omega)$ by a subspace $X_{\mathcal{N}}(\Omega) \subset X(\Omega)$ of finite dimension $\mathcal{N}$ in which the discrete numerical solution $u_{\mathcal{N}}$ shall reside.

Galerkin method We use the Galerkin method as internal approximation method. It reduces the continuous problem (1.1) to the approximated variational problem :

$$\text{Find } u_{\mathcal{N}} \in X_{\mathcal{N}}(\Omega) \mid a(u_{\mathcal{N}}, v_{\mathcal{N}}) = f(v_{\mathcal{N}}) \ \forall v_{\mathcal{N}} \in X_{\mathcal{N}}(\Omega) \tag{1.2}$$

whose solution $u_{\mathcal{N}}$ can be numerically computed as a linear combination of $X_{\mathcal{N}}(\Omega)$ basis functions $\{\phi_i\}_{1 \leqslant i \leqslant \mathcal{N}}$ (1.3), also called finite element basis functions :

$$u_{\mathcal{N}} = \sum_{j=1}^{\mathcal{N}} u_{\mathcal{N}}^j \phi_j \text{ with } X_{\mathcal{N}}(\Omega) =< \phi_i >_{i=1}^{\mathcal{N}} \tag{1.3}$$

Introducing the stiffness matrix $A_{\mathcal{N}} = (a(\phi_j, \phi_i)) \in \mathbb{R}^{\mathcal{N} \times \mathcal{N}}$ and the associated vector $B_{\mathcal{N}} = (f(\phi_i))$, the solution $u_{\mathcal{N}} = (u_{\mathcal{N}}^0, \ldots, u_{\mathcal{N}}^{\mathcal{N}})$ of (1.2) is the solution of the $\mathcal{N} \times \mathcal{N}$ system

$$A_{\mathcal{N}} \, u_{\mathcal{N}} = B_{\mathcal{N}} \tag{1.4}$$

Finite element definition The Galerkin approximation (1.2) supposes the knowledge of the discrete subspace $X_{\mathcal{N}}(\Omega)$. The definition of this approximation space can be provided by many numerical methods, such as the finite elements we focus on.

Considering the Ciarlet formalism [Ciarlet, 1978], the FE method defines $X_{\mathcal{N}}(\Omega)$ from a tuple (K, P_K, Σ_K) which describes the finite element. K is a geometrical domain – simplex or hypercube – resulting from the partitioning of Ω. P_K is a polynomial space of finite dimension in which the FE basis functions $\{\phi_i\}_{1 \leqslant i \leqslant \mathcal{N}}$ shall reside. P_K is commonly known as the primal space whose basis – called primal basis – is denoted as $\mathcal{B} = \{\zeta_i\}$. This basis is local to the element. The last component of the finite element is a set of linear functionnals $\Sigma_K = \{\sigma_i : P_K \longrightarrow \mathbb{R}\}_{i=1}^{\mathcal{N}}$, also known as the dual space which consists of the so-called degrees of freedom.

The definition of the discrete subspace $X_{\mathcal{N}}(\Omega)$ resides in the definition of its basis functions $\{\phi_i\}_{1 \leqslant i \leqslant \mathcal{N}}$ (1.3). As elements of P_K, they read as a linear combination of $\mathcal{B}$ elements such that

$$\exists c_i^k \ \mid \ \phi_i = \sum_{k=1}^{\mathcal{N}} c_i^k \zeta_k \ \forall j = 1, ..., \mathcal{N}, \quad i \in \mathbb{R} \tag{1.5}$$

The coefficients c_i^k of (1.5) are obtained from the definition of degrees of freedom Σ_K

of the finite element. They have to satisfy

$$\sigma_i(\phi_j) = \delta_{ij} \ \forall i,j = 1,...,\mathcal{N} \tag{1.6}$$

Thus, the FE method allows to define the discrete subspace $X_{\mathcal{N}}(\Omega)$ required to solve (1.1) applying the internal interpolation method (1.2). This space is defined from its basis functions which reads in the primal basis $\mathcal{B}$. Their coefficient $c_i^k \ \forall i = 1,...,\mathcal{N}, \ \forall k = 1,...,\mathcal{N}$ (1.5) are the solution of the system

$$\begin{pmatrix} \sigma_1(\zeta_1) & \cdots & \cdots & \sigma_1(\zeta_{\mathcal{N}}) \\ \vdots & \ddots & & \vdots \\ \vdots & & \ddots & \vdots \\ \sigma_{\mathcal{N}}(\zeta_1) & \cdots & \cdots & \sigma_{\mathcal{N}}(\zeta_{\mathcal{N}}) \end{pmatrix} \begin{pmatrix} c_1^1 & \cdots & \cdots & c_{\mathcal{N}}^1 \\ \vdots & \ddots & & \vdots \\ \vdots & & \ddots & \vdots \\ c_1^{\mathcal{N}} & \cdots & \cdots & c_{\mathcal{N}}^{\mathcal{N}} \end{pmatrix} = \begin{pmatrix} 1 & 0 & \cdots & 0 \\ 0 & \ddots & & \vdots \\ \vdots & & \ddots & 0 \\ 0 & \cdots & 0 & 1 \end{pmatrix} \tag{1.7}$$

Geometrical transformation The partitionning of the domain Ω is a finite collection Γ_h of non empty and disjoint open simplices or hypercubes $K \in \Gamma_h$. These simple geometrical elements $K \in \Gamma_h$ are either simplices – lines (1D), triangles (2D), tetrahedrons (3D) – or hypercubes – lines (1D), quadrangles (2D), hexaedrons, prisms or pyramids (3D). All further finite element descriptions are based on simplices, but similar arguments can meet with hypercubes.

The FE method connects each element K with its own finite element tuple (K, P_K, Σ_K) involving its proper basis functions. In practice, a wise solution consists in choosing a reference element $\hat{K}$ for which a reference finite element $\left(\hat{K}, P_{\hat{K}}, \Sigma_{\hat{K}}\right)$ is considered. Each real element $K \in \Gamma_h$ is supposed to be the image of $\hat{K}$ from a C^1-diffeomorphism ϕ_K^{geo} as illustrated in Figure 1.1.

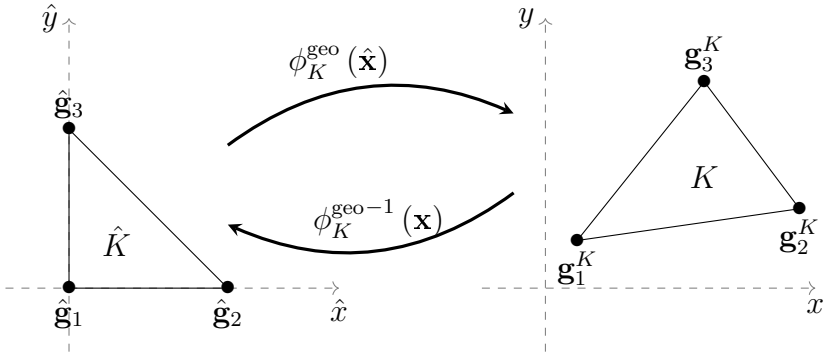

Figure 1.1 – Geometrical transformation on a 2D simplex

Many elementary computations can be performed once on the reference element. The set $\{\phi_i\}_{i=1}^{\mathcal{N}}$ (1.8) is thus deduced from the reference basis functions $\{\hat{\phi}_i\}_{i=1}^{\mathcal{N}}$ owned by the reference element $\hat{K}$ on which ϕ_K^{geo} is applied.

$$\phi_i = \phi_K^{\text{geo}}(\hat{\phi}_i) \ \forall i \in 1,\ldots,\mathcal{N} \tag{1.8}$$

However, the finite element basis functions $\{\phi_i\}_{i=1}^{\mathcal{N}}$ are arguments of the weak formulation integrals. The associated variable change thus supposes the knowledge of the Jacobian of the transformation ϕ_K^{geo}. In this context, we denote J_K^{geo} the Jacobian matrix

of ϕ_K^{geo}, and $det(J_K^{\text{geo}})$ its determinant.

De Rham complex diagram Depending on the considered problem, the space $X(\Omega)$ has to be carefully determined to guarantee that the solution it hosts has the expected properties. As mentionned in [Zaglmayr, 2006] or in [Boffi et al., 2013], the so-called De Rham complex diagram (1.10) establishes a sequence relating spaces from the main differential operators.

Let us introduce the standard differential form spaces, where d is the dimension of Ω :

$$\begin{aligned} &L_2(\Omega) = \{f \mid \textstyle\int f^2 < \infty\} \\ &H_1(\Omega) = \{f \in L_2(\Omega) \mid \nabla f \in L_2(\Omega)\} \\ &H_{\text{div}}(\Omega) = \{\boldsymbol{f} \in [L_2(\Omega)]^d \mid \nabla \cdot \boldsymbol{f} \in L_2(\Omega)\} \\ &H_{\text{curl}}(\Omega) = \{\boldsymbol{f} \in [L_2(\Omega)]^d \mid \nabla \times \boldsymbol{f} \in L_2(\Omega)\} \end{aligned} \tag{1.9}$$

The De Rham complex diagram is expressed as the sequence

$$H_1(\Omega) \xrightarrow{grad} H_{\text{curl}}(\Omega) \xrightarrow{curl} H_{\text{div}}(\Omega) \xrightarrow{div} L_2(\Omega) \xrightarrow{0} \{0\} \tag{1.10}$$

The range of each operator relating two spaces in (1.10) coincides with the null space of the next operator.

The discrete compactness property of the De Rham complex diagram makes it valuable for discrete finite element space $X_{\mathcal{N}} \subset X$ (1.2). Denoting $\pi_{\mathcal{N}} : X \longrightarrow X_{\mathcal{N}}$ the Galerkin interpolation operator resulting in discrete spaces $U_{\mathcal{N}} = \pi_{\mathcal{N}}^U(H_1(\Omega))$, $V_{\mathcal{N}} = \pi_{\mathcal{N}}^V(H_{\text{curl}}(\Omega))$, $W_{\mathcal{N}} = \pi_{\mathcal{N}}^W(H_{\text{div}}(\Omega))$ and $Z_{\mathcal{N}} = \pi_{\mathcal{N}}^Z(L_2(\Omega))$, the De Rham complex (1.10) becomes

$$\begin{array}{ccccccccc} H_1(\Omega) & \xrightarrow{grad} & H_{\text{curl}}(\Omega) & \xrightarrow{curl} & H_{\text{div}}(\Omega) & \xrightarrow{div} & L_2(\Omega) & \xrightarrow{0} & \{0\} \\ \downarrow \pi_{\mathcal{N}}^U & & \downarrow \pi_{\mathcal{N}}^V & & \downarrow \pi_{\mathcal{N}}^W & & \downarrow \pi_{\mathcal{N}}^Z & & \\ U_{\mathcal{N}} & \xrightarrow{grad} & V_{\mathcal{N}} & \xrightarrow{curl} & W_{\mathcal{N}} & \xrightarrow{div} & Z_{\mathcal{N}} & \xrightarrow{0} & \{0\} \end{array} \tag{1.11}$$

Many types of finite elements have been developed to suit each differential space. The selection of an appropriate finite element type is then essential to ensure that the properties of the solution are satisfied.

As discussed, this chapter describes the finite element types necessary to the development of the 3D multi-physics model for high fields magnets. Especially, the De Rham diagram (1.11) gives H_{div} and H_{curl} as appropriate Hilbert spaces for the solutions of the electromagnetic component of the model. Indeed, the Lagrange finite elements don't fully satisfy the conditions of the considered Maxwell's equations. As they weren't initially available in `Feel++`, we pay particular attention to detail the H_{div}-conforming elements of Raviart-Thomas elements and the H_{curl}-conforming elements of Nédélec. Their implementation within the library is detailed in Chapter 5.

1.1 H_1-conforming finite elements

Given as the most simple finite element, the Lagrange finite element is mostly sufficient to fulfill the requirements of a great number of PDEs. This nodal finite element is suitable

for variationnal problems whose solution resides in H_1 Hilbert space (1.9). The Hilbert space H_1 is associated with the standard dot product

$$(u, v)_{H_1} = (u, v)_{L_2} + (\nabla u, \nabla v)_{L_2} \tag{1.12}$$

which defines the H_1 norm

$$\| \cdot \|_{H_1} = \sqrt{(\cdot, \cdot)_{H_1}} = \sqrt{\| \cdot \|^2_{L_2} + \| \nabla \|^2_{L_2}} \tag{1.13}$$

and the projection operator Π_1 which defines the projection $\Pi_1 f$ of any function $f \in X$ into $Y \subset H_1$ such that

$$(\Pi_1 f, v)_{H_1} = (f, v)_{H_1} \ \forall v \in Y \tag{1.14}$$

1.1.1 Lagrange finite elements

From the definition of a finite element, the Lagrange finite elements are tuples $\left(K, \mathcal{L}_k, \Sigma^L_K\right)$ where k represents the finite element order. The functional space $\mathcal{L}_k$ coincides with $\mathbb{P}_k$ denoting the set of polynomials of degree less than k.

Building the vectorial space $\mathcal{L}_k$ supposes the knowledge of a basis $\mathcal{B}_k$ of $\mathbb{P}_k$. The primal basis $\mathcal{B}_k$ can be based on numerous polynomial families. For numerical stability reasons, we use Dubiner polynomials which are particularly suitable for simplices.

The degrees of freedom σ_i of Σ^L_K are the evaluation of the polynomials $p \in \mathbb{P}_k$ at the interpolation points of K, denoted as $\mathbf{d}_i$:

$$\sigma_i(p) = p(\mathbf{d}_i) \ \forall p \in \mathbb{P}_k \tag{1.15}$$

The Lagrange basis functions are the piecewise polynomial functions of order k on each $K \in \Gamma_h$, which are deduced from (1.6)

$$\phi_j(\mathbf{d}_i) = \begin{cases} 1 \text{ if } i = j \\ 0 \text{ if } i \neq j \end{cases} \tag{1.16}$$

Interpolant The Lagrange interpolation operator $\Pi_{\mathcal{L}_k}$ projects any continuous function $f \in \mathcal{C}_0(\Omega)$ to the associated discrete space $U_{\mathcal{N}}$ as described in the De Rham diagram (1.11). To this end, the local restriction $f\restriction_K$ of the function on any element $K \in \Gamma_h$ is the discretized local function $\Pi_{\mathcal{L}_k} f \in \mathcal{L}_k(K)$ expressed in the primal basis $\mathcal{B}_k = \{\zeta_i\}$:

$$\begin{aligned} \Pi_{\mathcal{L}_k} : \ \mathcal{C}_0(K) &\longrightarrow \mathcal{L}_k(K) \\ f\restriction_K &\longrightarrow \sum_{i=1}^{\mathcal{N}} \sigma_i(f\restriction_K)\zeta_i \end{aligned} \tag{1.17}$$

From the definition of the Lagrange degrees of freedom, the coefficients of the discrete projection of f in the primal basis consist in its evaluation at the interpolation points of

K. The Lagrange $\Pi_{\mathcal{L}_k}$ interpolant reads

$$\Pi_{\mathcal{L}_k} f = \sum_{i=1}^{\mathcal{N}} f(\mathbf{d}_i)\zeta_i \tag{1.18}$$

1.2 H_{div}-conforming Raviart-Thomas finite elements

Weak formulations involving the integral of divergence terms require to ensure these terms are square-integrable, i.e. in $L_2(\Omega)$. As previously mentionned, H_{div} (1.19) is the appropriate space to meet this condition.

$$H_{\text{div}} = \{\boldsymbol{f} \in [L_2(\Omega)]^d \mid \nabla \cdot \boldsymbol{f} \in L_2(\Omega)\} \text{ with } L_2(\Omega) = \{f \mid \int f^2 < \infty\} \tag{1.19}$$

The Hilbert space H_{div} (1.19) is associated with its dot product

$$(\mathbf{u}, \mathbf{v})_{H_{\text{div}}} = (\mathbf{u}, \mathbf{v})_{L_2} + (\nabla \cdot \mathbf{u}, \nabla \cdot \mathbf{v})_{L_2} \tag{1.20}$$

which defines the H_{div} norm (1.21)

$$\| \cdot \|_{H_{\text{div}}} = \sqrt{(\cdot, \cdot)_{H_{\text{div}}}} = \sqrt{\| \cdot \|_{L_2}^2 + \| \nabla \cdot \|_{L_2}^2} \tag{1.21}$$

and the projection operator Π_{div} which defines the projection $\Pi_{div}\mathbf{f}$ of any function $\mathbf{f} \in Y \subset H_{\text{div}}$ such that

$$(\Pi_{div}\mathbf{f}, \mathbf{v})_{H_{\text{div}}} = (\mathbf{f}, \mathbf{v})_{H_{\text{div}}} \ \ \forall \mathbf{v} \in Y \tag{1.22}$$

Finding the solution $\mathbf{u}_{\mathcal{N}} \in X_{\mathcal{N}} \subset H_{\text{div}}(\Omega)$ using the finite element method requires elements which meet H_{div} conditions. Especially, we have to ensure the continuity of the normal component $\mathbf{u} \cdot \mathbf{n}$ of the solution $\mathbf{u}$ along the interfaces between elements of the mesh Γ_h. Various divergence conforming finite elements are provided such as Brezzi-Doublas-Marini (BDM) [Brezzi et al., 1985] or Raviart-Thomas [Raviart and Thomas, 1977]. In this section, we will focus on the Raviart-Thomas finite elements.

1.2.1 Definition

According to Ciarlet's formalism [Ciarlet, 1978], the Raviart-Thomas finite elements are tuples $\left(K, \mathcal{D}_k, \Sigma_K^{RT}\right)$ where k represents the finite element order. $\mathcal{D}_k$ is a vectorial subspace of $[\mathbb{P}_{k+1}]^d$ defined as

$$\mathcal{D}_k = [\mathbb{P}_k]^d \oplus \mathbf{x}\mathbb{P}_k \subset [\mathbb{P}_{k+1}]^d \tag{1.23}$$

where $\mathbb{P}_k$ is the set of polynomials of total order less than k, and where d is the dimension of the domain Ω.

The set Σ_k^{RT} of degrees of freedom (dofs) is composed of two types of linear functionals. The faces degrees of freedom $\{\sigma_f\}_{f \in \mathcal{F}_h}$ defined at the lowest order zero, and the inner ones

$\{\sigma_K\}_{K\in\mathcal{T}_h}$ defined on elements from order one.

$$\Sigma_K^{RT} = \{\sigma_f\}_{f\in\mathcal{F}_h} \oplus \{\sigma_K\}_{K\in\mathcal{T}_h} = \{\sigma_i\}_{i=1}^{\mathcal{N}}$$

The linear functionals σ_f and σ_K are defined as follows

$$\begin{aligned} \sigma_f(\mathbf{u}) &= \int_f \mathbf{u}\cdot\mathbf{n}p \quad \forall p \in \mathbb{P}_k(f) \\ \sigma_K(\mathbf{u}) &= \int_K \mathbf{u}\cdot\mathbf{q} \quad \forall \mathbf{q} \in [\mathbb{P}_{k-1}(K)]^d \end{aligned} \tag{1.24}$$

We shall note that the normal $\mathbf{n}$ associated with each faces plays an important role in the definition of faces dofs. Especially, the orientation of $\mathbf{n}$ depending on the considered element has to be set for each face, ensuring its unicity.

1.2.2 Unicity of normals

The previously mentionned faces denote the entities of dimension $n-1$ associated with an element of dimension n. Classically, the normal $\mathbf{n}$ associated to a face (relative to a particular element) is outwardly oriented. Excepted for the faces located on the boundary of the domain, a face is shared by two elements K_0 and K_1. The orientation of the normal associated with this face is not unique, since it depends on the element from which the face is seen, as shown in Figure 1.2 for the 2D case.

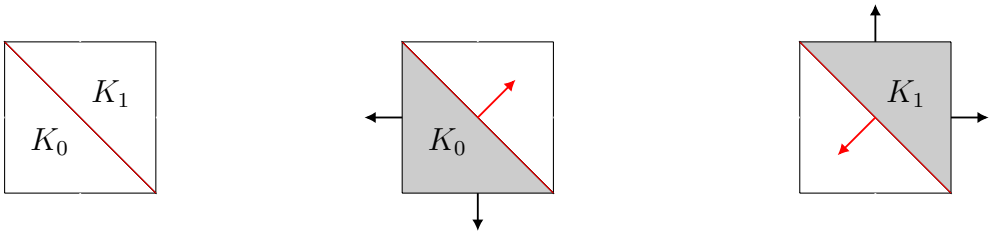

(a) 2D simplices (b) Normals of element K_0 (c) Normals of element K_1

Figure 1.2 – Orientation of the normal associated with shared face

Let us focus on the degree of freedom $\sigma_f(\mathbf{u})$ associated with the shared face f. We denote $\sigma_f^0(\mathbf{u})$ (resp. $\sigma_f^1(\mathbf{u})$) the degree of freedom of this face defined locally on element K_0 (resp. on element K_1).

$$\sigma_f^0(\mathbf{u}) = \int_f \mathbf{u}\cdot\mathbf{n_0}\; p \quad \text{and} \quad \sigma_f^1(\mathbf{u}) = \int_f \mathbf{u}\cdot\mathbf{n_1}\; p \quad \forall p \in \mathbb{P}_k(f) \tag{1.25}$$

with $\mathbf{n_0}$ (resp. $\mathbf{n_1}$) the outward normal to f seen by K_0 (resp. K_1). From the previous considerations illustrated in Figure 1.2, $\mathbf{n_0}$ and $\mathbf{n_1}$ have opposed signs which leads to

$$\sigma_f^0(\mathbf{u}) = -\sigma_f^1(\mathbf{u}) \tag{1.26}$$

Nevertheless, the global degree of freedom $\sigma_f(\mathbf{u})$ associated with this face has to be unique. In practice, we set the face attached with K_0 to have positive sign, and the other face to have negative sign. This corresponds to locally affect a sign to each degree of

freedom, setting the orientation of the associated normal as the one of K_0

$$\sigma_f^0(\mathbf{u}) = (-1) * (-\sigma_f^1(\mathbf{u})) = \sigma_f(\mathbf{u})$$

Further details are given in Chapter 5 in which the implementation is detailed.

1.2.3 Basis functions

Primal space Let's denote $\mathcal{B}_{k+1} = \{\zeta_{k+1,i}\}_i$ a basis of $\mathbb{P}_{k+1}$ composed with Dubiner polynomials as for Lagrange finite elements, and $\mathcal{B}_{k+1}^d = \{\boldsymbol{\zeta_{k+1,i}}\}_i$ a basis of $[\mathbb{P}_{k+1}]^d$.

We remind that the Raviart-Thomas basis functions are in $\mathcal{D}_k$ (1.23). Thus, we have to determine the primal basis $\mathcal{B}_{\mathcal{D}_k}$ of $\mathcal{D}_k$.

The first $dim([\mathbb{P}_k]^d)$ terms of $\mathcal{B}_{k+1}^d$ leads to a basis $\mathcal{B}_k^d$ of $[\mathbb{P}_k]^d$. From the definition of $\mathcal{D}_k$, it remains to find a basis $\mathcal{B}_{xk}$ for $\mathbf{x}\mathbb{P}_k \subset [\mathbb{P}_{k+1}]^d$. This basis is composed of polynomials $\mathbf{q}_l \in [\mathbb{P}_{k+1}]^d$ such that

$$\int_K \mathbf{q_l} \cdot \boldsymbol{\zeta_{k+1,i}} = \int_K (\mathbf{x}p)\boldsymbol{\zeta_{k+1,i}} \text{ with } p \in \mathbb{P}_k \ \forall i \tag{1.27}$$

The elements $\mathbf{q}_l$ of $\mathcal{B}_{xk}$ (1.27) are expressed as a combination of $[\mathbb{P}_k]^d$ basis functions.

$$\mathbf{q}_l \in [\mathbb{P}_{k+1}]^d \Rightarrow \exists \{q_{lj}\}_j \mid \mathbf{q}_l = \sum_{j=1}^{dim([\mathbb{P}_{k+1}]^d)} q_{lj}\boldsymbol{\zeta_{k+1,j}} \ \forall l \tag{1.28}$$

The coefficients $\{q_{lj}\}_j$ of each $\mathbf{q}_l$ in the basis $\mathcal{B}_{k+1}^d$ are obtained from (1.27) using the orthonormality property of the Dubiner polynomials, which leads to

$$q_{lj} = \int_K (\mathbf{x}\zeta_{k,j})\boldsymbol{\zeta_{k+1,j}} \ \forall j, l \tag{1.29}$$

The basis $\mathcal{B}_{\mathcal{D}_k} = \{\boldsymbol{\zeta}_j^{\mathcal{D}_k}\}$ of $\mathcal{D}_k$ we are looking for then consists in the sum $\mathcal{B}_k^d \oplus \mathcal{B}_{xk}$.

Dual space The next step aims to determine the basis functions $\{\boldsymbol{\phi_i} \in \mathcal{D}_k\}_{i=1}^{\mathcal{N}}$ which satisfy (1.6). As they belong to $\mathcal{D}_k$, they are defined as a linear combination of $\mathcal{B}_{\mathcal{D}_k}$ functions.

$$\exists c_i^k \mid \boldsymbol{\phi_i} = \sum_{k=1}^{\mathcal{N}} c_i^k \boldsymbol{\zeta}_k^{\mathcal{D}_k} \ \forall i = 1, .., \mathcal{N}$$

Considering $\mathcal{N}_f$ (resp. $\mathcal{N}_K$) the number of faces (resp. inner) degrees of freedom, the definition of the finite elements basis functions (1.6) depending on the set of degrees of

freedom (1.24) gives

$$
\begin{aligned}
0 \leqslant l < \mathcal{N}_f : & \sum_{k=1}^{\mathcal{N}_f} c_i^k \int_{face} \boldsymbol{\zeta}_k^{\mathcal{D}_k} \cdot \mathbf{n} p = \delta_{li} \ \forall p \in \mathbb{P}_k \\
\mathcal{N}_f \leqslant l < \mathcal{N} : & \sum_{k=1}^{\mathcal{N}_K} c_i^k \int_{K} \boldsymbol{\zeta}_k^{\mathcal{D}_k} \cdot \mathbf{q} = \delta_{li} \ \forall \mathbf{q} \in [\mathbb{P}_{k-1}]^d
\end{aligned}
\tag{1.30}
$$

The resolution of (1.30) for each $i = 1, .., \mathcal{N}$ gives the expression of the basis functions $\{\boldsymbol{\phi_i}\}_i$ giving their coefficients $\{c_i^k\}_{k=1}^{\mathcal{N}}$ in the primal basis.

As previously introduced (see Figure 1.1), the basis functions are computed once on a reference element $\hat{K}$. The $\{\boldsymbol{\phi_i}\}_i$ on any element K are then deduced applying the geometrical transformation $\phi_K^{\mathrm{geo}} : \hat{K} \longrightarrow K$ (1.8).

To ensure their correctness and to validate their implementation (see Chapter 5), we compare the numerically computed basis functions on $\hat{K}$ to their analytical expression. In this context, the following paragraphs describe the analytical expression of the set $\{\boldsymbol{\phi_i}\}_i$ on 2D and 3D reference elements. These reference elements are illustrated by Figure 1.3, where $\mathbf{n}_i$ denotes the outward normal associated with i^{th} face of $\hat{K}$.

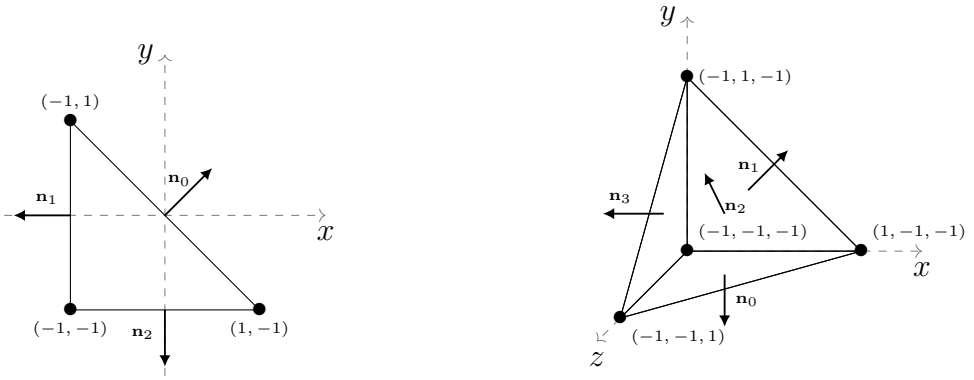

(a) 2D simplex (b) 3D simplex

Figure 1.3 – Reference elements - normals

2D lowest order basis functions The definition (1.23) of the 2D vectorial space $\mathcal{D}_k$ for the lowest order $k = 0$ reads

$$
\mathcal{D}_0 = [\mathbb{P}_0]^2 \oplus \begin{pmatrix} x_1 \\ x_2 \end{pmatrix} \mathbb{P}_0 \subset [\mathbb{P}_1]^2 \tag{1.31}
$$

The reference shape functions $\hat{\boldsymbol{\phi}}_{\boldsymbol{i}}$ $(i = 0, 1, 2)$ on $\hat{K}$ are in $\mathcal{D}_0$. The basis $\mathcal{B}_{\mathcal{D}_0}$ is the sum $\mathcal{B}_0^d \oplus \hat{x}\mathcal{B}_0$, leading to

$$
\mathcal{B}_{\mathcal{D}_0} = \left\{ \begin{pmatrix} 1 \\ 0 \end{pmatrix}, \begin{pmatrix} 0 \\ 1 \end{pmatrix}, \begin{pmatrix} \hat{x_1} \\ \hat{x_2} \end{pmatrix} \right\} \tag{1.32}
$$

The expressions of these basis functions $\hat{\boldsymbol{\phi}}_{\boldsymbol{i}}$ in $\mathcal{B}_{\mathcal{D}_0}$ are based on the coefficients c_i^k $(i, k =$

$0, 1, 2)$ such that

$$\hat{\boldsymbol{\phi}}_{\boldsymbol{i}} = c_i^0 \begin{pmatrix} 1 \\ 0 \end{pmatrix} + c_i^1 \begin{pmatrix} 0 \\ 1 \end{pmatrix} + c_i^2 \begin{pmatrix} \hat{x_1} \\ \hat{x_2} \end{pmatrix} \tag{1.33}$$

The c_i^k $(i, k = 0, 1, 2)$ coefficients are then deduced from (1.6) solving the system

$$\begin{cases} \sigma_0(\hat{\boldsymbol{\phi}}_{\boldsymbol{i}}) = \displaystyle\int_{\hat{f}_0} \hat{n_0} \cdot \hat{\boldsymbol{\phi}}_{\boldsymbol{i}} = \int_{\hat{x_1}=-1}^{1} \int_{\hat{x_2}=-\hat{x_1}} (1,1)^T \cdot \hat{\boldsymbol{\phi}}_{\boldsymbol{i}} = \delta_{0,i} \\ \sigma_1(\hat{\boldsymbol{\phi}}_{\boldsymbol{i}}) = \displaystyle\int_{\hat{f}_1} \hat{n_1} \cdot \hat{\boldsymbol{\phi}}_{\boldsymbol{i}} = \int_{\hat{x_1}=-1}^{1} \int_{\hat{x_2}=-1}^{1} (-1,0)^T \cdot \hat{\boldsymbol{\phi}}_{\boldsymbol{i}} = \delta_{1,i} \\ \sigma_2(\hat{\boldsymbol{\phi}}_{\boldsymbol{i}}) = \displaystyle\int_{\hat{f}_2} \hat{n_2} \cdot \hat{\boldsymbol{\phi}}_{\boldsymbol{i}} = \int_{\hat{x_1}=-1}^{1} \int_{\hat{x_2}=-1} (0,-1)^T \cdot \hat{\boldsymbol{\phi}}_{\boldsymbol{i}} = \delta_{2,i} \end{cases} \tag{1.34}$$

And the expressions of basis functions $\hat{\boldsymbol{\phi}}_{\boldsymbol{i}}$ $i = 0, 1, 2$ hence read

$$\hat{\boldsymbol{\phi}}_{\mathbf{0}}(\hat{x_1}, \hat{x_2}) = \frac{1}{4} \begin{pmatrix} 1 - \hat{x_1} \\ 1 + \hat{x_2} \end{pmatrix}, \quad \hat{\boldsymbol{\phi}}_{\mathbf{1}}(\hat{x_1}, \hat{x_2}) = -\frac{1}{4} \begin{pmatrix} -1 + \hat{x_1} \\ 1 - \hat{x_2} \end{pmatrix}, \quad \hat{\boldsymbol{\phi}}_{\mathbf{2}}(\hat{x_1}, \hat{x_2}) = \frac{1}{4} \begin{pmatrix} 1 - \hat{x_1} \\ -1 + \hat{x_2} \end{pmatrix}$$

The shape functions computed by `Feel++` on the reference element $\hat{K}$ (Figure 1.4) are in coherence with solutions of (1.34).

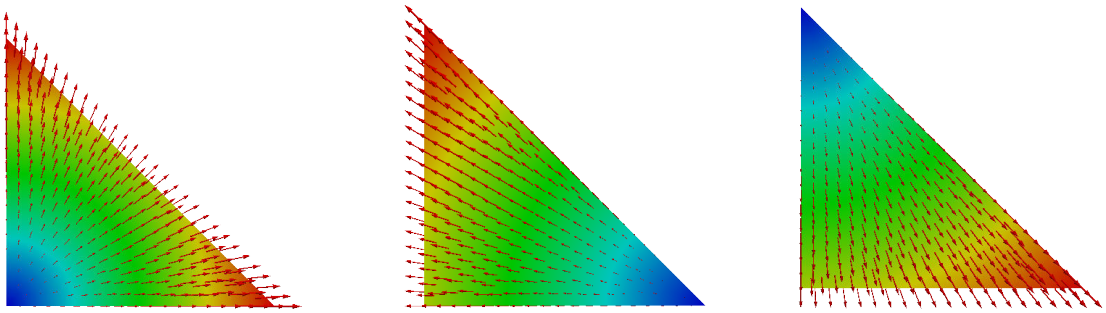

(a) $\hat{N}_0$ (b) $\hat{N}_1$ (c) $\hat{N}_2$

Figure 1.4 – Raviart-Thomas lowest order - 2D shape functions

3D lowest order basis functions In 3D, $\mathcal{D}_0$ is defined as

$$\mathcal{D}_0 = [\mathbb{P}_0]^3 \oplus \begin{pmatrix} x_1 \\ x_2 \\ x_3 \end{pmatrix} \mathbb{P}_0 \subset [\mathbb{P}_1]^3 == \langle \begin{pmatrix} 1 \\ 0 \\ 0 \end{pmatrix}, \begin{pmatrix} 0 \\ 1 \\ 0 \end{pmatrix}, \begin{pmatrix} 0 \\ 0 \\ 1 \end{pmatrix}, \begin{pmatrix} \hat{x_1} \\ \hat{x_2} \\ \hat{x_3} \end{pmatrix} \rangle \tag{1.35}$$

The expressions of $\hat{\boldsymbol{\phi}}_{\boldsymbol{i}}$ $(i = 0, 1, 2, 3)$ in the basis of 3D vectorial space $\mathcal{D}_0$ (1.35) depend on coefficients c_i^k $(i, k = 0, 1, 2, 3)$ which are deduced from (1.6) as for previous 2D case :

$$\hat{\boldsymbol{\phi}}_{\boldsymbol{i}} = c_i^0 \begin{pmatrix} 1 \\ 0 \\ 0 \end{pmatrix} + c_i^1 \begin{pmatrix} 0 \\ 1 \\ 0 \end{pmatrix} + c_i^2 \begin{pmatrix} 0 \\ 0 \\ 1 \end{pmatrix} + c_i^3 \begin{pmatrix} \hat{x_1} \\ \hat{x_2} \\ \hat{x_3} \end{pmatrix} \tag{1.36}$$

The condition (1.6) combined with (1.36) results in the system

$$
(1.37)\qquad \begin{cases}
\sigma_0(\hat{\boldsymbol{\phi}}_{\boldsymbol{i}}) = \displaystyle\int_{\hat{f}_0} \hat{n}_0 \cdot \hat{\boldsymbol{\phi}}_{\boldsymbol{i}} = \int_{\hat{x_1}=-1}^{1}\int_{\hat{x_2}=-1}^{-\hat{x_1}}\int_{\hat{x_3}=-1} (0,0,-1)^T \cdot \hat{\boldsymbol{\phi}}_{\boldsymbol{i}} = \delta_{0,i} \\
\sigma_1(\hat{\boldsymbol{\phi}}_{\boldsymbol{i}}) = \displaystyle\int_{\hat{f}_1} \hat{n}_1 \cdot \hat{\boldsymbol{\phi}}_{\boldsymbol{i}} = \int_{\hat{x_1}=-1}^{1}\int_{\hat{x_2}=-1}^{1}\int_{\hat{x_3}=-1}^{-\hat{x_2}} (-1,0,0)^T \cdot \hat{\boldsymbol{\phi}}_{\boldsymbol{i}} = \delta_{1,i} \\
\sigma_2(\hat{\boldsymbol{\phi}}_{\boldsymbol{i}}) = \displaystyle\int_{\hat{f}_2} \hat{n}_2 \cdot \hat{\boldsymbol{\phi}}_{\boldsymbol{i}} = \int_{\hat{x_1}=-1}^{-\hat{x_3}}\int_{\hat{x_2}=-(1+\hat{x_1}+\hat{x_3})}\int_{\hat{x_3}=-1}^{1} (1,1,1)^T \cdot \hat{\boldsymbol{\phi}}_{\boldsymbol{i}} = \delta_{2,i} \\
\sigma_3(\hat{\boldsymbol{\phi}}_{\boldsymbol{i}}) = \displaystyle\int_{\hat{f}_3} \hat{n}_3 \cdot \hat{\boldsymbol{\phi}}_{\boldsymbol{i}} = \int_{\hat{x_1}=-1}^{1}\int_{\hat{x_2}=-1}^{-\hat{x_1}}\int_{\hat{x_3}=-1} (0,-1,0)^T \cdot \hat{\boldsymbol{\phi}}_{\boldsymbol{i}} = \delta_{3,i}
\end{cases}
$$

whose solutions (1.38) are also in good agreement with basis functions computed by `Feel++` implementation (Figure 1.5).

$$
(1.38)\qquad \begin{aligned}
\hat{\boldsymbol{\phi}}_{\mathbf{0}}(\hat{x_1},\hat{x_2},\hat{x_3}) &= \frac{1}{4}\begin{pmatrix} 1+\hat{x_1} \\ 1+\hat{x_2} \\ -1+\hat{x_3} \end{pmatrix} \quad \hat{\boldsymbol{\phi}}_{\mathbf{1}}(\hat{x_1},\hat{x_2},\hat{x_3}) = -\frac{1}{4}\begin{pmatrix} -1+\hat{x_1} \\ 1-\hat{x_2} \\ 1+\hat{x_3} \end{pmatrix} \\
\hat{\boldsymbol{\phi}}_{\mathbf{2}}(\hat{x_1},\hat{x_2},\hat{x_3}) &= \frac{1}{4}\begin{pmatrix} 1+\hat{x_1} \\ 1+\hat{x_2} \\ 1+\hat{x_3} \end{pmatrix} \quad \hat{\boldsymbol{\phi}}_{\mathbf{3}}(\hat{x_1},\hat{x_2},\hat{x_3}) = \frac{1}{4}\begin{pmatrix} 1-\hat{x_1} \\ -1+\hat{x_2} \\ 1+\hat{x_3} \end{pmatrix}
\end{aligned}
$$

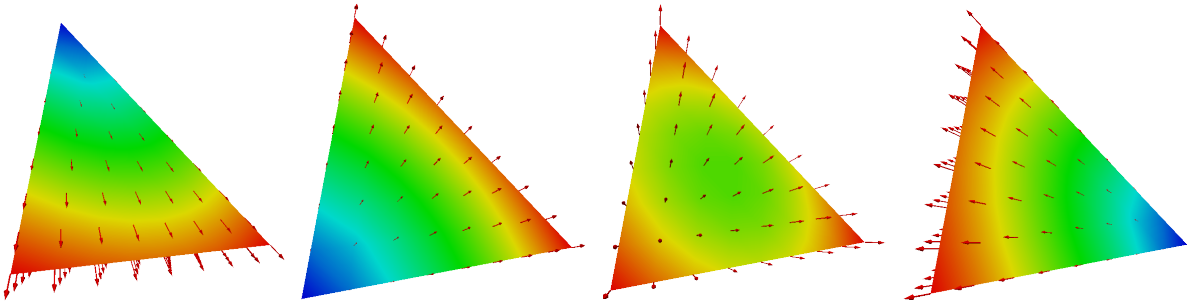

(a) $\hat{\boldsymbol{\phi}}_{\mathbf{0}}$ (b) $\hat{\boldsymbol{\phi}}_{\mathbf{1}}$ (c) $\hat{\boldsymbol{\phi}}_{\mathbf{2}}$ (d) $\hat{\boldsymbol{\phi}}_{\mathbf{3}}$

Figure 1.5 – Raviart-Thomas lowest order - 3D shape functions

1.2.4 Raviart-Thomas Interpolant

The Raviart-Thomas interpolant $\Pi_{\mathcal{D}_k}$ is a projection operator relating continuous function space $H_{\text{div}}(\Omega)$ with the associated discrete function space $W_{\mathcal{N}}$ as previously described in (1.11). Considering a continuous vectorial function $\mathbf{f} \in [\mathcal{C}_0(\Omega)]^d$, its restriction $\mathbf{f}\restriction_K$ on any element K is the discretized function $\Pi_{\mathcal{D}_k}\mathbf{f} \in \mathcal{D}_k(K)$ expressed from $\mathcal{D}_k(K)$ basis functions.

$$
(1.39)\qquad \begin{aligned}
\Pi_{\mathcal{D}_k} : \ [\mathcal{C}_0(K)]^d &\longrightarrow \mathcal{D}_k(K) \\
\mathbf{f}\restriction_K &\longrightarrow \sum_{i=1}^{\mathcal{N}} \sigma_i(\mathbf{f}\restriction_K)\boldsymbol{\zeta}_{\boldsymbol{i}}
\end{aligned}
$$

From definition of Σ_k^{RT} functionnals set (1.24), $\Pi_{\mathcal{D}_k}$ reads

$$\Pi_{\mathcal{D}_k}\mathbf{f} = \sum_{i=1}^{\mathcal{N}_f}\left[\int_{face}\mathbf{f}\cdot\mathbf{n}\zeta_{k-1,i}\right]\boldsymbol{\zeta_i} + \sum_{j=\mathcal{N}_f+1}^{\mathcal{N}}\left[\int_K \mathbf{f}\cdot\boldsymbol{\zeta_{k-2,j}}\right]\boldsymbol{\zeta_j} \tag{1.40}$$

The basis functions $\boldsymbol{\zeta_i} \in \mathcal{D}_k(K)$ should be deduced from the reference basis functions $\hat{\boldsymbol{\zeta}}_{\boldsymbol{i}} \in \mathcal{D}_k(\hat{K})$ applying the geometrical transformation ϕ_K^{geo} (1.8) which unfortunately doesn't preserve the properties of $H_{\text{div}}(\Omega)$.

Piola transformation Defined from the standard geometrical transformation ϕ_K^{geo}, the Piola transform (1.41) has the particularity to conserve H_{div} space properties. This bijective map gives restriction $\mathbf{u}(\mathbf{x})|_K$ of any function $\mathbf{u}$ on element K from its restriction on reference element $\hat{K}$ ensuring conservation of Raviart-Thomas finite element space properties. We remind that J_K^{geo} stands for the Jacobian of ϕ_K^{geo}, and that $det(J_K^{\text{geo}})$ refers to its determinant.

$$\mathbf{u}(\mathbf{x})|_K = \frac{1}{det(J_K^{\text{geo}})}J_K^{\text{geo}}\hat{\mathbf{u}}(\hat{\mathbf{x}}) \;\Leftrightarrow\; \mathbf{u}(\mathbf{x})|_K = \frac{1}{det(J_K^{\text{geo}})}J_K^{\text{geo}}\hat{\mathbf{u}}\circ\phi_K^{\text{geo}-1}(\mathbf{x}) \tag{1.41}$$

As a specific geometrical transformation for Raviart-Thomas finite elements, the Raviart-Thomas Piola transform (1.41) is especially used to deal with the computation of $\boldsymbol{\zeta_i}$ from $\hat{\boldsymbol{\zeta}}_{\boldsymbol{i}}$ needed by the interpolant. Moreover, standard operators applied on $\mathbf{u} \in H_{\text{div}}(\Omega)$ naturally derivates from their application of the reference element from (1.41)

$$\begin{aligned}
\nabla\mathbf{u} &= \frac{1}{det(J_K^{\text{geo}})}\hat{\nabla}\hat{\mathbf{u}} \\
\nabla\cdot\mathbf{u} &= \frac{1}{det(J_K^{\text{geo}})}\hat{\nabla}\cdot\hat{\mathbf{u}} \\
\int_K \mathbf{u}\cdot\mathbf{v} &= \int_{\hat{K}}\frac{1}{det(J_K^{\text{geo}})}J_K^{\text{geo}}\hat{\mathbf{u}}\cdot J_K^{\text{geo}}\hat{\mathbf{v}}
\end{aligned} \tag{1.42}$$

1.3 H_{curl}-conforming Nédélec finite elements

This section describes the characteristics of the H_{curl}-conforming finite elements of Nédélec in the same way as the previous H_{div}-conforming finite elements of Raviart-Thomas. These have been introduced in the 80's by J.C. Nédélec [Nédélec, 1980], [Nédélec, 1986] who gave them his name. Widely used since then, these elements are especially described in [Schneebeli, 2003] and [Zaglmayr, 2006].

Weak formulations involving the integral of curl terms require to ensure these terms are square-integrable, i.e. in $L_2(\Omega)$. As previously mentionned, H_{curl} (1.43) is the appropriate space to meet this condition.

$$H_{\text{curl}} = \{\mathbf{f} \in [L_2(\Omega)]^d | \nabla\times\mathbf{f} \in [L_2(\Omega)]^{d_{curl}}\} \text{ with } L_2(\Omega) = \{f \mid \int f^2 < \infty\}) \tag{1.43}$$

We shall note that the dimensional parameter d_{curl} appearing in (1.43) can differ from the dimension d of the domain Ω according to curl operator definition (1.44)

$$\nabla \times \begin{pmatrix} f_1 \\ f_2 \end{pmatrix} = \frac{\partial f_2}{\partial x} - \frac{\partial f_1}{\partial y} \qquad \nabla \times \begin{pmatrix} f_1 \\ f_2 \\ f_3 \end{pmatrix} = \begin{pmatrix} \frac{\partial f_3}{\partial y} - \frac{\partial f_2}{\partial z} \\ \frac{\partial f_1}{\partial z} - \frac{\partial f_3}{\partial x} \\ \frac{\partial f_2}{\partial x} - \frac{\partial f_1}{\partial y} \end{pmatrix} \tag{1.44}$$

Indeed, the curl of a 2D vector gives a scalar but the curl of a 3D vector stays a 3D vector which means $d_{curl} = 1$ for $d = 2$, and $d_{curl} = 3$ when $d = 3$.
H_{curl} is a Hilbert space supplied with the dot product

$$(\mathbf{u}, \mathbf{v})_{H_{\text{curl}}} = (\mathbf{u}, \mathbf{v})_{L_2} + (\nabla \times \mathbf{u}, \nabla \times \mathbf{v})_{L_2} \tag{1.45}$$

which defines the H_{div} norm (1.21)

$$\| \cdot \|_{H_{\text{curl}}} = \sqrt{(\cdot, \cdot)_{H_{\text{curl}}}} = \sqrt{\| \cdot \|_{L_2}^2 + \| \nabla \times \|_{L_2}^2} \tag{1.46}$$

and the projection operator Π_{curl} which defines the projection $\Pi_{curl}\mathbf{f}$ of any function $\mathbf{f} \in X$ into $Y \subset H_{\text{curl}}$ such that

$$(\Pi_{curl}\mathbf{f}, \mathbf{v})_{H_{\text{curl}}} = (\mathbf{f}, \mathbf{v})_{H_{\text{curl}}} \quad \forall \mathbf{v} \in Y \tag{1.47}$$

Many finite elements are suitable to be used within H_{curl} function space and they ensure the continuity of the tangential component of the solution. Nédélec finite elements are widely used in this context and group two elements types which especially differ from their primal space. The next section details the characteristics of the Nédélec elements of first kind whose implementation is described in Chapter 5.

1.3.1 Definition

The Nédélec finite elements of first type consist in tuples $(K, \mathcal{R}^{k,1}, \Sigma_k^{Ned,1})$ where $\mathcal{R}^{k,1}$ is a vectorial subspace of $[\mathbb{P}_{k+1}]^d$ defined as

$$\mathcal{R}^{k,1} = [\mathbb{P}_k]^d \oplus \mathcal{S}^k \subset [\mathbb{P}_{k+1}]^d \tag{1.48}$$

The space $\mathcal{S}^k$ of (1.48) is itself defined as

$$\mathcal{S}^k = \{\mathbf{p} \in [\mathbb{P}_k]^d \mid \mathbf{p} \cdot \hat{\mathbf{x}} = 0\} \tag{1.49}$$

with $\hat{\mathbf{x}} \in \hat{K}$ is in the reference element.

The set of linear functionals $\Sigma_k^{Ned,1}$ hosted by $\mathcal{R}^{k,1}$ consists in three kinds of functionals. The lowest order degrees of freedom $\{\sigma_e\}_{e \in \mathcal{E}_h}$ are located on the set $\mathcal{E}_h$ grouping the whole set of edges of the mesh Γ_h. For higher polynomial order, face located degrees of freedom

$\{\sigma_f\}_{f\in\mathcal{F}_h}$ and inner ones $\{\sigma_K\}_{K\in\mathcal{T}_h}$ have to be considered.

$$\Sigma_k^{Ned,1} = \{\sigma_e\}_{e\in\mathcal{E}_h} \oplus \{\sigma_f\}_{f\in\mathcal{F}_h} \oplus \{\sigma_K\}_{K\in\mathcal{T}_h} = \{\sigma_i\}_{i=1}^{\mathcal{N}} \tag{1.50}$$

In 2D case, the edges are combined with the faces leading to $\sigma_e \equiv \sigma_f$ with

$$\begin{aligned} \sigma_e(\mathbf{u}) &= \int_e (\mathbf{u}\cdot\mathbf{t})p \quad \forall p \in \mathbb{P}_k(e) \\ \sigma_K(\mathbf{u}) &= \int_K \mathbf{u}\cdot\mathbf{q} \quad \forall q \in [\mathbb{P}_{k-1}(K)]^2 \end{aligned} \tag{1.51}$$

In 3D case, σ_e and σ_f are distinguished such that

$$\begin{aligned} \sigma_e(\mathbf{u}) &= \int_e (\mathbf{u}\cdot\mathbf{t})p \quad \forall p \in \mathbb{P}_k(e) \\ \sigma_f(\mathbf{u}) &= \int_f (\mathbf{u}\times\mathbf{n})\cdot\mathbf{q} \quad \forall q \in [\mathbb{P}_{k-1}(f)]^2 \\ \sigma_K(\mathbf{u}) &= \int_K \mathbf{u}\cdot\mathbf{q} \quad \forall q \in [\mathbb{P}_{k-2}(K)]^2 \end{aligned} \tag{1.52}$$

The faces degrees of freedom (1.52) require to consider the normal $\mathbf{n}$ associated with each face which involves to ensure the unicity of the normal orientation. Already needed for H_{div}-conforming elements, this requirement is handled as described in Section 1.2.2. Moreover, the tangents defined along edges have also to be carefully considered since they are at least shared by two elements. Thus, the unicity of edges located degrees of freedom supposes to ensure the unicity of tangent orientation in a global point of view.

1.3.2 Unicity of tangents

The edges are the entities of dimension 1 associated with an element of dimension n. An edge e is caracterized by two nodes $\{e_1, e_2\}$ which form its boundary. A tangent of an edge can then be oriented either from e_1 to e_2 or conversely from e_2 to e_1. We consider here that a tangent connecting e_i to e_j is always oriented from e_i to e_j with $i < j$. As for normals in Section 1.2.2, the Figure 1.6 illustrates these considerations in 2D case. A similar process can obviously be performed in 3D case based on the same arguments.

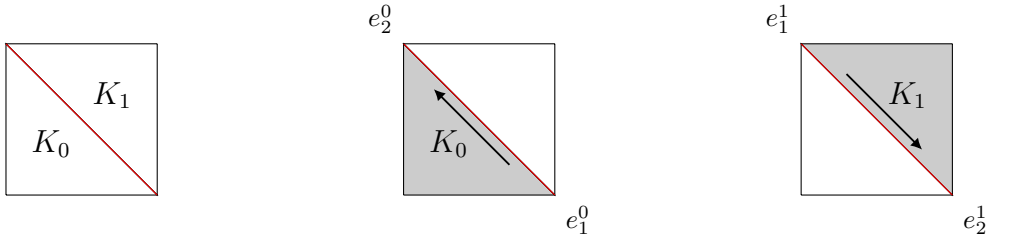

(a) 2D simplices (b) Tangent from K_0 (c) Tangent from K_1

Figure 1.6 – Orientation of the tangent associated with shared edge

Let us denote $\sigma_e(\mathbf{u})$ the lowest order degree of freedom associated with a inner edge, and then shared by two elements. Considering $\sigma_e^0(\mathbf{u})$ (resp. $\sigma_e^1(\mathbf{u})$) as this degree of

freedom defined locally from element K_0 (resp. K_1), we obtain

$$\sigma_e^0(\mathbf{u}) = \int_e \mathbf{u} \cdot \mathbf{t_0} p \quad \text{and} \quad \sigma_e^0(\mathbf{u}) = \int_e \mathbf{u} \cdot \mathbf{t_1} p$$

with $\mathbf{t_0}$ and $\mathbf{t_1}$ of opposed signs.
This leads to the non unicity of the concerned degree of freedom

$$\sigma_e^0(\mathbf{u}) = -\sigma_e^1(\mathbf{u})$$

In practice, we set the edge attached with K_0 to have a positive sign. In 2D (Figure 1.6), the edge attached with K_1 has the opposite orientation and hence the opposite sign.

$$\sigma_e^0(\mathbf{u}) = (-1) * \sigma_e^1(\mathbf{u}) = \sigma_e(\mathbf{u})$$

In 3D, the edges can be shared by more than two elements. The sign affected to the edges is defined from their orientation compared to the one attached with K_0.

1.3.3 Basis functions

Primal space As for Raviart-Thomas basis functions (Section 1.2.3), let us denote $\mathcal{B}_{k+1} = \{\zeta_{k+1,i}\}_i$ a basis of $\mathbb{P}_{k+1}$ composed with Dubiner polynomials, and $\mathcal{B}_{k+1}^d = \{\boldsymbol{\zeta_{k+1,i}}\}_i$ a basis of $[\mathbb{P}_{k+1}]^d$.

The Nédélec basis functions of first kind live in the previously described function space $\mathcal{R}^{k,1}$ (1.48). Hence, they can be written in the primal basis $\mathcal{B}_{\mathcal{R}^{k,1}}$ of $\mathcal{R}^{k,1}$.

The first $dim([\mathbb{P}_k]^d)$ terms of $\mathcal{B}_{k+1}^d$ give a basis $\mathcal{B}_k^d$ for $[\mathbb{P}_k]^d$ which has to be completed by a basis $\mathcal{B}_{\mathcal{S}^k}^d$ of $\mathcal{S}^k$ (1.49), leading to

$$\mathcal{B}_{\mathcal{R}^{k,1}} = \mathcal{B}_k^d \oplus \mathcal{B}_{\mathcal{S}^k}^d \tag{1.53}$$

Let us first focus on the case of $\mathcal{S}^0$, introducing $\mathbf{q}_l = (q_{l,1}, \ldots, q_{l,d})$ in $[\mathbb{P}_1]^d$. The condition for $\mathbf{q}_l$ to be in $\mathcal{S}^0$ becomes

$$\sum_{i=1}^{d} q_{l,i}\hat{x_i} = \sum_{i=1}^{d} \left(\sum_{j=1}^{d} a_{ij}\hat{x_j} \right) \hat{x_i} = 0 \tag{1.54}$$

where $\{a_{ij}\}_j$ are the coefficients of polynomials $q_{l,i} \in \mathbb{P}_1$ $i = 1, \ldots, d$. The identification of coefficients $\{a_{ij}\}_{i,j}$ from the definition of $\mathcal{S}^k$ (1.49) gives the 2D (resp. 3D) basis $\mathcal{B}_{\mathcal{S}^0}^2$ (resp. $\mathcal{B}_{\mathcal{S}^0}^3$) of $\mathcal{S}^0$

$$\mathcal{B}_{\mathcal{S}^0}^2 = \left\{ \begin{pmatrix} \hat{x_2} \\ -\hat{x_1} \end{pmatrix} \right\} \quad \text{and} \quad \mathcal{B}_{\mathcal{S}^0}^3 = \left\{ \begin{pmatrix} \hat{x}_2 \\ -\hat{x}_1 \\ 0 \end{pmatrix}, \begin{pmatrix} -\hat{x}_3 \\ 0 \\ \hat{x}_1 \end{pmatrix}, \begin{pmatrix} 0 \\ \hat{x}_3 \\ -\hat{x}_2 \end{pmatrix} \right\} \tag{1.55}$$

We shall remark that the elements of $\mathcal{B}_{\mathcal{S}^k}^d$ involve the curl operator $\nabla \times \hat{\mathbf{x}}$. Indeed, they are equivalent to the basis elements of $\mathbb{P}_k$ multiplied by $\nabla \times \hat{\mathbf{x}}$.

Consequently, $\mathcal{S}^k$ can be defined as $\mathcal{S}^k = (\nabla \times \hat{\mathbf{x}})\,\mathbb{P}_k$, and $\mathcal{R}^{k,1}$ becomes

$$\mathcal{R}^{k,1} = [\mathbb{P}_k]^d \oplus (\nabla \times \hat{\mathbf{x}})\,\mathbb{P}_k \tag{1.56}$$

The basis $\mathcal{B}^d_{\mathcal{S}^k}$ consists in the set $\{\mathbf{q_l} \in [\mathbb{P}_{k+1}]^d\}_l$ whose elements are defined such that

$$\int_K \mathbf{q_l} \cdot \boldsymbol{\zeta_{k+1,i}} = \int_K (\nabla \times \hat{\mathbf{x}})\; p\; \boldsymbol{\zeta_{k+1,i}}$$

with $p \in \mathbb{P}_k\ \forall i = 1, ..., dim([\mathbb{P}_{k+1}]^d),\ \forall l = 1, ..., dim(\mathcal{S}^k)$.

By definition, each $\mathbf{q_l} \in [\mathbb{P}_{k+1}]^d$ reads as linear combination of $\{\boldsymbol{\zeta_{k+1,i}}\}_i$ basis functions.

$$\exists \{q_{lj}\}_{j=1}^{N} \mid \mathbf{q_l} = \sum_{j=1}^{dim([\mathbb{P}_{k+1}]^d)} q_{lj}\ \boldsymbol{\zeta_{k+1,j}} \tag{1.57}$$

The $\{q_{lj}\}$ coefficients obtained from the orthonormality property of Dubiner polynomials then read

$$q_{li} = \int_K (\nabla \times \hat{\mathbf{x}}) \zeta_{k,i} \boldsymbol{\zeta_{k+1,i}}\ \forall i, l \tag{1.58}$$

The basis $\mathcal{B}_{\mathcal{R}^{k,1}} = \{\boldsymbol{\zeta}_i^{\mathcal{R}^{k,1}}\}$ of $\mathcal{R}^{k,1}$ can then be built as the concatenation $\mathcal{B}^d_k \oplus \mathcal{B}^d_{\mathcal{S}^k}$.

Dual space Let's remind that the basis functions $\{\boldsymbol{\phi_i}\}_{i=1}^{\mathcal{N}}$ live in $\mathcal{R}^{k,1}$. They can hence be written as a linear combination of the primal basis elements $\boldsymbol{\zeta}_i^{\mathcal{R}^{k,1}}$ such that

$$\exists c_i^k \mid \boldsymbol{\phi_i} = \sum_{k=1}^{\mathcal{N}} c_i^k \boldsymbol{\zeta}_k^{\mathcal{R}^{k,1}}\ \forall i = 1, .., \mathcal{N}$$

Considering $\mathcal{N}_e, \mathcal{N}_f$ and $\mathcal{N}_K$ respectively the number of edges, faces and inner degrees of freedom, the requirement (1.6) combined with (1.51) leads to

$$\begin{aligned} &0 \leqslant l < \mathcal{N}_e : \sum_{k=1}^{\mathcal{N}_e} c_i^k \int_{e_l} (\boldsymbol{\zeta}_k^{\mathcal{R}^{k,1}} \cdot \mathbf{t}) p = \delta_{li}\ \forall p \in \mathbb{P}_k \\ &\mathcal{N}_e \leqslant l < \mathcal{N} : \sum_{k=1}^{\mathcal{N}} c_i^k \int_{K_{l-\mathcal{N}_e}} \boldsymbol{\zeta}_k^{\mathcal{R}^{k,1}} \cdot \mathbf{q} = \delta_{li}\ \forall \mathbf{q} \in [\mathbb{P}_{k-1}]^2 \end{aligned} \tag{1.59}$$

while (1.52) gives

$$\begin{aligned} &0 \leqslant l < \mathcal{N}_e : \sum_{k=1}^{\mathcal{N}_e} c_i^k \int_{e_l} (\boldsymbol{\zeta}_k^{\mathcal{R}^{k,1}} \cdot \mathbf{t}) p = \delta_{li}\ \forall \in \mathbb{P}_k \\ &\mathcal{N}_e \leqslant l < \mathcal{N}_e + \mathcal{N}_f : \sum_{k=1}^{\mathcal{N}_f} c_i^k \int_{f_{l-\mathcal{N}_e}} (\boldsymbol{\zeta}_k^{\mathcal{R}^{k,1}} \times \mathbf{n}) \mathbf{q} = \delta_{li}\ \forall \mathbf{q} \in [\mathbb{P}_{k-1}]^3 \\ &\mathcal{N}_e + \mathcal{N}_f \leqslant l < \mathcal{N} : \sum_{k=1}^{\mathcal{N}} c_i^k \int_{K_{l-\mathcal{N}_f-\mathcal{N}_e}} \boldsymbol{\zeta}_k^{\mathcal{R}^{k,1}} \cdot \mathbf{q} = \delta_{li}\ \forall \mathbf{q} \in [\mathbb{P}_{k-2}]^3 \end{aligned} \tag{1.60}$$

The resolution of (1.59) and (1.60) for each $i = 1, .., \mathcal{N}$ gives the coefficients $\{c_i^k\}_{k=1}^{\mathcal{N}}$.

As for Raviart-Thomas, the numerically computed basis functions on $\hat{K}$ are compared with their analytical expression. This allows to ensure their correctness and validate their implementation. The following paragraphs describe analytical expression of $\{\boldsymbol{\phi_i}\}_i$ on 2D and 3D reference elements. The latter are illustrated in Figure 1.7, where $\mathbf{t}_i$ denotes the tangent associated with the i^{th} edge of $\hat{K}$.

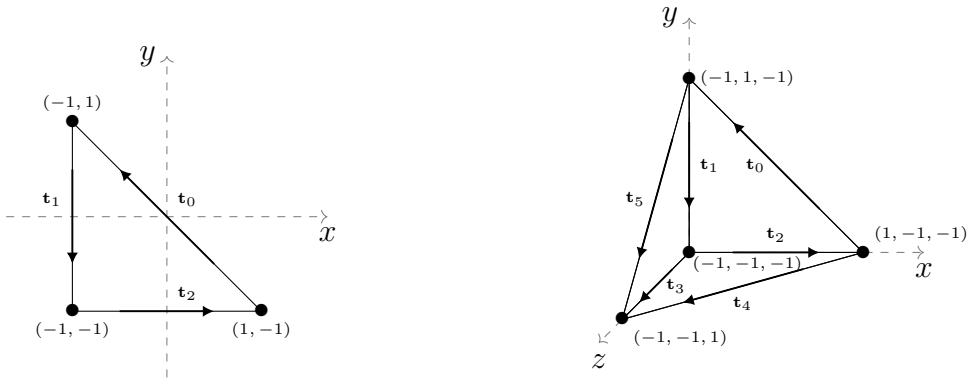

(a) 2D simplex (b) 3D simplex

Figure 1.7 – Reference elements - tangents

2D lowest order basis functions From the previously introduced basis $\mathcal{B}^2_{\mathcal{S}^0}$, the 2D function space $\mathcal{R}^0$ reads as

$$\mathcal{R}^0 = [P_0]^2 \oplus \langle \begin{pmatrix} \hat{x_2} \\ -\hat{x_1} \end{pmatrix} \rangle = \langle \begin{pmatrix} 1 \\ 0 \end{pmatrix}, \begin{pmatrix} 0 \\ 1 \end{pmatrix}, \begin{pmatrix} \hat{x_2} \\ -\hat{x_1} \end{pmatrix} \rangle \tag{1.61}$$

Each shape function $\hat{\boldsymbol{\phi}}_{\boldsymbol{i}}$ $(i = 1, 2)$ on reference element $\hat{K}$ is a element of $\mathcal{R}^0$ space and reads as a linear combination of its base (1.61).

$$\exists \lambda_{j,i} \ (j = 1, ..., 3) \mid \hat{\boldsymbol{\phi}}_{\boldsymbol{i}} = c_i^0 \begin{pmatrix} 1 \\ 0 \end{pmatrix} + c_i^1 \begin{pmatrix} 0 \\ 1 \end{pmatrix} + c_i^2 \begin{pmatrix} \hat{x_2} \\ -\hat{x_1} \end{pmatrix} \tag{1.62}$$

The condition (1.6) on the reference basis functions $\{\hat{\boldsymbol{\phi}}_{\boldsymbol{i}}\}_i$ leads to the system

$$\begin{cases} \sigma_0(\hat{\boldsymbol{\phi}}_{\boldsymbol{i}}) = \displaystyle\int_{\hat{e_0}} \hat{t_0} \cdot \hat{\boldsymbol{\phi}}_{\boldsymbol{i}} = \int_{\hat{x_1}=-1}^{1} \int_{\hat{x_2}=-\hat{x_1}} (-1, 1)^T \cdot \hat{\boldsymbol{\phi}}_{\boldsymbol{i}} = \delta_{0,i} \\ \sigma_1(\hat{\boldsymbol{\phi}}_{\boldsymbol{i}}) = \displaystyle\int_{\hat{e_1}} \hat{t_1} \cdot \hat{\boldsymbol{\phi}}_{\boldsymbol{i}} = \int_{\hat{x_1}=-1} \int_{\hat{x_2}=-1}^{1} (0, -1)^T \cdot \hat{\boldsymbol{\phi}}_{\boldsymbol{i}} = \delta_{1,i} \\ \sigma_2(\hat{\boldsymbol{\phi}}_{\boldsymbol{i}}) = \displaystyle\int_{\hat{e_2}} \hat{t_2} \cdot \hat{\boldsymbol{\phi}}_{\boldsymbol{i}} = \int_{\hat{x_1}=-1}^{1} \int_{\hat{x_2}=-1} (1, 0)^T \cdot \hat{\boldsymbol{\phi}}_{\boldsymbol{i}} = \delta_{2,i} \end{cases} \tag{1.63}$$

whose solutions results in the basis functions which are fully coherent with their computation from `Feel++` (Figure 1.8).

$$\hat{\boldsymbol{\phi}}_{\mathbf{0}}(\hat{x_1}, \hat{x_2}) = \frac{1}{4} \begin{pmatrix} -1 - \hat{x_2} \\ 1 + \hat{x_1} \end{pmatrix}, \quad \hat{\boldsymbol{\phi}}_{\mathbf{1}}(\hat{x_1}, \hat{x_2}) = -\frac{1}{4} \begin{pmatrix} 1 + \hat{x_2} \\ 1 - \hat{x_1} \end{pmatrix}, \quad \hat{\boldsymbol{\phi}}_{\mathbf{2}}(\hat{x_1}, \hat{x_2}) = \frac{1}{4} \begin{pmatrix} 1 - \hat{x_2} \\ 1 + \hat{x_1} \end{pmatrix}$$

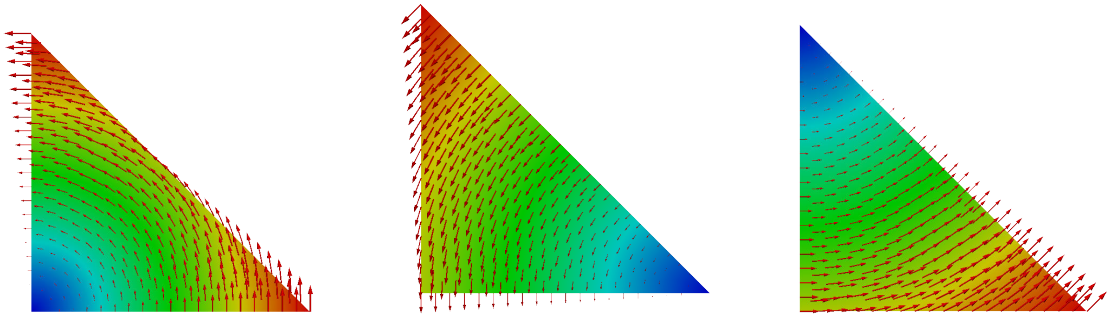

(a) $\hat{N}_0$ (b) $\hat{N}_1$ (c) $\hat{N}_2$

Figure 1.8 – Nedelec order 1 - shape functions

3D lowest order basis functions From the previously introduced basis $\mathcal{B}^3_{\mathcal{S}^0}$, the 3D space $\mathcal{R}^0$ is defined as

$$\mathcal{R}^0 = [\mathbb{P}_0]^3 \oplus \langle \begin{pmatrix} \hat{x}_2 \\ -\hat{x}_1 \\ 0 \end{pmatrix}, \begin{pmatrix} \hat{x}_3 \\ 0 \\ -\hat{x}_1 \end{pmatrix}, \begin{pmatrix} 0 \\ \hat{x}_3 \\ -\hat{x}_2 \end{pmatrix} \rangle \tag{1.64}$$

As previously, each shape function $\hat{\boldsymbol{\phi}}_{\boldsymbol{i}}$ is a element of $\mathcal{R}^0$ space and reads a linear combination of its basis functions.

$$\hat{\boldsymbol{\phi}}_{\boldsymbol{i}} = c_i^0 \begin{pmatrix} 1 \\ 0 \\ 0 \end{pmatrix} + c_i^1 \begin{pmatrix} 0 \\ 1 \\ 0 \end{pmatrix} + c_i^2 \begin{pmatrix} 0 \\ 0 \\ 1 \end{pmatrix} + c_i^3 \begin{pmatrix} \hat{x}_2 \\ -\hat{x}_1 \\ 0 \end{pmatrix} + c_i^4 \begin{pmatrix} \hat{x}_3 \\ 0 \\ -\hat{x}_1 \end{pmatrix} + c_i^5 \begin{pmatrix} 0 \\ \hat{x}_3 \\ -\hat{x}_2 \end{pmatrix} \tag{1.65}$$

The condition (1.6) results in a system whose solutions read

$$\begin{aligned}
\hat{\boldsymbol{\phi}}_{\mathbf{0}}(\hat{x}_1,\hat{x}_2,\hat{x}_3) &= \frac{1}{4}\begin{pmatrix} -1-\hat{x}_2 \\ 1+\hat{x}_1 \\ 0 \end{pmatrix} \quad \hat{\boldsymbol{\phi}}_{\mathbf{1}}(\hat{x}_1,\hat{x}_2,\hat{x}_3) = \frac{1}{4}\begin{pmatrix} -1-\hat{x}_2 \\ \hat{x}_1+\hat{x}_3 \\ -1-\hat{x}_2 \end{pmatrix} \\
\hat{\boldsymbol{\phi}}_{\mathbf{2}}(\hat{x}_1,\hat{x}_2,\hat{x}_3) &= \frac{1}{4}\begin{pmatrix} -\hat{x}_2-\hat{x}_3 \\ 1+\hat{x}_1 \\ 1+\hat{x}_1 \end{pmatrix} \quad \hat{\boldsymbol{\phi}}_{\mathbf{3}}(\hat{x}_1,\hat{x}_2,\hat{x}_3) = \frac{1}{4}\begin{pmatrix} 1+\hat{x}_3 \\ 1+\hat{x}_3 \\ -\hat{x}_1-\hat{x}_2 \end{pmatrix} \\
\hat{\boldsymbol{\phi}}_{\mathbf{4}}(\hat{x}_1,\hat{x}_2,\hat{x}_3) &= \frac{1}{4}\begin{pmatrix} -1-\hat{x}_3 \\ 0 \\ 1+\hat{x}_1 \end{pmatrix} \quad \hat{\boldsymbol{\phi}}_{\mathbf{5}}(\hat{x}_1,\hat{x}_2,\hat{x}_3) = \frac{1}{4}\begin{pmatrix} 0 \\ -1-\hat{x}_3 \\ 1+\hat{x}_2 \end{pmatrix}
\end{aligned} \tag{1.66}$$

Moreover, the basis functions computed with `Feel++` (Figure 1.9) are in good agreement with (1.66).

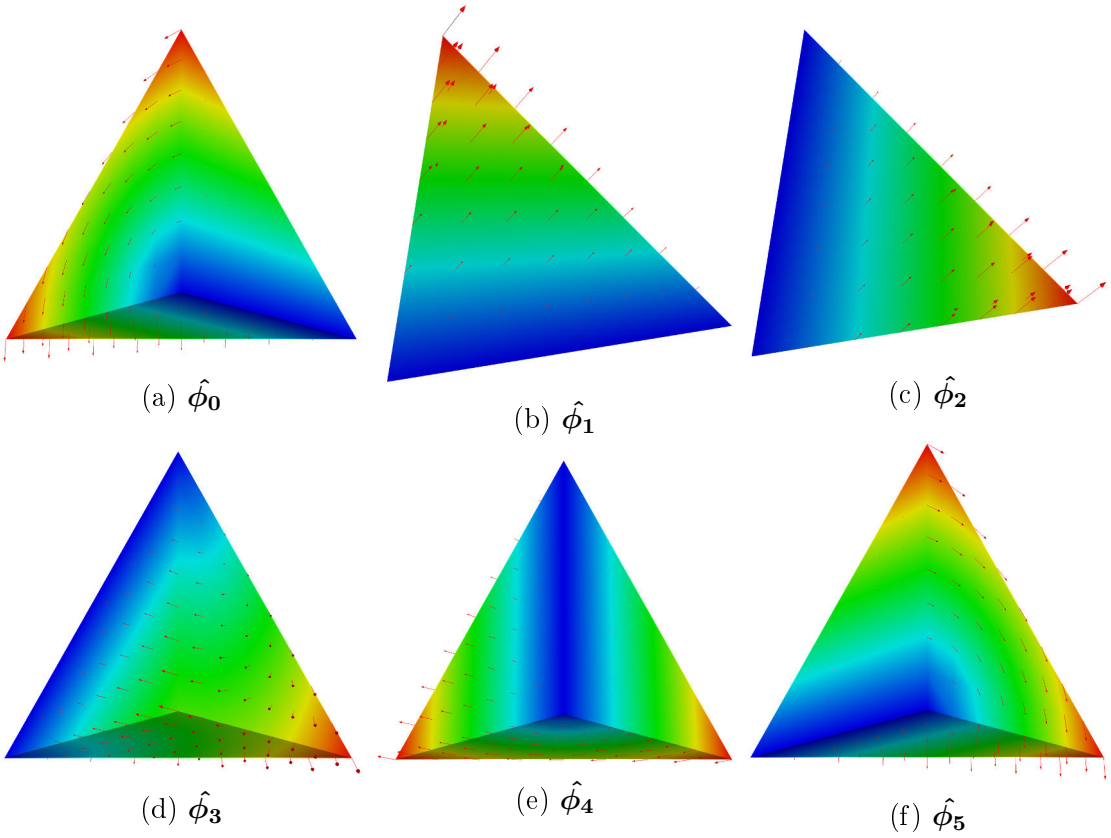

(a) $\hat{\boldsymbol{\phi}}_{\mathbf{0}}$ (b) $\hat{\boldsymbol{\phi}}_{\mathbf{1}}$ (c) $\hat{\boldsymbol{\phi}}_{\mathbf{2}}$

(d) $\hat{\boldsymbol{\phi}}_{\mathbf{3}}$ (e) $\hat{\boldsymbol{\phi}}_{\mathbf{4}}$ (f) $\hat{\boldsymbol{\phi}}_{\mathbf{5}}$

Figure 1.9 – Nédélec lowest order - 3D shape functions

1.3.4 Nédélec Interpolant

The Nédélec interpolant $\Pi_{\mathcal{R}^k}$ is a function which associates a continuous vectorial function $\mathbf{f} \in [\mathcal{C}_0(K)]^d$ to its interpolation $\Pi_{\mathcal{R}^k}\mathbf{f} \in \mathcal{R}_k(K)$ defined as

$$\Pi_{\mathcal{R}^k} : \quad [\mathcal{C}_0(K)]^d \longrightarrow \mathcal{R}_k(K) \tag{1.67}$$

$$\mathbf{f} \longrightarrow \sum_{i=1}^{\mathcal{N}} \sigma_i(\mathbf{f})\boldsymbol{\zeta}_i^{\mathcal{R}^{k,1}} \tag{1.68}$$

with $\{\sigma_i\}_{i=1}^{\mathcal{N}}$ the linear functionnals $\Sigma_k^{Ned,1}$ (1.50).

The 2D linear functionals previously defined by (1.51) lead to the expression of the interpolation of $\mathbf{f}$ in 2D case

$$\Pi_{\mathcal{R}^k}\mathbf{f} = \sum_{i=1}^{\mathcal{N}_e} \left[\int_{e_i} (\mathbf{f}\cdot\mathbf{t})\zeta_{k,i}\right] \boldsymbol{\zeta}_i^{\mathcal{R}^{k,1}} + \sum_{j=\mathcal{N}_e+1}^{\mathcal{N}} \left[\int_{K_{i-\mathcal{N}_e}} \mathbf{f}\cdot\boldsymbol{\zeta}_{\boldsymbol{k-1,j}}\right] \boldsymbol{\zeta}_j^{\mathcal{R}^{k,1}} \tag{1.69}$$

while 3D case distinguishes edges and faces degrees of freedom according to (1.52)

$$\Pi_{\mathcal{R}^k}\mathbf{f} = \sum_{i=1}^{\mathcal{N}_e}\left[\int_{e_i}(\mathbf{f}\cdot\mathbf{t})\zeta_{k,i}\right]\boldsymbol{\zeta}_i^{\mathcal{R}^{k,1}} + \sum_{j=\mathcal{N}_e+1}^{\mathcal{N}_f+\mathcal{N}_e}\left[\int_{f_{i-\mathcal{N}_e}}(\mathbf{f}\times\mathbf{n})\zeta_{k-1,j}\right]\boldsymbol{\zeta}_j^{\mathcal{R}^{k,1}} + \sum_{k=\mathcal{N}_f+\mathcal{N}_e+1}^{\mathcal{N}}\left[\int_{K_{i-\mathcal{N}_e-\mathcal{N}_f}}\mathbf{f}\cdot\boldsymbol{\zeta_{k-2,k}}\right]\boldsymbol{\zeta}_k^{\mathcal{R}^{k,1}} \tag{1.70}$$

As for Raviart-Thomas interpolant (1.67), the basis functions $\boldsymbol{\zeta}_i^{\mathcal{R}^{k,1}} \in \mathcal{D}_k(K)$ should be deduced from the reference basis functions $\hat{\boldsymbol{\zeta}}_i^{\mathcal{R}^{k,1}} \in \mathcal{D}_k(\hat{K})$ applying the geometrical transformation ϕ_K^{geo} (1.8) which unfortunately doesn't preserve the properties of $H_{\text{curl}}(\Omega)$.

Piola transformation Defined from the standard geometrical transformation ϕ_K^{geo}, a Piola transform (1.71) has been designed to conserve these properties. This is also a bijective map which gives restriction $\mathbf{u}(\mathbf{x})|_K$ of any function $\mathbf{u}$ on element K from its restriction on reference element $\hat{K}$ ensuring conservation of Nédélec finite element space properties. We remind that J_K^{geo} stands for the Jacobian of ϕ_K^{geo}, and that $det(J_K^{\text{geo}})$ refers to its determinant.

$$\mathbf{u}(\mathbf{x})|_K = J_K^{\text{geo}-T}\hat{\mathbf{u}}(\hat{\mathbf{x}}) \;\Leftrightarrow\; \mathbf{u}(\mathbf{x})|_K = J_K^{\text{geo}-T}\hat{\mathbf{u}}\circ\phi_K^{\text{geo}-1}(\mathbf{x}) \tag{1.71}$$

As a specific geometrical transformation for Nédélec finite elements, the Piola transform (1.71) is especially used to deal with the computation of $\boldsymbol{\zeta}_i^{\mathcal{R}^{k,1}}$ from $\hat{\boldsymbol{\zeta}}_i^{\mathcal{R}^{k,1}}$ needed by the interpolant. Moreover, standard operators applied on $\mathbf{u} \in H_{\text{curl}}(\Omega)$ naturally derivates from their application of the reference element from (1.71)

$$\begin{aligned}
&\nabla\mathbf{u} = J_K^{\text{geo}-T}\hat{\nabla}\hat{\mathbf{u}}\;(J_K^{\text{geo}})^{-1}\\
&\nabla\cdot\mathbf{u} = \text{tr}(J_K^{\text{geo}-T}\hat{\nabla}\hat{\mathbf{u}}\;(J_K^{\text{geo}})^{-1})\\
&\nabla\times\mathbf{u} = J_K^{\text{geo}-T}\widehat{\nabla\times}\hat{\mathbf{u}}\;(J_K^{\text{geo}})^{-1}\\
&\textstyle\int_K \mathbf{u}\cdot\mathbf{v} = \int_{\hat{K}}\left(J_K^{\text{geo}-T}\hat{\mathbf{u}}\right)\cdot\left(J_K^{\text{geo}-T}\hat{\mathbf{v}}\right)det(J_K^{\text{geo}})
\end{aligned} \tag{1.72}$$

Conclusion

At the basis of the multi-physics model consisting in the core ingredient of this work, this chapter gives an overview of the finite element method. More specifically, we are interested in the definition of the H_{div} and H_{curl} conforming elements which are necessary for the magnetostatic model further described in section 3.2.

The implementation of the Raviart-Thomas and Nédélec finite elements of lowest order within the library `Feel++` is a contribution of this thesis. Their description in this section is at the basis of the chapter 5 which details the implementation.

Chapter 2

Reduced Basis Method

In an industrial context, the optimal design of a component as well as the optimal choice in terms of material or experimental setup are based on the evaluation of a quantity of interest for various configurations. Essentially coming from experimental measurements, the variables describing these realizations are subject to uncertainties whose influence on the considered quantity of interest can be non negligible. Besides the simple prediction of a physical quantity for a given configuration, the current needs in engineering applications then reside both in optimization processes and uncertainty quantification. This is the case for the high field magnet design we focus on, which requires a fine constrained optimization aiming to achieve the expected magnetic field profile while ensuring good thermal and mechanical conditions. The reader can find examples of applications in chapters 8 and 11.

We have then to consider a large number of configurations denoted as inputs which are described by a set of parameters that appear in our model. We want to determine a quantity of interest called output which depends on the solution of the associated PDEs for each of these configurations. This input/output relation requires to efficiently solve parametrized PDEs.

Model order reduction methods aim to replace the parametrized problem – usually of large size – by a reduced problem whose dimension, and hence the cost, is much lower. Especially, the Reduced Basis (RB) method [Prud'homme et al., 2002], [Veroy et al., 2003a], [Veroy et al., 2003c], [Prud'homme and Patera, 2004], [Rozza et al., 2007], [Quarteroni et al., 2011] has been designed for real-time and many-query contexts. It consists in a Galerkin projection on a reduced approximation space based on FE snapshots, whose size is greatly lower than the FE approximation space. As the solution of a low-dimensional system, each evaluation is thus cheaper, allowing to cover a large range of parameters.

A core enabler of the reduced basis method is the so-called offline/online decomposition of the problem. It allows to compute the terms which don't depend on parameters only once. The dependence of the latter on the finite element dimension can indeed make them costly to compute. The affine decomposition is hence an essential ingredient for the efficiency of the RB method.

Besides its non-linearity, the multi-physics model we are interested in presents a non-affine dependence on parameters. In this context, a specific treatment is requested before the application of the reduced basis methodology as described in [Veroy et al., 2003a],

[Veroy et al., 2003c].

This chapter aims to describe how to apply the reduced basis methodology in such a context. To this end, it first introduces the Empirical Interpolation Method (EIM) [Barrault et al., 2004], [Grepl et al., 2007] which is necessary to deal with the non-affine parametrization of our model. Based on the use of this method, the second part focuses on the description of the reduced basis methodology applied to non-linear and non-affinely parametrized problems.

The Certified Reduced Basis (CRB) method [Prud'homme et al., 2002], [Veroy et al., 2003a], [Veroy et al., 2003c], [Prud'homme and Patera, 2004], [Rozza et al., 2007], [Patera and Rozza, 2007], [Quarteroni et al., 2011] combines the previous reduced basis method with error estimators allowing to quantify the error coming from the reduced basis approximation. These error estimators both allow to establish error bounds for the solutions of the reduced system, and to optimize the parameter selection involved in the built RB approximation space.

The application of this method to non-linear problems [Veroy et al., 2003b], [Veroy et al., 2003a], [Veroy and Patera, 2005], [Canuto et al., 2009], [Janon et al., 2013] is relatively recent. For non-affinely parametrized problems as in our case, the error estimation has also to take into account the approximation error resulting from the EIM use. In this context, [Canuto et al., 2009] provides a generalization of [Veroy and Patera, 2005] for non-affine problems. The computation of such error bounds is mainly based on the Brezzi-Rappaz-Raviart (BRR) theory which provides error bounds for non-linear equations. However, this method *(i)* is restrictive with respect of the form of the equations and *(ii)* involves limiting conditions on inf-sup and continuity constants, whose computational cost can be prohibitive. The problems that we are considering don't fully satisfy the BRR theory conditions, which prevents us from applying the method introduced in [Canuto et al., 2009].

In this chapter, we introduce the development of an error indicator allowing to guide the parameter selection process. Nevertheless, it doesn't enable to certify our reduced basis approximation since it isn't provably an error bound.

Finally, the last section concerns the so-called Simultaneous Empirical interpolation and Reduced basis (SER) method which consists in an original contribution of this thesis. Especially designed for non-linear and non-affinely parametrized problems, SER combines the EIM and RB methods in order to decrease the associated computational cost of the offline stage. We present some variants of this method, mainly based on the previous error indicator.

Contents

As mentioned before, each investigated configuration corresponds to a set of p parameters defined as the p-vector $\boldsymbol{\mu} = (\mu_1, \ldots, \mu_p) \in \mathcal{D} \subset \mathbb{R}^p$ combining both geometrical parameters, material properties or operating conditions. The PDE (1.1) handling

the considered physical phenomenon allows to relate the so-called input parameter $\boldsymbol{\mu}$ with the investigated quantity of interest denoted as output. We shall then consider the parametrized PDE which consists in finding the parameter dependent solution $u(\boldsymbol{\mu}) \in X$ such that

$$a(u(\boldsymbol{\mu}), v; \boldsymbol{\mu}) = f(v; \boldsymbol{\mu}) \; \forall v \in X(\Omega) \tag{2.1}$$

where $a : X(\Omega) \times X(\Omega) \times \mathcal{D} \longrightarrow \mathbb{R}$ is a continuous and coercive bilinear form, and $f : X(\Omega) \longrightarrow \mathbb{R}$ is a continuous linear form.

The outputs denoted as $s(\boldsymbol{\mu})$ are typically expressed as linear functionals $\ell : X \to \mathbb{R}$ of $u(\boldsymbol{\mu})$ related with (2.1) as

$$s(\boldsymbol{\mu}) = \ell(u(\boldsymbol{\mu})) \tag{2.2}$$

Considering a set of inputs, our problem thus consists in finding $s(\boldsymbol{\mu}) \in \mathbb{R}$ from the solution $u(\boldsymbol{\mu})$ of (2.1) for each given $\boldsymbol{\mu}$. The optimization methods as well as the uncertainty quantification require a large amount of realizations. Regarding the growing complexity of today's engineering problems coming both from their spatial and parametric dimensions, the cost of such processes can become prohibitive.

As mentioned, the Reduced Basis (RB) methodology consists in a fast but reliable approximation based on the projection on a low-dimensional space combined with a so-called offline/online strategy.

Reduced basis approximation As introduced in Chapter 1, the finite element method allows to compute a discrete approximation of $u(\boldsymbol{\mu})$. Let's remind that this approximation $u_{\mathcal{N}}(\boldsymbol{\mu})$ rests on the Galerkin projection on a subspace $X_{\mathcal{N}} \subset X$ of size $\mathcal{N}$ which consists in the resolution of the $\mathcal{N} \times \mathcal{N}$ system

$$a(u_{\mathcal{N}}(\boldsymbol{\mu}), v; \boldsymbol{\mu}) = f(v; \boldsymbol{\mu}) \; \forall v \in X_{\mathcal{N}}(\Omega) \tag{2.3}$$

The fast simulation response offered by the reduced basis method relies on a Galerkin projection on the low-dimensional subspace W_N of size $N \ll \mathcal{N}$, whose basis functions read from a set of finite element approximations. Typically, the size N of the reduced system doesn't exceed 100.

Let's introduce the sample $S_N = \{\boldsymbol{\mu}_1, \cdots, \boldsymbol{\mu}_N\} \in \mathcal{D}$ and its associated set of finite element solutions $S_N^u = \{u_{\mathcal{N}}(\boldsymbol{\mu}_i)\}_{i=1}^N$ obtained from (2.3). The parameters of S_N can be selected in various ways, ranging from a random selection process to more advanced methods. In particular, the Proper Orthogonal Decomposition (POD) method or the Greedy algorithms are commonly used to optimize the building of this sample. To select the parameters $\boldsymbol{\mu}$ of $\mathcal{D}$ which maximizes the RB approximation error, the Greedy algorithms require error estimation techniques. An error indicator is further described in this context.

The orthonormalization of S_N^u components from a Gram-Schmidt process with respect to the $<,>_X$ inner product associated with X results in the definition of $W_N = span\{\xi_i \equiv u_{\mathcal{N}}(\boldsymbol{\mu}_i), 1 \leqslant i \leqslant N\}$. By analogy with (1.3), the coming reduced basis approximation

$u_N(\boldsymbol{\mu}) \in W_N$ of $u(\boldsymbol{\mu}) \in X$ then reads as the linear combination

$$u_N(\boldsymbol{\mu}) = \sum_{i=1}^{N} u_{N,i}(\boldsymbol{\mu})\xi_i \tag{2.4}$$

whose computation resides in the resolution of the $N \times N$ reduced system

$$\sum_{i=1}^{N} a(\xi_i, \xi_j; \boldsymbol{\mu}) u_{N,i}(\boldsymbol{\mu}) = f(\xi_j; \boldsymbol{\mu}) \ \forall j \in 1, \dots, N \tag{2.5}$$

Affine decomposition When the considered problem is affinely parametrized – that is when a and f depend affinely on the parameters –, we shall be able to decouple the terms of (2.5) which don't depend on the input from the others. It amounts in fact to consider that for a finite integer Q_a (resp. Q_f), the bilinear form a (resp. the linear form f) can be expressed as

$$\begin{aligned} a(u, v; \boldsymbol{\mu}) &= \sum_{q=1}^{Q_a} \theta_a^q(\boldsymbol{\mu}) a^q(u, v) \quad \forall u, v \in X, \ \forall \boldsymbol{\mu} \in \mathcal{D} \ , \\ f(v; \boldsymbol{\mu}) &= \sum_{q=1}^{Q_f} \theta_f^q(\boldsymbol{\mu}) f^q(v) \quad \forall v \in X, \ \forall \boldsymbol{\mu} \in \mathcal{D} \end{aligned} \tag{2.6}$$

Then, the so-called offline stage prepares the parameter-independent quantities, computing them once. This allows the online simulations – which consist in the assembly and the resolution of (2.5)– to be even faster.

The affine decomposition (2.6) is an essential ingredient for the offline/online strategy. Such a decomposition is not necessarily available, in particular for non-affine or non-linear problems. Indeed, the multi-physics model we focus on for high field magnet study appears to be both non linear and non affinely parametrized, due to the non-affine dependence of the material properties on the unknowns as introduced in [Daversin et al., 2013]. In this context, the Empirical Interpolation Method (EIM) is standardly used to recover the required affine decomposition (2.6) building affine approximations of the concerned terms. The non-linearity is however handled by fixed point iterative methods.

2.1 Empirical Interpolation Method (EIM)

The non-affine parametrization of the PDE (2.3) comes from its dependence on at least one non-affine function $w(u(\boldsymbol{\mu}), \mathbf{x}; \boldsymbol{\mu})$. In this case, the problem (2.3) reads as

$$a(u(\boldsymbol{\mu}), v; \boldsymbol{\mu}; w(u(\boldsymbol{\mu}), \mathbf{x}; \boldsymbol{\mu})) = f(v; \boldsymbol{\mu}; w(u(\boldsymbol{\mu}), \mathbf{x}; \boldsymbol{\mu})) \ \forall v \in X(\Omega) \tag{2.7}$$

This prevents the affine decomposition (2.6) to be obtained.

The Empirical Interpolation Method (EIM) allows to recover such a decomposition

building an affine approximation w_M of w such that

$$w_M(u(\boldsymbol{\mu}), \mathbf{x}; \boldsymbol{\mu}) = \sum_{m=1}^{M} \beta_m^M(u(\boldsymbol{\mu}); \boldsymbol{\mu}) q_m(\mathbf{x}) \tag{2.8}$$

This section describes the EIM methodology based on an offline/online strategy as well. Let's introduce the sample $\bar{S}_M = \{\bar{\boldsymbol{\mu}}_1, \ldots, \bar{\boldsymbol{\mu}}_M\} \in \mathcal{D}^M$ and the associated function space $\bar{W}_M = span\{\bar{\boldsymbol{\xi}}_m \equiv w(u(\bar{\boldsymbol{\mu}}_m), \mathbf{x}; \bar{\boldsymbol{\mu}}_m), 1 \leqslant m \leqslant M\}$. We first define a subset Ξ of $\mathcal{D}$ in which the sample points of $\bar{S}_M$ are selected. The starting sample point $\bar{\boldsymbol{\mu}}_1$ is picked in Ξ assuming that $\bar{\boldsymbol{\xi}}_1 \neq 0$.

$$\bar{S}_1 = \{\bar{\boldsymbol{\mu}}_1\}, \quad \bar{\boldsymbol{\xi}}_1 = w(u(\bar{\boldsymbol{\mu}}_1), \mathbf{x}; \bar{\boldsymbol{\mu}}_1), \quad \bar{W}_1 = span\{\bar{\boldsymbol{\xi}}_1\} \tag{2.9}$$

The first interpolation point is chosen as the maximum of $\bar{\boldsymbol{\xi}}_1$, while q_1 is a normalization of $\bar{\boldsymbol{\xi}}_1$, which leads to

$$\boldsymbol{t}_1 = arg\sup_{\mathbf{x}\in\Omega} |\bar{\boldsymbol{\xi}}_1(\mathbf{x})|, \quad q_1 = \frac{\bar{\boldsymbol{\xi}}_1(\mathbf{x})}{\bar{\boldsymbol{\xi}}_1(\boldsymbol{t}_1)} \tag{2.10}$$

For $M \geqslant 2$, the sample points $\bar{\boldsymbol{\mu}}_M$ are determined from a Greedy algorithm choosing $\bar{\boldsymbol{\mu}}_M \in \Xi$ as maximizing the EIM approximation error.

$$\bar{\boldsymbol{\mu}}_M = arg\max_{\boldsymbol{\mu}\in\Xi} \inf_{z\in\bar{W}_{M-1}} ||w(.;.;\boldsymbol{\mu}) - z||_{L^\infty(\Omega)} \tag{2.11}$$

It completes $\bar{S}_M$ and allows to deduce the basis function $\bar{\boldsymbol{\xi}}_M$ enriching the RB approximation space $\bar{W}_M$.

$$\bar{\boldsymbol{\xi}}_M = w\left(\bar{\boldsymbol{\mu}}_M; \mathbf{x}; u(\bar{\boldsymbol{\mu}}_M)\right), \quad \bar{S}_M = \bar{S}_{M-1} \cup \{\bar{\boldsymbol{\mu}}_M\}, \quad \bar{W}_M = \bar{W}_{M-1} \oplus span\{\bar{\boldsymbol{\xi}}_M\} \tag{2.12}$$

The EIM approximation $w_{M-1}(u(\boldsymbol{\mu}), \mathbf{x}; \boldsymbol{\mu}_M)$ is defined from its coefficients $\{\beta_m^{M-1}\}_{m=1}^{M-1}$, evaluated on the parameter $\boldsymbol{\mu}_M$ (2.11). These are computed through the resolution of the $(M-1) \times (M-1)$ system ensuring the exactness of w_{M-1} at the $M-1$ interpolation points $\{t_i\}_{i=1}^{M-1}$. It then leads to the residual

$$\mathbf{r}_M(\mathbf{x}) = w(u(\boldsymbol{\mu}), \mathbf{x}; \bar{\boldsymbol{\mu}}_M) - w_{M-1}(u(\boldsymbol{\mu}), \mathbf{x}; \bar{\boldsymbol{\mu}}_M) \tag{2.13}$$

on which the next interpolation point $\boldsymbol{t}_M$ and basis functions q_M are based.

$$\boldsymbol{t}_M = arg\sup_{\mathbf{x}\in\Omega} |\mathbf{r}_M(\mathbf{x})|, \quad \boldsymbol{q}_M(\mathbf{x}) = \frac{\mathbf{r}_M(\mathbf{x})}{\mathbf{r}_M(\boldsymbol{t}_M)} \tag{2.14}$$

Once the EIM approximation space $\bar{W}_M$ together with the set of interpolation points $\{t_i\}_{i=1}^{M-1}$ are completed, the online step consists in the evaluation $w_M(u, \mathbf{x}; \boldsymbol{\mu})$ (2.8) for any given $\boldsymbol{\mu}$ through the resolution of the online system

$$w_M(u(\boldsymbol{\mu}), \boldsymbol{t}_i; \boldsymbol{\mu}) = \sum_{m=1}^{M} \beta_m^M(u(\boldsymbol{\mu}); \boldsymbol{\mu}) q_m(\boldsymbol{t}_i) = w(u(\boldsymbol{\mu}), \boldsymbol{t}_i; \boldsymbol{\mu}), \quad 1 \leqslant i \leqslant M \tag{2.15}$$

2.2 Reduced Basis for non-affinely parametrized and non linear problems

In this section, we focus on the reduced basis method applied to non-linear and non-affinely parametrized problems. As introduced in Section 2.1, the non affine parametrization comes from the dependence on at least one non affine function w as described in (2.3). The non-linearity is however handled by a fixed point iterative method, namely Picard or Newton's method.

In the sequel, we shall consider the Picard method whose solution at k-th iteration is denoted ${}^k u(\boldsymbol{\mu})$. Nevertheless, all the following considerations can easily be applied to a Newton algorithm considering the residual of (2.3) and its Jacobian.

The non-linear and non affinely parametrized considered problem thus amounts to find $u(\boldsymbol{\mu}) \in X$ such that

$$a(u(\boldsymbol{\mu}), v; \boldsymbol{\mu}; {}^k u(\boldsymbol{\mu}); w({}^k u(\boldsymbol{\mu}), \mathbf{x}; \boldsymbol{\mu})) = f({}^k u(\boldsymbol{\mu}), v; \boldsymbol{\mu}; w({}^k u(\boldsymbol{\mu}), \mathbf{x}; \boldsymbol{\mu})) \ \forall v \in X(\Omega) \tag{2.16}$$

As a reminder, the affine approximation w_M of w built through EIM (2.8) allows to recover an affine decomposition of (2.16). In what follows, the non-affine terms of a (resp. f) whose affine decomposition is obtained from EIM approximations (2.8), and the affine ones for which the affine decomposition (2.6) is naturally obtained, are considered separately. In this context, we consider Q_a^{eim} (resp. Q_f^{eim}) the number of non-affinely parametrized terms of a (resp. f), while Q_a^{aff} (resp. Q_f^{aff}) refers to the affine ones. The M_q^a (resp. M_q^f) coefficients $\gamma_{a,m}^q(u;\boldsymbol{\mu})$ (resp. $\gamma_{f,m}^q(u;\boldsymbol{\mu})$) are obtained from the EIM approximations coefficients, leading to

$$\underbrace{\sum_{q=1}^{Q_a^{eim}} \sum_{m=1}^{M_q^a} \gamma_{a,m}^q({}^k u;\boldsymbol{\mu}) a_m^q(u,v)}_{\text{non-affine part of } a} + \underbrace{\sum_{l=1}^{Q_a^{aff}} \theta_a^l(\boldsymbol{\mu}) a^l(u,v)}_{\text{affine part of } a} = \underbrace{\sum_{q=1}^{Q_f^{eim}} \sum_{m=1}^{M_q^f} \gamma_{f,m}^q({}^k u;\boldsymbol{\mu}) f_m^q(v)}_{\text{non-affine part of } f} + \underbrace{\sum_{l=1}^{Q_f^{aff}} \theta_f^l(\boldsymbol{\mu}) f^l(v)}_{\text{affine part of } f}$$

Let's now turn to the offline/online strategy made possible through the previous affine decomposition availability offered by EIM.

Offline stage The offline stage is first devoted to the building of the reduced basis approximation space W_N, spanned by finite elements approximations selected at N points of the parameter space. It starts with the construction of the previously defined $S_N^u = \{u_{\mathcal{N}}(\boldsymbol{\mu}_i)\}_{i=1}^N$. For each $\boldsymbol{\mu}_i \in S_N$, the non-linearity is handled by a fixed point method. Starting from a given initial guess ${}^0 u_{\mathcal{N}}(\boldsymbol{\mu}_i)$, we iterate on k solving the $\mathcal{N} \times \mathcal{N}$ system

$$\mathcal{A}^{\mathcal{N}} \, {}^k u_{\mathcal{N}}(\boldsymbol{\mu}_i) = \mathcal{F}^{\mathcal{N}} \quad \text{with} \quad 1 \leqslant i \leqslant N \tag{2.17}$$

until convergence. From the definition of the finite element solution $u_{\mathcal{N}}(\boldsymbol{\mu})$ (1.3), the matrix $\mathcal{A}^{\mathcal{N}}$ and vector $\mathcal{F}^{\mathcal{N}}$ at the k-th iteration are defined as

$$\mathcal{A}^{\mathcal{N}} = \sum_{q=1}^{Q_a^{eim}} \sum_{m=1}^{M_q^a} \gamma_{a,m}^q({}^k u_{\mathcal{N}}; \boldsymbol{\mu}) a_m^q(\phi_i, \phi_j) + \sum_{l=1}^{Q_a^{aff}} \theta_a^l(\boldsymbol{\mu}) a^l(\phi_i, \phi_j) \tag{2.18}$$

$$\mathcal{F}^{\mathcal{N}} = \sum_{q=1}^{Q_f^{eim}} \sum_{m=1}^{M_q^f} \gamma_{f,m}^q({}^k u; \boldsymbol{\mu}) f_m^q(\phi_j) + \sum_{l=1}^{Q_f^{aff}} \theta_f^l(\boldsymbol{\mu}) f^l(\phi_j) \tag{2.19}$$

The basis function ξ_i is obtained from the orthonormalization of the resulting $u_{\mathcal{N}}(\boldsymbol{\mu}_i)$. It then enriches the reduced basis approximation space $W_i = W_{i-1} \oplus \xi_i$, in which the reduced basis approximation $u_i(\boldsymbol{\mu})$ shall reside.

The parameter-independent terms of (2.17) correspond to

$$A_{i,j}^{N,q,m} = a_m^q(\xi_j, \xi_i) \quad \text{and} \quad F_j^{N,q,m} = f_m^q(\xi_j) \tag{2.20}$$

Their precomputation stands as a core ingredient of the reduced basis method. Once W_N is completed, these precomputations (2.20) finalize the RB offline stage.

The $N \times N$ online system, allowing to obtain the coefficients $u_{N,i}(\boldsymbol{\mu})$ of the reduced basis approximation $u_N(\boldsymbol{\mu}) \in W_N$ for any parameter $\boldsymbol{\mu}$, then reads as

(2.21)

$$\sum_{q=1}^{Q_a^{eim}} \sum_{m=1}^{M_q^a} \gamma_{a,m}^q({}^k u_N; \boldsymbol{\mu}) a_m^q(\xi_i, \xi_j) + \sum_{l=1}^{Q_a^{aff}} \theta_a^l(\boldsymbol{\mu}) a^l(\xi_i, \xi_j) = \sum_{q=1}^{Q_f^{eim}} \sum_{m=1}^{M_q^f} \gamma_{f,m}^q({}^k u_N; \boldsymbol{\mu}) f_m^q(\xi_j) + \sum_{l=1}^{Q_f^{aff}} \theta_f^l(\boldsymbol{\mu}) f^l(\xi_j)$$

Online stage The evaluation of $u_N(\boldsymbol{\mu})$ for any given μ then consists in the resolution of the reduced $N \times N$ system (2.21). From a given initial guess ${}^0 u_N(\boldsymbol{\mu})$, the fixed point method consists in solving the reduced system

$$\mathcal{A}^N \, {}^k u_N(\boldsymbol{\mu}) = \mathcal{F}^N \tag{2.22}$$

until the convergence of the iterative algorithm is reached. The matrix $\mathcal{A}^N$ as well as the vector $\mathcal{F}^N$ at the k-th iteration benefit from the precomputations (2.20) and read as

$$\mathcal{A}^N = \sum_{q=1}^{Q_a^{eim}} \sum_{m=1}^{M_q^a} \gamma_{a,m}^q({}^k u_N, \boldsymbol{\mu}) A^{N,q,m} + \sum_{l=1}^{Q_a^{aff}} \theta_a^l(\boldsymbol{\mu}) A^{N,l} \tag{2.23}$$

$$\mathcal{F}^N = \sum_{q=1}^{Q_f^{eim}} \sum_{m=1}^{M_q^f} \gamma_{f,m}^q({}^k u_N, \boldsymbol{\mu}) F^{N,q,m} + \sum_{l=1}^{Q_f^{aff}} \theta_f^l(\boldsymbol{\mu}) F^{N,l} \tag{2.24}$$

allowing the efficient assembly of the reduced system (2.22).

2.3 Simultaneous Empirical Interpolation and Reduced Basis Method (SER)

The recovery of the affine decomposition for the non-linear and non affinely parametrized problems (2.16) requires the use of EIM prior to the RB methodology. Thus, the EIM approximation is necessary to the RB offline step and is consequently built first.

As described in Section 2.1, the EIM Greedy algorithm

$$\boldsymbol{\mu}_M = arg \max_{\boldsymbol{\mu}\in\Xi} \inf_{z\in W_{M-1}} ||w(u_{\mathcal{N}}(\boldsymbol{\mu}); .; \boldsymbol{\mu}) - z||_{L^\infty(\Omega)} \tag{2.25}$$

performed during the offline step requires the finite element solution $u_{\mathcal{N}}(\boldsymbol{\mu})$ computed at all points of the EIM trainset $\Xi \in \mathcal{D}$. Depending on the expression of the non affine function w, the size of this trainset can have a significant influence on the quality of its EIM approximation w_M. The number of finite element approximations is proportional to the size of Ξ and can then become high, making the EIM cost prohibitive for large problems. Regarding the electro-thermal component of the multi-physics model for high field magnets (see Section 3.1), the Greedy algorithm (2.25) is clearly an obstacle due to the finite element dimension $\mathcal{N}$ raising to several millions.

The Simultaneous Empirical interpolation and Reduced basis (SER) method aims to reduce this computational cost benefiting from the readily available reduced basis approximation. The key ingredient resides in the simultaneous construction of the EIM and RB approximation spaces, allowing the Greedy algorithm (2.25) to be solely performed from RB approximations.

As reduced basis methodology needs an affine decomposition – and then an EIM approximation w_M for each non affine parameter dependent functions w –, SER starts with the initialization of the EIM approximation space which corresponds to the step $M = 1$ of the standard EIM offline stage.

$$\bar{S}_1 = \{\bar{\boldsymbol{\mu}}_1\}, \quad \bar{\boldsymbol{\xi}}_1 = w(u_{\mathcal{N}}(\bar{\boldsymbol{\mu}}_1), \mathbf{x}; \bar{\boldsymbol{\mu}}_1), \quad \bar{W}_1 = span\{\bar{\boldsymbol{\xi}}_1\} \tag{2.26}$$

At this step, $u_{\mathcal{N}}$ is the finite element solution obtained from (2.16).

The first EIM basis function $\bar{\boldsymbol{\xi}}_1$ is thus still based on a finite element approximation since no reduced basis approximation is yet available. The first interpolation point $\boldsymbol{t}_1$ and the associated basis function q_1 are standardly deduced as

$$\boldsymbol{t}_1 = arg \sup_{\mathbf{x}\in\Omega} |\bar{\boldsymbol{\xi}}_1(\mathbf{x})|, \quad q_1 = \frac{\bar{\boldsymbol{\xi}}_1(\mathbf{x})}{\bar{\boldsymbol{\xi}}_1(\boldsymbol{t}_1)} \tag{2.27}$$

At this stage, the first EIM approximation w_1 is composed of only one term

$$w_1(u(\boldsymbol{\mu}), \mathbf{x}; \boldsymbol{\mu}) = \beta_1^1(u(\boldsymbol{\mu}), \boldsymbol{\mu}) q_1(\mathbf{x}) \tag{2.28}$$

whose only coefficient $\beta_1^1(u(\boldsymbol{\mu}),\boldsymbol{\mu})$ in $\bar{W}_1$ is given by

$$\beta_1^1(u_{\mathcal{N}}(\boldsymbol{\mu}),\boldsymbol{\mu}) = w(u_{\mathcal{N}}(\boldsymbol{\mu}),\boldsymbol{t}_1;\boldsymbol{\mu}) \tag{2.29}$$

since $q_1(t_1) = 1$ from (2.27).

The first affine decomposition based on the rough EIM approximation (2.28) – with M_q^a and M_q^f equal to 1 – reads for all $u, v \in X$ and for all $\boldsymbol{\mu} \in \mathcal{D}$ as

$$a(u,v;\boldsymbol{\mu};w_1(u,\mathbf{x};\boldsymbol{\mu})) = \sum_{q=1}^{Q_a} \gamma_{q,1}^a(u,\boldsymbol{\mu}) a_{q,1}(u,v) + \sum_{l=1}^{Q_a^{aff}} \theta_a^l(\boldsymbol{\mu}) a^l(u,v) \tag{2.30}$$

$$f(v;\boldsymbol{\mu};w_1(u,\mathbf{x};\boldsymbol{\mu})) = \sum_{q=1}^{Q_f} \gamma_{q,1}^f(u,\boldsymbol{\mu}) f_{q,1}(v) + \sum_{l=1}^{Q_f^{aff}} \theta_f^l(\boldsymbol{\mu}) f^l(v) \tag{2.31}$$

Turning to the RB offline step, the resolution of the finite element system (2.17) results in the first RB basis function ξ_1 giving $W_1 = \{\boldsymbol{\xi}_1\}$. The reduced online system (2.21) whose parameter-independent terms $a_1^q(\xi_i,\xi_j)$, $a^l(\xi_i,\xi_j)$ and $f_1^q(\xi_j)$, $f^l(\xi_j)$ can then be precomputed becomes

(2.32)

$$\sum_{q=1}^{Q_a^{eim}} \gamma_{a,1}^q({}^k u_N;\boldsymbol{\mu}) a_1^q(\xi_i,\xi_j) + \sum_{l=1}^{Q_a^{aff}} \theta_a^l(\boldsymbol{\mu}) a^l(\xi_i,\xi_j) = \sum_{q=1}^{Q_f^{eim}} \gamma_{f,1}^q({}^k u_N;\boldsymbol{\mu}) f_1^q(\xi_j) + \sum_{l=1}^{Q_f^{aff}} \theta_f^l(\boldsymbol{\mu}) f^l(\xi_j)$$

where k stands for the current fixed point iteration.

Once the initialization stage is performed – which uses only one FE solve –, we no longer depend on the finite element dimension $\mathcal{N}$. Indeed, the EIM and RB approximation spaces are then enriched by turns. Each new EIM basis function q_M *(i)* is then built from reduced basis approximation $u_{M-1}(\boldsymbol{\mu})$ obtained at previous iteration $M-1$ *(ii)* complete the EIM approximation to then build the affine decomposition for the next RB approximation $u_M(\boldsymbol{\mu})$.

As a summary, SER modifies the EIM approximation space enrichment step into

$$\bar{\boldsymbol{\mu}}_M = arg \max_{\boldsymbol{\mu}\in\Xi} \inf_{z\in W_{M-1}} ||w(u_{M-1}(\boldsymbol{\mu});.;\boldsymbol{\mu}) - z||_{L^\infty(\Omega)} \tag{2.33}$$

$$\bar{\boldsymbol{\xi}}_M = w\left(u_{M-1}(\bar{\boldsymbol{\mu}}_M);\mathbf{x};\bar{\boldsymbol{\mu}}_M\right), \quad \bar{S}_M = \bar{S}_{M-1} \cup \{\bar{\boldsymbol{\mu}}_M\}, \quad \bar{W}_M = \bar{W}_{M-1} \oplus span\{\bar{\boldsymbol{\xi}}_M\} \tag{2.34}$$

The next EIM basis function q_M as the next interpolation point t_M are obtained from the residual $\mathbf{r}_M(\mathbf{x}) = w(u_{M-1},\mathbf{x};\bar{\boldsymbol{\mu}}_M) - w_{M-1}(u_{M-1},\mathbf{x};\bar{\boldsymbol{\mu}}_M)$ computed from the previous reduced basis approximation u_{M-1} as well.

$$\boldsymbol{t}_M = arg \sup_{\mathbf{x}\in\Omega} |\mathbf{r}_M(\mathbf{x})|, \quad \boldsymbol{q}_M(\mathbf{x}) = \frac{\mathbf{r}_M(\mathbf{x})}{\mathbf{r}_M(\boldsymbol{t}_M)} \tag{2.35}$$

The resulting change on w_M leads to the update of the affine decomposition on which the next reduced basis approximation $u_M(\boldsymbol{\mu})$ is based. Once the RB basis function ξ_M is

computed, the newest parameter-independent terms $a_M^q(\xi_j, \xi_i)$ and $f_M^q(\xi_j)$ of the online reduced system are precomputed for each $i, j = 1, \ldots, N$.

Restarting from the beginning, the reduced basis approximation $u_M(\boldsymbol{\mu}) \in W_M$ can then be used in the next Greedy algorithm and so on until either a sufficient accuracy or the user-defined number of basis functions.

Preliminary results To illustrate the previously introduced SER method and to confirm its pertinence, we now turn to its application on a 2D non-linear and non affinely parametrized benchmark introduced in [Grepl et al., 2007].

The considered problem states with the non linear elliptic equation

$$-\Delta u + \mu_1 \frac{e^{\mu_2 u} - 1}{\mu_2} = 100 sin(2\pi x) sin(2\pi y) \tag{2.36}$$

in the domain $\Omega =]0, 1[^2$, with $\boldsymbol{\mu} = (\mu_1, \mu_2) \in \mathcal{D} = [0.01, 10]^2$. The considered output s is the average of the solution u over the domain.

The function $g(u, x; \boldsymbol{\mu}) = \mu_1 \frac{e^{\mu_2 u} - 1}{\mu_2}$ is clearly non affinely parametrized. The Empirical Interpolation Method (see Section 2.1) is used to recover an affine decomposition for (2.36). This results in the affine approximation $g_M = \sum_{i=1}^{M} \beta_m^M(u, \boldsymbol{\mu}) q_m(\mathbf{x})$ of g.

The associated variationnal formulation consists in finding $u \in H^1(\Omega)$ such that

$$\int_\Omega \nabla u \nabla v + \int_\Omega g(u, x; \boldsymbol{\mu}) v = \int_\Omega 100 sin(2\pi x) sin(2\pi y) v \ \forall v \in H^1(\Omega) \tag{2.37}$$

The training set $\Xi \subset \mathcal{D}$ used for EIM is composed of 15 elements in each direction which represents a subset of size 225.

The SER method has been introduced as an alternate construction, for which EIM and RB approximations spaces are enriched once at each stage. As an intermediate method, we can imagine to update the RB approximation every r steps. In this way, $r = M$ corresponds to the standard methodology while $r = 1$ stands for the SER method.

Moreover, the update of the affine decomposition all through the RB offline step could deteriorate the resulting reduced approximation since each of the RB basis function $\xi_i,\ 1 \leqslant i \leqslant N$ results from the solve of a new problem. In this context, the SER method can be customized to rebuild the whole RB approximation space at each update of the affine decomposition.

We shall base on the absolute errors on the solution and on the output, defined as

$$\epsilon_{M,N}^{u,r} = \| u_{\mathcal{N}} - u_N^r \|_{L_2} \quad \epsilon_{M,N}^{s,r} = | s_{\mathcal{N}} - s_N^r | \tag{2.38}$$

where N and M respectively refer to the size of the RB and the EIM approximation space, while r is the frequency of the affine decomposition updates.

We start to apply the standard RB methodology to (2.36), in order to compare our results with the ones obtained in [Grepl et al., 2007]. To this end, we consider a set of 500 realizations. The resulting errors (2.38) displayed in Table 2.1a are in good agreement with [Grepl et al., 2007], which validates our implementation.

Serving as reference, this table is first compared with the results obtained with $r = 5$ illustrated in Table 2.1b. The tables 2.1c and 2.1d investigate the behavior of the SER method ($r = 1$) comparing the results obtained with or without rebuilding the RB approximation space.

N	M	$\max(\epsilon^{u,M}_{M,N})$	$\max(\epsilon^{s,M}_{M,N})$
4	5	7.38e-3	5.75e-3
8	10	1.01e-3	2.34e-4
12	15	1.49e-4	3.09e-5
16	20	2.21e-5	1.25e-5
20	25	5.88e-6	2.82e-6

(a) $r = M$

N	M	$\max(\epsilon^{u,5}_{M,N})$	$\max(\epsilon^{s,5}_{M,N})$
4	5	8.21e-3	6.31e-3
8	10	4.48e-3	6.18e-3
12	15	2.69e-4	2.36e-4
16	20	1.48e-4	9.31e-5
20	25	2.60e-5	1.46e-5

(b) $r = 5$

N	M	$\max(\epsilon^{u,1}_{M,N})$	$\max(\epsilon^{s,1}_{M,N})$
5	5	9.98e-3	7.77e-3
10	10	2.32e-3	1.86e-3
15	15	4.61e-4	3.75e-4
20	20	2.48e-4	2.02e-4
25	25	3.51e-5	2.33e-5

(c) $r = 1$ (W_N recomputed)

N	M	$\max(\epsilon^{u,1}_{M,N})$	$\max(\epsilon^{s,1}_{M,N})$
5	5	1.30e-2	1.02e-2
10	10	2.20e-3	1.50e-3
15	15	4.83e-4	4.05e-4
20	20	2.42e-4	1.98e-4
25	25	1.50e-5	1.24e-5

(d) $r = 1$ (W_N not recomputed)

Table 2.1 – SER - Maximum absolute errors on solution u and on output s

As expected, the errors (2.38) observed with SER method ($r = 1$) are slightly higher than with the case $r = 5$ which itself displays results slightly higher than the standard method $r = M$. This results show the pertinence of the SER method and that we can expect good results within a reasonable computational budget, since the number of finite element approximations can then be reduced to $N + 1$ (Table 2.1d).

2.3.1 Error estimation

We have mentioned that the RB sample $S_N = \{\boldsymbol{\mu}_1, \cdots, \boldsymbol{\mu}_N\} \in \mathcal{D}$ can be built from various methods. Its influence on the resulting reduced basis approximation accuracy could be important.

Moreover, the reduced basis approximation is used all through the offline step within the SER method. Its accuracy is then even more crucial, since it influences the accuracy of the affine decomposition. In this context, we propose to build the RB sample using a Greedy algorithm, itself based on error estimation methods.

Let us first define the error $e(\boldsymbol{\mu})$ associated with the reduced basis approximation

$u_N(\boldsymbol{\mu})$ obtained using EIM approximation w_M as

$$e(\boldsymbol{\mu}) = u(\boldsymbol{\mu}) - u_N(\boldsymbol{\mu}) \tag{2.39}$$

It exists various a posteriori error estimation techniques providing an upper bound $\Delta_{N,M}(\mu)$ for $\| e(\boldsymbol{\mu}) \|_X$. In this section, we stay on one of them dedicated to non-linear but affinely parameterized problems and especially feasible on a non-linear Poisson problem as described in [Veroy et al., 2003b]. After a brief description of the initial method, this section investigates its validity on non-affinely parameterized problems which concern us.

Affinely parametrized problems To deal with the non-linearity of the problem, [Veroy et al., 2003b] splits the linear (resp. non-linear) part a^L (resp. a^{NL}) of the bilinear form a.

$$a(u, v; \boldsymbol{\mu}) = a^L(u, v; \boldsymbol{\mu}) + a^{NL}(u, v; \boldsymbol{\mu}) \tag{2.40}$$

We now introduce the residual $R_N(v; \boldsymbol{\mu}) = f(v) - a(u_N(\boldsymbol{\mu}), v; \boldsymbol{\mu})$ reading from (2.39) and (2.40) as

$$R_N(v; \boldsymbol{\mu}) = a^L(e(\boldsymbol{\mu}), v; \boldsymbol{\mu}) + a^{NL}(u(\boldsymbol{\mu}), v; \boldsymbol{\mu}) - a^{NL}(u_N(\boldsymbol{\mu}), v; \boldsymbol{\mu}) \tag{2.41}$$

Assuming that the linear component a^L of a is coercive, we define its coercivity constant $\alpha(\boldsymbol{\mu})$ as

$$\alpha(\boldsymbol{\mu}) = \inf_{w \in X} \frac{a^L(w, w; \boldsymbol{\mu})}{\| w \|_X^2} \tag{2.42}$$

and we denote $\hat{\alpha}(\boldsymbol{\mu}) \leqslant \alpha(\boldsymbol{\mu})\ \forall \boldsymbol{\mu} \in \mathcal{D}$ a lower bound for $\alpha(\boldsymbol{\mu})$. There are various methods to compute the lower bound $\hat{\alpha}(\boldsymbol{\mu})$ of $\alpha(\boldsymbol{\mu})$, including the inspection method or the min-theta approach. When the assumptions required by these methods are not satisfied, the Successive Constraint Method (SCM) [Huynh et al., 2007], [Rozza et al., 2007], [Veys, 2014] can be used more generally.

Regarding the evaluation of the residual R_N (2.41) on $e(\boldsymbol{\mu})$, the definition of the coercivity constant $\alpha(\boldsymbol{\mu})$ (2.42) results in the inequality

$$R_N(e(\boldsymbol{\mu}); \boldsymbol{\mu}) \geqslant a^L(e(\boldsymbol{\mu}), e(\boldsymbol{\mu}); \boldsymbol{\mu}) \geqslant \hat{\alpha}(\boldsymbol{\mu}) \| e(\boldsymbol{\mu}) \|_X^2 \tag{2.43}$$

based on the condition $a^{NL}(u(\boldsymbol{\mu}), e(\boldsymbol{\mu}); \boldsymbol{\mu}) - a^{NL}(u_N(\boldsymbol{\mu}), e(\boldsymbol{\mu}); \boldsymbol{\mu}) \geqslant 0$.

Moreover, the error bound introduced by [Veroy et al., 2003b] relies on the Riesz representation $\mathcal{Y}$ defined for a given function $g \in X$ as

$$(\mathcal{Y}g, v)_X = g(v)\ \forall v \in X \tag{2.44}$$

The expected error bound $\Delta_N(\boldsymbol{\mu})$ of $\| e(\boldsymbol{\mu}) \|_X$ expressed from (2.44) then reads

$$\Delta_N(\boldsymbol{\mu}) \equiv \frac{\| \mathcal{Y} R_N(\cdot; \boldsymbol{\mu}) \|_X}{\hat{\alpha}(\boldsymbol{\mu})} \tag{2.45}$$

Non-affinely parametrized problems Let us remind that we are considering the solution $u(\boldsymbol{\mu})$ of a non affinely parameterized problem depending on at least one non-affine function w defined as

$$a(u, v; \boldsymbol{\mu}; w(u, \mathbf{x}; \boldsymbol{\mu})) = f(v; \boldsymbol{\mu}; (u, \mathbf{x}; \boldsymbol{\mu})) \tag{2.46}$$

The reduced approximation $u_N(\boldsymbol{\mu})$ requires an affine decomposition, which is commonly recovered through the EIM approximation w_M of w leading to

$$a(u_N, v; \boldsymbol{\mu}; w_M(u_N, \mathbf{x}; \boldsymbol{\mu})) = f(v; \boldsymbol{\mu}; w_M(u_N, \mathbf{x}; \boldsymbol{\mu})) \tag{2.47}$$

Related with the error coming from the EIM approximation, we introduce the residual $R_M^{eim}(u, v; \boldsymbol{\mu})$ defined as

$$R_M^{eim}(u, v; \boldsymbol{\mu}) = a(u, v; \boldsymbol{\mu}; w(u, \mathbf{x}; \boldsymbol{\mu})) - a(u, v; \boldsymbol{\mu}; w_M(u, \mathbf{x}; \boldsymbol{\mu})) \tag{2.48}$$

The global residual $R_{N,M}(v; \boldsymbol{\mu})$ inspired from [Veroy et al., 2003b] taking into account both EIM and reduced basis approximations errors then reads

$$\begin{aligned} R_{N,M}(v; \boldsymbol{\mu}) &= f(v; \boldsymbol{\mu}; w(u, \mathbf{x}; \boldsymbol{\mu})) - a(u_N, v; \boldsymbol{\mu}; w_M(u_N, \mathbf{x}; \boldsymbol{\mu})) \\ &= a(u, v; \boldsymbol{\mu}; w(u, \mathbf{x}; \boldsymbol{\mu})) - a(u_N, v; \boldsymbol{\mu}; w(u_N, \mathbf{x}; \boldsymbol{\mu})) + R_M^{eim}(u_N, v; \boldsymbol{\mu}) \end{aligned} \tag{2.49}$$

In practice, the accessed residual is based on the affine decomposition. Denoted as $R_{N,M}^{aff}(v; \boldsymbol{\mu})$, it is defined as

$$\begin{aligned} R_{N,M}^{aff}(v; \boldsymbol{\mu}) &= f(v; \boldsymbol{\mu}; w_M(u, \mathbf{x}; \boldsymbol{\mu})) - a(u_N, v; \boldsymbol{\mu}; w_M(u_N, \mathbf{x}; \boldsymbol{\mu})) \\ &= R_{N,M}(v; \boldsymbol{\mu}) - R_M^{eim}(u, v; \boldsymbol{\mu}) \end{aligned} \tag{2.50}$$

Decomposing the bilinear form into its linear and non linear part as performed in (2.40), the evaluation of the so-called affine residual $R_{N,M}^{aff}$ on $e(\boldsymbol{\mu})$ – aiming to define a bound inspired by (2.43) – gives

$$\begin{aligned} R_{N,M}^{aff}(e(\boldsymbol{\mu}); \boldsymbol{\mu}) &= a^L(e(\boldsymbol{\mu}), e(\boldsymbol{\mu}); \boldsymbol{\mu}; w(u, \mathbf{x}; \boldsymbol{\mu})) \\ &+ a^{NL}(u(\boldsymbol{\mu}), e(\boldsymbol{\mu}); \boldsymbol{\mu}; w(u, \mathbf{x}; \boldsymbol{\mu})) - a^{NL}(u_N(\boldsymbol{\mu}), e(\boldsymbol{\mu}); \boldsymbol{\mu}; w(u_N, \mathbf{x}; \boldsymbol{\mu})) \\ &+ R_M^{eim}(u_N, e(\boldsymbol{\mu}); \boldsymbol{\mu}) - R_M^{eim}(u, e(\boldsymbol{\mu}); \boldsymbol{\mu}) \end{aligned} \tag{2.51}$$

We consider again $\hat{\alpha}(\boldsymbol{\mu})$ as a lower bound of the coercivity constant of a^L. The previously obtained condition related to (2.43), allowing to define the error bound from

$$R_{N,M}^{aff}(e(\boldsymbol{\mu}); \boldsymbol{\mu}) \geqslant a^L(e(\boldsymbol{\mu}), e(\boldsymbol{\mu}); \boldsymbol{\mu}; w(u, \mathbf{x}; \boldsymbol{\mu})) \geqslant \hat{\alpha}(\boldsymbol{\mu}) \parallel e(\boldsymbol{\mu}) \parallel_X^2 \tag{2.52}$$

now reads from the residual R_M^{eim} taking into account the EIM approximation error as

$$a^{NL}(u(\boldsymbol{\mu}), e(\boldsymbol{\mu}); \boldsymbol{\mu}; w) - a^{NL}(u_N(\boldsymbol{\mu}), e(\boldsymbol{\mu}); \boldsymbol{\mu}; w) \geqslant R_M^{eim}(u, e(\boldsymbol{\mu}); \boldsymbol{\mu}) - R_M^{eim}(u_N, e(\boldsymbol{\mu}); \boldsymbol{\mu}) \tag{2.53}$$

Assuming the existence of the Riesz representations $\hat{a}_{q,m,n}$ and $\hat{f}_{q,m}$ defined as

$$(\hat{a}_{q,m,n}, v)_X = a_{q,m}(\xi_n, v) \text{ and } (\hat{f}_{q,m}, v)_X = f_{q,m}(v) \tag{2.54}$$

the Riesz representation of $\mathcal{Y}R^{aff}_{N,M}(\cdot;\boldsymbol{\mu})$ of $R^{aff}_{N,M}$ reads

$$\mathcal{Y}R^{aff}_{N,M}(\cdot;\boldsymbol{\mu}) = \sum_{q=1}^{Q_f}\sum_{m=1}^{M_q^f}\gamma^f_{q,m}(u;\boldsymbol{\mu})\hat{f}_{q,m} - \sum_{q=1}^{Q_a}\sum_{m=1}^{M_q^a}\sum_{n=1}^{N}\gamma^a_{q,m}(u;\boldsymbol{\mu})u_{N,n}\hat{a}_{q,m,n} \tag{2.55}$$

If (2.53) is satisfied, the expected error bound $\Delta_N(\boldsymbol{\mu})$ of $\| e(\boldsymbol{\mu}) \|_X$ shall read as

$$\Delta_{N,M}(\boldsymbol{\mu}) \equiv \frac{\| \mathcal{Y}R^{aff}_{N,M}(\cdot;\boldsymbol{\mu}) \|_X}{\hat{\alpha}(\boldsymbol{\mu})} \tag{2.56}$$

In a practical point of view, the validity of the condition (2.53) can be hard to determine. Moreover, $\hat{\alpha}(\boldsymbol{\mu})$ can be computationally costly when it exists. Although it is not an error bound, the norm of the Riesz representation $\mathcal{Y}R^{aff}_{N,M}$ could rank as an error indicator and could then serve as a guide for the RB Greedy algorithm.

Preliminary results Based on the same benchmark as previously, the use of the previous error indicator is illustrated in the following tables. It is employed in the parameter selection process on which the RB approximation is based. Table 2.2a first displays the absolute errors obtained with standard methodology combined with the use of the previous error indicator.

N	M	$\max(\epsilon^{u,1}_{M,N})$	$\max(\epsilon^{s,1}_{M,N})$
5	5	8.22e-3	6.27e-3
10	10	2.87e-4	2.09e-4
15	15	1.96e-5	1.47e-5
20	20	1.57e-5	1.32e-5
25	25	3.14e-6	2.52e-6

(a) Standard + error estimation

N	M	$\max(\epsilon^{u,1}_{M,N})$	$\max(\epsilon^{s,1}_{M,N})$
5	5	1.04e-2	8.09e-3
10	10	2.40e-3	1.87e-3
15	15	2.38e-4	2.01e-4
20	20	3.02e-5	1.67e-5
25	25	2.65e-5	1.94e-5

(b) $r = 1$ - RB Greedy

Table 2.2 – SER - Maximum absolute errors with error estimation

Although confirming the relevance of the Greedy algorithm in the RB approximation space build, the error indicator doesn't seem to improve the errors compared with the previous random selection. The same behavior is observed with both SER (Table 2.2b) and standard RB method (Table 2.2a).

2.3.2 SER variants

The previous section detailed the development of an error indicator adapted to non-linear and non-affinely parametrized problems. Its use all through the building of the RB approximation space consists in the first SER variant, whose results on the 2D benchmark

were already displayed in Table 2.2.

Besides its primary goal, this error indicator can however serve as a quantifier of the reduced basis approximation accuracy all through the SER offline procedure. This section describes the various alternatives that have been investigated in this direction. Each of them is illustrated with results coming from its application of the previously considered 2D benchmark.

r-adaptation The SER method offers the possibility to perform the alternative enrichment of the EIM and RB approximation spaces, by groups of size r. Table 2.1 compares the errors obtained with various values of the update frequency. These results tend to show that the increase of r could help the RB approximation error decrease. It is therefore difficult to determine a suitable value for r beforehand and to ensure this value would be adapted for the whole offline step.

The construction of both EIM and RB approximations is based on a Greedy algorithm, which enables to select the maximizer of a functional mimicking the approximation error. Regarding the RB approximation space, this functional is based on the previous error indicator. Its increment between two affine decomposition updates allows to quantify the gain in terms of accuracy. The error indicator then appears as a criterion providing guidance to perform a smart adaptation of r during the SER process. The so-called r-adaptation method thus aims to continue the enrichment until a relevant decrease of the approximation error.

We distinguish the criterions used for the two EIM and RB approximation spaces. Each are based on the increment of the maximal value of its Greedy algorithm's functional. For EIM, this functional (2.11) stands for the EIM approximation error. Regarding the RB space, it relies on the error indicator introduced in Section 2.3.1 as the norm of the Riesz representation $\mathcal{Y}R^{aff}_{N,M}$.

Table 2.4 takes as reference the results previously obtained with $r = 1$ combined with the use of the error indicator (Table 2.3a). These results are compared with the errors obtained from the use of the $r-$adaptation method.

Table 2.3b adapts the update frequency of EIM approximation space only, with a given tolerance of 20%. Table 2.4a focuses on the RB approximation space only, with the same tolerance. Finally, Table 2.4b investigate the $r-$adaptation on both approximation spaces.

Compared with the reference Table 2.3a, the obtained results don't allow to assess the pertinence of the proposed r-adaptation method. Indeed, the resulting errors remains at the same order of magnitude whatever the approximation space considered for adaptation.

N	M	$\max(\epsilon^{u,1}_{M,N})$	$\max(\epsilon^{s,1}_{M,N})$
5	5	1.04e-2	8.09e-3
10	10	2.40e-3	1.87e-3
15	15	2.38e-4	2.01e-4
20	20	3.02e-5	1.67e-5
25	25	2.65e-5	1.94e-5

(a) $r = 1$ - RB Greedy

N	M	$\max(\epsilon^{u,1}_{M,N})$	$\max(\epsilon^{s,1}_{M,N})$
5	5	1.04e-2	8.09e-3
10	10	2.40e-3	1.87e-3
15	15	2.34e-4	1.95e-4
20	20	4.36e-5	2.74e-5
25	25	2.16e-5	1.36e-5

(b) $r-$adaptation - EIM 20%

N	M	$\max(\epsilon^{u,1}_{M,N})$	$\max(\epsilon^{s,1}_{M,N})$
5	5	1.04e-2	8.09e-3
10	10	2.40e-3	1.87e-3
15	15	5.90e-4	4.16e-4
20	20	2.87e-5	1.61e-5
25	25	2.35e-5	6.35e-6

(a) $r-$adaptation - RB 20%

N	M	$\max(\epsilon^{u,1}_{M,N})$	$\max(\epsilon^{s,1}_{M,N})$
5	5	1.04e-2	8.09e-3
10	10	2.40e-3	1.87e-3
15	15	2.34e-4	1.95e-4
20	20	3.46e-5	2.01e-5
25	25	1.61e-5	9.19e-6

(b) $r-$adaptation - EIM 20% - RB 20%

Table 2.4 – SER $r-$adaptation - Maximum absolute errors on solution u and on output s

Hybrid Greedy algorithm The core of the proposed SER method resides in the use of a reduced basis approximation in the EIM offline stage. The accuracy of the current reduced basis approximation thus plays a key role in the $\bar{S}_M$ building step. Especially regarding the first basis functions, a reduced basis approximation of poor quality could damage the EIM approximation, and consequently the quality of the affine decomposition.

The proposed error indicator, used as a quantifier of the current reduced basis approximation quality, allows to sort the considered reduced approximations from their accuracy. In this context, the Greedy algorithm can employ the reduced basis approximation solely on parameters for which it proves relevant.

Nevertheless, the maximizer of the functional could be one of the remaining parameters. In order not to ignore them, the reduced basis approximations qualified as irrelevant is replaced by a parametric finite element solution. Although more costly, these approximations rely on the affine decomposition which allows to benefit from the offline precomputations.

As a compromise between the standard reduced basis methodology introduced in Section 2.2 and the initial SER method, this variant consists in a hybrid Greedy algorithm within the EIM offline stage combining finite element and reduced basis approximations.

Turning back to the previous benchmark, Table 2.5 illustrates the errors obtained with the proposed method for two given selection tolerances. The combination of these two types of approximation appears to deteriorate the behavior of the SER method. This underscores the importance of considering only one single model all through the EIM training set.

N	M	$\max(\epsilon^{u,1}_{M,N})$	$\max(\epsilon^{s,1}_{M,N})$
5	5	9.10e-3	7.11e-3
10	10	3.10e-3	2.49e-3
15	15	1.94e-4	7.62e-5
20	20	2.61e-4	1.49e-4
25	25	5.21e-5	3.74e-5

(a) EIM hybrid Greedy - 20%

N	M	$\max(\epsilon^{u,1}_{M,N})$	$\max(\epsilon^{s,1}_{M,N})$
5	5	7.59e-3	5.70e-3
10	10	2.68e-3	2.23e-3
15	15	7.05e-4	4.26e-4
20	20	1.90e-4	1.11e-4
25	25	8.18e-5	4.19e-5

(b) EIM hybrid Greedy - 10%

Table 2.5 – Hybrid Greedy algorithm - Maximum absolute errors on solution u and on output s

Multi-levels SER(l) The last proposed SER variant rests on the application of the SER methodology several times during the offline stage.

The first level consists in the previously described SER offline stage, resulting in a first reduced basis approximation. Instead of settling for such a reduced basis approximation, the multi-levels SER(l) variant proposes to continue the offline stage by making a second application. The Greedy algorithm allowing to build the EIM approximation space is that time based on the reduced basis approximation coming from the previous level.

More generally, let us denote u^l_N the reduced basis approximation obtained at the level l. The EIM Greedy algorithm reads for $l \leqslant 2$ as

$$\bar{\boldsymbol{\mu}}_M = arg \max_{\boldsymbol{\mu}\in\Xi} \inf_{z\in W_{M-1}} ||w(u^{l-1}_N(\boldsymbol{\mu}); .; \boldsymbol{\mu}) - z||_{L^\infty(\Omega)} \tag{2.57}$$

From the second level, the EIM approximation is computed from a more accurate reduced approximation than at first level. It is consequently expected that the accuracy of the EIM approximations is improved, resulting in a better affine decomposition. Thus, we expect the reduced basis approximation coming from the second application of the offline step to be improved as well.

We shall note that the multi-levels SER variant is not limited to a single SER configuration. All the previously proposed variants can be used in this context as long as it is applied several times.

Table 2.6 shows the errors resulting from the fourfold application of the initial SER methodology on the 2D benchmark. Each level is based on a random selection process in the building of the RB approximation space.

The overall online simulations are performed at the end of each offline stage to evaluate the gain brought by each level. By construction, the first level (Table 2.6a) gives errors whose order of magnitude is similar to those obtained in Table 2.1d. As to the tables 2.6b, 2.6c and 2.6d, they illustrate the errors at the next levels highlighting the expected error decrease.

N	M	$\max(\epsilon^u_{M,N})$	$\max(\epsilon^s_{M,N})$
5	5	1.06e-2	8.40e-3
10	10	2.33e-3	1.72e-3
15	15	6.51e-4	5.12e-4
20	20	2.32e-4	1.94e-4
25	25	7.08e-5	5.64e-5

(a) SER(1)

N	M	$\max(\epsilon^u_{M,N})$	$\max(\epsilon^s_{M,N})$
5	5	9.13e-3	7.12e-3
10	10	3.19e-4	1.12e-4
15	15	7.56e-5	5.36e-5
20	20	1.54e-4	2.67e-5
25	25	3.52e-5	2.76e-5

(b) SER(2)

N	M	$\max(\epsilon^u_{M,N})$	$\max(\epsilon^s_{M,N})$
5	5	7.26e-3	5.58e-3
10	10	2.00e-3	1.13e-3
15	15	5.50e-4	4.43e-4
20	20	2.08e-4	3.27e-5
25	25	1.37e-5	6.87e-6

(c) SER(3)

N	M	$\max(\epsilon^u_{M,N})$	$\max(\epsilon^s_{M,N})$
5	5	8.67e-3	6.58e-3
10	10	5.07e-3	3.35e-3
15	15	2.78e-4	2.30e-4
20	20	2.67e-4	4.35e-5
25	25	5.62e-6	2.56e-6

(d) SER(4)

Table 2.6 – SER multi-levels - Random

Table 2.7 reproduces the previous study using a Greedy algorithm in the RB approximation space, instead of a random selection.

As expected, the reference Table 2.7a is exactly the same as the one previously obtained in Section 2.3.1. The tables 2.7b, 2.7c and 2.7d confirm the behavior observed in Table 2.6, emphasizing on the decrease of the errors through the SER levels.

N	M	$\max(\epsilon^u_{M,N})$	$\max(\epsilon^s_{M,N})$
5	5	1.04e-2	8.09e-3
10	10	2.39e-3	1.86e-3
15	15	2.38e-4	2.00e-4
20	20	3.03e-5	1.65e-5
25	25	3.42e-5	2.45e-5

(a) SER(1)

N	M	$\max(\epsilon^u_{M,N})$	$\max(\epsilon^s_{M,N})$
5	5	9.17e-3	6.99e-3
10	10	2.89e-4	2.07e-4
15	15	4.12e-5	1.87e-5
20	20	1.44e-5	7.61e-6
25	25	2.72e-5	2.20e-5

(b) SER(2)

N	M	$\max(\epsilon^u_{M,N})$	$\max(\epsilon^s_{M,N})$
5	5	7.93e-3	6.01e-3
10	10	2.99e-4	1.80e-4
15	15	1.75e-4	1.35e-4
20	20	1.69e-5	6.02e-6
25	25	7.86e-6	5.37e-6

(c) SER(3)

N	M	$\max(\epsilon^u_{M,N})$	$\max(\epsilon^s_{M,N})$
5	5	8.46e-3	6.36e-3
10	10	4.34e-4	2.24e-4
15	15	6.28e-5	5.05e-5
20	20	1.76e-5	1.17e-5
25	25	1.92e-5	1.51e-5

(d) SER(4)

Table 2.7 – SER multi-levels - RB Greedy

Finally, the previous comments concerning the tables 2.6 and 2.7 are supported by the convergence study of the considered EIM approximation.

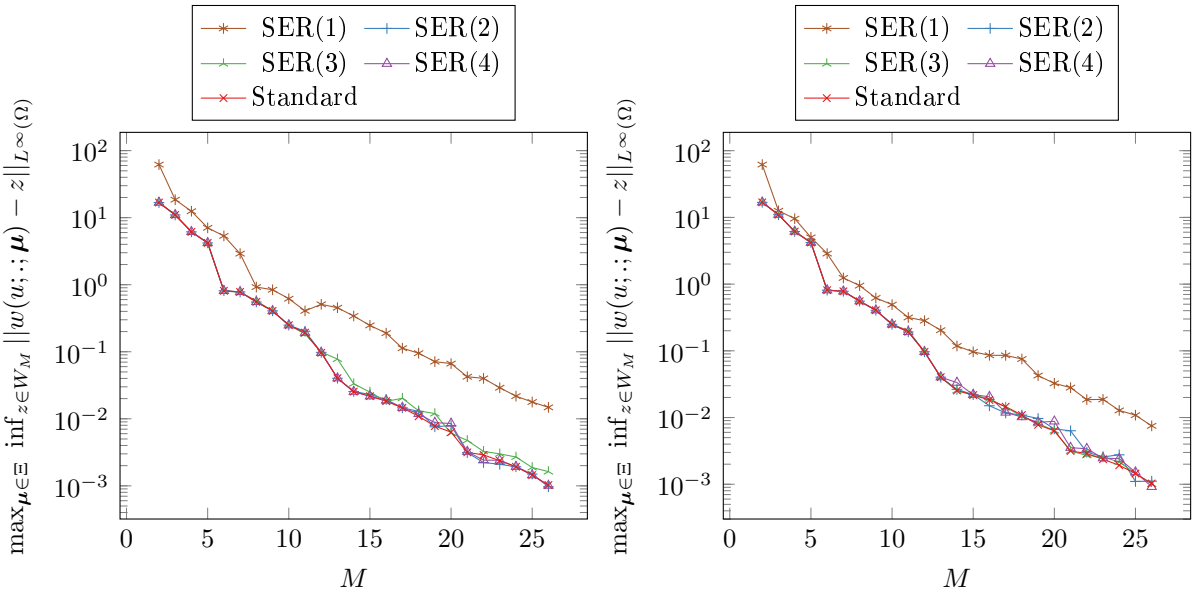

(a) RB Random (b) RB Greedy

Figure 2.1 – SER multi-levels - EIM convergence

Figure 2.1 plots the maximal value of the functional used in the EIM Greedy algorithm, depending on the number of basis functions which compose the EIM approximation space. We can indeed notice a significant improvement of the quality of our EIM approximation from the second level.

The next levels remains comparable to the latter, already very close to the EIM approximation performed from the standard method.

Conclusion

This chapter deals with the application of the Reduced Basis method to non-linear and non-affinely parametrized problems which concern us. In this context, the Empirical Interpolation Method is introduced to recover the affine decomposition necessary to apply the Reduced Basis methodology.

We propose the Simultaneous Empirical interpolation and Reduced basis (SER) method, which combines these two methods in order to benefit from the efficiency of the reduced basis approximation within the EIM offline stage. This provides a huge computational gain for the offline step since it requires only $N + 1$ finite element solves, where N is the dimension of the RB approximation. Especially, the number of FE approximations required in the EIM offline stage no longer depends on the size of the considered trainset.

This section introduces the SER method drawing on results obtained on a 2D benchmark introduced in [Grepl et al., 2007]. These results show the pertinence of this method for non-linear and non-affine PDEs, and prove that we can expect good results within a reasonable computational budget.

We present also some variants investigated for this method. They are mainly based

on the development of an error indicator we propose for non-linear and non affinely parametrized problems. Although it doesn't provide error bounds for the reduced basis approximation, this error indicator serves to guide the parameter selection performed to build the RB approximation space. On the 2D benchmark, the impact of the Greedy algorithm in the selection process is limited. But we will see in Chapter 11 that it is significant on other applications.

The multi-levels SER(l) method appears as the most promising variant for SER. However, many other variants remain to be investigated.

Part II

Multi-physics modeling of high field magnets

Chapter 3

Three-dimensional non-linear multi-physics FE model

Although electromagnetism equations are at the basis of high field magnet modeling, physics involved in electromagnets study are many. Indeed, high field magnet design is not only driven by magnetic field considerations, but also by others physics. The magnetic field intensity is controlled by the current density provided to the electromagnet. An important current supply (typically few tens of kA) is necessary to produce high magnetic field. This current induces Joule losses within the magnet insert, leading to an important heating which could degrade the mechanical properties of the material. Thus, a magnet design study asks for an accurate account of this temperature increase which consists in computing Joule losses term to be considered as the source of a standard heat equation.

This temperature increase leads to thermal dilatation which causes deformations. Added to the mechanical forces induced by magnetic field, these stresses form a supplementary constraint for high field magnets design. This confirms the need of an efficient and reliable multi-physics model in the context of high field magnets design.

Most high magnetic field facilities use Bitter magnet technology described in the introduction of this thesis. The optimization of such magnets is performed from 2D axisymmetrical models, based on the hypothesis that these objects are symmetric. Nevertheless, the polyhelix magnets developped at LNCMI present an asymmetry which makes this hypothesis inaccurate. The accurate modeling of such magnets cannot simply rely on the existing 2D axisymmetrical models. This chapter gives an overview of the three-dimensional non-linear multi-physics model developped through this thesis.

The current density computation being at the basis of other quantities of interest, the electrical model is the first to be considered. Due to the temperature dependence of material properties, the latter is coupled with the heat equation leading to the electro-thermal model described in Section 3.1. Coupled with the resulting current density, the magnetic field computation can be performed in different ways. Two of which are considered in this section, both coming from Maxwell's equations. Section 3.2 details the finite element magnetostatic model, while the next (Section 3.3) describes the computation of the magnetic field from the Biot & Savart's law. Finally, the mechanical stresses coming both from magnetic and thermal forces are computed from a linear elasticity model described

in Section 3.4. The induced displacements as well as the yield strength criterions are deduced from this model to help the optimization in terms of materials.

Contents

Each of these sections detail the equations of the concerned model along with convergence studies required for its verification. The coupling between the components of the multi-physics model is established all through this chapter. The validation of this model is further described in the last part of the manuscript.

3.1 Electro-thermal model

3.1.1 Equations

Electric potential

Magnetic field variation over time induces an electric field proportional to this variation. Discovered by Faraday in 1831, this relation became an assumption for electromagnetism and appears in the so-called Maxwell's equation as the Maxwell-Faraday equation (3.1).

$$\nabla \wedge \mathbf{E} = -\frac{\partial \mathbf{B}}{\partial t} \tag{3.1}$$

The current density $\mathbf{j}$ we focus on is proportional to this electric field $\mathbf{E}$ from the local form of the Ohm's law

$$\mathbf{j} = \sigma \mathbf{E} \tag{3.2}$$

where σ is the electrical conductivity of the material.

This section focuses on the steady case. Thus, the time derivative term in the previous Maxwell-Faraday equation (3.1) is null. Since its rotational is zero, the electrical field $\mathbf{E}$ can read as the gradient of a scalar potential V defined as the electrical potential.

$$\nabla \wedge \mathbf{E} = 0 \quad \Rightarrow \quad \exists V \mid \mathbf{E} = -\nabla V \tag{3.3}$$

The charge conservation principle gives the electric charge variation over time as the opposite of the electric charge flux $\mathbf{j}.\mathbf{n}$ through the surface. In steady case, this ensures a divergence-free condition for current density $\mathbf{j}$.

The steady electrical potential equation then reads

$$\nabla \cdot (-\sigma \nabla V) = 0 \tag{3.4}$$

Temperature

The heat equation is determined by the first thermodynamic principle ensuring the energy conservation in the systems. The energy variation δU over time reads as the sum of heat δQ and work δW variations in the system. In our case, δW is neglected as we consider small deformations assuming that the volume of the system remains unchanged. The energy variation is then only controlled by heat which involves temperature variation in the system

$$\delta U = \delta Q = C_p \rho_Q \frac{\partial T}{\partial t} \tag{3.5}$$

where C_p and ρ_Q are respectively the specific heat capacity and the mass density of the material.

The heat variation δQ reads also from the heat flux density $\mathbf{j}_Q$, which defines the heat received by surface unit as $\mathbf{j}_Q \cdot \mathbf{n}$, with $\mathbf{n}$ the outward normal. Eventual internal sources of heat P (as Joule effect) are also added to δQ which becomes

$$\delta Q = \nabla \cdot \mathbf{j}_Q + P \tag{3.6}$$

The heat flux density $\mathbf{j}_Q$ is proper to the material. Fourier's law defines it from the thermal conductivity k of the material giving $\mathbf{j}_Q = k\nabla T$, allowing to deduce the heat equation from (3.5) and (3.6)

$$-\nabla \cdot (k\nabla T) + C_p \rho_Q \frac{\partial T}{\partial t} = P \tag{3.7}$$

The internal source of heat is limited to Joule effect in our case. The local form of Joule's law then defines the source term P as $P = \mathbf{j} \cdot \mathbf{E}$, where $\mathbf{j}$ and $\mathbf{E}$ are the current density and the electric field previously defined. From relations (3.2) and (3.3), the internal heat source term reads

$$P = \sigma \nabla V \cdot \nabla V \tag{3.8}$$

The steady heat equation used for electro-magnet study then reads

$$-\nabla \cdot (k\nabla T) = \sigma \nabla V \cdot \nabla V \tag{3.9}$$

Material properties

The electrical potential and temperature equations (3.4) and (3.9) involve electrical (resp. thermal) conductivities σ (resp. k), which are proper to the material used. The electrical conductivity describes the ability of electric charges to move in the material. Metals at room temperature or higher have resistance, and the electric charges mobility is countered by the resistivity of material defined as the inverse of its conductivity. For metals at room temperature or higher as for high field magnets, the material's resistivity ρ increases linearly with the temperature such that

$$\rho(T) = \rho_0(1 + \alpha(T - T_0)) \tag{3.10}$$

with ρ_0 the resistivity at reference temperature T_0, and α the so-called temperature coefficient obtained empirically from measurements.

The electrical conductivity expression can then be easily deduced from the linear relation (3.10) considering σ_0 the electrical conductivity at reference temperature T_0

$$\sigma(T) = \frac{\sigma_0}{1 + \alpha(T - T_0)} \tag{3.11}$$

Moreover, the thermal conductivity of a metal is proportionnal to its electrical conductivity and its temperature. This relation is established by Wiedemann–Franz law leading to the expression of the thermal conductivity

$$k(T) = \sigma(T)LT \tag{3.12}$$

where L is a constant known as the Lorentz number which is proper to the considered material.

This dependence on temperature for conductivities involved in (3.4) and (3.9) leads to a non-linearity in the coupled electro-thermal model.

Boundary conditions

The current circulation in the magnet is imposed as a difference of potential V_D between current input and output. This corresponds to an homogeneous Dirichlet boundary condition imposed on current input V_{in}, associated with the Dirichlet condition $V = V_D$ on current output V_{out}.

$$\begin{aligned} V &= 0 \text{ on } V_{in} \\ V &= V_D \text{ on } V_{out} \end{aligned} \tag{3.13}$$

The air and the cooling water surrounding the magnets are considered as electrically insulating. This means that the current density flux $\mathbf{j} \cdot \mathbf{n}$ accross the borders is null. From (3.2) and (3.3) this leads to an homogeneous Neumann boundary condition

$$-\sigma(T)\nabla V \cdot \mathbf{n} = 0 \text{ on } \partial\Omega \backslash (V_{in} \cup V_{out}) \tag{3.14}$$

The thermal flux $\mathbf{j}_Q \cdot \mathbf{n}$ is controlled by the water cooling of the magnet, and is non zero only accross the cooled surfaces denoted $\partial\Omega_{\text{cooled}}$. The thermal exchange between the conductor and the cooling water is governed by a convection phenomenon. The amount of heat exchanged depends on a heat tranfer coefficient h, and defines the thermal flux on cooled regions as $\mathbf{j}_Q \cdot \mathbf{n} = h(T - T_w)$. The heat transfer coefficient is determined from the thermal conductivity $k(T)$, the hydraulic diameter D_h and the Nusselt number Nu commonly used in heat transfer considerations [Colburn, 1933].

$$h = \frac{k(T)Nu}{D_h} \tag{3.15}$$

The Nusselt Number Nu is proper to the considered flow and can be determined by stan-

dard hydraulic correlations. For perpendicular flows in annular region between cylinders as for high field magnet cooling, the Colburn correlation is used.

The cooling process is thus handled by a Robin condition applying the Fourier's laws to the thermal flux on the cooled regions

$$-k(T)\nabla T \cdot \mathbf{n} = h(T - T_w) \text{ on } \partial\Omega_{\text{cooled}} \tag{3.16}$$

The thermal exchanges in uncooled regions are not considered, leading to a null thermal flux accross the concerned surfaces giving the homogeneous Neumann condition

$$-k(T)\nabla T \cdot \mathbf{n} = 0 \text{ on } \partial\Omega \backslash \partial\Omega_{\text{cooled}} \tag{3.17}$$

Considering the electrical conductor as a domain Ω, the resulting non-linear coupled electro-thermal model reads as follows with the considered boundary conditions

$$\begin{cases} -\nabla \cdot (\sigma(T)\nabla V) = 0 \text{ in } \Omega \\ -\nabla \cdot (k(T)\nabla T) = \sigma(T)\nabla V \cdot \nabla V \text{ in } \Omega \\ V = 0 \text{ on } V_{in} \\ V = V_D \text{ on } V_{out} \\ -\sigma(T)\nabla V \cdot \mathbf{n} = 0 \text{ on } \partial\Omega \backslash (V_{in} \cup V_{out}) \\ -k(T)\nabla T \cdot \mathbf{n} = 0 \text{ on } \partial\Omega \backslash \partial\Omega_{\text{cooled}} \\ -k(T)\nabla T \cdot \mathbf{n} = h(T - T_w) \text{ on } \partial\Omega_{\text{cooled}} \end{cases} \tag{3.18}$$

3.1.2 Variational formulation

The variational formulation of the non-linear coupled electro-thermal model (3.18) consists in finding $(V, T) \in X_V \times X_T$ such that

$$\begin{aligned} a_V(V, \phi_V) &= f_V(\phi_V) \ \forall \ \phi_V \in X_V \\ a_T(T, \phi_T) &= f_T(\phi_T) \ \forall \ \phi_T \in X_T \end{aligned} \tag{3.19}$$

with ϕ_V (resp. ϕ_T) the test functions associated with electrical potential V (resp. with the temperatue T), and X_V (resp. X_T) function spaces to be defined.

Electrical potential From electrical potential equation (3.4) and associated boundary conditions, the variational formulation consists in finding $V \in X_V \subset H_1(\Omega)$ such that $\forall \ \phi_V \in X_{\phi_V} \subset H_1(\Omega)$

$$\int_\Omega \sigma(T)\nabla V \cdot \nabla \phi_V - \int_{\partial\Omega} \sigma(T)(\nabla V \cdot \mathbf{n})\phi_V = 0 \tag{3.20}$$

Imposed in strong form, Dirichlet conditions (3.13) are embedded into the X_V function space definition and the boundary term of (3.20) vanishes as we have a Neumann homogeneous condition (3.14) on $\partial\Omega$. By this way, the formulation (3.20) with strong Dirichlet boundary conditions consists in finding $V \in X_V = \{v \in H_1(\Omega) \mid v = 0 \text{ on } V_{in}, |$

$v = V_D$ on $V_{out}\}$ such that $\forall\ \phi_V \in X_{\phi_V} = \{v \in H_1(\Omega) \mid v = 0$ on $V_{in} \cup V_{out}\}$

$$\int_\Omega \sigma(T)\nabla V \cdot \nabla \phi_V = 0 \tag{3.21}$$

Dirichlet conditions can also be weakly imposed using Nitsche's method which consists in adding symetrization and penalisation terms without conditions in the function space definition. In this case, (3.20) consists in finding $V \in X_V = H_1(\Omega)$ such that $\forall\ \phi_V \in X_V$

$$\begin{aligned}\int_\Omega \sigma(T)\nabla V \cdot \nabla \phi_V - \int_{V_{in}\cup V_{out}} \sigma(T)(\nabla V \cdot \mathbf{n})\phi_V - \int_{V_{in}\cup V_{out}} \sigma(T)(\nabla \phi_V \cdot \mathbf{n})V \quad &+ \int_{V_{in}\cup V_{out}} \frac{\gamma}{h}\sigma(T)V\phi_V \\ = -\underbrace{\int_{V_{out}} \sigma(T)(\nabla \phi_V \cdot \mathbf{n})V_D}_{\text{symetrization}} \quad &+ \underbrace{\int_{V_{out}} \frac{\gamma}{h}\sigma(T)V_D\phi_V}_{\text{penalisation}}\end{aligned} \tag{3.22}$$

Temperature From the heat equation (3.9) and its boundary conditions, the variational formulation consists in finding $T \in X_T \subset H_1(\Omega)$ such that $\forall\ \phi_T \in X_T$

$$\int_\Omega k(T)\nabla T \cdot \nabla \phi_T - \int_{\partial\Omega} k(T)(\nabla T \cdot \mathbf{n})\phi_T = \int_\Omega \sigma(T)\nabla V \cdot \nabla V \phi_T \tag{3.23}$$

Contrary to previous electrical potential formulation, there is no Dirichlet boundary conditions for temperature. Boundary conditions are naturally applied to the formulation and X_T is simply $H_1(\Omega)$. The variationnal formulation then consists in finding $V \in X_T = H_1(\Omega)$ such that $\forall\ \phi_T \in X_T$

$$\int_\Omega k(T)\nabla T \cdot \nabla \phi_T + \int_{\partial\Omega_{\text{cooled}}} hT\phi_T = \int_\Omega \sigma(T)\nabla V \cdot \nabla V + \int_{\partial\Omega_{\text{cooled}}} hT_w\phi_T \tag{3.24}$$

The non-linearity due to the dependence of material properties σ and k on temperature is handled by iterative methods. Either Picard or Newton are used for this model.

Picard method The Picard method is the most standard way to deal with such a non-linearity. From an initial guess $X^0 = (V^0, T^0)$ value given for the couple potential-temperature, this methods consists in computing $X^{n+1} = (V^{n+1}, T^{n+1})$ from $X^n = (V^n, T^n)$ solving alternately (3.20) and (3.23) until convergence. Convergence is based on the increment $\Delta = X^{n+1} - X^n$ and is considered as reached when Δ becomes lower than a user-defined tolerance.

Newton method The solution $X = (V, T)$ of the previous electro-thermal problem (3.18) can be seen as the root of a functional R (3.25)

$$R : \begin{pmatrix} V \\ T \end{pmatrix} \longmapsto \begin{pmatrix} R_1(V,T) \\ R_2(V,T) \end{pmatrix} = \begin{pmatrix} a_V(V,\phi_V) - f_V(\phi_V) \\ a_T(T,\phi_T) - f_T(\phi_T) \end{pmatrix} \tag{3.25}$$

where R_1 and R_2 are defined from (3.20) and (3.23)

The Newton's method allows to find the zeros of (3.25) solving the matricial system

$$J_R(X^n) * (X^{n+1} - X^n) = -R(X^n)$$

where $X^n = (V^n, T^n)$ is the solution at the n^{th} iteration and J_R the Jacobian of R given by (3.25).

$$J_R = \begin{pmatrix} \frac{\partial R_1}{\partial V} & \frac{\partial R_1}{\partial T} \\ \frac{\partial R_2}{\partial V} & \frac{\partial R_2}{\partial T} \end{pmatrix} \tag{3.26}$$

3.1.3 Convergence study

Let u_{ex} be the exact solution of a considered problem (electrical potential or heat equation solution) and u its approximation. The approximation error reads

$$e = u_{ex} - u \tag{3.27}$$

The verification step ensures that convergence order properties are satisfied, that is

$$\| e \|_{L_2} \leqslant ch^{k+1} \quad \text{and} \quad \| e \|_{H_1} \leqslant ch^k \tag{3.28}$$

with h the mesh size, k the polynomial order of the approximation and c a constant.
The convergence study checks that requirements (3.28) are satisfied by our approximation, plotting $\| e \|_{L_2}$ and $\| e \|_{H_1}$ depending on the mesh size h. In logarithmic scale, (3.28) corresponds to a linear function of slope $k+1$ (resp. k) for $\| e \|_{L_2}$ (resp. $\| e \|_{H_1}$). However, the computation of such an error norm $\| e \|$ (3.27) obviously induces the knowledge of the exact solution u_{ex}, which is usually unknown. Based on axisymmetrical considerations, an analytical solution is available for the linearized electro-thermal model – that is with constant electrical and thermal conductivities – and serves as initial verification. This solution doesn't work for the non-linear model, due to the dependence of material properties on temperature. In this context, a posteriori error estimators are used to estimate $\| e \|$.

Introduced by Zienkiewicz and Zhu in [Zienkiewicz and Zhu, 1992], the gradient recovery based error estimators apply in this context. The latter are based on the approximation of the error $e_\nabla = \nabla e$ on the gradient. This error is estimated by a global error estimator $e^\star_\nabla$ (3.29) mimicking the gradient ∇u_{ex} of the exact solution using the gradient recovery operator $Rh(\nabla u)$ interpolating ∇u from its nodal values.

$$e_\nabla \approx e^\star_\nabla = Rh(\nabla u) - \nabla u \tag{3.29}$$

This section first gives the convergence results performed on linear electro-thermal model both from analytical solution as an initial verification step and from a posteriori

error estimators in order to prove their efficiency. The convergence study for non-linear electro-thermal model is based on these error estimators and is performed with both Picard and Newton iterative methods.

Linear model - Analytical solution

The expression of an analytical solution for the linear electro thermal model can be established in a cylindrical frame from axisymmetrical considerations. The considered axisymmetrical geometry (Figure 3.2a) illustrates the sector of a magnet turn traversed by a current and longitudinaly water cooled. We shall note the similarity with a Bitter magnet without the cooling holes. Input parameters are given in table 3.1.

σ_0	k_0	L	α	h	T_w	V_D
4.8×10^7	377	2.47^{-8}	3.35^{-3}	6×10^4	303	0.25

Figure 3.1 – Thermo-electric analytical solution - Parameter values

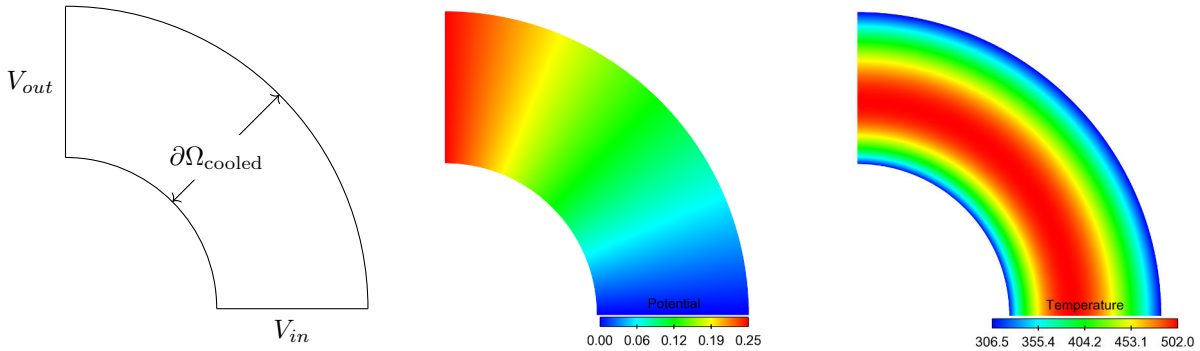

(a) Geometry (b) Potential (c) Temperature

Figure 3.2 – Analytical solution of axisymmetrical geometry

The linear electro-thermal model (3.30) is obtained from (3.18) considering that the electrical (resp. thermal) conductivity σ (resp. k) doesn't depend on temperature.

$$
\left\{
\begin{array}{l}
-\nabla \cdot (\nabla V) = 0 \text{ in } \Omega \\
-\nabla \cdot (\nabla T) = \dfrac{\sigma}{k} \nabla V \cdot \nabla V \text{ in } \Omega \\
V = 0 \text{ on } V_{in} \\
V = V_D \text{ on } V_{out} \\
-\sigma_0 \nabla V \cdot \mathbf{n} = 0 \text{ on } \partial\Omega \backslash (V_{in} \cup V_{out}) \\
-k_0 \nabla T \cdot \mathbf{n} = 0 \text{ on } \partial\Omega \backslash \partial\Omega_{\text{cooled}} \\
-k_0 \nabla T \cdot \mathbf{n} = h(T - T_w) \text{ on } \partial\Omega_{\text{cooled}}
\end{array}
\right. \tag{3.30}
$$

The electrical current circulation from V_{in} ($\theta = 0$) to V_{out} ($\theta = \frac{\pi}{2}$) imposed by Dirichlet boundary conditions induces that V_{ana} depends only on θ. From divergence and gradient operators in cylindrical coordinates system, we easily deduce that V_{ana} reads as a first order polynomial

$$
V_{ana}(\theta) = A_V \theta + B_V \tag{3.31}
$$

The Dirichlet boundary conditions on V_{in} and V_{out} satisfied by V_{ana} allow to determine the values of A_V and B_V constants and consequently the expression of V_{ana} to be replaced in the heat equation as

$$V_{ana} = \frac{2V_D\theta}{\pi}, \qquad -\nabla \cdot (\nabla T_{ana}) = \frac{\sigma_0}{k_0}\frac{4V_D^2}{r^2\pi^2} \text{ in } \Omega \tag{3.32}$$

Moreover, the zero flux boundary conditions on temperature and the current orientation suppose that T_{ana} depends only on r. From this consideration, T_{ana} can be expressed as the second order $log(r)$ polynomial

$$T_{ana} = A_T log(r)^2 + B_T log(r) + C_T \tag{3.33}$$

with A_T, B_T and C_T constants. The cooling boundary conditions allows to determine those constants to be replaced in (3.33) where r_e (resp. r_i) names the external (resp. internal) radius

$$\begin{aligned} A_T &= -\frac{2\sigma_0 V_D^2}{\pi^2 k_0} \qquad B_T = \frac{-A_T(B_i + B_e)}{B_r}; \\ C_T &= \frac{1}{2hr_e r_i}\left[(B_i - B_e)A_T + (k_0(r_e - r_i) - hr_e r_i log(r_e r_i))B_T\right] + T_w \end{aligned} \tag{3.34}$$

where

$$\begin{aligned} B_i &= 2k_0 r_e log(r_i) - hr_e r_i log(r_i)^2 \quad \text{and} \quad B_e = 2k_0 r_i log(r_e) + hr_e r_i log(r_e)^2 \\ B_r &= k_0(r_i + r_e) + hr_e r_i log(\frac{r_e}{r_i}) \end{aligned}$$

Figures 3.3 to 3.6 illustrate the 2D and 3D convergence studies performed on this model. These graphs plot the L_2 and H_1 norms of approximation error obtained with the linear model depending on the mesh size. They display both exact and estimated errors for two polynomials orders, where $P1$ refers to the first polynomial order while $P2$ refers to the second one.

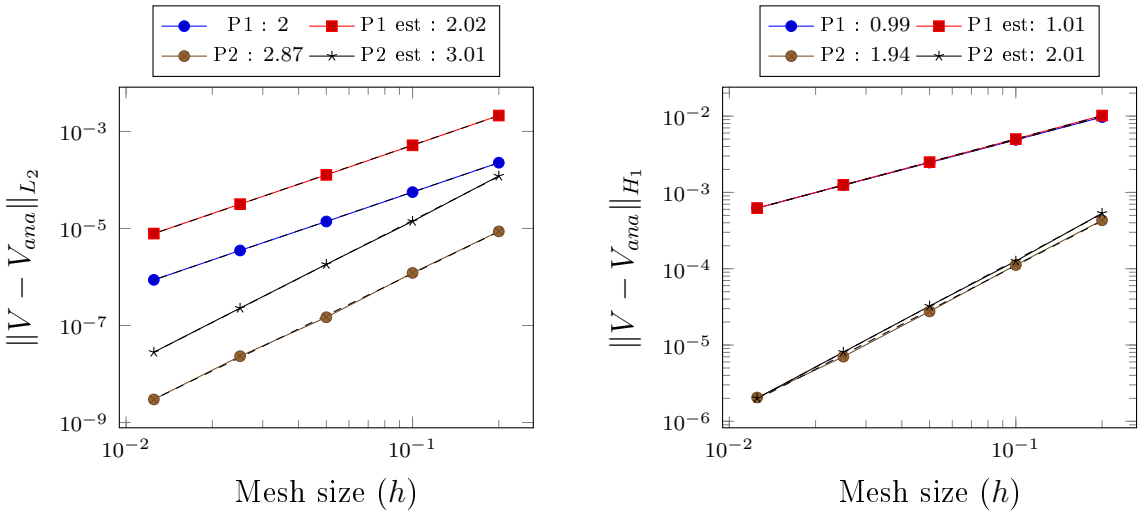

Figure 3.3 – Linear electrical potential - 2D convergence study

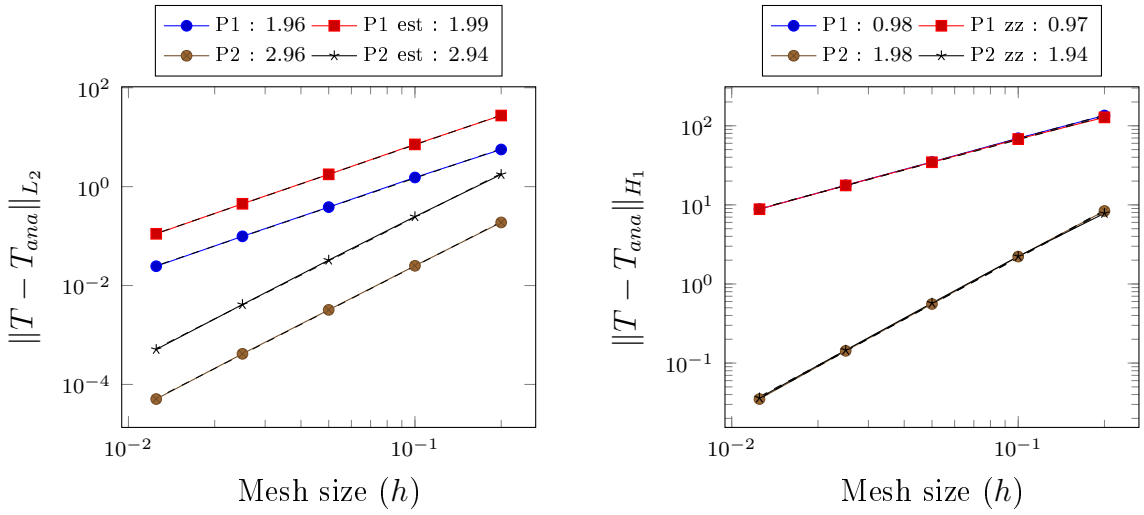

Figure 3.4 – Linear temperature - 2D convergence study

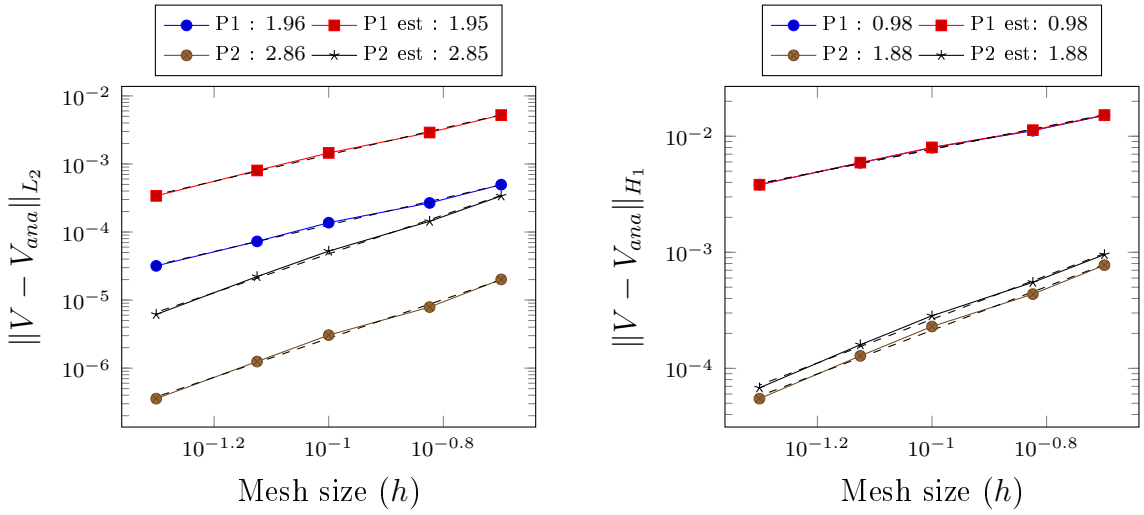

Figure 3.5 – Linear electrical potential - 3D convergence study

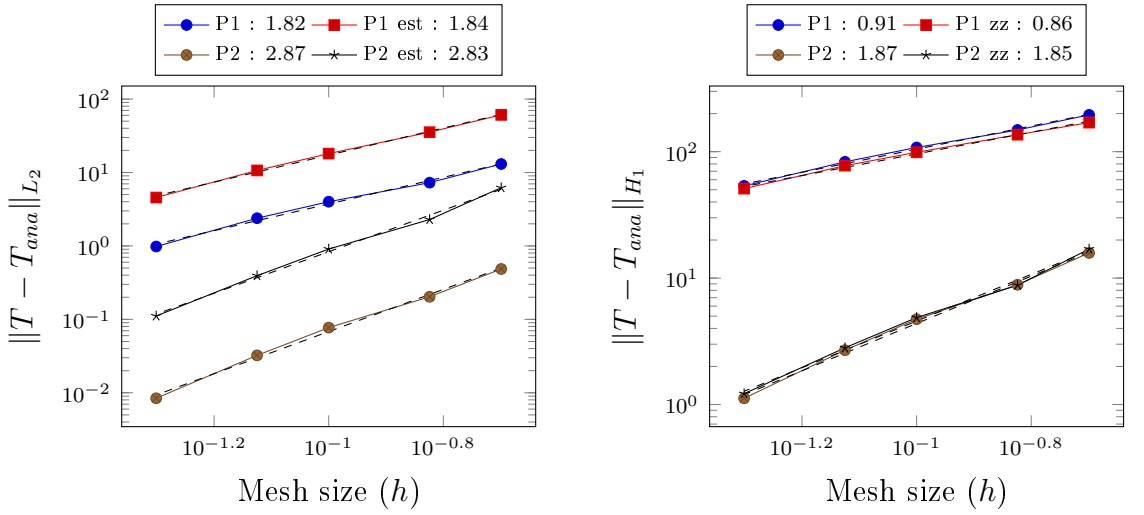

Figure 3.6 – Linear temperature - 3D convergence study

Non-linear model - A posteriori error estimation

As previously mentionned, exhibiting an analytical solution (V_{ana}, T_{ana}) is not feasible for the non-linear case. In this context, the verification is performed from errors estimators whose relevance has been emphasized in the previous convergence studies.

Similarly with the previous study, the figures 3.7 and 3.8 focus on the 2D non-linear model, while the figures 3.9 and 3.10 illustrate the convergence of the 3D one. These convergence studies conclude the verification of the electro-thermal model for its two versions namely linear and non-linear. They confirm as well its validity at high polynomial orders.

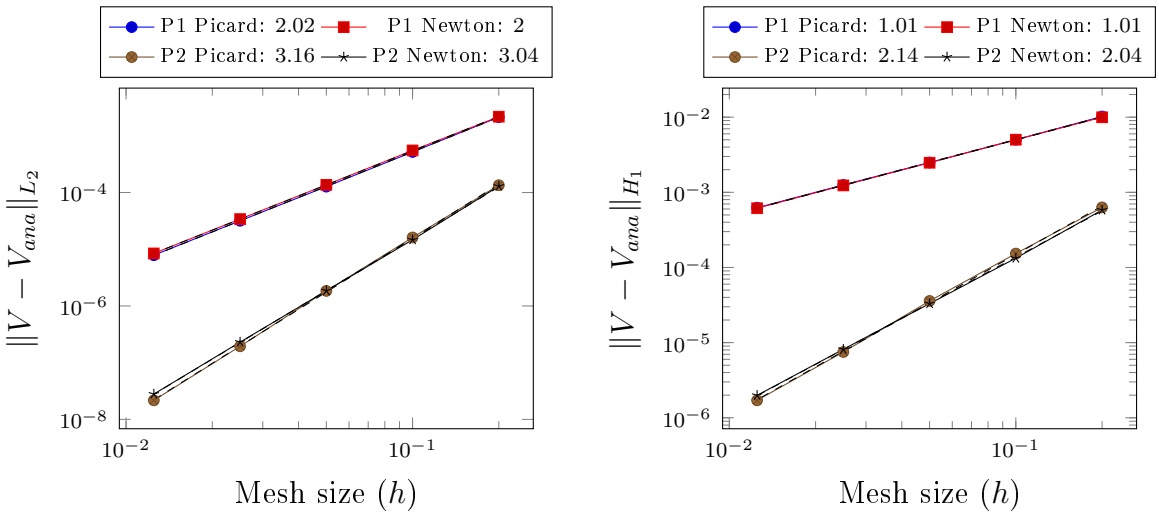

Figure 3.7 – Non-linear electrical potential - 2D convergence study

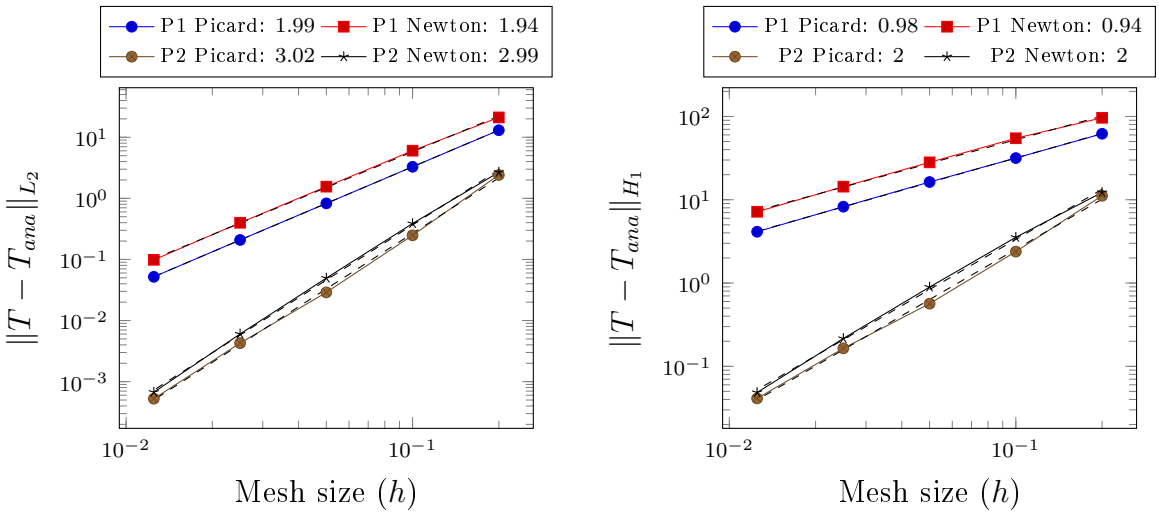

Figure 3.8 – Non-linear temperature - 2D convergence study

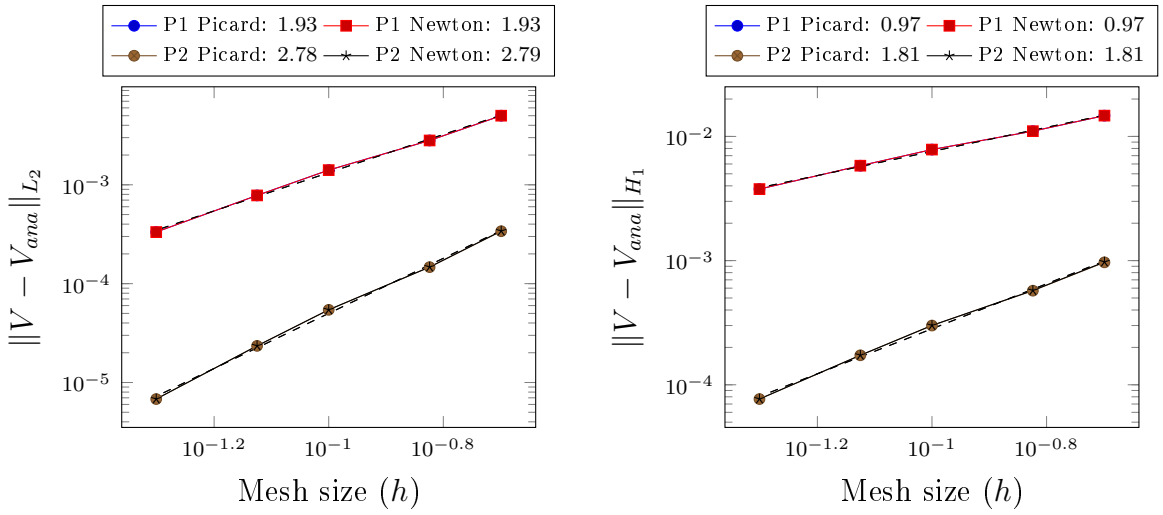

Figure 3.9 – Non-linear electrical potential - 3D convergence study

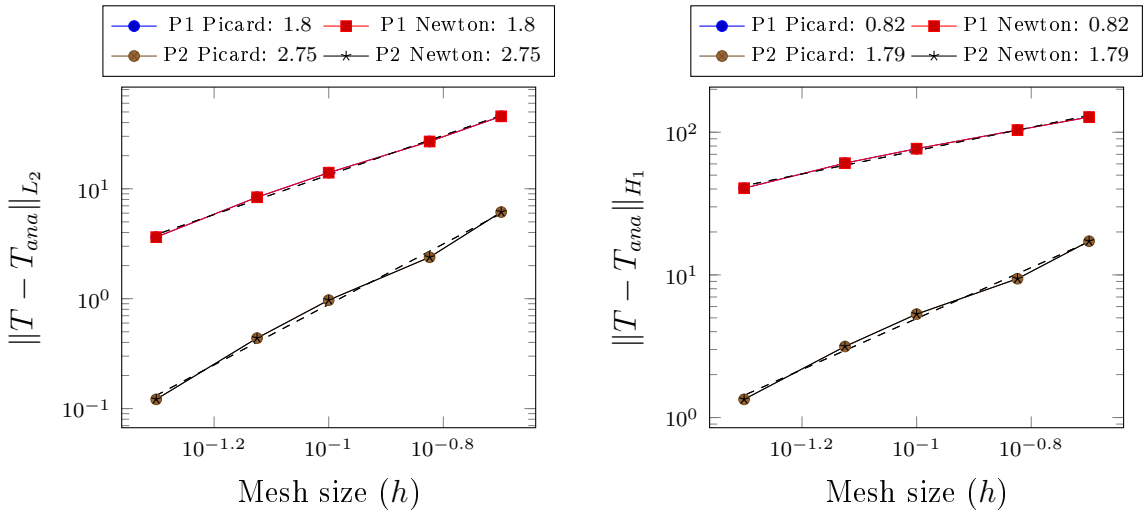

Figure 3.10 – Non-linear temperature - 3D convergence study

3.2 Magnetostatic model

3.2.1 Equations

The magnetic field is defined as a quantifier of the magnetic effect coming from the current flow into magnetic materials. Relating magnetic and electric fields, Maxwell's equations are at the core of the magnetic field computation.

Established in 1823, Ampère's law relates the magnetic field to its electrical current source, considering the integral of magnetic field around a closed curve C as proportional to the intensity of this current source. Expressed from the current density $\mathbf{j}$, the current intensity defines the current flow through the surface S surrounded by the curve C.

$$\oint_C \mathbf{H} = I = \int_S \mathbf{j} \cdot \mathbf{n} \tag{3.35}$$

where $\mathbf{n}$ denotes the outward normal to the surface S.

Introduced in Section 3.1, Omh's law (3.2) expresses the current density $\mathbf{j}$ as the product of the temperature dependent electrical conductivity σ by the electric field. Deriving from an electrical potential, the electric field coming into (3.2) reads from the solution of the previously introduced electro-thermal model (3.4). Thus, the magnetostatic model is naturally coupled with the previous electro-thermal one by the current density $\mathbf{j}$ defined as

$$\mathbf{j} = -\sigma(T)\nabla V \tag{3.36}$$

From (3.36), Ampère's law (3.35) reads in differential form as

$$\nabla \times \mathbf{H} = -\sigma(T)\nabla V \tag{3.37}$$

The contribution of the displacement current defined as the time derivative of the electrical charge has to be added to the original Ampère's law (3.35) to ensure the charge conservation principle. But as we focus on the steady model, we are not concerned by this term.

Most commonly used in the study of magnetism, the magnetic induction $\mathbf{B}$ is related to the magnetic field $\mathbf{H}$ (3.37) by the magnetic permeability μ through the constitutive law

$$\mathbf{B} = \mu\mathbf{H} \tag{3.38}$$

The magnetic permeability of the so-called ferromagnetic materials composed for example of iron or steel depends on the magnetic field $\mathbf{H}$ leading to a non-linear model. Nevertheless, the resistive magnets we focus on are composed of diamagnetic materials based on copper alloys whose magnetization is negligible. In our case, the magnetic permeability μ relating $\mathbf{B}$ to $\mathbf{H}$ is the vacuum permeability $\mu_0 = 4\pi \times 10^{-7} T.m.A^{-1}$. Considering the linear relation (3.38) in this context, the magnetic induction $\mathbf{B}$ is often abusively refered as the magnetic field.

As part of Maxwell's equations, the Gauss law describes the magnetic induction $\mathbf{B}$ as divergence free. Thus, the magnetic induction derives from a magnetic potential A :

$$\nabla \cdot \mathbf{B} = 0 \quad \Rightarrow \quad \exists A \mid \mathbf{B} = \nabla \times \mathbf{A} \tag{3.39}$$

Combining Ampère's law (3.35) with the constitutive law (3.38) relating $\mathbf{H}$ to $\mathbf{B}$, the considered model whose solution is the magnetic potential $\mathbf{A}$ then reads

$$\nabla \times \left(\frac{1}{\mu} \nabla \times \mathbf{A} \right) = \mathbf{j} \tag{3.40}$$

We shall also note that the current density $\mathbf{j}$ is divergence-free from the electrical potential equation (3.4). The De-Rham diagram (1.11) defined in Chapter 1 thus places $\mathbf{j}$ in H_{div} space, $\mathbf{A}$ in H_{curl} space from (3.37) and $\mathbf{B}$ in H_{div} as the curl of an element of H_{curl}. The finite element method used to compute $\mathbf{A}$ solving (3.40) consequently have

to preserve the properties of H_{curl} function space. Defined to this end, the Nédélec finite elements introduced in Section 1.3 are definitely convenient. Their use especially allows to impose only the continuity of the tangential component. Turning to Ampère's law (3.35), we shall remark that this condition is inherent to the Maxwell's equations. The divergence free condition (3.39) coming from Maxwell's equations imposes the continuity of the normal component of $\mathbf{B}$ accross the boundary of two media, which confirms that $\mathbf{B}$ is an H_{div} element. And the definition of the magnetic potential $\mathbf{A}$ (3.39) then leads to the continuity of the tangential component of $\mathbf{A}$ on interfaces.

The well posedness of the magnetostatic problem (3.40) requires the definition of boundary conditions. Assuming that the current density is located to some finite region in space, the boundary condition consists in considering $\mathbf{B}$ is zero at infinity. Nevertheless, the finite element method supposes the spatial discretization of the domain and then imposes Ω to be of finite dimension. In practice, the domain is composed of the conductor plus a surrounding box whose boundaries model the infinity. In 3D, the boundary condition is expressed in terms of magnetic potential such that

$$\mathbf{A} \times \mathbf{n} = 0 \text{ on } \partial\Omega \tag{3.41}$$

Since the curl of any gradient field is null, the problem (3.40) doesn't admit a unique solution. Considering $\mathbf{A}$ as a solution of (3.40), any $\bar{\mathbf{A}} = \mathbf{A} + \nabla\phi$ defined as the sum of $\mathbf{A}$ with the gradient of a function ϕ satisfies (3.40) as well. Although the gradient field $\nabla\phi$ doesn't affect the magnetic flux $\mathbf{B}$ in a physical point of view, the unicity of the solution $\mathbf{A}$ is essential in terms of numerical solving.

As a first option to guarantee the unicity of the solution, we consider (3.40) as a specific case of the potential-based full Maxwell problem expressed in frequency domain. The regularization method [Bebendorf and Ostrowski, 2009] amounts to consider the additional terms coming from Fourier transforms of time derivatives as a regularization term which tends to zero. A second option consists to impose an additional condition on the divergence $\nabla \cdot \mathbf{A}$. The Coulomb gauge corresponds to a divergence-free condition leading to a saddle-point problem. Further details can be found in [Dumitru, 2013].

Other methods can be employed to regularize the curl-curl matrix of (3.40), such as the tree-cotree gauging [Biro et al., 1996] which is not discussed here.

Regularized formulation Based on the Maxwell's equation in frequency domain, the regularized formulation rests on Fourier transform $\mathcal{F}$, defined for any time dependent function $f(t)$ as

$$\mathcal{F}[f(t)](\omega) : f(t) \longrightarrow \mathcal{F}[f(t)](\omega) = \int_{-\infty}^{+\infty} f(t) e^{-iwt} dt \tag{3.42}$$

As mentionned, the ungauged magnetostatic problem (3.40) reading as the time harmonic Maxwell's problem with frequency zero doesn't admit a unique solution. Considering that electromagnetic fields obtained at low frequencies are a good approximation of magnetostatic fields, the regularized formulation enjoys from the regularity of full Maxwell

problem with $\omega \neq 0$. Coming back to the Maxwell-Faraday equation (3.1), the electric field expresses from the magnetic potential $\mathbf{A}$ such that

$$\mathbf{E} = -\frac{\partial \mathbf{A}}{\partial t} \tag{3.43}$$

Let's consider the contribution of the displacement current in the previous Ampère's law (3.35) ensuring the charge conservation

$$\nabla \times \left(\frac{1}{\mu}\nabla \times \mathbf{A}\right) = \mathbf{j} + \sigma\mathbf{E} + \epsilon\frac{\partial \mathbf{E}}{\partial t} \tag{3.44}$$

The relation (3.43) leads to the unsteady problem

$$\nabla \times \left(\frac{1}{\mu}\nabla \times \mathbf{A}\right) + \epsilon\frac{\partial^2 \mathbf{A}}{\partial t^2} + \sigma\frac{\partial \mathbf{A}}{\partial t} = \mathbf{j} \tag{3.45}$$

on which we apply the Fourier transform (3.42), resulting in the time harmonic equation

$$\nabla \times \left(\frac{1}{\mu}\nabla \times \mathbf{A}\right) + (\sigma i\omega - \epsilon\omega^2)\mathbf{A} = \mathbf{j} \tag{3.46}$$

The considered regularization method aims to mimick the last term $(\sigma i\omega - \epsilon\omega^2)\mathbf{A}$ of (3.46) with low frequencies. To this end, the regularization term consists in the addition of a weighted term tending to zero to get closer to the initial formulation such that

$$\nabla \times \left(\frac{1}{\mu}\nabla \times \mathbf{A}_\epsilon\right) + \epsilon\mathbf{A}_\epsilon = \mathbf{j} \tag{3.47}$$

with $\mathbf{A}_\epsilon$ the solution of the corresponding regularized problem converging to the solution $\mathbf{A}$ of the initial problem (3.40) when $\epsilon \longrightarrow 0$.

Saddle-point formulation As previously mentionned, the so-called Coulomb gauge guarantee the unicity of the solution of (3.40) imposing a divergence free condition to $\mathbf{A}$. This extra condition is handled by a Lagrange multiplier p as an additional scalar unknown of (3.40) on which homogeneous Dirichlet boundary conditions are imposed leading to

$$\begin{aligned} \nabla \times \left(\frac{1}{\mu}\nabla \times \mathbf{A}\right) + \nabla p &= \mathbf{j} \text{ on } \Omega \\ \nabla \cdot \mathbf{A} &= 0 \end{aligned} \tag{3.48}$$

with $\mathbf{A} \times \mathbf{n} = 0$ and $p = 0$ on $\partial\Omega$.

3.2.2 Variational formulation

Regularized formulation Let us remind that the regularized formulation (3.47) results in a vectorial solution $\mathbf{A}_\epsilon$ which tends to $\mathbf{A}$ when ϵ decreases. Denoting $\boldsymbol{\phi}_{\mathbf{A}_\epsilon} \in X \subset$

$H_{\text{curl}}(\Omega)$ the associated test functions, the variational formulation of (3.47) consists in finding $\mathbf{A}_\epsilon \in X \subset H_{\text{curl}}(\Omega)$ such that

$$\begin{aligned}\int_\Omega \frac{1}{\mu}(\nabla \times \mathbf{A}_\epsilon)\cdot(\nabla \times \boldsymbol{\phi}_{\mathbf{A}_\epsilon}) + \int_{\partial\Omega} \frac{1}{\mu}(\nabla \times \mathbf{A}_\epsilon)\cdot(\boldsymbol{\phi}_{\mathbf{A}_\epsilon} \times \mathbf{n}) \\ + \int_\Omega \epsilon \mathbf{A}_\epsilon \cdot \boldsymbol{\phi}_{\mathbf{A}_\epsilon} = \int_\Omega \mathbf{j}\cdot\boldsymbol{\phi}_{\mathbf{A}_\epsilon} \qquad \forall \boldsymbol{\phi}_{\mathbf{A}_\epsilon} \in X\end{aligned} \tag{3.49}$$

As for the thermoelectric model, Dirichlet boundary conditions can be imposed on their strong or weak form. In their strong form, they are inherent to the space $X = H_{0,\text{curl}}(\Omega) = \{\mathbf{v} \in H_{\text{curl}}(\Omega) \mid \mathbf{v}\times\mathbf{n} = 0 \text{ on } \partial\Omega\}$. This definition of X allows to vanish the boundary term of (3.49), leading to a problem which consists in finding $\mathbf{A}_\epsilon \in H_{0,\text{curl}}(\Omega)$ such that

$$\int_\Omega \frac{1}{\mu}(\nabla \times \mathbf{A}_\epsilon)\cdot(\nabla \times \boldsymbol{\phi}_{\mathbf{A}_\epsilon}) + \int_\Omega \epsilon \mathbf{A}_\epsilon \cdot \boldsymbol{\phi}_{\mathbf{A}_\epsilon} = \int_\Omega \mathbf{j}\cdot\boldsymbol{\phi}_{\mathbf{A}_\epsilon} \ \forall \boldsymbol{\phi}_{\mathbf{A}_\epsilon} \in H_{0,\text{curl}}(\Omega) \tag{3.50}$$

In their weak form, the Dirichlet boundary conditions are imposed through Nitsche's method adding symetrization and penalisation terms without any additional condition on $X = H_{\text{curl}}(\Omega)$. Considering h the mesh size and γ the penalization term, the weak formulation thus consists in finding $\mathbf{A}_\epsilon \in H_{0,\text{curl}}(\Omega)$ such that

(3.51)

$$\begin{aligned}\int_\Omega \frac{1}{\mu}(\nabla \times \mathbf{A}_\epsilon)\cdot(\nabla \times \boldsymbol{\phi}_{\mathbf{A}_\epsilon}) + \int_{\partial\Omega} \frac{1}{\mu}(\nabla \times \mathbf{A}_\epsilon)\cdot(\boldsymbol{\phi}_{\mathbf{A}_\epsilon} \times \mathbf{n}) + \int_\Omega \epsilon \mathbf{A}_\epsilon \cdot \boldsymbol{\phi}_{\mathbf{A}_\epsilon} \\ + \underbrace{\int_{\partial\Omega} \frac{1}{\mu}(\nabla \times \boldsymbol{\phi}_{\mathbf{A}_\epsilon})\cdot(\mathbf{A}_\epsilon \times \mathbf{n})}_{\text{symetrization}} + \underbrace{\int_{\partial\Omega} \frac{\gamma}{h\mu}(\boldsymbol{\phi}_{\mathbf{A}_\epsilon} \times \mathbf{n})\cdot(\mathbf{A}_\epsilon \times \mathbf{n})}_{\text{penalisation}} \\ = \int_\Omega \mathbf{j}\cdot\boldsymbol{\phi}_{\mathbf{A}_\epsilon} \quad \forall \boldsymbol{\phi}_{\mathbf{A}_\epsilon} \in H_{\text{curl}}(\Omega)\end{aligned}$$

Saddle-point formulation Considering the Lagrange multiplier introduced to deal with the divergence free condition on $\mathbf{A}$, the saddle-point problem (3.48) consists in finding the couple $(\mathbf{A}, p) \in X \subset (H_{\text{curl}}(\Omega), H_1(\Omega))$ such that

$$\int_\Omega \frac{1}{\mu}(\nabla \times \mathbf{A})\cdot(\nabla \times \boldsymbol{\phi}_A) + \int_{\partial\Omega} \frac{1}{\mu}(\nabla \times \mathbf{A})\cdot(\boldsymbol{\phi}_A \times \mathbf{n}) + \int_\Omega \nabla p \cdot \boldsymbol{\phi}_A = \int_\Omega \mathbf{j}\cdot\boldsymbol{\phi}_A \tag{3.52}$$

$$\int_{\partial\Omega} (\mathbf{A}\cdot\mathbf{n})\phi_p - \int_\Omega \mathbf{A}\cdot\nabla\phi_p = 0 \quad \forall(\boldsymbol{\phi}_A, \phi_p) \in X \tag{3.53}$$

where $\boldsymbol{\phi}_A$ (resp. $\boldsymbol{\phi}_p$) are the tests functions associated with A (resp. p).

If the Dirichlet boundary conditions on $(\mathbf{A}, p)$ are imposed in strong form, they are inherent to the function space X which defines as $X = (V, Q) = (H_{0,\text{curl}}(\Omega), H_0^1(\Omega))$. The boundary term of (3.52) is eliminated since $\boldsymbol{\phi}_A \in H_{0,\text{curl}}(\Omega)$, while the one of (3.53)

vanishes from the definition of $\phi_p \in H^1_0(\Omega)$. The variational formulation then reads : Find $(\mathbf{A}, p) \in (H_{0,\text{curl}}(\Omega), H^1_0(\Omega))$ such that

$$\int_\Omega \frac{1}{\mu}(\nabla \times \mathbf{A}) \cdot (\nabla \times \boldsymbol{\phi}_A) + \int_\Omega \nabla p \cdot \boldsymbol{\phi}_A = \int_\Omega \mathbf{j} \cdot \boldsymbol{\phi}_A \quad \forall \boldsymbol{\phi}_A \in H_{0,\text{curl}}(\Omega) \tag{3.54}$$

$$\int_\Omega \mathbf{A} \cdot \nabla \phi_p = 0 \quad \forall \phi_p \in H^1_0(\Omega) \tag{3.55}$$

As for the weak Dirichlet conditions, Nitsche's method is applied on both two variables $\mathbf{A}$ and p with $X = (V, Q) = (H_{\text{curl}}(\Omega), H_1(\Omega))$. The variational formulation then consists in finding $(\mathbf{A}, p) \in (H_{\text{curl}}(\Omega), H_1(\Omega))$ such that

(3.56)

$$\begin{aligned}
\int_\Omega \frac{1}{\mu}(\nabla \times \mathbf{A}) \cdot (\nabla \times \boldsymbol{\phi}_A) \quad &+ \int_{\partial\Omega} \frac{1}{\mu}(\nabla \times \mathbf{A}) \cdot (\boldsymbol{\phi}_A \times \mathbf{n}) + \int_\Omega \nabla p \cdot \boldsymbol{\phi}_A \\
&+ \underbrace{\int_{\partial\Omega} \frac{1}{\mu}(\nabla \times \boldsymbol{\phi}_A) \cdot (\mathbf{A} \times \mathbf{n})}_{\text{symetrization}} + \underbrace{\int_{\partial\Omega} \frac{\gamma}{h\mu}(\mathbf{A} \times \mathbf{n}) \cdot (\boldsymbol{\phi}_A \times \mathbf{n})}_{\text{penalisation}} \\
&= \int_\Omega \mathbf{j} \cdot \boldsymbol{\phi}_A \quad \forall \boldsymbol{\phi}_A \in H_{0,\text{curl}}(\Omega) \\
\int_{\partial\Omega} (\mathbf{A} \cdot \mathbf{n})\phi_p - \int_\Omega \mathbf{A} \cdot \nabla \phi_p &+ \int_{\partial\Omega} \frac{\gamma}{h} p\phi_p = 0 \quad \forall \phi_p \in H^1_0(\Omega)
\end{aligned}$$

3.2.3 Preconditionning

The discretization of problems (3.47) and (3.48) are solved from their matricial form $\mathcal{K}\mathbf{x} = \mathbf{b}$. Thus, the conditionning of the matrix $\mathcal{K}$ plays an important role in the convergence of the iterative solvers used to compute the magnetic potential $\mathbf{A}$. Especially, the definition of $\mathbf{A} \in H_{\text{curl}}$ from Nédélec finite elements whose degrees of freedom are located on the edges of the mesh can highly deteriorate this conditioning.

The resolution of such problems could then require adapted preconditioning techniques to ease the convergence of the iterative solvers. Moreover, we have to pay particular attention to the scalability of these methods to be used in a high performance computing context. This section gives an overview of appropriate preconditioning techniques, proposed in [Greif and Schötzau, 2007] and [Hiptmair and Xu, 2007]. These have been implemented within `Feel++`, to be applied on our magnetostatic model.

Regularized formulation The discretized system associated with (3.49) whose solution is denoted as $\mathbf{A}_{\epsilon,h}$ consists in finding $\mathbf{A}_{\epsilon,h} \in X_h \subset X$ – with X depending on the Dirichlet boundary condition treatment – such that

$$a_\epsilon(\mathbf{A}_{\epsilon,h}, \boldsymbol{\phi}_{A_{\epsilon,h}}) = f_\epsilon(\boldsymbol{\phi}_{A_{\epsilon,h}}) \; \forall \boldsymbol{\phi}_{A_{\epsilon,h}} \in X_h \tag{3.57}$$

where a_ϵ (resp. f_ϵ) are the bilinear (resp. linear) forms defines from (3.50) as

$$a_\epsilon(\mathbf{A}_{\epsilon,h}, \boldsymbol{\phi}_{A_\epsilon,h}) = \int_\Omega \frac{1}{\mu}(\nabla \times \mathbf{A}_{\epsilon,h}) \cdot (\nabla \times \boldsymbol{\phi}_{A_\epsilon,h}) + \int_\Omega \epsilon \mathbf{A}_{\epsilon,h} \cdot \boldsymbol{\phi}_{A_\epsilon,h} \tag{3.58}$$

$$f_\epsilon(\boldsymbol{\phi}_{A_\epsilon,h}) = \int_\Omega \mathbf{j} \cdot \boldsymbol{\phi}_{A_\epsilon,h} \tag{3.59}$$

The expression of a_ϵ and f_ϵ with weak Dirichlet conditions can be easily obtained adding corresponding terms from (3.51).

Let's now introduce $\{\boldsymbol{\psi}_i\}_{i=1}^{\mathcal{N}_{curl}}$ the shape functions of the discrete function space $X_h \subset H_{\text{curl}}$ of size $\mathcal{N}_{curl}$. The finite element $\mathbf{A}_{\epsilon,h} \in Xh$ of (3.57) consists in a linear combination of these shape functions whose coefficients as denoted as a_i^ϵ, $1 \leqslant i \leqslant \mathcal{N}_{curl}$.

$$\mathbf{A}_{\epsilon,h} = \sum_{i=1}^{\mathcal{N}_{curl}} a_i^\epsilon \boldsymbol{\psi}_i \tag{3.60}$$

Turning to (3.57), the solution $\mathbf{A}_{\epsilon,h} = (a_1^\epsilon, \ldots, a_{\mathcal{N}_{curl}}^\epsilon)$ is the solution of the matricial system $\mathcal{A}_\epsilon \mathbf{A}_{\epsilon,h} = \mathbf{b}_\epsilon$ with $\mathcal{A}_{\epsilon,i,j} = a_\epsilon(\boldsymbol{\psi}_j, \boldsymbol{\psi}_i)$ and $\mathbf{b}_{\epsilon,i} = f_\epsilon(\boldsymbol{\psi}_i)$ for $1 \leqslant i, j \leqslant \mathcal{N}_{curl}$. The large number of non zero entries in $\mathcal{A}_\epsilon$, coming from the definition of the unknown using H_{curl}-conforming finite elements, could lead to a poor conditionning for $\mathcal{A}_\epsilon$.

The mass matrix $\mathcal{M}$ can be added to $\mathcal{A}_\epsilon$, serving as a preconditionner to (3.57) [Greif and Schötzau, 2007]

$$\mathcal{P}_\mathcal{M} = \mathcal{A}_\epsilon + \mathcal{M} \text{ with } \mathcal{M}_{i,j} = \int_\Omega \boldsymbol{\psi}_j \cdot \boldsymbol{\psi}_i, \quad 1 \leqslant i, j \leqslant \mathcal{N}_{curl} \tag{3.61}$$

Saddle-point formulation The saddle-point formulation introduced as (3.52) and (3.53) results in a discretized system as well. Let's denote $(\mathbf{A}_h, p_h)$ the solution of the discrete formulation consisting in finding $(\mathbf{A}_h, p_h) \in X_h = (V_h, Q_h) \subset X$ such that

$$a((\mathbf{A}_h, p_h), (\boldsymbol{\phi}_{A,h}, \phi_{p,h})) = f((\boldsymbol{\phi}_{A,h}, \phi_{p,h})) \; \forall (\boldsymbol{\phi}_{A,h}, \phi_{p,h}) \in X_h \tag{3.62}$$

where a (resp. f) are the bilinear (resp. linear) forms are defined from the sum of (3.54) and (3.55) as

$$a((\mathbf{A}_h, p_h), (\boldsymbol{\phi}_{A,h}, \phi_{p,h})) = \int_\Omega \frac{1}{\mu}(\nabla \times \mathbf{A}_h) \cdot (\nabla \times \boldsymbol{\phi}_{A,h}) + \int_\Omega \nabla p_h \cdot \boldsymbol{\phi}_{A,h} + \int_\Omega \mathbf{A}_h \cdot \nabla \phi_{p,h}$$

$$f((\boldsymbol{\phi}_{A,h}, \phi_{p,h})) = \int_\Omega \mathbf{j} \cdot \boldsymbol{\phi}_{A,h}$$

Considering $\{\boldsymbol{\psi}_i\}_{i=1}^{\mathcal{N}_{curl}}$ the shape functions of V_h, we introduce $\{\varphi_i\}_{i=1}^{\mathcal{N}}$ the basis functions of Q_h. The finite element approximations $\mathbf{A}_h$ and p_h are described from their

coefficients a_i $1 \leqslant i \leqslant \mathcal{N}_{curl}$ and p_i $1 \leqslant i \leqslant \mathcal{N}$ in these basis as

$$\mathbf{A}_h = \sum_{i=1}^{\mathcal{N}_{curl}} a_i \boldsymbol{\psi}_i \quad \text{and} \quad p_h = \sum_{i=1}^{\mathcal{N}} p_i \varphi_i \tag{3.63}$$

Coming back to (3.62), the couple of solutions $(\mathbf{A}_h, p_h) = (a_1, \ldots, a_{\mathcal{N}_{curl}}, p_1, \ldots, p_{\mathcal{N}})$ is obtained from the resolution of the block matricial system

$$\begin{pmatrix} \mathcal{A} & \mathcal{B}^T \\ \mathcal{B} & 0 \end{pmatrix} \begin{pmatrix} \mathbf{A}_h \\ p_h \end{pmatrix} = \begin{pmatrix} \mathbf{f} \\ 0 \end{pmatrix} \tag{3.64}$$

where $\mathcal{A}_{i,j} = \int_\Omega \mu^{-1} (\nabla \times \boldsymbol{\psi}_j) \cdot (\nabla \times \boldsymbol{\psi}_i)$, $\mathcal{B}_{i,j} = \int_\Omega \boldsymbol{\psi}_j \cdot \nabla \varphi_i$ and $f_i = \int_\Omega \mathbf{j} \cdot \boldsymbol{\psi}_i$.
The expression of a and f, as well as the corresponding components of (3.64) corresponding to weak Dirichlet boundary conditions can be deduced from (3.56).

For same reasons as previously, the poor conditioning of the block matrix of (3.64) can degrade the convergence of the iterative solvers used. The block diagonal preconitioner $\mathcal{P}_{\mathcal{M},\mathcal{L}}$ is proposed in [Hiptmair and Xu, 2007] to solve (3.64). Further details on auxiliary space based preconditioners employed in this context can be found in [Kolev and Vassilevski, 2009].

Defined from *(i)* the previously introduced $\mathcal{P}_{\mathcal{M}}$ (3.61) as the first block and *(ii)* from the scalar Laplacian matrix $\mathcal{L}$ as the second one, $\mathcal{P}_{\mathcal{M},\mathcal{L}}$ reads

$$\mathcal{P}_{\mathcal{M},\mathcal{L}} = \begin{pmatrix} \mathcal{P}_{\mathcal{M}} & 0 \\ 0 & \mathcal{L} \end{pmatrix} = \begin{pmatrix} \mathcal{A} + \mathcal{M} & 0 \\ 0 & \mathcal{L} \end{pmatrix} \tag{3.65}$$

with $\mathcal{M}$ the mass matrix on V_h and $\mathcal{L}$ defined as

$$\mathcal{M}_{i,j} = \int_\Omega \boldsymbol{\psi}_j \cdot \boldsymbol{\psi}_i \quad \text{and} \quad \mathcal{L} = \int_\Omega \nabla \phi_j \cdot \nabla \phi_i, \quad 1 \leqslant i, j \leqslant m \tag{3.66}$$

Handling the whole system (3.64), the so-called outer solver is preconditioned by $\mathcal{P}_{\mathcal{M},\mathcal{L}}$ (3.65) leading to the linear system

$$\begin{pmatrix} \mathcal{P}_{\mathcal{M}} & 0 \\ 0 & \mathcal{L} \end{pmatrix} \begin{pmatrix} \mathbf{v}_h \\ q_h \end{pmatrix} = \begin{pmatrix} \mathbf{c}_h \\ 0 \end{pmatrix} \tag{3.67}$$

where $\mathbf{v}_h = \mathcal{A}\mathbf{A}_h + \mathcal{B}^T p_h$, $q_h = \mathcal{B}\mathbf{A}_h$ and $\mathbf{c}_h = \mathcal{P}_{\mathcal{M},\mathcal{L}}\mathbf{f}$ from (3.64).

While the solving of the scalar elliptic problem $\mathcal{L} q_h = 0$ can be efficiently performed with standard methods, the conditioning of the first block $\mathcal{P}_{\mathcal{M}} \mathbf{v}_h = \mathbf{c}_h$ of (3.67) suffers the consequences of H_{curl}-conforming elements use. As for the previous regularized system, this block requires to be itself preconditioned. To this end, the use of the auxiliary space preconditioner is proposed in [Hiptmair and Xu, 2007] resulting in the so-called inner solver. Denoted as $\mathcal{P}_V$, this second level preconditionner is defined such that

$$\mathcal{P}_V^{-1} = diag(\mathcal{P}_{\mathcal{M}})^{-1} + P(\bar{\mathcal{L}} + \bar{\mathcal{Q}})^{-1} P^T + C(\bar{\mathcal{L}}^{-1}) C^T \tag{3.68}$$

leading to the system $\mathcal{P}_V \mathbf{w}_h = \mathbf{r}_h$ where $\mathbf{w}_h = \mathcal{P}_{\mathcal{M}} \mathbf{v}_h$ and $\mathbf{r}_h = \mathcal{P}_V \mathbf{c}_h$ from (3.67).

The matrix P of (3.68) denotes the nodal interpolation operator Π_h^{curl} from Q_h^3 to V_h, while $\mathcal{Q}$ is the scalar mass matrix on Q_h

$$\mathcal{Q} = \int_\Omega \phi_j \cdot \phi_i, \quad 1 \leqslant i, j \leqslant m \tag{3.69}$$

The block matrices $\bar{\mathcal{Q}}$ and $\bar{\mathcal{L}}$ are defined from $\mathcal{Q}$ (3.69) and $\mathcal{L}$ (3.66) as

$$\bar{\mathcal{L}} = \frac{1}{\mu} diag(\mathcal{L}, \mathcal{L}, \mathcal{L}) \quad \text{and} \quad \bar{\mathcal{Q}} = diag(\mathcal{M}, \mathcal{M}, \mathcal{M}) \tag{3.70}$$

The matrix C is composed by the coefficient vector of $\nabla \varphi_j$ in $V_h =< \boldsymbol{\psi}_i >_{i=1}^{\mathcal{N}}$ such that

$$\nabla \varphi_j = \sum_{i=1}^{n} C_{i,j} \boldsymbol{\psi}_i, \quad 1 \leqslant j \leqslant m \tag{3.71}$$

Thus, the solution $\mathbf{w}_h = \mathcal{P}_{\mathcal{M}} \mathbf{v}_h$ of the preconditionned system $\mathcal{P}_V \mathbf{w}_h = \mathbf{r}_h$ reads

$$\mathbf{w}_h = diag(\mathcal{P}_{\mathcal{M}})^{-1} \mathbf{r} + P\mathbf{y} + C\mathbf{z} \;\text{ with } \mathbf{y} = (\bar{\mathcal{L}} + \bar{\mathcal{Q}})^{-1} P^T \mathbf{r} \;\text{ and } \mathbf{z} = \bar{\mathcal{L}}^{-1} C^T \mathbf{r} \tag{3.72}$$

In practice, the solution $\mathbf{w}_h$ (3.72) is obtained from the resolution of two linear problems

$$(\bar{\mathcal{L}} + \bar{\mathcal{Q}})\mathbf{y} = P^T \mathbf{r} \tag{3.73}$$

$$\mathcal{L}\mathbf{z} = C^T \mathbf{r} \tag{3.74}$$

The iterative solvers used in the inner solve for the problems (3.73) and (3.74) and the ones solving the second block of the outer problem can be independently customized, leading to a large number of available setups.

3.2.4 Convergence study

Let $\mathbf{A}_{ex}$ be the exact solution of the initial problem (3.40) with magnetic permeability μ set to 1. We denote as $e = \mathbf{A}_{ex} - \mathbf{A}$ (resp. $e_\epsilon = \mathbf{A}_{ex} - \mathbf{A}_\epsilon$) the approximation error resulting from the saddle-point (resp. regularized) formulation. Considering h as the mesh size, it exists a constant c defining the expected convergence properties as

$$\| e \|_{L_2} \leqslant ch, \| e_\epsilon \|_{L_2} \leqslant ch \quad \text{and} \quad \| e \|_{H_{\text{curl}}} \leqslant ch, \| e_\epsilon \|_{H_{\text{curl}}} \leqslant ch \tag{3.75}$$

which corresponds to a straight line of slope one for the L_2 and H_{curl} norms within a logarithmic scale. We shall remark that the polynomial order is not considered in (3.75) compared to (3.28). Indeed, we only focus on the lowest polynomial order for $H_{\text{curl}}-$conforming elements to which our implementation is limited (see Section 5.4).

This section illustrates the convergence properties obtained from the magnetostatic formulations of Section 3.2.2, captionned with the value of the slope obtained with logarithmic scale. Many values of the regularization coefficient ϵ have been considered aiming to investigate its influence. As to the saddle-point formulation, many configurations have

been tested from various solving techniques within the preconditionned blocks. An intermediate method corresponds to a simple block solve, preconditionned by the standard LU or GAMG methods. Denoted as Auxiliary space Maxwell Solver (AMS) from [Falgout et al., 2006], the latest introduced two levels preconditionning method is tested as well.

The 2D convergence study is based on the square domain $\Omega = [-1, 1] \times [-1, 1]$ on which the considered exact solution $\mathbf{A}_{ex}$ reads

$$\mathbf{A}_{ex} = \begin{pmatrix} 1 - y^2 \\ 1 - x^2 \end{pmatrix} \tag{3.76}$$

Figure 3.11 plots the L_2 and H_{curl} norms of the magnetic potential $\mathbf{A}_\epsilon$ coming from the regularized formulation (3.50) with various values of ϵ. These experiments are based on the standard LU preconditionner, without specific treatment. As expected, the convergence requirements (3.75) are only obtained for low values of ϵ.

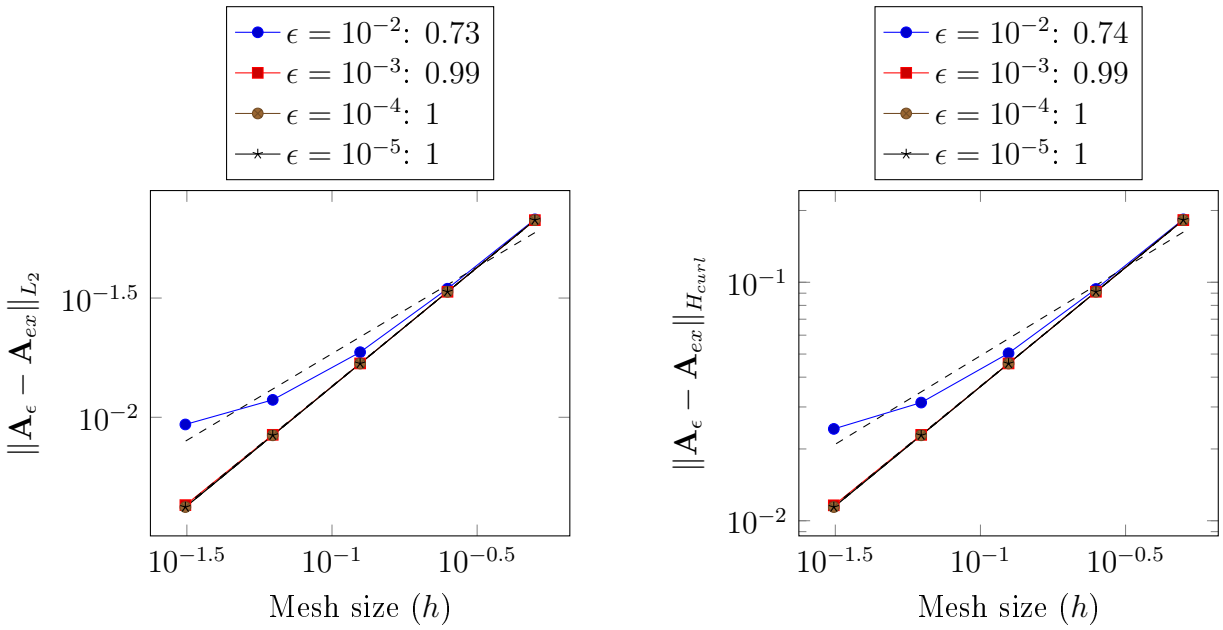

Figure 3.11 – Magnetic potential $\mathbf{A}$ convergence - 2D regularized formulation

Figure 3.12 plots the L_2 and H_{curl} norm of the magnetic potential $\mathbf{A}$ obtained from the saddle-point formulation. Although the conditioning of the considered system is good enough to ensure the convergence with a standard LU preconditionner, this study aims to compare the results obtained with various preconditioning techniques. The requirements (3.75) are satisfied for all configurations, which confirms the pertinence of the preconditioners.

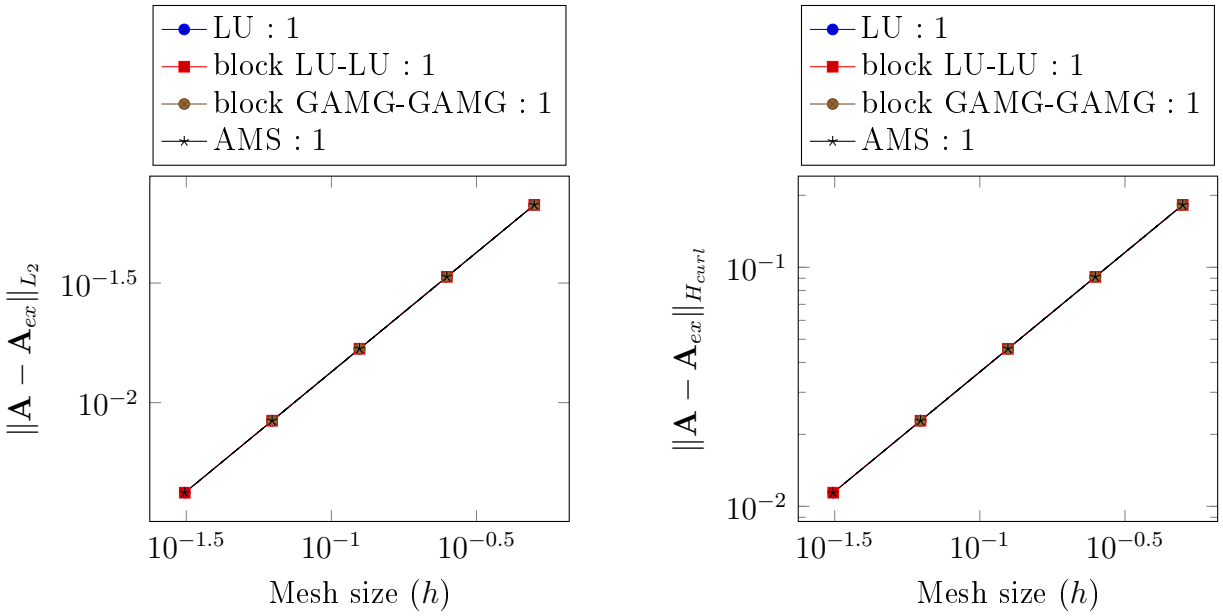

Figure 3.12 – Magnetic potential $\mathbf{A}$ convergence - 2D block saddle point formulation

The figures 3.13a (resp. 3.13b) focus on the convergence properties of $\mathbf{B}$ obtained with the regularized (resp. saddle-point) formulation.

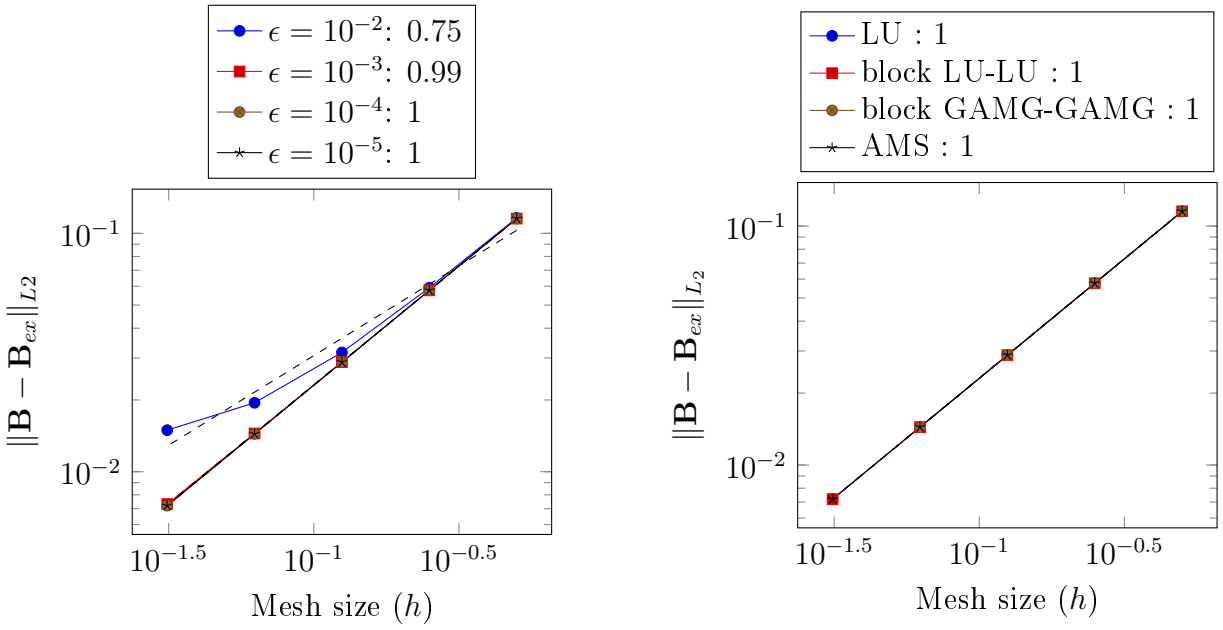

(a) Regularized formulation

(b) Saddle-point formulation

Figure 3.13 – Magnetic flux $\mathbf{B}$ - 2D Convergence study

The resulting behaviour is similar to the one of the magnetic potential, which conclude the verification step of the 2D magnetostatic model.
As an extension of the previously described 2D one, the 3D convergence study is based on the square domain $\Omega = [-1, 1] \times [-1, 1] \times [-1, 1]$ for which the exact solution $\mathbf{A}_{ex}$ is

defined as

$$\mathbf{A}_{ex} = \begin{pmatrix} (1-y^2)(1-z^2) \\ (1-x^2)(1-z^2) \\ (1-x^2)(1-y^2) \end{pmatrix} \tag{3.77}$$

As in 2D case, Figure 3.14 plots the L_2 and H_{curl} norms of the magnetic potential $\mathbf{A}_\epsilon$ coming from the regularized formulation (3.50), with adapted values of ϵ tending to zero. As expected, the convergence requirements (3.75) are as well obtained for the lowest values of ϵ.

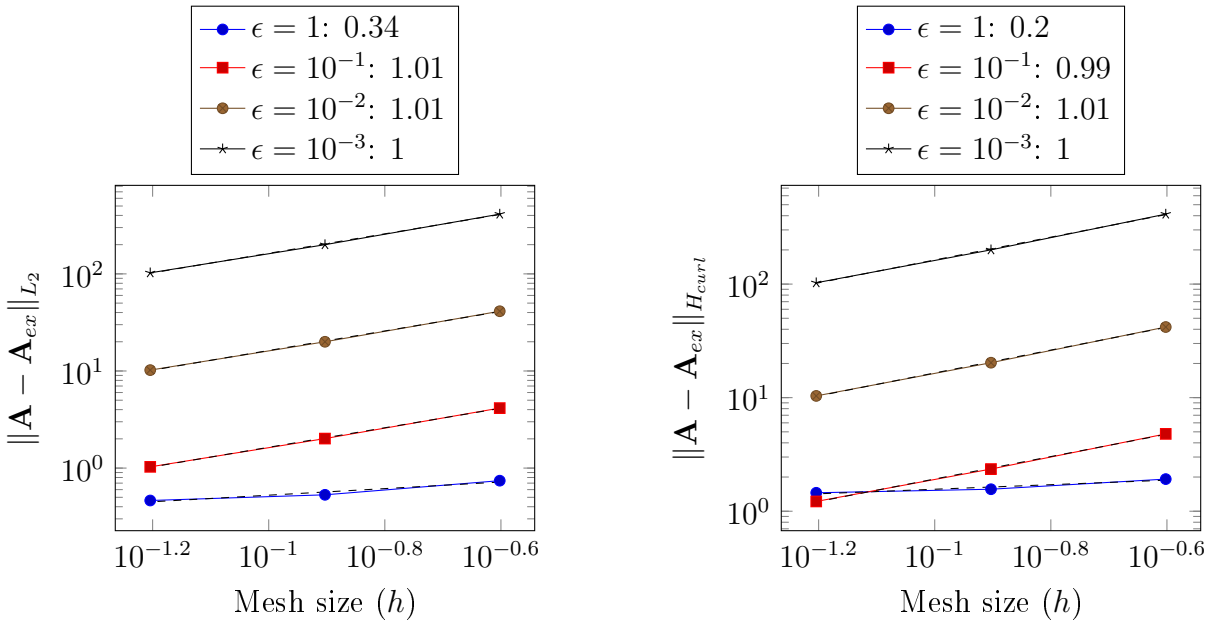

Figure 3.14 – Magnetic potential $\mathbf{A}$ convergence - 3D regularized formulation

The tested configurations for the saddle-point formulations are the same as in 2D case, for which convergence study is illustrated by Figure 3.15. The conditioning of the initial system is reasonable for such a problem, leading to the expected convergence properties with the standard LU preconditionner. The convergence order obtained with other preconditionning techniques is similar to the latter and confirms the relevance of these methods in 3D case.

The convergence order of the magnetic induction $\mathbf{B}$ is finally considered in Figure 3.16a and 3.16b for both regularized and saddle-point formulation. As previously, the behaviour of $\mathbf{B}$ is similar to the one of the magnetic potential $\mathbf{A}$.

Concerning the computational cost, the use of the saddle-point formulation is more expensive. Indeed, the system to solve with this formulation is larger than the one associated with the regularized problem, due to the use of the Lagrange multiplier. Nevetheless, the saddle-point formulation is freed of the regularization coefficient which has to be chosen carefully.

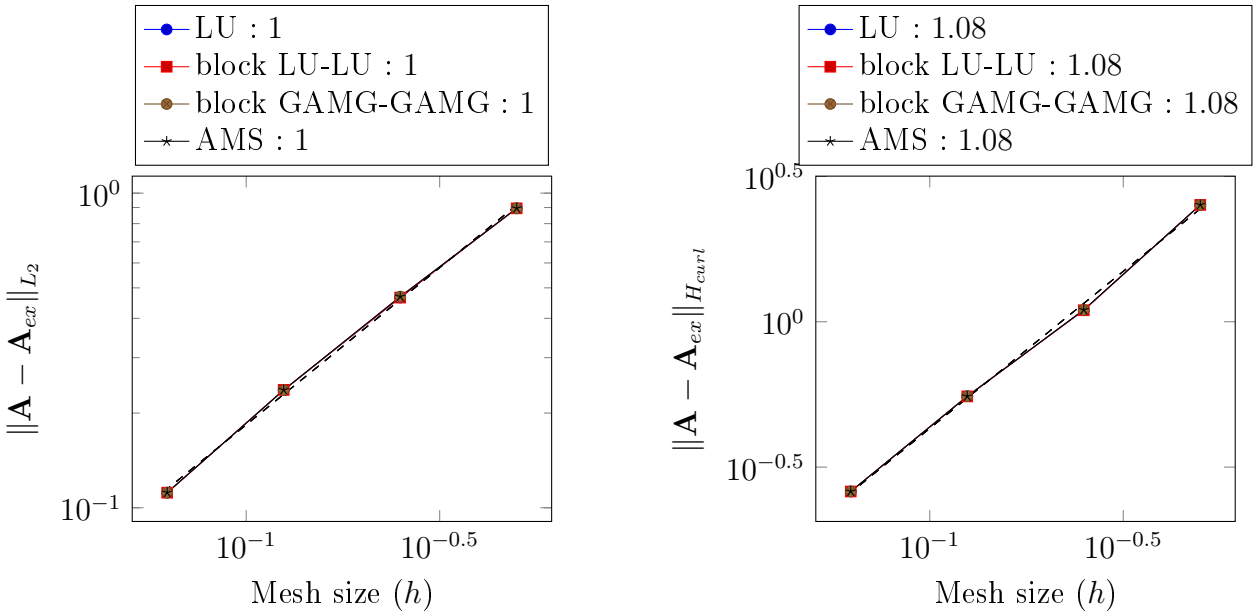

Figure 3.15 – Magnetic potential **A** convergence - 3D block saddle point formulation

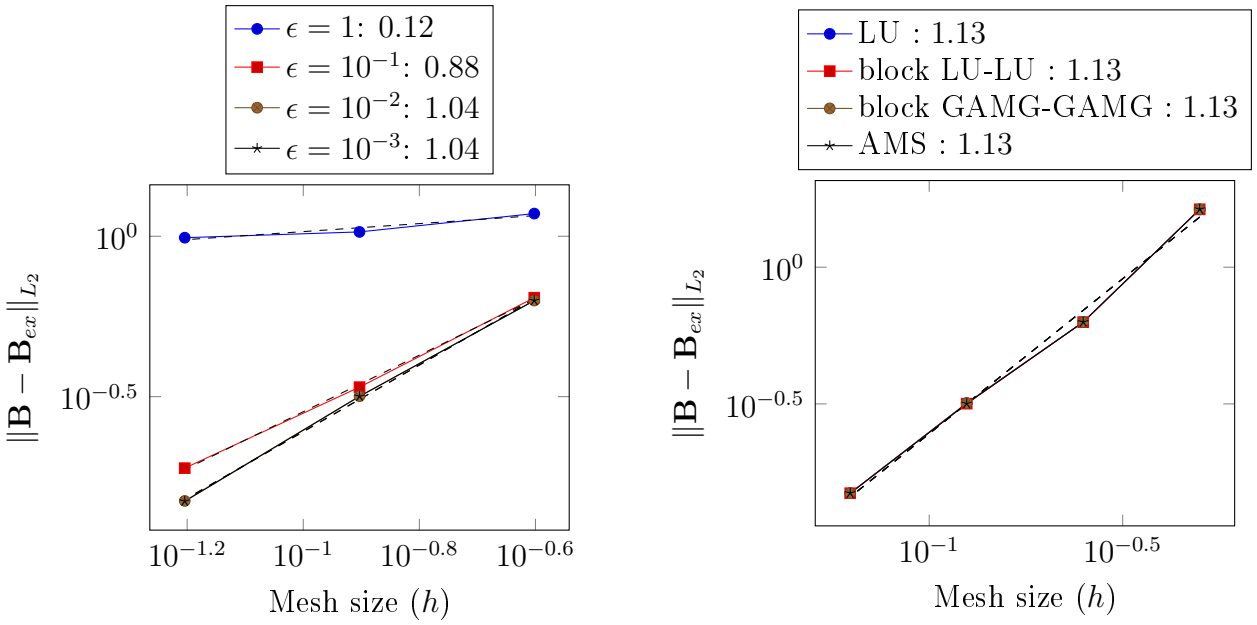

(a) Regularized formulation

(b) Saddle-point formulation

Figure 3.16 – Magnetic flux **B** - 3D Convergence study

3.3 Biot & Savart's law

Besides the magnetostatic model introduced in Section 3.2, the Biot and Savart law is a standard way to compute magnetic potential and magnetic field in a delimited region outside the current conductor.

We denote Ω_{cond} the conductor in which the current is passing, and Ω_{mgn} the domain on which we want to evaluate the generated magnetic field. We consider here that $\Omega_{cond} \cap \Omega_{mgn} = \varnothing$ which is a necessary condition to apply Biot and Savart's formulation.

Turning to the magnetostatic equation (3.40) with a constant magnetic permeability combined with the divergence-free condition enforced by Coulomb Gauge, the magnetic potential $\mathbf{A}$ is the solution of the Poisson's equation

$$\nabla^2 \mathbf{A} = -\mu \mathbf{j} \tag{3.78}$$

The general solution to this equation (3.78) reads from the Green's function $G(\mathbf{r}, \mathbf{r}')$ with $\mathbf{r} \in \Omega_{mgn}$ and $\mathbf{r}' \in \Omega_{cond}$ as

$$A(\mathbf{r}) = -\mu \int_{\Omega_{cond}} G(\mathbf{r}, \mathbf{r}') \mathbf{j}(\mathbf{r}') \tag{3.79}$$

Considering the 3D Green's function for Poisson's equation defined as

$$G(\mathbf{r}, \mathbf{r}') = \frac{-1}{4\pi} \frac{1}{\mid \mathbf{r} - \mathbf{r}' \mid} \tag{3.80}$$

we deduce the expression of the magnetic potential $\mathbf{A}$ from (3.79) as

$$A(\mathbf{r}) = \frac{\mu_0}{4\pi} \int_{\Omega_{cond}} \frac{\mathbf{j}(\mathbf{r}')}{\mid \mathbf{r} - \mathbf{r}' \mid} d\mathbf{r}' \quad \mathbf{r} \in \Omega_{mgn} \tag{3.81}$$

The definition (3.39) of $\mathbf{B}$ as the curl of $\mathbf{A}$ (3.81) then leads to the so-called Biot & Savart's law

$$\mathbf{B}(\mathbf{r}) = \frac{\mu_0}{4\pi} \int_{\Omega_{cond}} \frac{\mathbf{j}(\mathbf{r}') \times (\mathbf{r} - \mathbf{r}')}{\mid \mathbf{r} - \mathbf{r}' \mid^3} d\mathbf{r}' \quad \mathbf{r} \in \Omega_{mgn} \tag{3.82}$$

We shall indeed remark that the distance $\mid \mathbf{r} - \mathbf{r}' \mid$ between $\mathbf{r} \in \Omega_{mgn}$ and $\mathbf{r}' \in \Omega_{cond}$ in the Green's function (3.80) makes the use of the Biot & Savart's law difficult on points inside the conductor, that is with $\Omega_{cond} \cap \Omega_{mgn} \neq \varnothing$.

As a first validation of our Biot and Savart law implementation, we make a comparison with a 2D model introduced in [A. Hervé, 1997],[Conway, 2001] based on axisymmetrical hypothesis. To this end, we consider the conductor Ω_{cond} as a torus of rectangular cross section on which the analytical current density $\mathbf{j}$ is analytically imposed. The region Ω_{mgn} on which the magnetic induction is computed consists in a z-oriented cylinder. Considering (r, θ, z) the cylindrical coordinates suitable for the 2D axisymmetrical model and (x, y, z) the cartesian ones to be used in our 3D model, the current density $\mathbf{j}$ reads

$$\mathbf{j} = \frac{j_0}{r} \begin{pmatrix} -sin(\theta) \\ cos(\theta) \end{pmatrix} \text{ (cylindrical)} \quad \Leftrightarrow \quad \mathbf{j} = \frac{j_0}{x^2 + y^2} \begin{pmatrix} -y \\ x \end{pmatrix} \text{ (cartesian)} \tag{3.83}$$

with $j_0 = 10^6 \ A.m^{-2}$.

Figure 3.17a displays the magnetic induction map obtained on the Ω_{mgn} cylinder with the 3D model. The match between the two considered models is illustrated in Figure

3.17b which compares the results obtained along z axis. The relative error between the two models doesn't exceed 2×10^{-4} in this example which validate the considered 3D model.

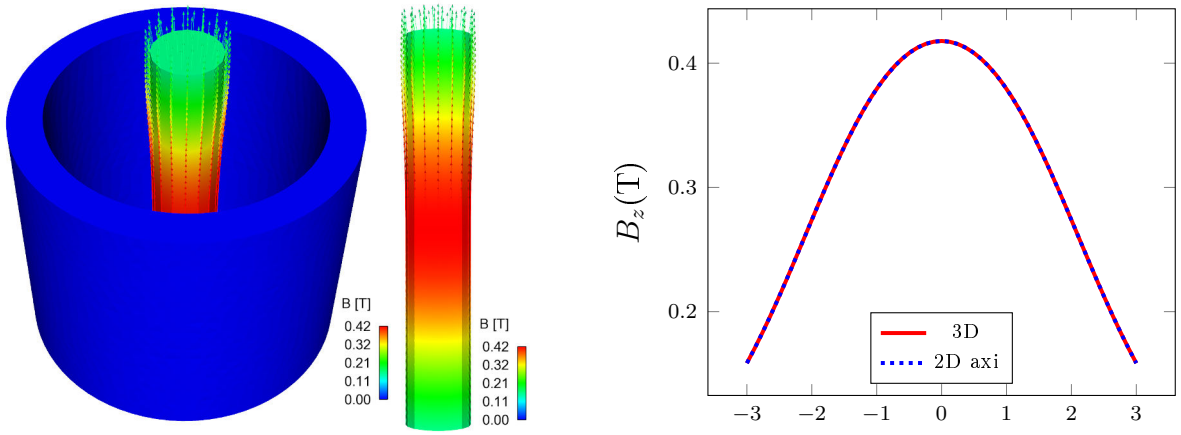

(a) Magnetic induction in Ω_{mgn} (b) B_z along z axis

Figure 3.17 – Magnetic field produced by a torus

As long as $\mathbf{r} \in \Omega_{mgn}$ and $\mathbf{r}' \in \Omega_{cond}$ are far enough from each other as in Figure 3.17a, the standard integration methods gives good results. Nevertheless, it is no longer the case when the point $\mathbf{r} \in \Omega_{mgn}$ at which we compute the magnetic field is too close to the conductor Ω_{cond}.

We introduce the distance d expressed as the minimal distance Ω_{cond} and Ω_{mgn}.

$$d = min_{\mathbf{r}\in\Omega_{mgn},\mathbf{r}'\in\Omega_{cond}}(|\ \mathbf{r} - \mathbf{r}'\ |) \tag{3.84}$$

To investigate the impact of this distance d on the Biot & Savart integrals computation, we consider a domain Ω_{mgn} whose boundary are close to the conductor Ω_{cond} – which remains the same as in Figure 3.17a.

We consider Ω_{mgn} as a cylinder of radius close to the one of Ω_{mgn}, and whose height is centred around the top extremity of the conductor.

This study compares the z-component of the magnetic field obtained along vertical axis, taken at various distance d with 2D axisymmetrical model and with Biot & Savart's law. Figure 3.18a plots the value of B_z along the z axis for various distances d, while Figure 3.18b displays the associated absolute error.

As expected, the highest errors are obtained for the smallest distance since the 3D Green kernel (3.80) used in (3.82) becomes almost singular. Nevertheless, the results are good at the points located in the region above the extremity of the conductor.

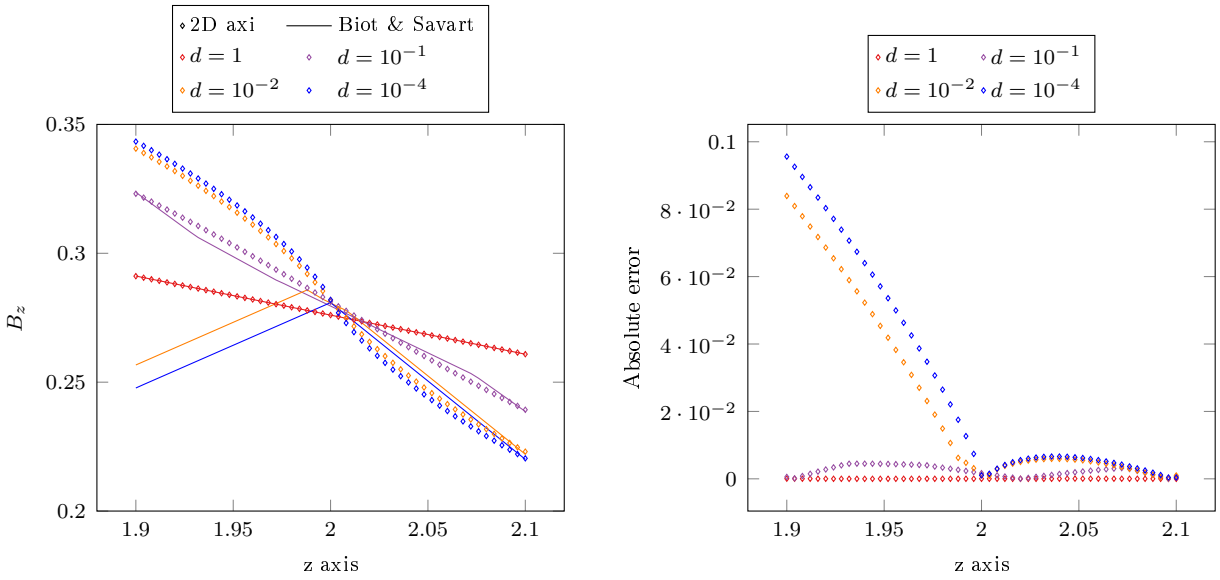

(a) Torus 2 : B_z along z with various d (b) Torus 2 : Error on B_z with various d

Figure 3.18 – Impact of the distance between Ω_{mgn} and Ω_{cond} on Biot & Savart

Although they have not been investigated in our implementation, there are various approaches allowing to deal with the singularity. These are mainly based on the numerical integration of a singular kernel over a triangle. Two of them relying on exact integration can be found in [Graglia, 1993] and [Masserey et al., 2005].

To complete the validation, other numerical experiments have been performed on real magnet geometries, to be compared both with 2D axisymmetrical results and with experimental measurements (see Chapter 9).

The application of Biot & Savart's law on real magnets is very expensive computationally. Thus, we have developed an efficient parallel algorithm for this model. If the sequential implementation is trivial since the unique processors computing the integrals (3.81) and (3.82) owns the whole $\Omega = \Omega_{cond} \cup \Omega_{mgn}$, the condition is no longer satisfied in the parallel implementation which supposes the partitionning of the domain Ω. In this context, a smart strategy to manage communications between partitions is proposed in Chapter 6. This algorithm allows to compute both (3.81) and (3.82) even though the computation of $\mathbf{B}$ (3.82) is preferred from a practical point of view.

3.4 Linear elasticity model

In addition to the Lorentz forces induced by the magnetic field (Section 3.2), there are also dilatation forces coming from the Joule heating (Section 3.1). The linear elasticity model – coupled with electro-thermal and magnetostatic models – aims to study both deformation and stresses induced by these forces.

3.4.1 Equations

Let us consider Ω_0 a domain at initial state (no forces). The forces applied on our object will submit it to a deformation $\mathcal{D}$, until an equilibrium final state Ω_T is reached. We denote M_0 a point in Ω_0 with coordinates p_0, and the corresponding point $M_T = \mathcal{D}(M_0)$ in Ω_T with coordinates p_T. The objective is to calculate the displacement vector $\mathbf{u} = (u_1, u_2, u_3)^T = p_T - p_0$ for each point M of our domain.

As Ω_T is at equilibrium state, the equation of motion becomes the following equilibrium equation

$$div(\bar{\bar{\sigma}}) + \mathbf{f} = 0 \tag{3.85}$$

where $\bar{\bar{\sigma}}$ is the stress tensor and $\mathbf{f}$ represents the volume forces applied on Ω.

The quantity we focus on is the displacement vector $\mathbf{u}$, which doesn't appear in the equilibrium equation (3.85).
We have to introduce the tensor of small deformations $\bar{\bar{\varepsilon}}$:

$$\bar{\bar{\varepsilon}} = \frac{1}{2}(\nabla \mathbf{u} + \nabla \mathbf{u}^T) \tag{3.86}$$

Hooke's law allows to link the stress tensor $\bar{\bar{\sigma}}$ with the tensor of small deformation $\bar{\bar{\varepsilon}}$:

$$\bar{\bar{\sigma}}^E(\bar{\bar{\varepsilon}}) = \frac{E}{1+\nu}\left(\bar{\bar{\varepsilon}} + \frac{\nu}{1-2\nu} Tr(\bar{\bar{\varepsilon}}) I\right) \tag{3.87}$$

where E is the Young modulus, ν is Poisson's ratio and I is the identity tensor.

The forces coming from Joule heating are modeled by adding a thermal dilatation term $\bar{\bar{\sigma}}^T$ to the stress tensor $\bar{\bar{\sigma}}^E$. This term involves the linear dilatation coefficient α_T :

$$\bar{\bar{\sigma}}(\bar{\bar{\varepsilon}}) = \bar{\bar{\sigma}}^E(\bar{\bar{\varepsilon}}) + \bar{\bar{\sigma}}^T(\bar{\bar{\varepsilon}}) \quad \text{with} \quad \bar{\bar{\sigma}}^T(\bar{\bar{\varepsilon}}) = -\frac{E}{1-2\nu}\alpha_T(T - T_0) I \tag{3.88}$$

3.4.2 Variational formulation

Let $\boldsymbol{\phi} = (\phi_1, ..., \phi_d)$ (where d is the space dimension) be the test functions of the weak formulation.
The integration of (3.85) multiplied by test functions over the domain Ω gives

$$-\int_\Omega \sum_{j=1}^{d} \frac{\partial \sigma_{ij}}{\partial x_j}\phi_i = \int_\Omega f_i \phi_i \quad \forall i = 1, \ldots, d \tag{3.89}$$

Rewriting previous equation into matricial form, we obtain

$$-\int_\Omega (\nabla \cdot \bar{\bar{\sigma}}) \circ \boldsymbol{\phi} = \int_\Omega \mathbf{f} \circ \boldsymbol{\phi} \tag{3.90}$$

where $\circ$ denote the element-wise product.

To ensure well posedness of the problem, boundary conditions have to be considered. Positions of $M_T = \mathcal{D}(M_0)$ can be set imposing the displacement vector $\mathbf{u}$ on $\partial\Omega_D$ as the Dirichlet boundary condition

$$\mathbf{u} = \mathbf{u}_D \text{ on } \partial\Omega_D \tag{3.91}$$

Surface forces – namely pressure forces – can also be imposed in $\partial\Omega_P$ as

$$\bar{\bar{\sigma}} \cdot \mathbf{n} = \mathbf{g} \text{ on } \partial\Omega_P \tag{3.92}$$

Using Green's theorem on (3.89) and including boundary conditions, we obtain

$$\int_\Omega \sum_{j=1}^{d} \sigma_{ij}^E \frac{\partial \phi_i}{\partial x_j} - \int_{\partial\Omega} \sum_{j=1}^{d} (\sigma_{ij} n_j)\phi_i = \int_\Omega f_i \phi_i + \int_\Omega \frac{E\alpha_T}{1-2\nu} \frac{\partial \phi_i}{\partial x_i}(T - T_0) \quad \forall i = 1, \ldots, d \tag{3.93}$$

Let $H_1^d(\Omega) = \{\mathbf{v} = (v_1, v_2, v_3)^T \mid v_i \in H_1(\Omega), 1 \leqslant i \leqslant d\}$ be the set vectorial functions whose components are in H_1. Dirichlet conditions imposed in strong form lead to define the function spaces

$$H_{1,\mathbf{u}}^d(\Omega) = \{\mathbf{u} \in H_1^d(\Omega) \mid \mathbf{u} = \mathbf{u}_D \text{ on } \partial\Omega_D\} \quad \text{and} \quad H_{1,\boldsymbol{\phi}}^d(\Omega) = \{\boldsymbol{\phi} \in H_1^d(\Omega) \mid \boldsymbol{\phi} = 0 \text{ on } \partial\Omega_D\}$$

Using the tensor of small deformations and Hooke's law, we obtain the final variational formulation consists in finding $\mathbf{u} \in H_{1,\mathbf{u}}^d(\Omega)$ such that

$$\begin{aligned} & \frac{E}{(1+\nu)} \int_\Omega Tr\left(\frac{1}{2}(\nabla \mathbf{u} + \nabla \mathbf{u}^T)^T * \frac{1}{2}(\nabla \boldsymbol{\phi} + \nabla \boldsymbol{\phi}^T)\right) + \frac{E\nu}{(1+\nu)(1-2\nu)} \int_\Omega (\nabla \cdot \mathbf{u})(\nabla \cdot \boldsymbol{\phi}) \\ = & \int_\Omega \mathbf{f} \cdot \boldsymbol{\phi} + \int_{\partial\Omega_P} \mathbf{g} \cdot \boldsymbol{\phi} + \int_\Omega \frac{E\alpha_T}{1-2\nu}(T - T_0)(\nabla \cdot \boldsymbol{\phi}) \end{aligned}$$

for all $\boldsymbol{\phi} \in H_{1,\boldsymbol{\phi}}^d(\Omega)$.

We can also impose Dirichlet boundary conditions in weak form that don't need additional function space definition. To this end, we introduce

$$\bar{\bar{s}} = \frac{1}{2}(\nabla \boldsymbol{\phi} + \nabla \boldsymbol{\phi}^T) \quad \text{such that} \quad \bar{\bar{\sigma}}(\bar{\bar{s}}) = \frac{E}{1+\nu}\left(\bar{\bar{s}} + \frac{\nu}{1-2\nu} Tr(\bar{\bar{s}}) I\right) - \frac{E}{1-2\nu}\alpha_T (T - T_0) I$$

Adding the penalization and consistance terms, the variational formulation with weak Dirichlet conditions consists in finding $\mathbf{u} \in H_1^d(\Omega)$ such that

$$\begin{aligned} & \frac{E}{(1+\nu)} \int_\Omega Tr\left(\frac{1}{2}(\nabla \mathbf{u} + \nabla \mathbf{u}^T)^T * \frac{1}{2}(\nabla \boldsymbol{\phi} + \nabla \boldsymbol{\phi}^T)\right) + \frac{E\nu}{(1+\nu)(1-2\nu)} \int_\Omega (\nabla \cdot \mathbf{u})(\nabla \cdot \boldsymbol{\phi}) \\ - & \int_{\partial\Omega_D} (\bar{\bar{\sigma}}(\bar{\bar{\varepsilon}}) \cdot \mathbf{n}) \cdot \boldsymbol{\phi} - \int_{\partial\Omega_D} (\bar{\bar{\sigma}}(\bar{\bar{s}}) \cdot \mathbf{n}) \cdot \mathbf{u} + \int_{\partial\Omega_D} \frac{\gamma}{h_s} \mathbf{u} \cdot \boldsymbol{\phi} = \int_\Omega \mathbf{f} \cdot \boldsymbol{\phi} + \int_{\partial\Omega_P} \mathbf{g} \cdot \boldsymbol{\phi} \\ + & \int_\Omega \frac{E\alpha_T}{1-2\nu}(T - T_0)(\nabla \cdot \boldsymbol{\phi}) - \int_{\partial\Omega_D} (\bar{\bar{\sigma}}(\bar{\bar{s}}) \cdot \mathbf{n}) \cdot \mathbf{u}_D + \int_{\partial\Omega_D} \frac{\gamma}{h_s} \mathbf{u}_D \cdot \boldsymbol{\phi} \end{aligned}$$

for all $\boldsymbol{\phi} \in H_1^d(\Omega)$.

3.4.3 Convergence study

As for electro-thermal model, the verification of the previously described elasticity model needs a convergence study to ensure that the convergence order is the awaited one. To this end, we provide an exact solution $\mathbf{u}_{ex}$ for the displacement $\mathbf{u}$ to study the error $\mathbf{e} = \mathbf{u} - \mathbf{u}_{ex}$ which has to satisfy

$$\| \mathbf{e} \|_{L_2} \leqslant ch^{k+1} \quad \text{and} \quad \| \mathbf{e} \|_{H_1} \leqslant ch^k \tag{3.94}$$

with h the mesh size, k the polynomial order of the approximation and c a constant.

The volumic forces are deduced from the equilibrium equation (3.85) with $\bar{\bar{\sigma}}$ evaluated from $\mathbf{u}_{ex}$. The thermal dilatation term in not taken into account here since it doesn't depend on the displacement and consequently doesn't have any effect on the matrix of the system to solve.

The figures 3.20 and 3.21 illustrate respectively the 2D and 3D convergence studies performed on the cubic domain $[-1:1]^d$ with $d = 2, 3$. The provided solution $\mathbf{u}_{ex}$ is the vectorial polynomial $(cos(y), sin(x))$, with a null z-component in 3D.

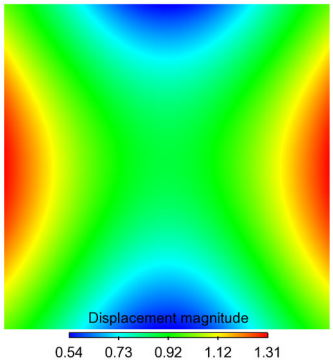

Figure 3.19 – Elasticity - 2D exact solution $\mathbf{u}_{ex} = (cos(y), sin(x))$

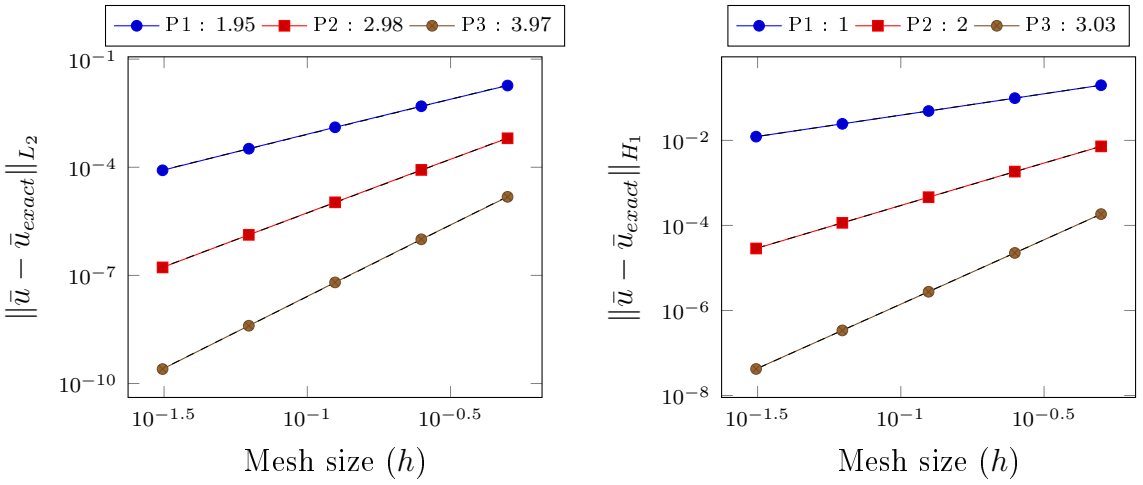

Figure 3.20 – Linear elasticity - 2D convergence study

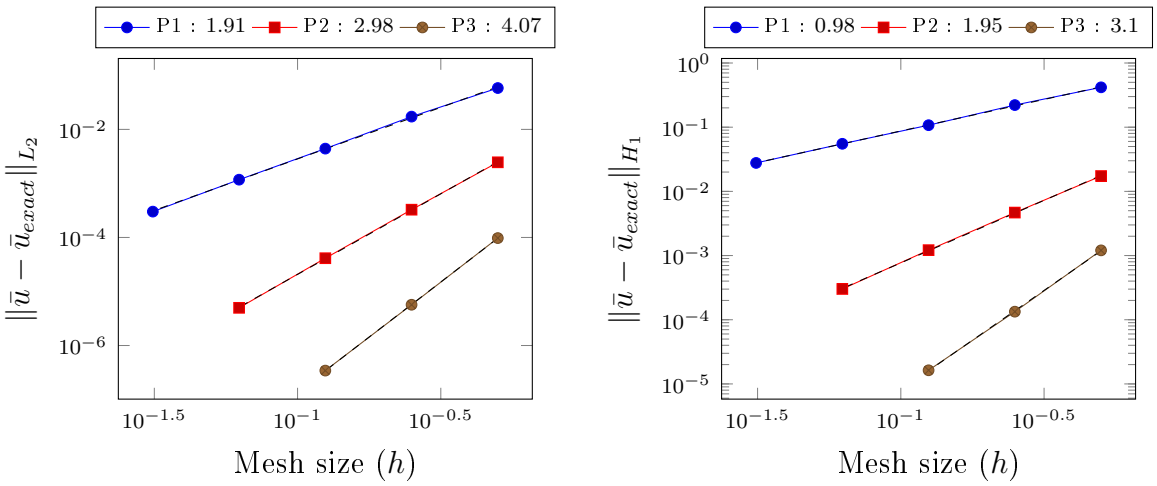

Figure 3.21 – Linear elasticity - 3D convergence study

3.4.4 Tresca and Von-Mises criterions

From an engineering point of view, it is a common practice to use some criteria based on the stress tensor $\bar{\bar{\sigma}}$ (3.85) to determine the nature of the deformation. Tresca and Von Mises yield surfaces are the most commonly used in isotropic materials study.

Tresca Also known as the maximal shear criterion, the Tresca yield surface tr is built from the components of the diagonalized stress tensor $\bar{\bar{\sigma}}^d$ obtained from $\bar{\bar{\sigma}}$. The Tresca criterion tr is built from the components of the diagonalized stress tensor $\bar{\bar{\sigma}}^d$ obtained from $\bar{\bar{\sigma}}$ as

$$tr_{\bar{\bar{\sigma}}^d} = \max_{1 \leqslant i < j \leqslant Dim} (\mid \bar{\bar{\sigma}}^d_{ii} - \bar{\bar{\sigma}}^d_{jj} \mid) \tag{3.95}$$

Von Mises The Von-Mises criterion is an energy based criterion which evaluates the elastic distorsion energy coming from both pulling, compression and shearing. This yield

surface can be computed directly from $\bar{\bar{\sigma}}$ (3.96) or using the diagonalized tensor $\bar{\bar{\sigma}}^d$ (3.97) as for Tresca (3.95)

$$vm_{\bar{\bar{\sigma}}} = \sqrt{\sum_{1 \leqslant i < j \leqslant Dim} \frac{1}{2} \left(\bar{\bar{\sigma}}_{i,i} - \bar{\bar{\sigma}}_{j,j}\right)^2 + 3\bar{\bar{\sigma}}_{i,j}^2} \tag{3.96}$$

$$vm_{\bar{\bar{\sigma}}^d} = \sqrt{\sum_{1 \leqslant i < j \leqslant Dim} \frac{1}{2} \left(\bar{\bar{\sigma}}_{ii}^d - \bar{\bar{\sigma}}_{jj}^d\right)^2} \tag{3.97}$$

In a context of optimization in terms of materials, these criterions prove essential to determine the necessary yield strength which indicates whether or not the material is deformed plastically. The development of materials which exhibit high yield strength while keeping a good electrical conductivities is a technological research challenge for high field magnets development. Typically, we expect to reach a yield strength higher than 500 MPa with an electrical conductivity which remains higher than 52 $MS.m^{-1}$.

Conclusion

In this chapter, we describe the physics involved in the multi-physics model designed for the study of high field magnets. The equations as well as the variational formulations necessary to apply the finite element method are given for each considered physic, together with the suitable boundary conditions.

We also establish the coupling between these equations leading to a non-linear multi-physics coupled model. The implementation of this full 3D multi-physics model within the `Feel++` library represents a contibution of this thesis.

We present in this chapter the convergence studies performed for each of the components, showing that the expected mathematical properties are satisfied. Especially, we propose to use a posteriori error estimators in the context of the non-linear electro-thermal model for which the exact solution is not readily available.

Regarding the magnetostatic model, three formulations are investigated. Two of which are based on the H_{curl}-conforming elements introduced in Section 1.

In our multi-physics model, the water cooling of the magnets is mimicked through a constant heat transfer coefficient, as a boundary condition of the heat equation. There is a need to improve the cooling model, with a more advanced hydaulic model based on Navier Stokes equations. Nevertheless, the development of such model is challenging due to the complexity of the water flow coming from the high flowrate.

Finally, the hybrid Galerkin methods are currently investigated to improve the quality of our approximations. The Hybridized Discontinuous Galerkin (HDG) method [Egger and Schöberl, 2010] provides an optimal approximation of both the primal and flux variables. In our model, it should allow to obtain a better approximation of the current density and hence of the current intensity which reads as its flux. It should be helpful to the preconditionners, for which the divergence free condition on the current density is a key ingredient.

Chapter 4

Reduced electro-thermal model

The electro-thermal model presented in Section 3.1 is a core ingredient for the high field magnet design, as it gives an estimation of the temperature and the current density. However, the input data involved in this model may not be as well understood. The material properties – electrical conductivity and temperature coefficient – are measured by the material supplier, which only provides an interval of definition for this quantities. As for the Lorentz number, many values can be found in the literature depending on the type of copper alloy.

The magnet operating conditions – the current intensity or the voltage as well as the cooling conditions – can also be flawed. The water temperature is only measured at the input and at the output of the magnet. In the model, we assume that it is a constant defined as the mean of these two measurements. The heat transfer coefficient is also difficult to measure, due to the complexity of the water flow to consider. For now, it is approximated through standard hydraulic correlations and considered as constant in all cooled regions.

In this context, parametric studies and uncertainty quantification are essential, both to cover the whole parameter ranges and to evaluate the influence of their uncertainty on specific quantities of interest. The Reduced Basis method introduced in Chapter 2 is perfectly suited to address these issues.

The development of the reduced electro-thermal model, in addition to the finite element one described in Section 3.1, relies on the establishment of the ingredients requested by the Reduced Basis method.

This chapter thus starts with the description of the affine decomposition of the considered problem obtained from the Empirical Interpolation Method introduced in Section 2.1. The convergence studies allowing to assess the pertinence of this reduced model on real magnet geometries consists in the second part of this chapter.

Contents

Let's remind that this model considers the heat equation with Joule losses as source term. Driven by the electrical potential, the right hand side of the heat equation is obtained from the resolution of a diffusion problem, coupled with the latter.

$$\begin{aligned} &-\nabla \cdot (\sigma(T)\nabla V) = 0 \text{ in } \Omega \\ &-\nabla \cdot (k(T)\nabla T) = \sigma(T)\nabla V \cdot \nabla V \text{ in } \Omega \end{aligned} \tag{4.1}$$

Two Dirichlet boundary conditions on electrical potential mimic the current flow from a difference of potential between the current input V_{in} and output V_{out}. As to the boundary conditions on temperature, we consider that the heat exchanges are limited to the water cooled region $\partial\Omega_{\text{cooled}}$.

$$\begin{aligned} &V = 0 \text{ on } V_{in} \\ &V = V_D \text{ on } V_{out} \\ &-\sigma(T)\nabla V \cdot \mathbf{n} = 0 \text{ on } \partial\Omega \backslash (V_{in} \cup V_{out}) \\ &-k(T)\nabla T \cdot \mathbf{n} = 0 \text{ on } \partial\Omega \backslash \partial\Omega_{\text{cooled}} \\ &-k(T)\nabla T \cdot \mathbf{n} = h(T - T_w) \text{ on } \partial\Omega_{\text{cooled}} \end{aligned} \tag{4.2}$$

Section 3.1 presents two formulations for the electrical potential equation, depending on the Dirichlet boundary conditions treatment. In the context of the reduced basis method, the framework offered by the `Feel++` imposes – at least for now – to implement the boundary conditions on their weak form. The associated variationnal formulations detailed in (3.22) and (3.24) thus form a single problem whose variationnal formulation is given as the sum of the two.

$$\begin{aligned} &\int_\Omega \sigma(T)\nabla V \cdot \nabla \phi_V - \int_{V_{in}\cup V_{out}} \sigma(T)\Big((\nabla V \cdot \mathbf{n})\phi_V - (\nabla \phi_V \cdot \mathbf{n})V + \frac{\gamma}{h} V\phi_V\Big) \\ &\qquad + \int_\Omega k(T)\nabla T \cdot \nabla \phi_T + \int_{\partial\Omega_{\text{cooled}}} hT\phi_T \\ &= \int_\Omega \sigma(T)\nabla V \cdot \nabla V - \int_{V_{out}} \sigma(T)(\nabla \phi_V \cdot \mathbf{n})V_D + \int_{V_{out}} \frac{\gamma}{h}\sigma(T)V_D\phi_V + \int_{\partial\Omega_{\text{cooled}}} hT_w\phi_T \end{aligned} \tag{4.3}$$

We also remind that the considered electro-thermal model exhibits a non-linearity coming from the dependence of its coefficients on temperature. Indeed, the electrical and thermal conductivities involved in (4.2) are expressed as

$$\sigma(T) = \frac{\sigma_0}{1 + \alpha(T - T_0)} \quad \text{and} \quad k(T) = \sigma(T)LT \tag{4.4}$$

with σ_0 the electrical conductivity measured at reference temperature T_0, α the temperature coefficient and L the Lorentz number. These materials properties and the magnet operation conditions form the considered input parameter

$$\boldsymbol{\mu} = (\sigma_0, \alpha, L, V_D, h, T_w) \tag{4.5}$$

The quantities of interest we are concerned for are many. We investigate the current

intensity, the power, the resistance of the magnet and the mean temperature over the domain defined as

$$s(T(\boldsymbol{\mu})) = \frac{1}{|\Omega|}\int_{\Omega} T(\boldsymbol{\mu})d\Omega \tag{4.6}$$

In the following, we focus on the mean temperature (4.6) as output.

The efficiency of the Reduced Basis method is especially based on an offline/online strategy. This methodology supposes the availability of an affine decomposition for (4.3) enabling the precomputation of terms which don't depend on the parameter $\boldsymbol{\mu}$ (4.5). Turning back to the expression of material properties depending on temperature (4.4), we note that the considered electro-thermal model is non-affinely parametrized.

4.1 Affine decomposition

We are thus in the situation where the Reduced Basis method is applied to a non-linear and non-affinely parametrized problem detailled in Section 2.2. In this context, the Empirical Interpolation Method (EIM, see Section 2.1) is mandatory to recover the necessary affine decomposition. Since the non-affine parametrization results from the definition of the electrical and thermal conductivities on temperature, both of them are approximated through EIM. Their affine approximations respectively denoted as σ_{M^σ} and k_{M^k} are expressed as

$$\sigma(T) \approx \sigma_{M^\sigma} = \sum_{m=1}^{M^\sigma} \beta_m^\sigma q_m^\sigma \quad \text{and} \quad k(T) \approx k_{M^k} = \sum_{m=1}^{M^k} \beta_m^k q_m^k \tag{4.7}$$

Moreover, the source term of the heat equation presents also a non-affine parametrization due to its dependence on $\sigma(T)$. We consequently introduce the EIM approximation Q_{M^Q} of this term as

$$\sigma(T)\nabla V \cdot \nabla V \approx Q_{M^Q} = \sum_{m=1}^{M^Q} \beta_m^Q q_m^Q \tag{4.8}$$

Replacing the non-affinely parametrized terms of 4.3 by their approximations EIM (4.7) and (4.8), the affine decomposition of the electro-thermal model reads as

$$\begin{aligned}
&\sum_{m=1}^{M^\sigma} \beta_m^\sigma \left[\int_\Omega q_m^\sigma \nabla V \cdot \nabla \phi_V - \int_{V_{in}\cup V_{out}} q_m^\sigma \Big((\nabla V \cdot \mathbf{n})\phi_V \;-\; (\nabla \phi_V \cdot \mathbf{n})V + \frac{\gamma}{h} V\phi_V\Big)\right] \\
&\qquad + \sum_{m=1}^{M^k} \beta_m^k \int_\Omega q_m^k \nabla T \cdot \nabla \phi_T + h\int_{\partial\Omega_{\text{cooled}}} T\phi_T \\
&= \sum_{m=1}^{M^Q} \beta_m^Q \int_\Omega q_m^Q + \sum_{m=1}^{M^\sigma} \beta_m^\sigma \left[-\int_{V_{out}} q_m^\sigma (\nabla \phi_V \cdot \mathbf{n}) V_D \;+\; \int_{V_{out}} \frac{\gamma}{h} q_m^\sigma V_D \phi_V\right] + hT_w \int_{\partial\Omega_{\text{cooled}}} \phi_T
\end{aligned} \tag{4.9}$$

The decomposition (4.9) enables us to apply the offline/online strategy introduced in Section 2.2.

4.2 Convergence study

The last section of this chapter focuses on the convergence study of the considered reduced electro-thermal model. In the context of non-linear and non-affinely parametrized problem, this convergence study involves two levels. The first of them consists in the study of the EIM approximations errors depending on the size of the EIM approximation space. To this end, we introduce the L_2 relative error of each approximation EIM w_M of w as

$$e_{L_2} = \frac{\| w - w_M \|_{L_2}}{\| w \|_{L_2}} \tag{4.10}$$

The second level aims to study the convergence of the reduced basis approximation itself. The error on the solution (resp. on the output) is obtained from the corresponding finite element solution (resp. output) computed from the affine decomposition. The considered finite element model – denoted as PFEM – thus takes into account the involved EIM approximations. The relative L_2 (resp. H_1) error on the reduced approximation u_{RB} then reads from the finite element solution u_{PFEM} as

$$e_{L_2} = \frac{\| u_{RB} - u_{PFEM} \|_{L_2}}{\| u_{PFEM} \|_{L_2}} \quad \text{and} \quad e_{H_1} = \frac{\| u_{RB} - u_{PFEM} \|_{H_1}}{\| u_{PFEM} \|_{H_1}} \tag{4.11}$$

The next subsections deal with the EIM and RB convergence studies performed on different problems, all based on existing high field magnets.

4.2.1 Sector of a Bitter magnet

The first convergence study focus on a sector of a Bitter magnet (see Figure 4.1a). We are interested in the mean temperature over the domain as output. It is obtained from the reduced basis approximation of temperature as illustrated in Figure 4.1b.

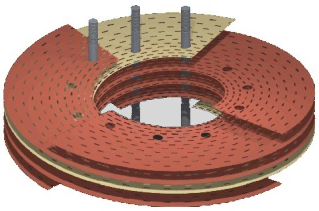

(a) Bitter magnet

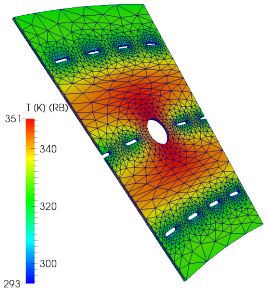

(b) RB-temperature

Figure 4.1 – RB approximation on a sector of a Bitter magnet

The next results are based on an EIM approximation space of size 40 whose basis functions are built from an EIM trainset of size 300. The parameters used to built the reduced

basis functions are selected randomly through a sampling of size 1000. The resulting RB approximation space in which the reduced basis approximation shall resides is composed of 15 finite element solutions. The mean as well as the extremum of the relative error are obtained from a set of 50 online realizations.

As previously introduced, the EIM convergence study investigates the L_2 error of the considered EIM approximations. Figure 4.2a (resp. 4.2b) plots the L_2 error defined in (4.10) for the EIM approximation σ_{M_σ} (resp. k_{M^k}) of $\sigma(T)$ (resp. $k(T)$) depending on the number of EIM basis functions comprising the EIM approximation space.

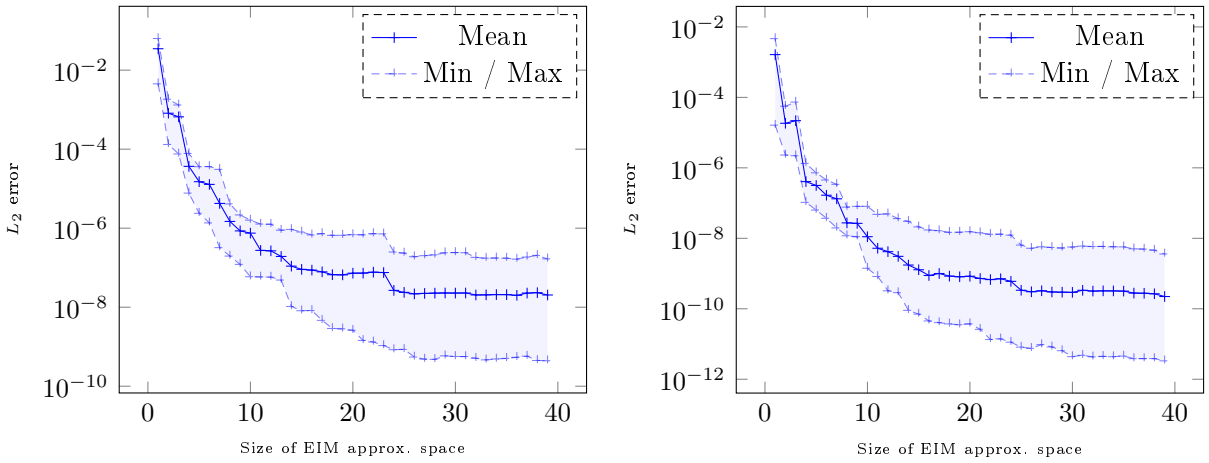

(a) EIM - σ(T) (b) EIM - k(T)

Figure 4.2 – Convergence of EIM approximations of a helix sector

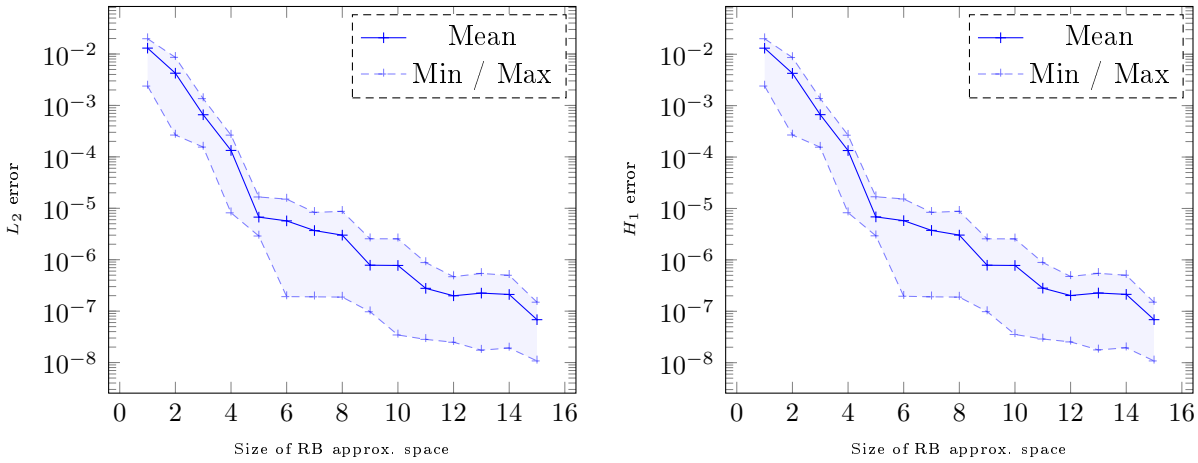

(a) L_2 error (b) H_1 error

Figure 4.3 – Convergence of RB approximation of a helix sector

As expected, the relative error decreases with the number of EIM basis functions. Taking a better look on these graphs, we observe that the decrease ends with a plateau from a number of basis function close to 25. Regarding the value of the relative error in this region, we assess that the convergence of the considered EIM approximations is ensured and that an EIM approximation space of size 25 is sufficient in this context. Although it is not illustrated, the last EIM approximation dealing with the heat equation source term

has the same behavior.

Figure 4.3a (resp. 4.3b) displays the L_2 (resp. H_1) relative errors defined in (4.11) depending on the size of the RB approximation space. As to the previous EIM approximations, the relative error decreases with the size of the approximation space. This behavior was expected to confirm the good convergence of the electro-thermal model reduced model.

4.2.2 Sector of a radially cooled helix magnet

As mentioned in introduction, the radially cooled helices (see Figure 4.4a) is a promising solution to reach higher magnetic field. Indeed, their design allows a larger cooling surface and hence a better cooling enabling to impose a higher current density thus resulting in higher magnetic field. Nevertheless, the corresponding geometry is more complex due to the insulators which have to be inserted between the turns.

The use of the reduced model is even more significant for such a complex application. In order to confirm the convergence properties are ensured for this problem as well, the following convergence study focus on a sector of this type of helix. Mimicking the presence of insulators, the sector illustrated by Figure 4.4a is chosen as centered around an insulator at halfway up the helix.

Based on the previous numerical experiment, we take only 30 EIM basis functions whose parameters are selected in a trainset of size 100. By constrast, we choose to slightly increase the size of the RB approximation space composed of 20 bases selected randomly among a sampling of size 1000.
As previously, the results are based on a set of 50 realizations.

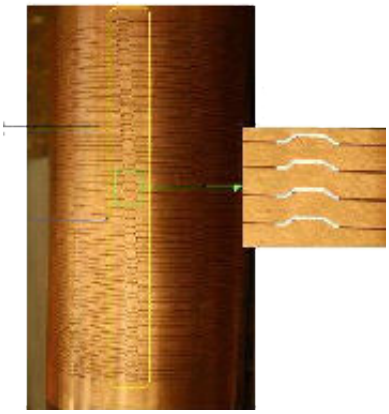

(a) Radially cooled helix

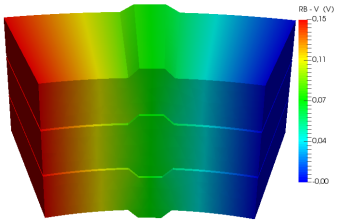

(b) RB-Potential

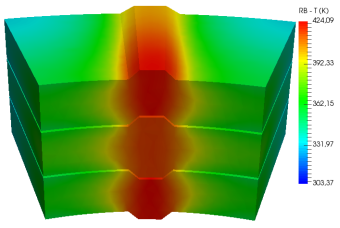

(c) RB-Temperature

Figure 4.4 – RB approximations on a sector of a radially cooled helix magnet

Figure 4.5a and 4.5b display the relative L_2 errors on the EIM approximations σ_{M_σ} and k_{M^k} respectively. These results confirm the previous ones obtained on the Bitter

magnet. Regarding the value of the relative errors, the considered EIM approximations thus provide an accurate affine decomposition for this problem. The EIM approximation obtained for $k(T)$ is even limited to 27 basis functions since the error tolerance has been exceeded before reaching the expected approximation space size.

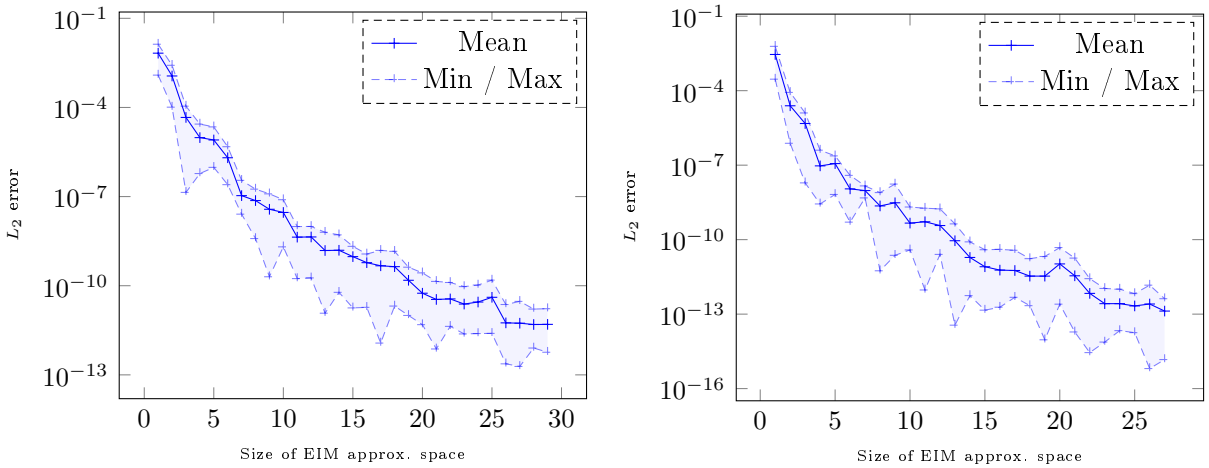

(a) EIM - σ (b) EIM - k

Figure 4.5 – Convergence of EIM approximations of a helix sector

Finally, the RB convergence study illustrated in Figure 4.6a (resp. 4.6b) is ensured as well. Indeed, the L_2 (resp. H_1) relative errors between the reduced basis solution and the corresponding parametric finite element model (PFEM) are satisfactory.

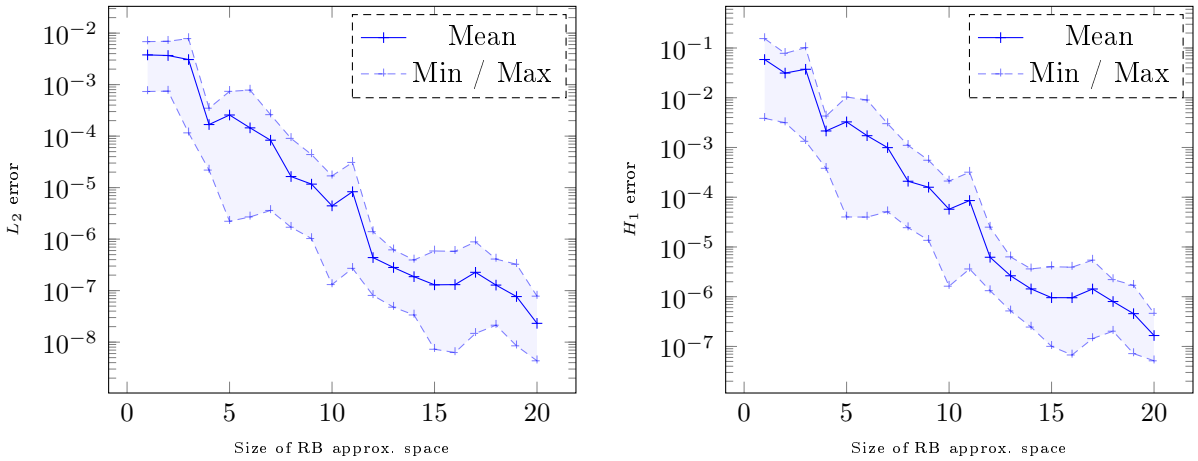

(a) L_2 error (b) H_1 error

Figure 4.6 – Convergence of RB approximation of a helix sector

4.2.3 Radially cooled helix magnet

Following on the previous convergence study, the last one focus on the complete radially cooled helix. Concerning EIM, we keep the same set up expecting a similar behavior for the complete helix and for the considered sector. For computational cost reasons, we nevertheless limit the size of the RB approximation space to 10 regarding the previous

study which gives satisfying relative errors for this number of basis. These basis functions are as previously built from a random selection through a sampling of size 1000.

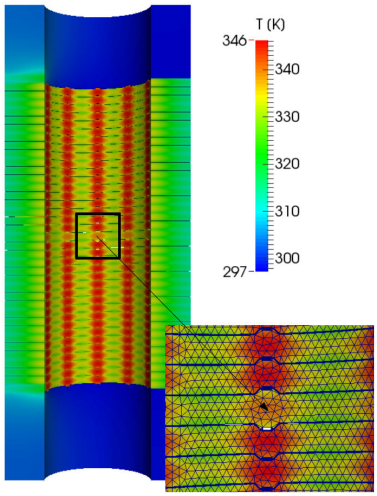

Figure 4.7 – Temperature map of a radially cooled helix

Figure 4.8a displays the relative L_2 error on the reduced basis approximation, while Figure 4.8b plots the L_2 error corresponding to the output. In both cases, we assess that the convergence properties are satisfied which confirms the relevance of our reduced electro-thermal model in the high field simulations context.

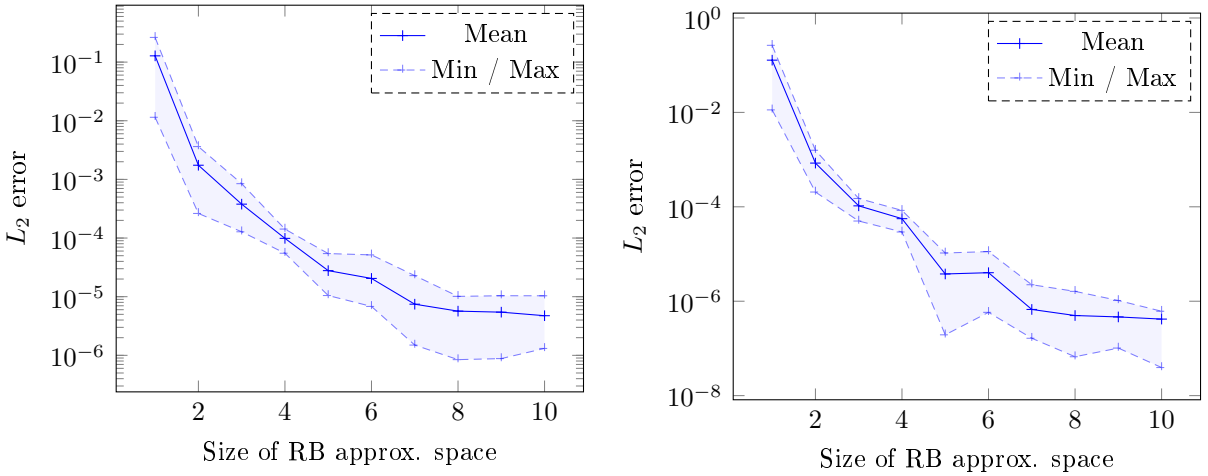

(a) L_2 error - solution

(b) L_2 error - output

Figure 4.8 – Convergence of RB approximation of a radially cooled helix

Conclusion

Drawing on the reduced basis methodology introduced in the Chapter 2 for non-linear and non-affinely parametrized problems, this chapters describes the ingredients of the reduced electro-thermal model, established from its finite element equivalent described in Section

3.1. Especially, we detail the affine decomposition recovered through EIM approximations of the non-affinely parametrized terms of the formulation.

The second part of this chapter is dedicated to the convergence study of this reduced model, considering both EIM and RB approximation spaces. Based on two concrete applications related with high field magnets modeling, this study assesses the feasability and the relevance of the reduced basis method on such problem. Various studies based on this reduced electro-thermal model are depicted in Chapter 8 dedicated to numerical applications.

Part III

Contributions to Feel++ library

Chapter 5

H_{div} and H_{curl} conforming elements

As stated in Chapter 1, the resolution of the discrete problem (1.2) supposes the knowledge of the discrete subspace $X_{\mathcal{N}}(\Omega) \subset X(\Omega)$. In this context, the definition of $X_{\mathcal{N}}(\Omega)$ required to apply the Galerkin method is handled by the finite element method which defines it from its basis function $\{\phi_i\}_{i=1}^{\mathcal{N}}$.

$$X_{\mathcal{N}}(\Omega) = span\{\phi_1, \cdots, \phi_{\mathcal{N}}\} \tag{5.1}$$

As a reminder, each element K of the mesh Γ_h is the image of a reference element $\hat{K}$ from the geometrical transformation ϕ_K^{geo} (see figure 1.1). In the following, we distinguish the global number of degrees of freedom $\mathcal{N}_g$ – which corresponds to the size $\mathcal{N}$ of the FE approximation space – and the local number of degrees of freedom $\mathcal{N}_l$ in each element of Γ_h. The relationship between local and global degrees of freedom is given through a correlation table, allowing to deduce the global index of each degree of freedom from *(i)* the element K to which it belongs and *(ii)* its local index within this element.

The finite element basis functions are deduced from the reference basis functions $\{\hat{\phi}_i\}_{i=1}^{\mathcal{N}_l}$ computed only on $\hat{K}$. They are themselves described from their expression in the primal basis $\mathcal{B} = \{\zeta_k\}_{k=1}^{\mathcal{N}_l}$.

The essential ingredients serving to define the polynomial space $X_{\mathcal{N}}(\Omega)$ are *(i)* the primal basis $\mathcal{B}$ hosting the finite element basis functions, *(ii)* the reference basis functions $\{\hat{\phi}_i\}_{i=1}^{\mathcal{N}_l}$ in $\hat{K}$ expressed from their coefficients in the primal basis and *(iii)* the geometrical transformation ϕ_K^{geo} allowing to deduce the $\{\phi_i\}_{i=1}^{\mathcal{N}_l}$.

The `Feel++` library offers a generic finite element framework, using a language very close to mathematics. The development of the multi-physics model for high field magnets requires the use of H_{div} and H_{curl} finite elements, as mentioned in Chapter 3. We remind that the description of these elements is given in Chapter 1.

Starting from a short description of the `Feel++` finite element framework, we first sum up how Lagrange finite elements come within this scope. This section then focuses on the implementation of the H_{div} and H_{curl}-conforming finite elements within the `Feel++` framework. It takes on the same structure as Chapter 1. As a complement, some details

on the assembly of these kind of finite element can be found in [Rognes et al., 2009].

This development allows Feel++ to fully support the De-Rham complex diagram.

Contents

5.1 Feel++ finite element framework

The implementation of any additional finite element family in Feel++ implies to become familiar with the framework. To this end, this section focuses on the key ingredients of a finite element definition within the framework.

5.1.1 General structure

class PolynomialSet In Feel++, the elements identified as defining the polynomial space $X_{\mathcal{N}}(\Omega)$ are grouped in an object PolynomialSet, illustrated in figure 5.1. The polynomials of the primal basis $\mathcal{B}$, as well as the coefficient $\{c_i^k\}$ of the reference basis functions $\{\hat{\phi}_i\}$ in this basis, are variable members of this class. The member class PreCompute handles all the precomputations which can be performed on $\hat{K}$, while the class Context carries the geometrical transformation ϕ_K^{geo}.

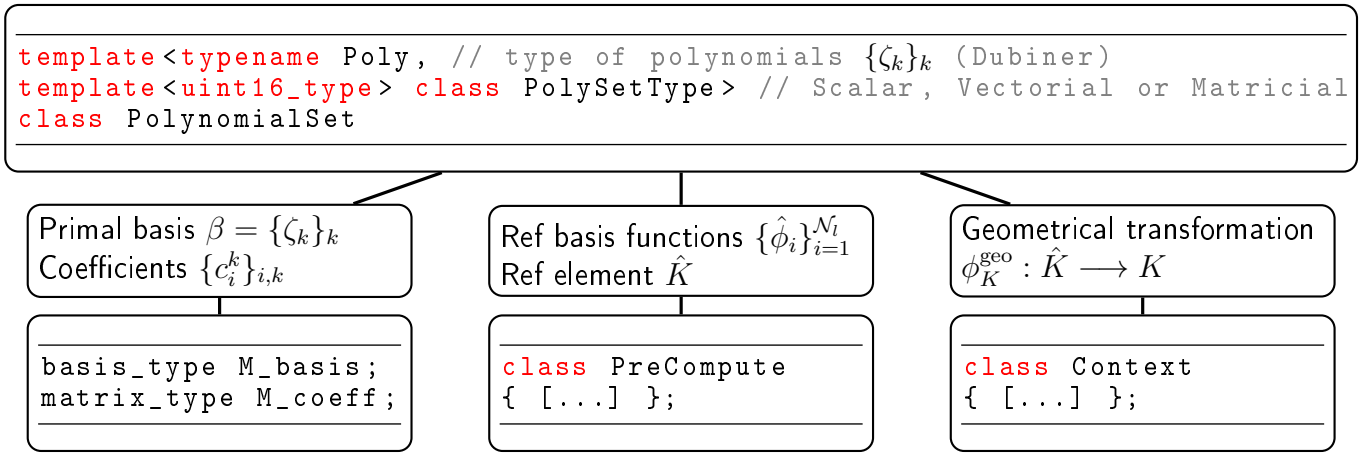

Figure 5.1 – The class PolynomialSet contains $X_{\mathcal{N}}$ ingredients

Let's remind that each finite element is characterized by a tuple (K, P_K, Σ_K). Its basis functions are defined by their coefficient $\{c_i^k\}$ in the primal basis. These are the solutions of the system (1.7) which read from the finite element degrees of freedom.

class FiniteElement The generic class `FiniteElement` defines any finite element as its tuple (K, P_K, Σ_K) from template parameters, which makes it compatible with any finite element type, provided that such a definition is available. As illustrated in figure 5.2, this class assembles the system (1.7) from the definitions of the primal and dual spaces. It then computes the coefficients $\{c_i^k\}$, which are given to the `M_coeff` member of the object `PolynomialSet` describing $X_{\mathcal{N}}(\Omega)$ (figure 5.1). We remind that all of these computations are performed on the reference element $\hat{K}$ only.

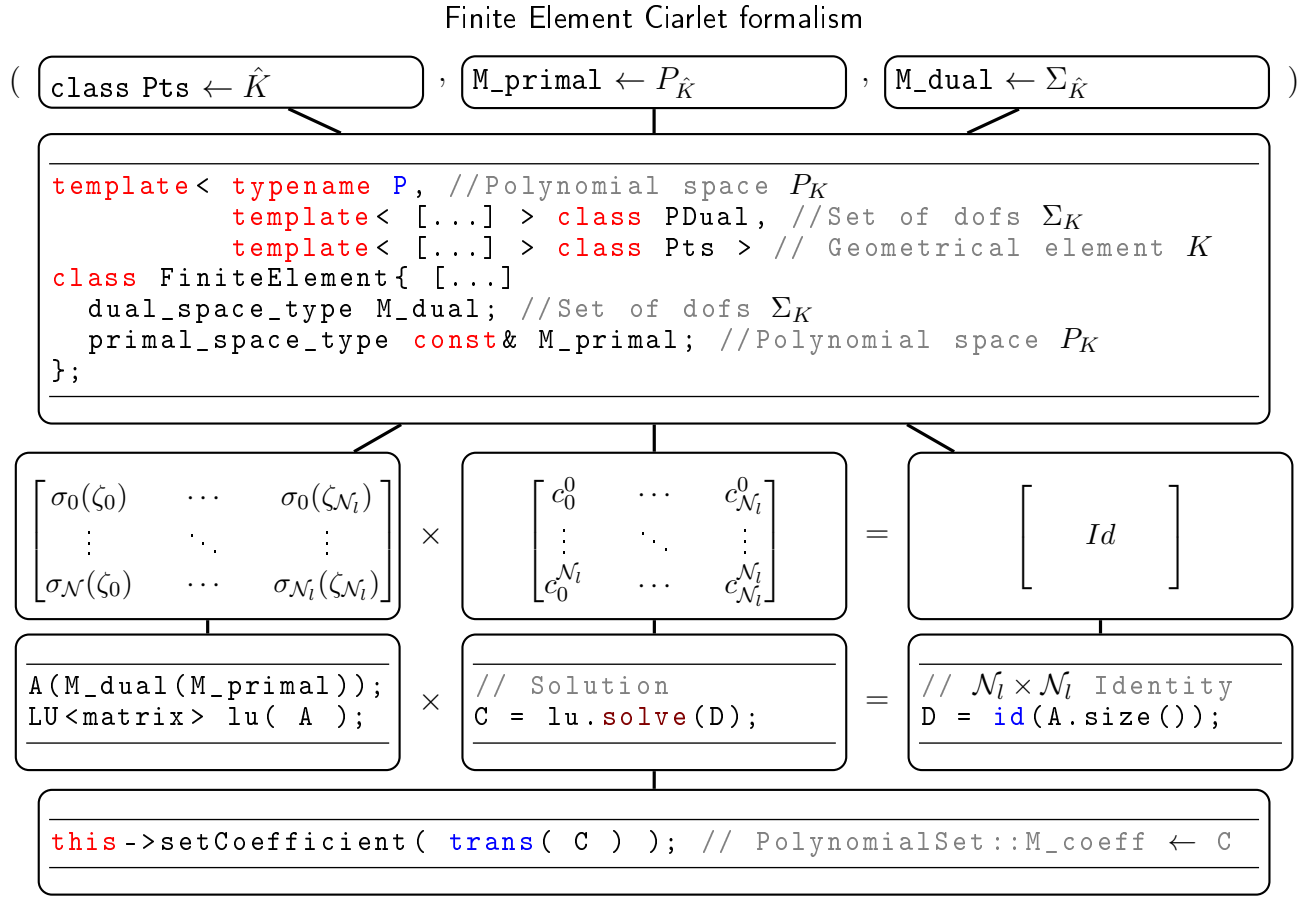

Figure 5.2 – The class `FiniteElement` computes the c_i^k coefficients from $(\hat{K}, P_{\hat{K}}, \Sigma_{\hat{K}})$

Each finite element type then consists in a specific class which derives from this generic object `FiniteElement`, to which the characteristics (K, P_K, Σ_K) are given.

5.1.2 Interpolation

The interpolation operators $\pi_{\mathcal{N}}$ in the De-Rham diagram (1.11) allow to relate continuous spaces with their discrete equivalent. Each finite element type provides an interpolant, as described in Chapter 1.

In `Feel++`, the interpolation process is implemented in a generic way, within a unique function `on`, which seamlessly selects the appropriate interpolation operator. Let's introduce u as a discrete function of $X_{\mathcal{N}}$. The following example gives u as the interpolant of a continuous expression f on the whole mesh.

```
auto u = Xh->element(); // u ∈ X_N
u.on( _range=elements(mesh), _expr=f); //u = π_N(f)
```

Each finite element type has its own interpolant operator, depending on the definition of its degrees of freedom. In practice, this corresponds for each finite element class to have its own version of the `interpolate` function which implements the appropriate operator. The generic function `on` simply calls the `interpolate` embedded in the definition of the function space $X_{\mathcal{N}}$.

Covering all geometrical elements of the range given to the function `on`, the `interpolate` function builds the local interpolant `IhLoc` to be assigned to the current element K.

```
auto* __fe = this->functionSpace()->fe().get(); // Get FE from X_N
__fe->interpolate( [...], IhLoc ); // IhLoc : local interpolant
this->assign( curElt, IhLoc ); //
```

5.1.3 Unicity of normals and tangent

The description of H_{div} and H_{curl} conforming elements in sections 1.2 and 1.3 addresses the importance of the unicity of normals and tangents shared with more than one element. This requires to consider the mesh in a global point of view, and not only elements by elements. To this end, the class `dofTable` defines the global numbering of the mesh related to the local numbering of its entities. Although essential to the `Feel++` finite element framework, we won't details this part but simply consider this numbering as available.

It is essential to have a coherent global numbering. We have thus to take care of the numbering of each real element K. Each of the real elements results from the application of the geometrical transformation ϕ_K^{geo} to $\hat{K}$ which has its own numbering.

Actually, the reference element $\hat{K}$ hides several reference elements $\hat{K}_i$ allowing to cover all permutations of its local numbering. Going back to the example introduced with figures 1.2 and 1.6 in Chapter 1, K_0 (resp. K_1) consists in the image of $\hat{K}_0$ (resp. $\hat{K}_1$) by a geometrical transformation $\phi_{K_0}^{geo}$ (resp. $\phi_{K_1}^{geo}$).

$$\exists \phi_{K_0}^{geo}, \phi_{K_1}^{geo} \ \mid \ K_0 = \phi_{K_0}^{geo}(\hat{K}_0), K_1 = \phi_{K_1}^{geo}(\hat{K}_1)$$

The local numbering of $\hat{K}_1$ is a permutation of $\hat{K}_0$ local numbering. As mentioned, the unicity of the normals and tangents is handled affecting a sign to the concerned entities of the mesh from this permutation.

Considering the example of Nédélec finite elements for which the degrees of freedom are attached to the edges, we remind that the unique orientation of each shared edge is the one seen by K_0 (figure 1.6).

From K_1 element, the numbering of the concerned edge is a reverse permutation compared to one of K_0. The sign affected to the corresponding degree of freedom is embedded in the `dofTable` object as illustrated in the following sample of code.

```
if (__elt.edgePermutation( i ).value()==IDENTITY)
  M_doftable->M_locglob_signs[ie][lc] = 1;
else if (__elt.edgePermutation( i ).value()==REVERSE_PERMUTATION)
  M_doftable->M_locglob_signs[ie][lc] = -1;
```

All key ingredients of finite element implementation have now been introduced. The next sections focus on the three finite element type considered in Chapter 1.

5.2 Lagrange finite elements

The Lagrange finite elements are tuples $\left(K, \mathcal{L}_k, \Sigma_K^L\right)$ (see Section 1.1).

Primal space The primal space $\mathcal{L}_k$ is the set of polynomials of degree less than k. We remind that the $X_\mathcal{N}$ ingredients are contained in an object of type `PolynomialSet`. The object `OrthonormalPolynomialSet` defining $\mathcal{L}_k$ derives from `PolynomialSet` to which the orthonormality condition is added. The Dubiner polynomials are used as the basis of the primal space.

```
class OrthonormalPolynomialSet<Dim, Order, [...] >
    :
    public PolynomialSet<Dubiner<Dim, Order, Scalar, [...] >,
                         PolySetType >
```

The `Dubiner` class gives access to the set of Dubiner polynomials, to build the primal basis. As $\mathcal{B}$ is simply composed of Dubiner polynomials, the coefficients in this basis are set to identity.

```
OrthonormalPolynomialSet()
    :
    super( Dubiner<Dim, RealDim, Order [...] >() )
{
    this->setCoefficient( m );// m is identity
}
```

Dual space The dual space Σ_K^L (1.15) is the set of linear functionals which correspond to the evaluation of the polynomials of $\mathcal{L}_K$ at interpolation points. In practice, this functional set is built from the class `PointsEvaluation`, which computes the coefficients of its elements in the primal basis. The class `LagrangeDual` implements the building of the corresponding dual space.

```
template<typename Basis, // primal basis type
         template< [...] > class PointSetType>
class LagrangeDual
{
  // Compute functionals σ_i on set of points M_pts
  M_fset.setFunctionalSet(PointsEvaluation<[...]>( primal,__pts ));
}
```

The primal and dual spaces we just built are given to the main class `Lagrange`, defined from `FiniteElement`.

```
class Lagrange
  :
  public FiniteElement<OrthonormalPolynomialSet<Dim, Order, [...]>,
                       LagrangeDual,
                       Pts >
```

Interpolant The interpolant for Lagrange finite elements simply consists in the evaluation of the concerned expression on points. Its definition resides in the `interpolate` function embedded to the dedicated class. The following sample of code illustrates the filling of the local interpolant `IhLoc` to be assigned to each geometrical element K.

```
template<typename ExprType>
void
interpolate( ExprType& expr, local_interpolant_type& Ihloc ) const
{
  for(int q=0; q<nLocalDof; ++q) // K dofs
    for(int c1=0; c1<M; ++c1) // vectorial components
      for(int c2=0; c2<N; ++c2) // matricial components
        Ihloc((c2+N*c1)*nLocalDof+q) = expr.evalq( c1, c2, q );
}
```

5.3 Raviart-Thomas finite elements

The section 1.2 introduces the Raviart-Thomas finite elements as tuples $\left(K, \mathcal{D}_k, \Sigma_K^{RT}\right)$ where k represents the polynomial order.

Primal space The primal space $\mathcal{D}_k$ (1.23) associated with Raviart-Thomas finite elements is a subspace of $[\mathbb{P}_{k+1}]^d$ consisting in the sum $\mathcal{D}_k = [\mathbb{P}_k]^d \oplus \mathbf{x}\mathbb{P}_k$.

The dedicated object `RaviartThomasPolynomialSet` derives from the definition of $[\mathbb{P}_{k+1}]^d$ handled by the class `OrthonormalPolynomialSet` introduced to define $\mathbb{P}_k$ for Lagrange primal space (see Section 5.2).

As for the Lagrange primal space $\mathbb{P}_k$ (Section 5.2), the definition of $[\mathbb{P}_{k+1}]^d$ is handled by the class `OrthonormalPolynomialSet`. The dedicated object `RaviartThomasPolynomialSet` naturally derives from this class.

```
class RaviartThomasPolynomialSet
    :
    public OrthonormalPolynomialSet<Dim, Order+1, Vectorial,[...]>
```

The primal space $\mathcal{D}_k$ is built as the sum of $[\mathbb{P}_k]^d$ – built from the $dim(\mathbb{P}_k)$ first terms of $[\mathbb{P}_{k+1}]^d$ basis – and $\mathbf{x}\mathbb{P}_k$ – where $\mathbb{P}_k$ is obtained from the $\mathbb{P}_{k+1}$ basis functions. The sum is performed using a Singular Value Decomposition embedded in the `unite` function.

```
RaviartThomasPolynomialSet()
{
  Pkp1_s_type Pkp1; // P_{k+1}
  Pkp1_v_type Pkp1_v; // [P_{k+1}]^d
  vectorial_type Pk_v(Pkp1_v.polynomialsUpToDimension(dim_Pk));
  scalar_type Pk(Pkp1.polynomialsUpToDimension(dim_Pk));
  // xPk ← x P_k
  this->setCoefficient( unite( Pk_v, xPk ).coeff(), true );
}
```

Dual space The dual space Σ_K^{RT} is composed by face located degrees of freedom $\{\sigma_f\}_{f\in\mathcal{F}_h}$ at lowest order, completed by degrees of freedom $\{\sigma_K\}_{K\in\mathcal{T}_h}$ on elements. For now, only lowest order degrees of freedom are available in `Feel++` for these elements. We will hence restrict ourselves to the lowest order, even though the implementation of high order Raviart-Thomas elements is currently in progress.

The corresponding degrees of freedom (1.24) consist in the integral of the normal component on faces. In practice, we instead perform ponctual computations to approach these integrals. This is handled by the class `DirectionalComponentPointsEvaluation`, whose constructor needs the unit normal besides the primal space definition. The points `M_pts_per_face` – on which the functionals $\{\sigma_f\}_{f\in\mathcal{F}_h}$ are evaluated – are local to the current face `e`.

```
RaviartThomasDual( primal_space_type const& primal )
{
  // Iterates on faces of K̂
  auto it = M_convex_ref.entityRange( nDim-1 );
  typedef DirectionalComponentPointsEvaluation<[...]> dcpe_type;
  for (int e=it.begin();e!=it.end();++e )
  {
    node_type dir = M_convex_ref.normal( e ); // Normal
    // Compute σ_f(u)
    dcpe_type __dcpe( primal, dir, M_pts_per_face[e] );
    // Complete the functional set
    copy(__dcpe.begin(),__dcpe.end(), back_inserter(fset));
  }
  M_fset.setFunctionalSet( fset );
}
```

The `RaviartThomas` class also derives from the `FiniteElement` object. It needs *(i)* the primal space $\mathcal{D}_k$ embedded in `RaviartThomasPolynomialSet`, and *(ii)* the set of functionals Σ_K^{RT} contained by `RaviartThomasDual`.

```
class RaviartThomas
  :
  public FiniteElement<RaviartThomasPolynomialSet<Dim, Order, [...]>,
                       RaviartThomasDual,
                       PointSetEquiSpaced >
```

Interpolant In a silimar way to Lagrange (Section 5.2), the function `interpolate` fills the locate interpolant `IhLoc` from the interpolant operator $\Pi_{\mathcal{D}_k}$ (1.39).

The evaluation of the integral of the normal component is computed as the sum of its evaluation on local interpolation points.

To this end, we need access to the normal of each faces. The function `faceNormal` is used to this purpose. The next code illustrates the implementation of the `interpolate` function.

```
template<typename ExprType>
void
interpolate( ExprType& expr, local_interpolant_type& Ihloc ) const
{
  for( int f = 0; f < convex_type::numTopologicalFaces; ++f )
  {
    expr.geom()->faceNormal( f, n, true ); // n : normal of face f
    for (int l=0; l<nLocalDof; ++l ) // K dofs
    {
      for(int c1=0; c1<M; ++c1 ) // K components
        Ihloc(f*nLocalDof+l)+=expr.evalq(c1,0,f*nLocalDof+l )*n(c1);
    }
  }
}
```

Piola transformation The class `Context` contains as member `M_phi` the geometrical transformation ϕ_K^{geo} to be applied on reference finite element basis functions. As mentioned in Chapter 1, this transformation doesn't naturally preserve the properties of H_{div} function space and has to be combined with the so-called Piola transform. The Raviart-Thomas Piola transformation introduced by (1.41) then has to be embedded updating this variable member.

```
void
PolynomialSet<[...]>::Context< [...] >::
update( geometric_mapping_context_ptrtype const& __gmc, [...] )
{
  for (uint16_type ii=0; ii<I; ++ii) //Reference dofs
  {
    for (uint16_type q=0; q<Q; ++q)
    {
      // phi_K^geo <- 1/|grad phi_K^geo| grad phi_K^geo
      M_phi[ii][q].noalias() = K*(*M_pc)->phi(ii,q); // K : grad phi_K^geo
      M_phi[ii][q] /= gmc->J(q); // J : |grad phi_K^geo|
    }
  }[...]
}
```

5.4 Nédélec finite elements

The last component required to support the De-Rham sequence are the H_{curl}-conforming elements. This section describes the implementation of the Nédélec finite elements of first kind describes in Section 1.3.1 as the tuples $(K, \mathcal{R}^{k,1}, \Sigma_k^{Ned,1})$ where k is the polynomial order.

Primal space The primal space $\mathcal{R}^{k,1}$ to be considered for Nédélec elements of first kind is – as for Raviart-Thomas – a subspace of $[\mathbb{P}_{k+1}]^d$.

Thus, the class `NedelecPolynomialSet` also derives from the definition of $[\mathbb{P}_{k+1}]^d$ handled by `OrthonormalPolynomialSet`.

```
class NedelecPolynomialSet<Dim,Order,NedelecKind::NED1,[...]>
    :
    public OrthonormalPolynomialSet<Dim, Order+1, Vectorial,[...]>
```

$\mathcal{R}^{k,1}$ is defined as the sum of the vectorial polynomial spaces $[\mathbb{P}_k]^d$ and $\mathcal{S}^k$ (1.49). The building of such a space is performed in a similar way as the Raviart-Thomas primal space $\mathcal{D}_k$. Indeed, $\mathcal{S}^k$ reads as the product $(\nabla \times \hat{\mathbf{x}})\,\mathbb{P}_k$ from the remark (1.56).

```
NedelecPolynomialSet()
{
  Pkp1_s_type Pkp1; // P_{k+1}
  Pkp1_v_type Pkp1_v; // [P_{k+1}]^d
  vectorial_type Pk_v(Pkp1_v.polynomialsUpToDimension(dim_Pk));
  scalar_type Pk (Pkp1.polynomialsUpToDimension(dim_Pk));
  // rxPk ← (∇ × x̂) P_k
  this->setCoefficient( unite( Pk_v, rxPk ).coeff(), true );
}
```

Dual space The set of linear functionals $\Sigma_k^{Ned,1}$ is composed of degrees of freedom on edges (at lowest polynomial order), on faces and on elements (at high order). As for H_{div}-conforming elements, the current implementation is limited to lowest order, that is with degrees of freedom located on edges only.

The edges degrees of freedom consists in the integrals of the tangential component, as introduced in (1.51) and (1.52). The principle is the same as for Raviart-Thomas dual space definition. But we give the tangential direction to `DirectionalComponentPointsEvaluation` instead of the normal.

```
NedelecDualFirstKind( primal_space_type const& primal )
{
  // Iterates on edges of K̂
  auto it = M_convex_ref.entityRange( (nDim== 2)?nDim-1:1 );
  typedef DirectionalComponentPointsEvaluation<[...]> dcpe_type;
  for (e=it.begin();e!=it.end();++e )
  {
    node_type dir= M_convex_ref.tangent(e); //Tangent
```

```
    // Compute σ_e(u)
    dcpe_type __dcpe( primal, dir, Gt );
    // Complete the functional set
    copy( __dcpe.begin(), __dcpe.end(), back_inserter(fset));

  }
}
```

As for the previous two cases, the dedicated class `Nedelec` is built from the `FiniteElement` object. We use the primal space `NedelecPolynomialSet` and the set of degrees of freedom embedded in `NedelecDualFirstKind`.

```
class Nedelec
  :
  public FiniteElement<NedelecPolynomialSet<Dim, Order, [...]>,
                       NedelecDualFirstKind,
                       PointSetEquiSpaced >
```

Interpolant As other finite element kind, Nedelec defines its own `interpolate` functions filling the local interpolant `IhLoc` as the integral of the tangential component of the considered expression.

The implementation is very similar to Raviart-Thomas interpolant where the tangent along edges replaces the normal of faces.

```
template<typename ExprType>
void
interpolate( ExprType& expr, local_interpolant_type& Ihloc ) const
{
  for( int e = 0; e < convex_type::numEdges; ++e )
  {
    expr.geom()->edgeTangent(e, t, true); // t : tangent of edge e
    for (int l=0; l<nDofPerEdge; ++l)
    {
      for(int c1=0; c1<M; ++c1)
        Ihloc(e*nDofPerEdge+l)+=expr.evalq(c1,0,e*nDofPerEdge+l)*t(c1);
    }
  }
}
```

Piola transformation As for Raviart-Thomas (Section 5.3), the geometrical transformation ϕ_K^{geo} from reference element to real one doesn't allow to preserve the H_{curl} function space properties.

The application of the Nédélec Piola transform (1.71) which ensures that interpolated values remains in H_{curl}, consists as previously in updating the member variable `M_phi` of the `Context` class.

```
void
PolynomialSet<[...]>::Context< [...] >::
update( geometric_mapping_context_ptrtype const& __gmc, [...] )
{
  for (uint16_type ii=0; ii<I; ++ii) //Reference dofs
  {
    for (uint16_type q=0; q<Q; ++q)
    {
      // phi_K^geo <- grad phi_K^{geo-T}
      M_phi[ii][q].noalias() = Bt*(*M_pc)->phi(ii,q); //Bt : phi_K^{geo-T}
    }
  }[...]
}
```

Conclusion

Needed in the context of the magnetostatic model development, the implementation of lowest order H_{div} and H_{curl} conforming finite elements completes the De Rham sequence in Feel++. The implementation described in this chapter offers the possibility to work with discrete subspace of H_{div} and H_{curl} in addition to H_1.

The flexibility of the Feel++ language and the genericity of its implementation eases the definition of these discrete spaces.

```
auto H1 = Pch<k>(mesh) //H_1 based on Lagrange
auto Hcurl = Nh<k=0>(mesh) //H_curl based on Nedelec
auto Hdiv = Dh<k=0>(mesh) //H_div based on Raviart-Thomas
auto L2 = Pdh<0>(mesh) //L_2 based on Lagrange (P_0 discontinuous)
```

The main differential operators gradient, curl and divergence are simply defined as relating the previous spaces

```
Igrad = Grad( _domainSpace=H1, _imageSpace=Hcurl);
Icurl = Curl( _domainSpace=Hcurl, _imageSpace=Hdiv);
Idiv = Div( _domainSpace=Hdiv, _imageSpace=L2);

u = H1->element();
auto grad_u = Igrad( u );
```

which allows to fully support the De Rham diagram within the library

$$\mathbb{R} \xrightarrow{id} \texttt{H1} \xrightarrow{\texttt{Igrad}} \texttt{Hcurl} \xrightarrow{\texttt{Icurl}} \texttt{Hdiv} \xrightarrow{\texttt{Idiv}} \texttt{L2}$$

Table 5.1 – De Rham diagram in now fully supported in Feel++

As the implementation of these finite element types as new features, elementary tests has been developed to ensure its validity. These tests, carried out regularly, checks the basis functions definition and the interpolant, but also on their use on toy problems.

Further developments quite naturally aims to the implementation of the high order H_{div} and H_{curl} conforming finite elements. Other kinds of finite element can also be investigated, such as Brezzi-Doublas-Marini (BDM) or Nédélec elements of second type.

Chapter 6

Parallel algorithm for Biot & Savart

The Biot & Savart's law allows to compute the magnetic field (see Section 3.3). To avoid dealing with the singularity of this method – due to the definition of the underlying Green function –, we restrict the use of this formula to a region without current. Typically, the considered region is the zone of interest for researchers.

In high field magnets context, the complexity of the considered geometries requires to pay a particular attention on the efficiency of the associated model. The computation of the magnetic induction $\mathbf{B}$ (3.82) and the magnetic potential $\mathbf{A}$ (3.81) requires the knowledge of the whole Ω_{cond} by each $\mathbf{r} \in \Omega_{mgn}$, Ω_{cond} and Ω_{mgn} being respectively the current conductor and the region on which $\mathbf{B}$ and $\mathbf{A}$ are computed. The parallel computation of (3.82) and (3.81) supposes the partitioning of $\Omega = \Omega_{cond} \cup \Omega_{mgn}$, distributed on a set of processors, which conflicts with the previous requirement.

To deal with this issue, we propose a parallel algorithm dedicated to the Biot & Savart law application, aiming to establish a smart communication strategy between processors. In the literature, we found various ways to compute the magnetic field through Biot & Savart's law. The low-rank approximation [White et al., 2006] consists of a low-dimensional approximation of the matricial system mimicking the Biot & Savart's calculation on a large set of points. We find also multipole expansion techniques [Sabariego et al., 2006].

The proposed development is an original contribution to our knowledge. In this chapter, we detail the design of our parallel algorithm. The last two parts focus on the performances of the algorithm, through numerical experiments on a supercomputer.

Contents

Let's denote $\{p_k\}_{k=1}^n$ the set of n processors, and Ω_{p_k} the subdomain associated with the processors p_k with $1 \leqslant k \leqslant n$. As displayed in Figure 6.1, the partitionning of Ω leads to $\Omega_{cond} = \bigcup_i \Omega^i_{cond}$ and $\Omega_{mgn} = \bigcup_j \Omega^j_{cond}$. Since the partitioning is performed in such a way that the work load is equidistributed, each partition Ω_{p_k} could be *(i)* only composed of Ω_{cond} points as $\Omega_{p_k} = \Omega^i_{cond}$ *(ii)* only composed of Ω_{mgn} points as $\Omega_{p_k} = \Omega^i_{mgn}$ *(ii)* composed of both Ω_{cond} and Ω_{mgn} points as $\Omega_{p_k} = \Omega^i_{cond} \cup \Omega^j_{mgn}$.

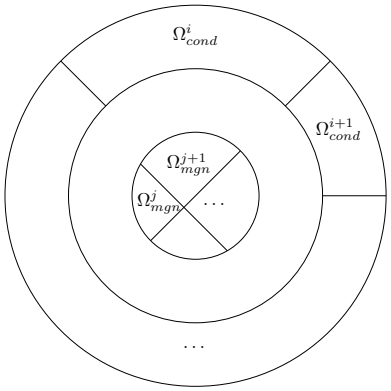

Figure 6.1 – Repartition of subdomains

6.1 Classification of processors

The first step of the proposed algorithm provides a ranking of the processors, depending on their partition Ω_{p_k}. We distinguish the processors owning points of Ω_{mgn}, from the ones owning points of Ω_{cond}. Locally assigned to each processor, the vector `isIn[ ]` owns this information through two integers. The first component `isIn[0]` focuses on Ω_{cond} while the second one `isIn[1]` focuses on Ω_{mgn}.

Step 1 Processors classification

if proc has dofs in Ω_{cond} **then**
  isIn[0] = 1
end if
if proc has dofs in Ω_{mgn} **then**
  isIn[1] = 1
end if

▷ isIn[ ] = [(proc has dofs in Ω_{cond}), (proc has dofs in Ω_{mgn})]

Readily available with `Feel++`, the number of degrees of freedom associated with the function space allows to easily perform this step 1.

Listing 6.1 – Processors classification

```
if( Xh_cond_global->nLocalDof()  > 0 )
  isIn[0] = 1;
if( Xh_box_global->nLocalDof() > 0 )
  isIn[1] = 1;
```

Once locally established, the ranking of processors from their degrees of freedom localization has to be shared by all processors. To this end, the previous local arrays `isIn[ ]` are gathered into one global array `isInGlob[ ]`. This is the step 2.

Step 2 Localization gathering

ALL_GATHER(worldcomm, isIn.data(), isInGlob)

In `Feel++`, the parallel communications are handled by the `Boost::mpi` [Boost, 2008] library.

Listing 6.2 – Localization gathering

```
std::vector<int> isInGlob(2*Environment::worldComm().size());
mpi::all_gather(Environment::worldComm(),isIn.data(),2,isInGlob);
```

At this point, the information is known by all the processors of the global communicators through an array illustrated in Table 6.1.

p_1		...	p_i		...	p_n	
$\Omega_{p_1} \subset \Omega_{cond}$	$\Omega_{p_1} \subset \Omega_{mgn}$	...	$\Omega_{p_i} \subset \Omega_{cond}$	$\Omega_{p_i} \subset \Omega_{mgn}$	...	$\Omega_{p_n} \subset \Omega_{cond}$	$\Omega_{p_n} \subset \Omega_{mgn}$

Table 6.1 – Global localization table

6.2 Sub-communicators

The computation of $\mathbf{B}(\mathbf{r})$ and $\mathbf{A}(\mathbf{r})$ through Biot & Savart's law involves the knowledge of the concerned $\mathbf{r} \in \Omega_{mgn}$ and all $\mathbf{r}' \in \Omega_{cond}$. The processor owning $\mathbf{r} \in \Omega_{mgn}$ has to communicate with all processors having degrees of freedom in Ω_{cond}. The communication strategy we propose is based on the definition of subcommunicators. Each of these communication group (Figure 6.2) is composed of one processor having degrees of freedom in Ω_{mgn}, plus all processors having dofs on Ω_{cond}. That amounts to consider as many subcommunicators as processors having degrees of freedom in Ω_{mgn}.

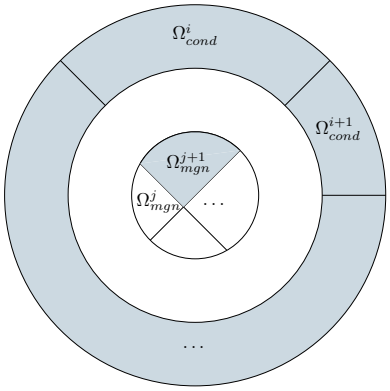

Figure 6.2 – Sub-communicators

For each of these groups, the coordinates of all $\mathbf{r} \in \Omega^i_{mgn}$ are sent to all processors forming Ω_{cond}, allowing them to compute the integrals. From an algorithmic point of view, this corresponds to a broadcast operation from the processor of rank zero which

owns points of Ω^j_{mgn}, to the whole set of processors which compose the rest of the group. This operation (Figure 6.3) uses the standard MPI `broadcast` function (step 3).

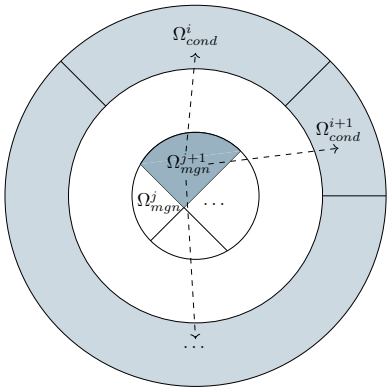

Figure 6.3 – Broadcast operation

Step 3 Broadcast : Ω^j_{mgn} to $\{\Omega_{cond}\}_i$

```
if processor has rank 0 (Ω^j_mgn) then
    dofM = [set of Ω^j_mgn dofs]
end if
BROADCAST(subcomm, dofM.data(), 2, 0)
```

6.3 Integral computation

As soon as the data of Ω^j_{mgn} has been received by processors composing $\Omega_{cond} = \bigcup_i \Omega^i_{cond}$, the latter computes their contribution $A_i(r)$ and $B_i(r)$ for magnetic potential $\mathbf{A}$ and magnetic field $\mathbf{B}$ defined as

$$A_i(\mathbf{r}) = \frac{\mu_0}{4\pi} \int_{\Omega^i_{cond}} \frac{\mathbf{j}(\mathbf{r}')}{\mid \mathbf{r} - \mathbf{r}' \mid} d\mathbf{r}', \qquad B_i(\mathbf{r}) = \frac{\mu_0}{4\pi} \int_{\Omega^i_{cond}} \frac{\mathbf{j}(\mathbf{r}') \wedge (\mathbf{r} - \mathbf{r}')}{\mid \mathbf{r} - \mathbf{r}' \mid^3} d\mathbf{r}' \quad \mathbf{r} \in \Omega^j_{mgn}$$

All are stored into an array `intM[ ]`, in order to ease the sum of these contributions. This is the step 4.

Step 4 Integral computation : $A(\mathbf{r})$, $B(\mathbf{r})$ with $\mathbf{r} \in \Omega^i_{mgn}$

```
if isIn[0] == 1 (Ω_{p_k} ⊂ Ω_cond) then
    for d = 0 to d =size of dofM (r ∈ Ω^j_mgn) do
        intM[2d]   = ∫_{Ω^i_cond} (μ0/4π) j/|r−r'|        ▷ Magnetic potential
        intM[2d+1] = ∫_{Ω^i_cond} (μ0/4π) j∧(r−r')/|r−r'|^3   ▷ Magnetic field
    end for
end if
```

6.4 Reduction operation

Once the local contributions are computed, the integrals (3.82) and (3.81) may be deduced from the reduction operation illustrated by Figure 6.4.

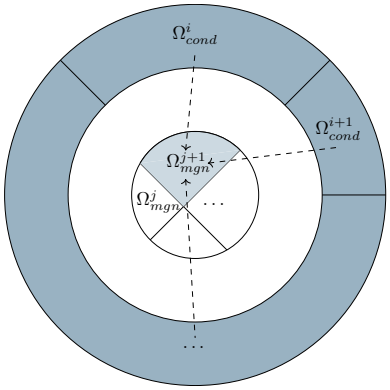

Figure 6.4 – Reduction operation

The reduction operation consists of the sum of the local arrays `intM[ ]`, filled by the processors owning Ω_{cond}. The result of this operation is sent to processor of rank zero – related with Ω^{j}_{mgn} – allowing its degrees of freedom to be assigned with the corresponding values.

Step 5 Reduction : $A(\mathbf{r}) = \sum_j A_j(\mathbf{r}),\ B(\mathbf{r}) = \sum_j B_j(\mathbf{r})$

```
REDUCE(subcomm,intM.data(),intM.size(),plus<double>(), 0)
if processor has rank 0 (Ω^j_mgn) then
    for d = 0 to d =size of dofM (∀ r ∈ Ω^j_mgn) do
        A(r) ← intMsum[2 * d]
        B(r) ← intMsum[2 * d + 1]
    end for
end if
```

Processed one after the other, each considered subcommunicator follows the similar procedure.

6.5 Scalability analysis on a real magnet

The first validation of the sequential Biot & Savart's law implementation was presented in Section 3.3 (figures 3.17a and 3.17b). This section details the validation of its parallel version on a more complex geometry.

Let's consider Ω_{cond} the innermost helix of a magnet insert, into which Ω_{mgn} consists of a centered thin cylinder oriented along the vertical axis. In this use, the current density in the magnet Ω_{cond} is not known analytically. Therefore, it is obtained from the previously described electro-thermal model (see Section 3.1).

Figure 6.5 displays the computed current density $\mathbf{j}$ in Ω_{cond}, while the cylinder cor-

responding to Ω_{mgn} is colored from the parallely computed magnetic field values. This simulation has been carried out on a mesh composed of 333005 nodes, forming $1.7 \cdot 10^6$ tetrahedrons. Composed of 24 subdomains, the partitionning is such that the domain Ω_{mgn} – itself composed of 1730 nodes – is owned by a unique processor.

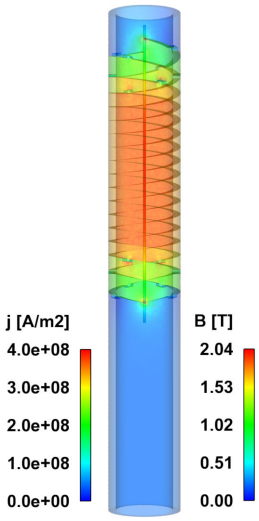

Figure 6.5 – Innermost helix with $\mathbf{j}$ obtained from $I = 29974A$

Commonly used as quantity of interest, we introduce the homogeneity defined as

$$h = \frac{B_z - B_z(0)}{B_z(0)} \tag{6.1}$$

where B_z is the vertical component of the magnetic field.

Let's denote h_{3D} (resp. h_{axi}) the homogeneity (6.1) obtained from the 3D parallel Biot & Savart's algorithm (resp. from the existing 2D axisymmetrical one). Figure 6.6a compares the resulting values of homogeneity, while Figure 6.6b plots the difference between 3D and 2D axisymmetrical results.

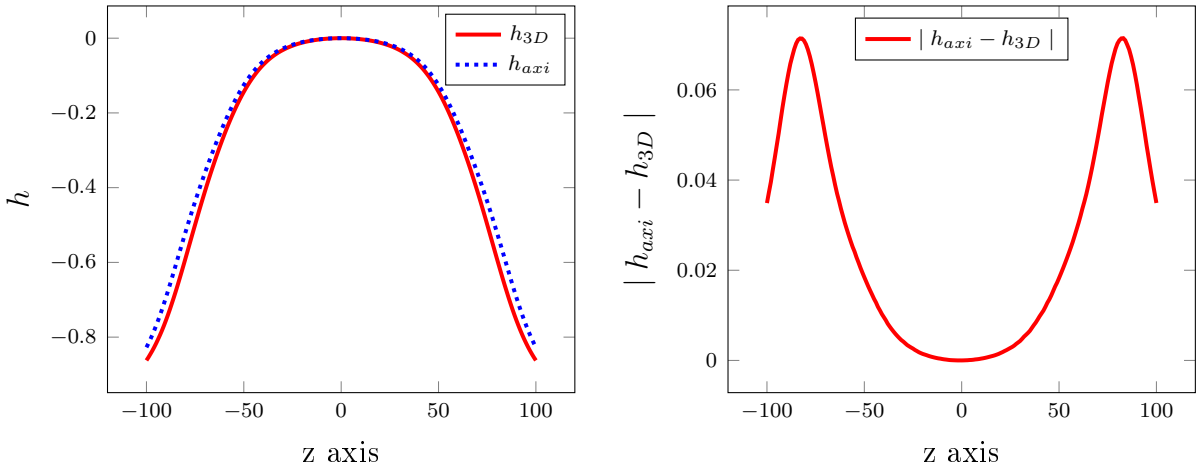

(a) Homogeneity along z axis at $r = 0$ (b) Difference on homogeneity

Figure 6.6 – Innermost helix

Figure 6.6 confirms that the two models are coherent. However, Figure 6.6b emphasizes on the difference between the models. The maximum difference is observed in the regions near the end of the helical cut.

Besides the validation, the setup of this simulation is used to assess the performances of the proposed algorithm. Simulations were run on various number of processors to this purpose, on Curie supercomputer (TGCC,France).

With n times more processors, a linear scaling supposes a gain of a factor n in terms of computational time. Considering a reference number of processors n_{ref} and its associated reference time t_{ref}, we define the scaling efficiency as

$$\frac{t_{ref} * n_{ref}}{t * n} \tag{6.2}$$

Table 6.2 gives the scaling efficiency (6.2) on various number of processors.

nb procs	total time (s)	scaling efficiency
48	$1.4 \cdot 10^4$	1
96	$7.05 \cdot 10^3$	0.99
144	$4.98 \cdot 10^3$	0.93
192	$4.31 \cdot 10^3$	0.81

Table 6.2 – Scalability analysis

We observe that the speed-up (Figure 6.7) is ideal up to 100 processors, and that it deteriorates with higher number of processors.

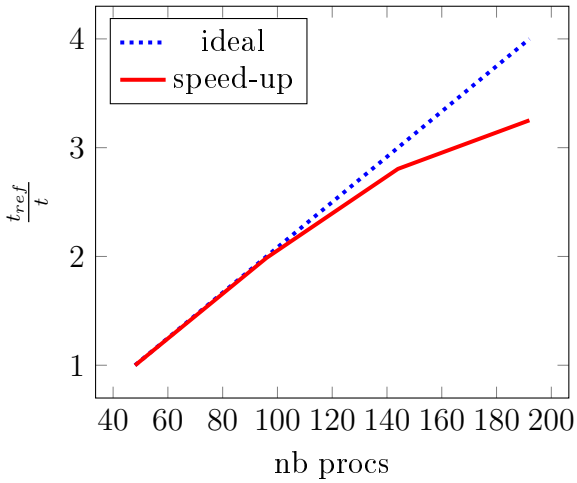

Figure 6.7 – Speed-up

To better understand, Table 6.3 shows the repartition of the total time. As expected, the computation of the integrals is the most costly operation. The cost of the broadcast operation logically increases with the size of the global communicator, since the number of processors sharing Ω_{cond} increases, which make the number of communications increase.

nb procs	broadcast dofs (s)	integrals (s)	reduction (s)
96	$2.40 \cdot 10^{-1}$	$6.89 \cdot 10^{3}$	$1.44 \cdot 10^{-4}$
144	$3.14 \cdot 10^{-1}$	$4.84 \cdot 10^{3}$	$2.63 \cdot 10^{-4}$
192	$4.32 \cdot 10^{-1}$	$4.04 \cdot 10^{3}$	$1.59 \cdot 10^{-4}$

Table 6.3 – Scalability analysis : details

The number of integrals to compute is 1.7 millions of tetras $\times$ 1730 points for which we evaluate the magnetic field $\times$ 3 components. Given this number of integrals, Table 6.4 gives the computational time needed per integral, obtained from Table 6.3.

nb procs	time for one integrals (s)
96	$7.81 \cdot 10^{-7}$
144	$5.48 \cdot 10^{-7}$
192	$4.58 \cdot 10^{-7}$

Table 6.4 – Scalability analysis : time per integral

The time per integral decreases when we increase the number of processors. Nevertheless, we see that the integrals computation doesn't scale well up to 100 processors. Which explains the speed-up results displayed in Figure 6.7.

6.6 Optimization of integrals computation

The important computational cost related with the magnetic field computation resides in the number of integrals to compute, even though the time needed by integral remains reasonable.

The numerical integration requires the setting up of various ingredients within the implementation. For each integral, we need to compute the geometrical transformation and the interpolants for each point of the domain on which we integrate, namely Ω_{cond}. This is what was done in the initial version of our parallel algorithm.

However, the domain Ω_{cond} – and its subdomains Ω^i_{cond} distributed among the processors – remains the same all along the computation. The geometrical transformation and the interpolants associated with its points could then be computed once.

The proposed optimization hence consists in defining the integral as a operator, which consider the whole set of points $\mathbf{r} \in \Omega^j_{mgn}$, for each partition Ω^j_{mgn} of Ω_{mgn}. By this way, we benefit from the computation of the geometrical transformation and the interpolants of all $\mathbf{r}' \in \Omega^i_{cond}$, for all the integral computations of Ω^j_{mgn}.

Table 6.5 displays the computational time necessary to compute the whole set of integrals, to be compared with Table 6.3. The second column of Table 6.5 displays the corresponding gain factor, which exceeds 300.

nb procs	integrals (s)	gain factor
48	$4.04 \cdot 10^1$	.
96	$2.07 \cdot 10^1$	332.8
144	$1.38 \cdot 10^1$	350.7
192	$1.03 \cdot 10^1$	392.2

Table 6.5 – Integrals computation : time needed

The impact of this change on the scalability of our algorithm is clearly seen on Figure 6.8. Now, the speed up is ideal whatever the number of processors, contrary to what was observed in Figure 6.7.

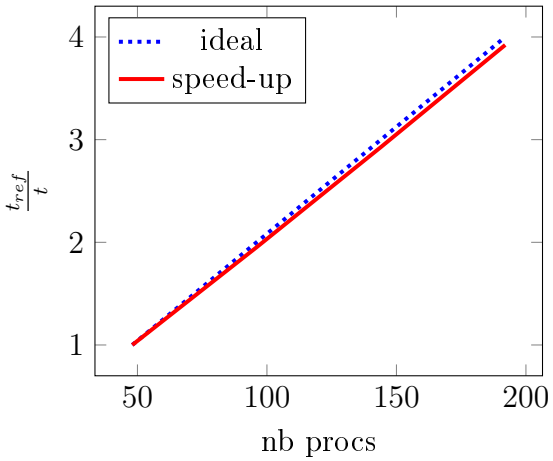

Figure 6.8 – Integrals computation : Speed-up

Regarding the detail of the time consumption for each step of the algorithm displayed in Table 6.6, most of the time is still spent within the integrals computation. Nevertheless, the required computational time is reduced with a 10^2 factor thanks to the proposed optimization. The time required by broadcast and reduction operations remains similar to the previous runs (see Table 6.3).

nb procs	broadcast dofs (s)	integrals (s)	reduction (s)
96	$2.39 \cdot 10^{-1}$	$2.07 \cdot 10^1$	$1.43 \cdot 10^{-4}$
144	$3.07 \cdot 10^{-1}$	$1.38 \cdot 10^1$	$1.25 \cdot 10^{-4}$
192	$4.24 \cdot 10^{-1}$	$1.03 \cdot 10^1$	$1.42 \cdot 10^{-4}$

Table 6.6 – Scalability analysis : details

Conclusion

In this chapter, we detail the parallel implementation of the Biot & Savart's law introduced in Section 3.3. From its definition, this formulation is not readily parallelizable and requires to smartly handle the communications between processors.

The proposed parallel algorithm represents, to our knowledge, an original contribution in this context. Illustrated on a real magnet geometry, the performances of this algorithm prove its relevance on large problems, as well as its scalability in HPC context.

Chapter 7

SER in the Reduced Basis framework

The reduced basis method detailed in Chapter 2 consists in a Galerkin projection on a low-dimensional space, spanned by finite element approximations. This method relies on the availability of an affine decomposition of the considered problem, which then allows to develop an offline/online strategy. The `Feel++` library offers a reduced basis framework providing an interface to which the specification of the model are passed (Figure 7.1).

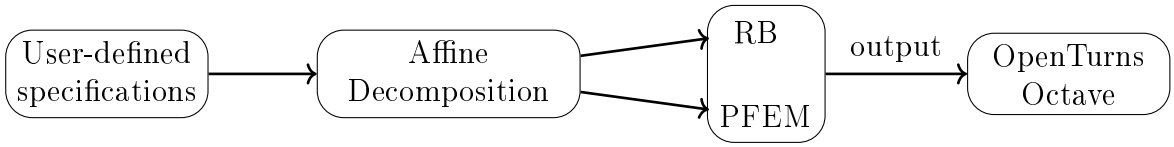

Figure 7.1 – `Feel++` Reduced Basis framework

From the mesh and the PDE together with its affine decomposition, the reduced basis framework builds seamlessly the RB approximation space W_N, and performs the precomputations consisting in the offline stage. Once W_N is computed and stored, the coming reduced basis approximation $u_N(\boldsymbol{\mu}) \in W_N$ can be evaluated, for any given $\boldsymbol{\mu}$ leading to the output computation.

As illustrated in Figure 7.1, the resulting input/output relation can be provided to external libraries such as `Octave` or `Openturns` [Dutfoy et al., 2009], for further studies such as sensitivity analysis (see Chapter 8). The `Feel++` RB framework covers a large range of problems, from linear elliptic to parabolic non-linear ones, and also provides error estimators. Further details can be found in [Daversin et al., 2013] or [Veys, 2014].

The Empirical Interpolation Method (EIM) introduced in Section 2.1 is available in the framework, allowing to tackle non-affinely parametrized problems. This method is employed prior to the reduced basis methodology (Figure 7.2), in order to recover the affine decomposition when it is not readily available.

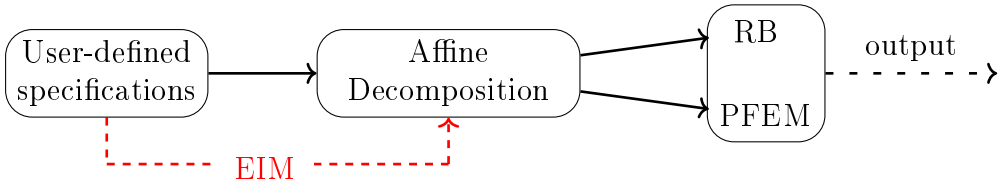

Figure 7.2 – `Feel++` RB framework for non-affinely parametrized problem

In Section 2.3, we introduced the possibility to build alternately the EIM and RB approximation spaces making the EIM offline stage more efficient. As illustrated in Figure 7.3, the so-called SER method consists in using solely RB approximations in the EIM algorithm.

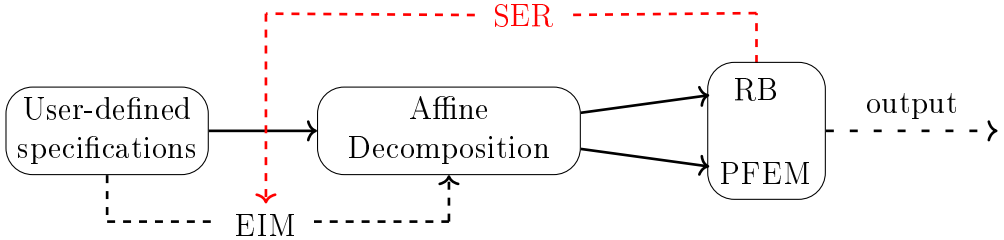

Figure 7.3 – SER in the `Feel++` RB framework

This method provides a good trade-off between the results accuracy and the computational budget, since the number of finite elements approximation is greatly reduced.

The SER method is presently available into the `Feel++` library. This section details its implementation within the RB framework.

First of all, we start with a brief description of the existing components on which this implementation is based. The next part then focuses on their use within SER, and on the changes to be made to set up the method. The changes related to the investigated variants of SER introduced in Section 2.3.2 are as well presented in the last part.

Contents

7.1 Preliminaries

Let's remind that SER applies in the context of non-linear and non-affinely parametrized problems. Based on these considerations, the standard reduced basis methodology combined with the empirical interpolation method – used to deal with the non-affine dependence on parameters – is described in Section 2.2.

First, let's start with an illustration of the method described in Section 2.2 from an algorithmic point of view. To deal with the non-linearity, the computation of the reduced basis functions at the offline stage, as well as the resolution of the online reduced system, are based on the Picard's method.

Keeping the same notations as in Section 2.2, the algorithm 6 (resp. 7) illustrates the steps needed to perform these offline (resp. online) resolutions.

The online stage remains unchanged within the SER algorithm. Indeed, it simply consists in applying the algorithm 7 for each considered parameter $\boldsymbol{\mu}$. The function de-

scribed in the algorithm 6 is used to build each basis functions which compose the RB approximation space. These functions are at the root of the changes to be made in the offline stage to implement the SER method introduced in Section 2.3.

Algorithm 6 Offline fixed point : compute finite element solution $u_{\mathcal{N}}(\boldsymbol{\mu})$

function OFFLINEFIXEDPOINT($\boldsymbol{\mu}$, $\{a_m^q\}_{q,m}$, $\{a^l\}_l$, $\{f_m^q\}_{q,m}$, $\{f^l\}_l$)
  ${}^0u_{\mathcal{N}} \leftarrow$ initialGuess($\boldsymbol{\mu}$), $k \leftarrow 0$
  while $k <$ nbIterMax **and** increment $>$ tolerance **do**
    Compute $\gamma_{a,m}^q({}^k u_{\mathcal{N}}(\boldsymbol{\mu});\boldsymbol{\mu})$, $\theta_a^l(\boldsymbol{\mu})$, $\gamma_{f,m}^q({}^k u_{\mathcal{N}}(\boldsymbol{\mu});\boldsymbol{\mu})$, $\theta_f^l(\boldsymbol{\mu})$
    $\mathcal{A}^{\mathcal{N}} \leftarrow \sum_{q=1}^{Q_a^{eim}} \sum_{m=1}^{M_q^a} \gamma_{a,m}^q({}^k u_{\mathcal{N}};\boldsymbol{\mu}) a_m^q + \sum_{l=1}^{Q_a^{aff}} \theta_a^l(\boldsymbol{\mu}) a^l$
    $\mathcal{F}^{\mathcal{N}} \leftarrow \sum_{q=1}^{Q_f^{eim}} \sum_{m=1}^{M_q^f} \gamma_{f,m}^q({}^k u;\boldsymbol{\mu}) f_m^q + \sum_{l=1}^{Q_f^{aff}} \theta_f^l(\boldsymbol{\mu}) f^l$
    ${}^{k+1}u_{\mathcal{N}}(\boldsymbol{\mu}) \leftarrow solve(\mathcal{A}^{\mathcal{N}}\ {}^{k+1}u_{\mathcal{N}}(\boldsymbol{\mu}) = \mathcal{F}^{\mathcal{N}})$
    increment $\leftarrow \| {}^{k+1}u_{\mathcal{N}}(\boldsymbol{\mu}) - {}^k u_{\mathcal{N}} \|$
  end while
  $u_{\mathcal{N}}(\boldsymbol{\mu}) \leftarrow {}^{k+1}u_{\mathcal{N}}(\boldsymbol{\mu})$
end function

Algorithm 7 Online fixed point : compute reduced basis approximation $u_N(\boldsymbol{\mu})$

function ONLINEFIXEDPOINT($\boldsymbol{\mu}$, N, $\{a_m^q\}_{q,m}$, $\{a^l\}_l$, $\{f_m^q\}_{q,m}$, $\{f^l\}_l$)
  ${}^0u_N \leftarrow$ initialGuess($\boldsymbol{\mu}$), $k \leftarrow 0$
  while $k <$ nbIterMax **and** increment $>$ tolerance **do**
    Compute $\gamma_{a,m}^q({}^k u_{\mathcal{N}}(\boldsymbol{\mu});\boldsymbol{\mu})$, $\theta_a^l(\boldsymbol{\mu})$, $\gamma_{f,m}^q({}^k u_{\mathcal{N}}(\boldsymbol{\mu});\boldsymbol{\mu})$, $\theta_f^l(\boldsymbol{\mu})$
    $\mathcal{A}^N = \sum_{q=1}^{Q_a^{eim}} \sum_{m=1}^{M_q^a} \gamma_{a,m}^q({}^k u^N,\boldsymbol{\mu}) A^{N,q,m} + \sum_{l=1}^{Q_a^{aff}} \theta_a^l(\boldsymbol{\mu}) A^{N,l}$
    $\mathcal{F}^N = \sum_{q=1}^{Q_f^{eim}} \sum_{m=1}^{M_q^f} \gamma_{f,m}^q({}^k u^N,\boldsymbol{\mu}) F^{N,q,m} + \sum_{l=1}^{Q_f^{aff}} \theta_f^l(\boldsymbol{\mu}) F^{N,l}$
    ${}^{k+1}u_N(\boldsymbol{\mu}) \leftarrow solve(\mathcal{A}^N\ {}^{k+1}u_N(\boldsymbol{\mu}) = \mathcal{F}^N)$
  end while
end function

From these considerations, the next sections provide the details about the implementation of the SER method within the `Feel++` reduced basis framework. We start with the initial version of SER, that is the alternate enrichment of the EIM and RB approximation spaces per groups of size r. The changes related to the investigated variants (see Section 2.3.2) are then described.

7.2 SER algorithm

The first stage of the SER method (Section 2.3) consists in the initialization of the EIM approximation space. The first rough EIM approximation resulting from this initialization

provides the first affine decomposition, allowing to apply the reduced basis methodology. The algorithm 8 illustrates this initialization step as the starting point of the method.

Algorithm 8 SER method : Initialization of SER offline step

for all non-affinely parametrized function w **do**
  $\bar{S}_1 \leftarrow \{\bar{\boldsymbol{\mu}}_1\}$ ▷ Choose $\bar{\boldsymbol{\mu}}_1$
  $\bar{\boldsymbol{\xi}}_1 \leftarrow w(u(\bar{\boldsymbol{\mu}}_1), \mathbf{x}; \bar{\boldsymbol{\mu}}_1) \quad \bar{W}_1 \leftarrow span\{\bar{\boldsymbol{\xi}}_1\}$
  $\boldsymbol{t}_1 \leftarrow arg\sup_{\mathbf{x}\in\Omega} |\bar{\boldsymbol{\xi}}_1(\mathbf{x})|$ ▷ Interpolation point
  $q_1 \leftarrow \frac{\bar{\boldsymbol{\xi}}_1(\mathbf{x})}{\bar{\boldsymbol{\xi}}_1(\boldsymbol{t}_1)}$ ▷ Deduce EIM basis
end for

At this step, EIM approximation for w reads $w_1(u(\boldsymbol{\mu}), \mathbf{x}; \boldsymbol{\mu}) = \beta_1^1(u(\boldsymbol{\mu}), \boldsymbol{\mu}) q_1(\mathbf{x})$
$\{a_1^q\}_q$ and $\{f_1^l\}_l$ terms are precomputed and stored (no dependence on $\boldsymbol{\mu}$)

$S_1 \leftarrow \{\boldsymbol{\mu}_1\}$
OfflineFixedPoint($\boldsymbol{\mu}_1$, $\{a_1^q\}_q$, $\{a^l\}_l$, $\{f_1^q\}_q$, $\{f^l\}_l$) ▷ Compute $u_{\mathcal{N}}(\boldsymbol{\mu}_1)$
$\boldsymbol{\xi}_1 \leftarrow orthonormalization(u_{\mathcal{N}}(\boldsymbol{\mu}_1))$ ▷ Gram-Schmitt orthonormalization
$W_1 \leftarrow span\{\boldsymbol{\xi}_1\}$ ▷ Deduce RB basis

Within the `Feel++` reduced basis framework, the algorithm 8 corresponds to *(i)* the EIM initialization step illustrated by 7.1 and *(ii)* the building of the first reduced basis function illustrated in 7.2. This step requires no change in the framework. It simply uses the existing functions.

Listing 7.1 – EIM initialization step

```
// ****** For each EIM approximations ******
// Pick the first parameter and add it to the parameter space
mu = M_model->parameterSpace()->max();
M_model->addParameter( mu );
// Solve the finite element problem and store the solution
solution = M_model->solve( mu );
M_model->addSolution( solution );
// Compute the interpolation point
auto t = M_model->computeMaximumOfExpression( mu , solution );
M_model->addInterpolationPoint( t );
// The first EIM basis function is the residual (w-0)
auto q = M_model->Residual(0);
// Enrich the EIM approximation space
M_model->addBasis( q );
```

Listing 7.2 – RB initialization step

```
// Compute affine decomposition from the rough EIM basis approx.
boost::tie( Mqm, Aqm, Fqm ) = M_model->computeAffineDecomposition();
// Solve the finite element non-linear problem
u = offlineFixedPointPrimal( mu );
// Enrich the RB approximation space
M_model->rBFunctionSpace()->addPrimalBasisElement( u );
```

Once this initialization step is performed, we have access to a first rough reduced basis approximation, which can be used within the EIM Greedy algorithm. The algorithm 9 summarizes the necessary steps for the simultaneous construction of r EIM and RB basis functions. It hence corresponds to the construction of a single group of basis functions between two affine decomposition updates.

Algorithm 9 SER method : Offline step

while $M \leqslant M_{max}$ **do**

Build r **EIM basis functions**
for $i = M$ **to** $i = M + r$ **do**
OnlineFixedPoint($\boldsymbol{\mu}$, $i-1$, $\{a_m^q\}_{q,m}$, $\{a^l\}_l$, $\{f_m^q\}_{q,m}$, $\{f^l\}_l$)
$\bar{\boldsymbol{\mu}}_i \leftarrow arg\max_{\boldsymbol{\mu}\in\Xi} \inf_{z\in W_{i-1}} ||w(u_{i-1}(\boldsymbol{\mu}); .; \boldsymbol{\mu}) - z||_{L^\infty(\Omega)}$
$\bar{S}_i \leftarrow \bar{S}_{i-1} \cup \{\bar{\boldsymbol{\mu}}_i\}$

$\bar{W}_i \leftarrow \bar{W}_{i-1} \oplus span\{\bar{\boldsymbol{\xi}}_i = w(u_{i-1}(\bar{\boldsymbol{\mu}}_i), \mathbf{x}; \bar{\boldsymbol{\mu}}_i)\}$
$\mathbf{r}_i(\mathbf{x}) \leftarrow w(u_{i-1}, \mathbf{x}; \bar{\boldsymbol{\mu}}_i) - w_{i-1}(u_{i-1}, \mathbf{x}; \bar{\boldsymbol{\mu}}_i)$ ▷ Residual
$\boldsymbol{t}_i \leftarrow arg\sup_{\mathbf{x}\in\Omega} |\mathbf{r}_i(\mathbf{x})|$ ▷ Interpolation point
$q_i(\mathbf{x}) \leftarrow \frac{\mathbf{r}_i(\mathbf{x})}{\mathbf{r}_i(\boldsymbol{t}_i)}$ ▷ Deduce EIM basis
end for
At this step, EIM approximation reads $w_i(u(\boldsymbol{\mu}), \mathbf{x}; \boldsymbol{\mu}) = \sum_{m=1}^{i} \beta_m^i(u, \boldsymbol{\mu}) q_m(\mathbf{x})$
$\{a_i^q\}_q$ and $\{f_i^l\}_l$ terms are precomputed and stored (no dependence on $\boldsymbol{\mu}$)

Build r **RB basis functions**
for $j = M$ **to** $j = M + r$ **do**
$\boldsymbol{\mu}_j \leftarrow \boldsymbol{\mu} \in \mathcal{D}$ ▷ Random or from Greedy algorithm
$S_j \leftarrow \{\boldsymbol{\mu}_j\}$
OfflineFixedPoint($\boldsymbol{\mu}_j$, $\{a_{q,m}\}_{q,m}$, $\{f_{q,m}\}_{q,m}$) ▷ Compute $u_{\mathcal{N}}(\boldsymbol{\mu}_j)$

$\boldsymbol{\xi}_j \leftarrow orthonormalization(u_{\mathcal{N}}(\boldsymbol{\mu}_j))$ ▷ Gram-Schmitt orthonormalization
$W_j \leftarrow W_{j-1} \oplus span\{\boldsymbol{\xi}_j\}$ ▷ Deduce RB basis
end for

end while

The implementation of the SER method given in the algorithm 9 uses as much as possible the existing components of the `Feel++` RB framework. The already implemented `offline()` functions – performing the offline steps both for EIM (listing 7.3) and for RB (listing 7.4) – are slightly changed to be used in a global function `SER()`, as displayed in the listing 7.5. This allows to apply the algorithm 9 for each groups of basis functions.

In the two `offline()` functions, the number of basis functions to build has to be adapted in the case of SER. The group size r is contained in the variable `ser_freq`, and `max` denotes the total number of functions to build all through the offline step. The key point of the implementation resides in the use of the RB approximation instead of the FE

one within the EIM `offline()` function.

Regarding the main `SER()` function, it simply consists in alternate calls to the `offline()` functions of RB and EIM. We shall note that we start with the RB offline step. Indeed, the EIM initialization step (see algorithm 8 and listing 7.1) is performed out, and before the call to `SER()`. Since it changes between each simultaneous build, the affine decomposition is updated through the function `assemble()`.

Listing 7.3 – EIM offline

```
void offline()
{
  // Number of functions to build is adapted for SER
  if ( ser && M_model->mMax() + ser_freq  <= max )
    Mmax = M_model->mMax() + ser_freq;
  else
    Mmax = max;
  // Build group of EIM basis functions
  for( ; M_M <=Mmax; ++M_M ) //err >= this->M_tol )
  {
    // EIM Greedy algorithm
    for( auto mu : *subtrainset )
    {
      if( ser )
        solution = M_model->computeRbExpansion( mu ); //RB
      else
        solution = M_model->solve( mu ); //FEM

      resmax = M_model->computeMaximumOfResidual(mu,solution);
      maxerr(i) = resmax.template get<0>();
    }
    // Update mu from Greedy algorithm
    auto err = maxerr.array().abs().maxCoeff( &index );
    mu = trainset->at(index);
    // Compute the solution (using RB for SER)
    if( ser )
      solution = M_model->computeRbExpansion( mu ); // RB
    else
      solution = M_model->solve( mu ); //FEM
    M_model->addSolution( solution );
    // Compute the interpolation point
    auto t = M_model->computeMaximumOfResidual( mu,solution);
    M_model->addInterpolationPoint( t );
    // Deduce the new EIM basis function
    element_type res = M_model->Residual( M_M-1 );
    // Enrich the EIM approximation space
    M_model->addBasis( q );
  }
}
```

Listing 7.4 – RB offline

```
void offline()
{
  // Number of functions to build is adapted for SER
  if( ser && Nold + ser_freq <= max ) // SER
    M_iter_max = Nold + ser_freq;
  else
    M_iter_max = max;
  while ( M_N < max  )
  {
    // Compute affine decomposition
    tie( Mqm, Aqm, Fqm ) = M_model->computeAffineDecomposition();
    // Solve the finite element non-linear problem
    u = offlineFixedPointPrimal( mu );
    // Enrich the RB approximation space
    M_model->rBFunctionSpace()->addPrimalBasisElement( u );
  }
}
```

Listing 7.5 – SER offline

```
void SER()
{
  do
  {
    // Perform RB offline
    rb->offline();
    // Perform offline step for each EIM
    for( auto eim : eim_vector )
    {
      eim->setRB( crb );
      eim->setModel( model );
      eim->offline();
    }
    // Update the affine decomposition
    model->assemble();
  }
  while( crb->continueOfflineStep() );
}
```

7.3 SER variants

We have just described the implementation of the initial SER method within the `Feel++` RB framework. This last section then focuses on the SER variants, introduced in Section 2.3.2.

The variants investigated within the SER method are based on the error indicator introduced in Section 2.3.1. This error estimator is itself based on the Riesz representation of the residual.

The Riesz representation $\{\hat{a}_{q,m,n}\}_{q,m,n}$ (resp. $\{\hat{f}_{q,m}\}_{q,m}$) of $a_{q,m}(\xi_n, v)$ (resp. $f_{q,m}(v)$) defined in (2.54) is part of the precomputations performed during the offline stage. Thus, these terms are computed simultaneously with the $\{a_{q,m}\}_{q,m}$ and $\{f_{q,m}\}_{q,m}$. The compu-

tation of the error indicator (algorithm 10) then simply consists in assembling the Riesz representation of the residual (2.55), and compute its norm.

Algorithm 10 Riesz representation of $R^{aff}_{N,M}$

function RieszResidualNorm($\boldsymbol{\mu}$, u, $\{\hat{a}_{q,m,n}\}_{q,m,n}$, $\{\hat{f}_{q,m}\}_{q,m}$)
  Compute $\gamma^a_{q,m}(u,\boldsymbol{\mu})$, $\gamma^f_{q,m}(u,\boldsymbol{\mu})$ $\forall q,m$
  Assemble $\mathcal{Y}R^{aff}_{N,M}(u;\boldsymbol{\mu})$ from $\gamma^a_{q,m}$, $\gamma^f_{q,m}$, $\hat{a}_{q,m,n}$ and $\hat{f}_{q,m}$
  Returns $\| \mathcal{Y}R^{aff}_{N,M}(\cdot;\boldsymbol{\mu}) \|$
end function

The use of this error indicator fits well into the SER offline stage (algorithm 9), as displayed in the algorithm 11. The EIM offline stage remains unchanged, while the parameter used to enrich the RB approximation space is now selected from a Greedy algorithm based on the previous error indicator.

Algorithm 11 SER method : Offline step with error estimation

while $M \leqslant M_{max}$ **do**

  Build r EIM basis functions
  for $i = M$ **to** $i = M + r$ **do**
    OnlineFixedPoint($\boldsymbol{\mu}$, $i-1$, $\{a^q_m\}_{q,m}$, $\{a^l\}_l$, $\{f^q_m\}_{q,m}$, $\{f^l\}_l$)
    $\bar{\boldsymbol{\mu}}_i \leftarrow arg\max_{\boldsymbol{\mu}\in\Xi} \inf_{z\in W_{i-1}} ||w(u_{i-1}(\boldsymbol{\mu});.;\boldsymbol{\mu}) - z||_{L^\infty(\Omega)}$
    $\bar{S}_i \leftarrow \bar{S}_{i-1} \cup \{\bar{\boldsymbol{\mu}}_i\}$

    $\bar{W}_i \leftarrow \bar{W}_{i-1} \oplus span\{\bar{\boldsymbol{\xi}}_i = w(u_{i-1}(\bar{\boldsymbol{\mu}}_i), \mathbf{x}; \bar{\boldsymbol{\mu}}_i)\}$
    $\mathbf{r}_i(\mathbf{x}) \leftarrow w(u_{i-1}, \mathbf{x}; \bar{\boldsymbol{\mu}}_i) - w_{i-1}(u_{i-1}, \mathbf{x}; \bar{\boldsymbol{\mu}}_i)$ ▷ Residual
    $\boldsymbol{t}_i \leftarrow arg\sup_{\mathbf{x}\in\Omega} |\mathbf{r}_i(\mathbf{x})|$ ▷ Interpolation point
    $q_i(\mathbf{x}) \leftarrow \frac{\mathbf{r}_i(\mathbf{x})}{\mathbf{r}_i(\boldsymbol{t}_i)}$ ▷ Deduce EIM basis
  end for

  Build r RB basis functions
  for $j = M$ **to** $j = M + r$ **do**
    $\boldsymbol{\mu}_j \leftarrow arg\ max_{\boldsymbol{\mu}\in\mathcal{D}}$ [RieszResidualNorm($\boldsymbol{\mu}$, u_{j-1}, $\{\hat{a}_{q,m,n}\}_{q,m,n}$, $\{\hat{f}_{q,m}\}_{q,m}$)]
    $S_j \leftarrow \{\boldsymbol{\mu}_j\}$
    OfflineFixedPoint($\boldsymbol{\mu}_j$, $\{a_{q,m}\}_{q,m}$, $\{f_{q,m}\}_{q,m}$) ▷ Compute $u_{\mathcal{N}}(\boldsymbol{\mu}_j)$

    $\boldsymbol{\xi}_j \leftarrow orthonormalization(u_{\mathcal{N}}(\boldsymbol{\mu}_j))$ ▷ Gram-Schmitt orthonormalization
    $W_j \leftarrow W_{j-1} \oplus span\{\boldsymbol{\xi}_j\}$ ▷ Deduce RB basis
  end for

end while

The function `computeRieszResidualNorm` has been added to the reduced basis framework to mimic the one described in the algorithm 10. As displayed in the listing 7.6,

the Greedy algorithm – performed through the RB offline step – thus simply consists in finding the parameter maximizing the error. This allows to prepare the construction of next RB basis function.

Listing 7.6 – RB Greedy

```
for( auto mu : *sampling )
{
  // Computes error indicator for each mu
  error_indicator(i) = computeRieszResidualNorm( mu, uN );
}
//Selects the maximizer
mu = *max_element(error_indicator.begin(),error_indicator.end());
```

r-adaptation Based on the increment of the maximal values resulting from both EIM and RB Greedy algorithms, the $r-$adaptation method – introduced as the first SER variant in Section 2.3.2 – is illustrated in the algorithm 12.

In terms of implementation, the steps remain the same, except for the number of basis functions to build which has to be distinguished for the two approximation spaces. The update of r depends on the criterion resulting from the considered increment.

Algorithm 12 SER method : offline step with $r-$adaptation

$r_{EIM} \leftarrow r$; $r_{RB} \leftarrow r$
while $M \leqslant M_{max}$ **do**

  Build r **EIM basis functions**
  for $i = M$ **to** $i = M + r_{EIM}$ **do**
    [...] ▷ Compute q_i
    current_max_err$_{EIM} \leftarrow \max_{\boldsymbol{\mu}\in\Xi} \inf_{z\in W_{i-1}} ||w(u_{i-1}(\boldsymbol{\mu});.;\boldsymbol{\mu}) - z||_{L^\infty(\Omega)}$
    if | ref_max_err$_{EIM}$ - current_max_err$_{EIM}$ |< adaptation tolerance **then**
      $r_{EIM} \leftarrow r_{EIM} + 1$ ▷ Continue EIM offline
    end if
    ref_max_err$_{EIM} \leftarrow$ current_max_err$_{EIM}$ ▷ Update reference error
  end for

  Build r **RB basis functions**
  for $j = M$ **to** $j = M + r_{RB}$ **do**
    [...] ▷ Compute $\boldsymbol{\xi}_j$
    current_error$_{RB} \leftarrow$ RieszResidualNorm($\boldsymbol{\mu}_j$, u_j, $\{\hat{a}_{q,m,j}\}_{q,m,j}$, $\{\hat{f}_{q,m}\}_{q,m}$)
    if | ref_error$_{RB}$ - current_error$_{RB}$ |< adaptation tolerance **then**
      $r_{RB} \leftarrow r_{RB} + 1$ ▷ Continue RB offline
    end if
    ref_error$_{RB} \leftarrow$ current_error$_{RB}$ ▷ Update reference error
  end for
  $r_{EIM} \leftarrow r$; $r_{RB} \leftarrow r$
end while

In the framework, the update of the previous r_{EIM} and r_{RB} simply amounts to the add

of a new condition within the `offline()` function. The considered increment is computed each time the approximation space is enriched, allowing to update the adaptation criterion and to continue the enrichment if needed. The listing 7.7 provides the ingredients of such implementation within the EIM offline stage. The equivalent change is applied to the RB `offline()` function.

Listing 7.7 – $r-$adaptation in EIM

```
// New condition for r-adaptation
if ( radaptation && M_model->mMax() < max )
  Mmax = M_model->mMax() + 1;
else if ( M_model->mMax() + ser_freq  <= max )
  Mmax = M_model->mMax() + ser_freq;
else
  Mmax = max;
// Continue enrichment if needed
double increment = abs(err-previous_err)/abs(previous_err);
if( increment < adaptation_tolerance )
  radaptation=true;
```

Hybrid Greedy algorithm Introduced as the second SER variants of Section 2.3.2, the so-called hybrid Greedy algorithm is used within the EIM offline stage. As illustrated in the algorithm 13, the RB approximation is considered only if it is sufficiently reliable. Its relevance for each parameter $\boldsymbol{\mu}$ is based on the previous error indicator available from the function described in the algorithm 10.

Algorithm 13 SER method : offline step with Hybrid Greedy algorithm

while $M \leqslant M_{max}$ **do**

  Build r **EIM basis functions**
  for $i = M$ **to** $i = M + r$ **do**
    if $\text{RieszResidualNorm}(\boldsymbol{\mu}, u_{j-1}, \{\hat{a}_{q,m,n}\}_{q,m,n}, \{\hat{f}_{q,m}\}_{q,m}) < \text{tol}$ **then**
      $u \leftarrow \text{OnlineFixedPoint}(\boldsymbol{\mu}, i-1, \{a^q_m\}_{q,m}, \{a^l\}_l, \{f^q_m\}_{q,m}, \{f^l\}_l)$
    else
      $u \leftarrow \text{OfflineFixedPoint}(\boldsymbol{\mu}_j, \{a_{q,m}\}_{q,m}, \{f_{q,m}\}_{q,m})$
    end if
    $\bar{\boldsymbol{\mu}}_i \leftarrow arg\max_{\boldsymbol{\mu}\in\Xi} \inf_{z\in W_{i-1}} ||w(u(\boldsymbol{\mu}); .; \boldsymbol{\mu}) - z||_{L^\infty(\Omega)}$
    $\bar{W}_i \leftarrow \bar{W}_{i-1} \oplus span\{\bar{\boldsymbol{\xi}}_i = w(u(\bar{\boldsymbol{\mu}}_i), \mathbf{x}; \bar{\boldsymbol{\mu}}_i)\}$
    $\mathbf{r}_i(\mathbf{x}) \leftarrow w(u, \mathbf{x}; \bar{\boldsymbol{\mu}}_i) - w_{i-1}(u, \mathbf{x}; \bar{\boldsymbol{\mu}}_i)$ ▷ Residual
    $\boldsymbol{t}_i \leftarrow arg\sup_{\mathbf{x}\in\Omega} |\mathbf{r}_i(\mathbf{x})|$ ▷ Interpolation point
    $q_i(\mathbf{x}) \leftarrow \frac{\mathbf{r}_i(\mathbf{x})}{\mathbf{r}_i(\boldsymbol{t}_i)}$ ▷ Deduce EIM basis
  end for

  Build r **RB basis functions** [...]

end while

The corresponding changes in the code take place within the Greedy algorithm introduced in the listing 7.3. The criterion describing the quality of the reduced basis

approximation is determined for each parameter of the trainset. It then allows to choose the approximation to use on a case-by-case basis. The function `computePfem` uses the affine decomposition to benefit from the already performed precomputations.

Listing 7.8 – Hybrid Greedy algorithm

```
for( auto mu : *trainset )
{
  if( ser && error_estimation && hybrid_eim )
  {
    // Compute the error indicator with mu
    auto error_indicator = M_model->RieszResidualNorm( mu );
    // Criterion associated with current mu
    error_criterion[i] = error_indicator/err < rtol;
  }

  if( ser ) //Use SER
  {
    // Consider RB only if sufficiently relevant
    if( ser && error_criterion[i] )
      solution = M_model->computeRbExpansion( mu, uN ); //RB
    else
      solution = M_model->computePfem( mu ); //PFEM
  }
  else
  solution = M_model->solve( mu ); //FEM

  resmax = M_model->computeMaximumOfResidual(mu,solution);
  maxerr(i) = resmax.template get<0>();
}
```

Multi-levels SER(l) Finally, the last variant for SER consists in the application of the initial method on several levels. To this end, we turn back to the main function `SER()` (see listing 7.5) which drives the whole SER offline step.

The use of the SER method at multiple levels requires the construction of one RB approximation space per level. The corresponding objects are stored in the vector `rbs` allowing to build the RB approximation associated to each level.

As mentioned in Section 2.3.2, the first iteration is equivalent to the initial method, using the RB approximation of the current level. From the second level, the RB approximation resulting from the previous run is used. We shall note that the affine decomposition – carried out by the model – and the resulting reduced basis approximation has always to come from the same level.

Listing 7.9 – Multi-levels SER(l)

```
void SER()
{
  for( int ser_level=0; ser_level < nb_levels; ++ser_level )
  {
    if ( ser_level > 0 )
    {
      rbs.push_back( newRB( ser_level ) );
      rb = rbs.back();
    }
    do
    {
      rb->offline();
      for( auto eim : eim_vector )
      {
        // From the second level, use the previous RB approx
        if ( crbs.size() > 1 )
        {
          eim->setRB( rbs[ser_level-1] );
          eim->setModel( models[ser_level-1] );
        }
        else
        {
          eim->setRB( rb );
          eim->setModel( model );
        }
      }
      // Update the affine decomposition
      model->assemble();
    }while( crb->continueOfflineStep() );
}
```

Conclusion

As seen in Chapter 2, the SER method is a combination of the EIM and RB methodologies, aiming to decrease the computational related with the recovery of the necessary affine decomposition. This chapter describes its introduction within the `Feel++` reduced basis framework, discussing the changes made to the existing implementation. We describe also the inclusion of each SER variants (Section 2.3.2) in the previous algorithm.

All these features are now part of the framework, making them usable for any non-linear and/or non-affinely parametrized model. Their use on high field magnets applications are illustrated in Chapter 11.

Part IV

Numerical applications

Chapter 8

Parametric studies and uncertainty quantification

The thermal increase due to Joule losses within the conductor is a key point of the high field magnets study. The heating could alter the mechanical properties of the materials, which is why we shall take great care of temperature in the design process. Nevertheless, we remind that the input data – materials properties, operation conditions – are generally not exactly known. The ranges in which these input parameters vary have thus to be investigated to cover all possible configurations.

Although the finite element model introduced in Section 3.1 could be suitable in this context, its computational cost could become prohibitive depending on the number of simulations considered. Especially designed for many-query context, the reduced basis method provides a much more appropriate solution. The reduced electro-thermal model detailed in Chapter 4 is thus preferred for this kind of study.

This chapter focus on the influence of these inputs on temperature. A ranking of how inputs affect the temperature is established, in order to determine in which directions the optimizations should be carried out. The second part illustrates the use of the reduced electro-thermal model within two concrete examples of parametric studies. Performed both with FE and RB electro-thermal models, these studies aim to validate the two models in real situations.

This kind of analysis had not been performed for LNCMI high field magnets up to now. However, this provides essential informations on the behavior of operating magnets.

Contents

8.1 Sensitivity analysis on mean temperature

The sensitivity analysis consists in the study of how the uncertainties on inputs can influence a given quantity of interest. In this section, we focus on the mean temperature over the domain as output.

The electro-thermal model detailed in chapters 3 and 4 is used to establish the input/output relation between the inputs denoted as X, and the outputs denoted as Y. Its acts as a function F relating X and Y as

$$Y = F(X) \tag{8.1}$$

We shall note that this kind of analysis requires a sampling X of sufficiently large size. The sensitivity indices [Sobol, 1993], [Prieur, 2014], [Janon et al., 2014a] which quantify the influence of the inputs can be computed from various approaches. The Monte-Carlo method is commonly used in this context. The number of simulations it requires depends both on the size of the sampling – typically several hundreds – and on the dimension of the parameter space – 6 in our case. For large problems, the cost related with the FE electro-thermal model (see Section 3.1) is prohibitive for such studies. However, its reduced version (see Chapter 4) is well suitable. We propose to use it as the previous function F (8.1). We also point out that meta-models [Sudret, 2008], [Janon et al., 2014b] can be used prior to the Monte-Carlo method in order to further decrease its cost.

The next studies rely on the library `Openturns` [Dutfoy et al., 2009], dedicated to the treatment of uncertainties. `Openturns` firstly provides a sample of input parameters X in the wanted ranges following a given probability distribution. In our case, we consider an uniform distribution.

This section focuses on the sensitivity analyses performed both on the sector of Bitter magnet and on the radially cooled helix for which convergence studies are given in Section 4.2.

8.1.1 Bitter magnet

In this example, the input parameter related with the electrical current is the current density $\mathbf{j}$ instead of the voltage (see Chapter 4). Other input parameters namely the materials properties and the cooling conditions are the ones introduced in Chapter 4, making $\boldsymbol{\mu}$ read as

$$\boldsymbol{\mu} = (\sigma_0, \alpha, L, \mathbf{j}, h, T_w) \tag{8.2}$$

In the model, the difference of potential between the current input and output which appears as boundary condition is determined from $\mathbf{j}$ through the computation of the current intensity and the Ohm's law. For this application, we consider an input parameters sampling of size 300, selected from a uniform distribution on the ranges displayed in Table 8.1. This ranges are typical of copper alloys and operating conditions used in practice.

σ_0	$[55, 60]$ $MS.m^{-1}$
α	$[3.3 \times 10^{-3}, 3.5 \times 10^{-3}]$ $K^{-}1$
L	$[2.5 \times 10^{-8}, 2.9 \times 10^{-8}]$
$\mathbf{j}$	$[60 \times 10^{6}, 70 \times 10^{6}]$ $A.m^{-2}$
h	$[70000, 90000]$ $W.m^{-2}.K^{-1}$
T_w	$[293, 313]$ K

Table 8.1 – Input parameters for sensitivity analysis on Bitter magnet

`Openturns` provides the mean of outputs resulting from the 300 realizations, and the associated standard deviation (Table 8.2). This results allow to determine a range for the mean temperature, considering the uncertainties on inputs (Table 8.1). Thus, the mean temperature in the Bitter magnet varies from $53.22°C$ to $65.28°C$.

Mean of outputs	$332.25K \approx 59.25°C$
Standard deviation	6.03

Table 8.2 – Mean and standard deviation for mean temperature in Bitter magnet

However, we remind that the objective is to ensure that the temperature in the magnet doesn't exceed a critical value. In this context, the quantiles provide a threshold value for the output which amounts to consider the worst case. From the set of resulting outputs Y, the quantiles consist in finding the threshold value y which won't be exceeded with a given probability p. That is find y such that

$$P(Y \leqslant y) \geqslant p \tag{8.3}$$

Table 8.3 displays the quantiles obtained for two probabilities. We are thus 99% sure that the mean temperature shall not exceed $70°C$. This reference value is particularly useful for control system to tighten the limit temperature and to better anticipate potential incidents.

99.0%	$343K = 70°C$
80.0%	$336.5K = 63.5°C$

Table 8.3 – Quantiles for mean temperature in Bitter magnet

Lastly, the sensitivity indices answer the question on parameters influence on mean temperature. The Sobol indices [Sobol, 1993] quantify it from the expected value and the variance of the outputs. This study simply consider that the input parameters $X_i \in X$ are independent. To this end, the first order Sobol index S_i associated with the i^{th} input X_i (8.2) is expressed as

$$S_i = \frac{V(E[Y \mid X_i])}{V(Y)} \tag{8.4}$$

Table 8.4 displays the resulting sensitivity indices. As expected, the current density is the most influent parameter.

σ_0	0.022
α	3.6×10^{-5}
L	0.0042
$\mathbf{j}$	0.77
h	0.044
T_w	0.16

Table 8.4 – Sobol indices for mean temperature in Bitter magnet

Moreover, the sum of the Sobol indices listed in Table 8.4 is equal to 1. The model is then said to be additive, which means that the function $F(X)$ (8.1) reads as a sum $F(X) = \sum_{i=1}^{d} F_i(X_i)$ with d the parametric dimension.

The water cooling temperature comes in second place. This result is counter intuitive as we could have expected h to be more influent. Efforts have thus to be concentrated on T_w to decrease the magnet temperature associated with a given current density.

8.1.2 Radially cooled helix

The second example focuses on the radially cooled helix introduced in Chapter 4. Offering a better cooling for the magnet, this technology leads to a much more complicated temperature field than in longitudinally cooled helices. Indeed, the insulators introduced between the helix turns give rise to local hot spots. In this context, the study of temperature for this kind of magnet is all the more crucial since the problem is bigger.

The following sensitivity analysis is as previously based on the reduced electro-thermal model. The simulations (Figure 8.1) are performed on a mesh composed of 500 000 degrees of freedom, distributed to 12 processors. Each FE simulation requires about 16 minutes compared to 6.7 seconds for the corresponding reduced basis approximation. This gain in terms of computational time – a factor 150 – confirms the pertinence of the reduced model for this kind of study.

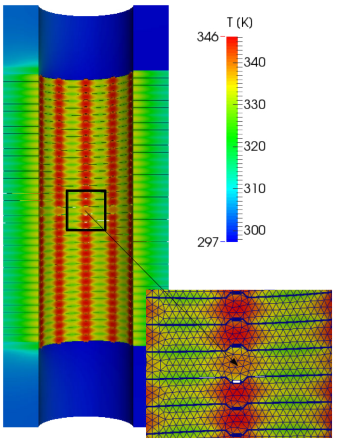

Figure 8.1 – RB simulation on radially cooled helix

As for the Bitter magnet, the next results are based on a sampling of size 300 whose parameters are selected from a uniform distribution. The parameter driving the electrical current within the magnet is the current intensity. Other parameters are the same as in

Section 8.1.1, giving $\boldsymbol{\mu}$ as

$$\boldsymbol{\mu} = (\sigma_0, \alpha, L, I, h, T_w) \tag{8.5}$$

The ranges for this application are given in Table 8.5.

σ_0	$[50; 50.2] \quad MS.m^{-1}$
α	$[3.3 \times 10^{-3}; 3.5 \times 10^{-3}] \quad K^{-1}$
L	$[2.5 \times 10^{-8}; 2.9 \times 10^{-8}]$
I	$[25000; 35000] \quad A$
h	$[70000; 90000] \quad W.m^{-2}.K^{-1}$
T_w	$T_w \in [293, 313] \quad K$

Table 8.5 – Input parameters for sensitivity analysis on a helix

The standard deviation displayed in Table 8.6 shows that the mean temperature can vary from $90.5°C$ to $114.5°C$ in the specified ranges.

Mean of outputs	$375.5K \approx 103°C$
Standard deviation	12

Table 8.6 – Mean and standard deviation for mean temperature on a helix

Due to the local hot spots near insulators, the thresholds values given by quantiles computation are higher than in the case of Bitter magnet. Table 8.7 indicates that we are 99% sure that the mean temperature shall not exceed $129°C$.

99.0%	$401.3K = 129°C$
80.0%	$385.3K = 113°C$

Table 8.7 – Quantiles for mean temperature on a helix

Finally, Table 8.8 displays the first order Sobol indices allowing to establish a ranking on the inputs parameters according to their influence on the mean temperature over the helix. As expected, the current intensity is – as the current density is the previous example – the most influent parameter. As for the Bitter, the cooling water temperature is the second one, followed by the heat transfer coefficient. From a designer point of view, these results imply that it is worth investigating how to improve the cooling parameter to decrease the magnet temperature.

σ_0	1.9×10^{-5}
α	2.3×10^{-4}
L	0.0028
I	0.75
h	0.069
T_w	0.16

Table 8.8 – Sobol indices for mean temperature on a helix

Besides the current which remains the most influence parameter on the temperature, the impact of the cooling parameters is more important that the one of material properties.

In this context, the emphasis is placed on the water temperature and on the heat transfer coefficient rather than on the materials.

Nevertheless, the sum of the Sobol indices is equal to 0.98 – and not to 1 as for the Bitter magnet – which means that the model is not additive in this case. The computation of the Sobol indices of higher order should help to identify the interactions between the parameters.

8.2 Parametric study on current density

The increase of the magnetic field mainly resides in the increase of the current density. In order to reach the highest possible magnetic field, the question of how much the current density can be increased while keeping a reasonable mean temperature – that remains beyond some heuristic limit – is often asked.

To address this question, the following parametric study fixes all the previous parameters except for the current density **j**. The values of each parameters are displayed in Table 8.9.

σ_0	58 $MS.m^{-1}$
α	3.5×10^{-3} $K^{-}1$
L	2.5×10^{-8}
j	$[30 \times 10^6, 100 \times 10^6]$ $A.m^{-2}$
h	80000 $W.m^{-2}.K^{-1}$
T_w	293 K

Table 8.9 – Input parameters

Figure 8.2b plots the behavior of the mean temperature obtained with FE and RB electro-thermal models depending on the current density. We shall first note that both models are coherent, somehow validating the reduced model.

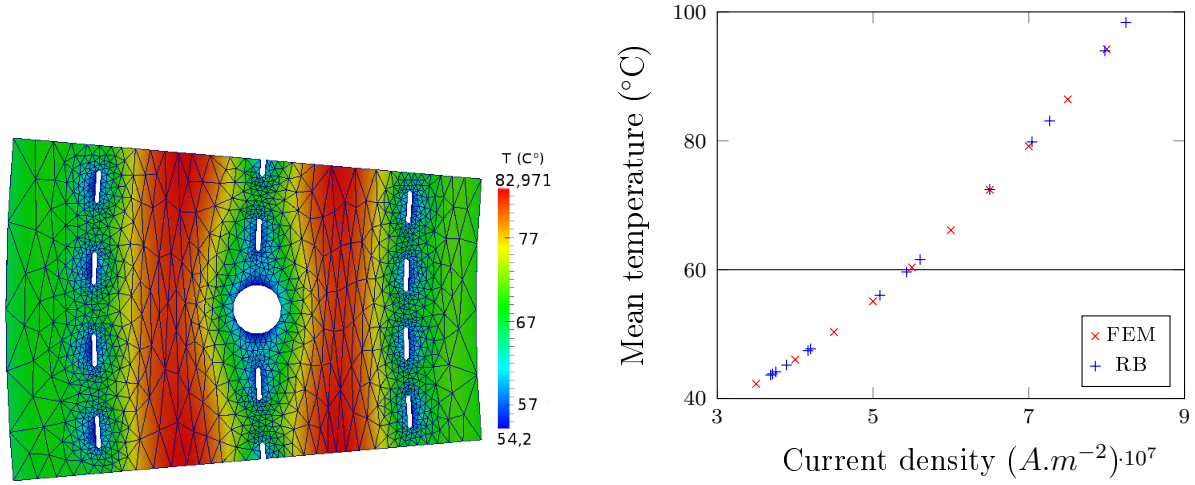

(a) RB simulation (b) Outputs

Figure 8.2 – Parametric study on Bitter: Mean temperature VS current density

The initial operating conditions for this Bitter magnet correspond to a mean temperature of $40°C$. From the results displayed in Figure 8.2b, the increase of the current density from 30 $A.mm^{-2}$ to 60 $A.mm^{-2}$ would raise the temperature from $40°C$ to $60°C$. With such increase, a gain of about 1 T in terms of magnetic field is expected. From a engineering point of view, this result is of great interest since a limited raise of $20°C$ on the mean temperature – which remains safe for the materials – allows a significant gain in magnetic field.

8.3 Parametric study on heat transfer coefficient

Besides the influence of the current density illustrated in the previous study, the sensitivity analysis introduced in Section 8.1 has proven the impact of the cooling parameters on the mean temperature. This confirms that we have to pay particular attention to the cooling process, ensuring that it behaves as expected. This section illustrates this insight, with a concrete example of issue related to the water cooling.

We are interested here in the commissioning of a Bitter magnet whose cooling is performed by water circulation through cooling holes distributed over the copper disks. When operating for the first time, this magnet has not given the expected performances. Cooling problems induced by assembly issues were suspected.

We proposed to employ our electro-thermal model in order to determine the heat transfer coefficient which reproduces the operating conditions. This should indeed helps to precisely identify potential cooling problems. We have at our disposal the voltage V_D measured at the magnet terminals, the mean water temperature and an approximation of the material properties. The parameter μ considered in the reduced model of Chapter 4 reads

$$\boldsymbol{\mu} = (\sigma_0, \alpha, L, V_D, h, T_w) \tag{8.6}$$

But in this study the heat transfer coefficient h is the only parameter which vary. We also know the intensity of the current which powers the magnet, which is the considered output in this study.

As a sort of inverse problem, the objective of this study is to vary the value of h until reaching the experimental value of the current intensity. The value obtained for h can be compared to its theoretical value given by standard hydraulic correlations which are based on the water flowrate. In the considered situation, the h is expected to be close than $h_{ex} = 5.46 \times 10^4\ W.m^{-2}.K^{-1}$. Figure 8.3 shows the values of current intensity obtained for various heat transfer coefficients using FE and RB models.

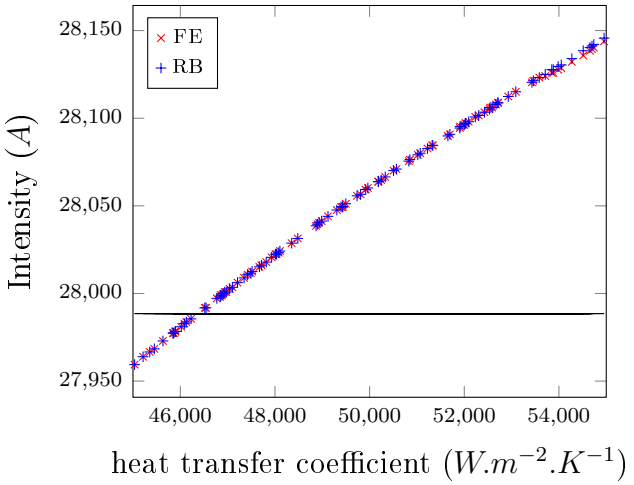

Figure 8.3 – Current intensity depending on heat transfer coefficient with initial conditions

From Figure 8.3, the measured current intensity $I_{ex} = 27988.5\ A$ indicated as a black line on the graph corresponds to a heat transfer coefficient $h = 4.64 \times 10^4\ W.m^{-2}.K^{-1}$. We note that the mean difference between FE and RB outputs remains below 10^{-2}. Being far from the expected value $h_{ex} = 5.46 \times 10^4\ W.m^{-2}.K^{-1}$, these results on h confirm a cooling problem in the magnet. Thereafter, a water leak has been indeed identified within the magnet. The latter has been disassembled to be repaired.

Figure 8.4 consists in the same study for which the input data has been updated in accordance with the measurements carried out after magnet repairing.

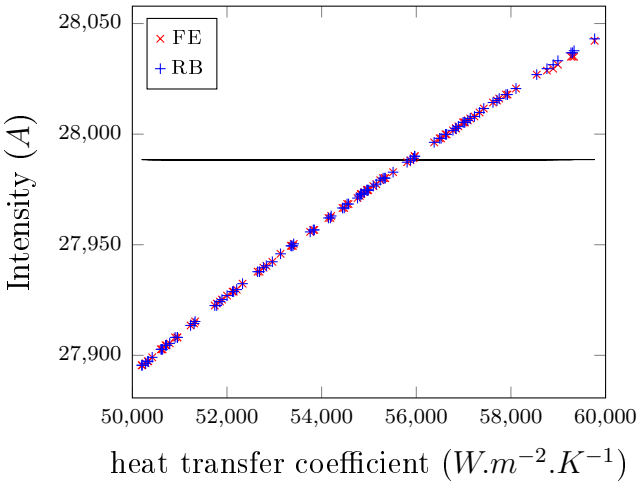

Figure 8.4 – Current intensity depending on heat transfer coefficient after repairing

Due to the voltage value, the results obtained in Figure 8.4 are different from ones of Figure 8.3. Consequently, the heat transfer coefficient value corresponding to the measured current intensity $I_{ex} = 27988.5\ A$ has changed to $h = 5.58 \times 10^4\ W.m^{-2}.K^{-1}$. Really closer to $h_{ex} = 5.46 \times 10^4\ W.m^{-2}.K^{-1}$ than previously, the result of this second study confirms that the repair has been successfully performed.

Conclusion

This chapter illustrates the use of the reduced electro-thermal described in Chapter 4 in the context of uncertainty quantification. The first part of this chapter is dedicated to sensitivity analysis, from which we deduce various quantities of interest related with the mean temperature in the magnet. These studies have been performed on two real magnet geometries. In particular, this allows to rank the input parameters from their input of the mean temperature.

The water temperature comes in first, confirming its non negligible impact. In the Grenoble High Magnetic Field Laboratory, the magnet cooling is based on a double loop system as for nuclear facilities. In this system, the secondary loop is alimented with water which is extracted from the river and whose temperature depends on the season. Therefore, the facility doesn't operate during the hottest seasons.

Furthermore, this ranking can serve to identify the parameters on which we have to focus for future experimental measure campaigns. It can also result in the simplification of our model fixing the parameters which appears are the least relevant. Finally, the quantiles can also be useful in the context of magnet control system to better prevent the incidents.

The second part deals with two concrete examples of parametric studies meeting the specific needs the research and development department of the LNCMI. It allows to assess the scope of applications which can be addressed by our model.

Chapter 9

Validation of 3D magnetic field

Up to now, the magnetic field was considered as axisymmetrical even if the geometry of the magnets are 3D. However, some experiments in magneto-science dealing with the studies of the magnetic field effects on physical or biological process have given indications that the magnetic field is 3D. These come both from NMR experiments [Trophime et al., 2006] and from experiments on magnetic levitation of alcohol droplets, which have shown that the magnetic forces induced by polyhelix magnets were not axisymmetrical. This indicates that the magnetic field itself is not axisymmetrical, unlike what is supposed in the design optimization process performed from a 2D axisymmetrical model.

The 3D magnetic field computation offered by the Biot & Savart's model introduced in Section 3.3 allows nevertheless to capture this plausible "3D effect". Moreover, the parallel implementation of this formulation detailed in Chapter 6 enables us to closely approach the experimental conditions relying on the real magnet geometry.

A magnetic field measurement campaign has been performed at LNCMI, in order to assess the relevance of these observations, and to validate our Biot & Savart model. The experimental process has been specially designed to this end. It is the focus on the first part of this chapter. The setting up of the experiment at LNCMI, as well as the achievement of the measurements have been performed as part of this thesis.

The comparison between the obtained experimental data and the numerical results is detailed in the second part. We also discuss the follow-up of these results.

Contents

9.1 Description of the experiment

The 3D magnetic field measurement requires sensors able to measure the magnetic field in all directions. In this context, Hall effect sensors are commonly used. Moreover, this kind of sensor has the advantage of being small, allowing measurements at numerous points within a small volume.

This section introduces the experimental set up that has been realized to perform such magnetic field measurements in an operating magnet at LNCMI. The M10 magnet on which the experiment has been undertaken is an insert composed of 12 longitudinally cooled helices which are electrically connected in series. Powered of up to 12MW with an electrical current of 30000 A, this magnet can produce up to 21 T – and up to 31 T with additional Bitter magnets – in 50mm bore.

The probe employed to perform the measurements is limited to a magnetic field magnitude of 3 T. Moreover, we set the current to 500 A with an external power supply as the 12MW power supply was not available at that time.

Hall effect probe These Hall effect probe consists in a set of Hall effect sensors, each composed of a semi-conductor plate fitted with two pairs of electrodes on its boundaries.

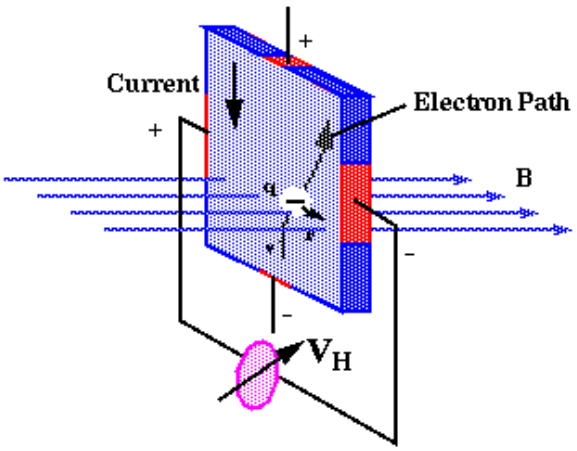

Figure 9.1 – *Image taken from www.mfg.mtu.edu*

The electrical current imposed to the semi-conductor plate is modeled as a uniform electron flow. When it is subjected to a magnetic field, this flow is deflected due to the induced Lorentz forces. As shown in Figure 9.1, this deflection then creates a voltage difference called Hall voltage across the electrical conductor, for a magnetic field perpendicular to the current. The magnetic field – the component of magnetic field which is orthogonal to the conductor plate – can then be deduced from the measured Hall voltage. This voltage has a sign which gives the sign of the magnetic field component.

The Hall sensor detects the component of the magnetic field which is orthogonal to it. For our measurements, we use a tri-axis probe (Figure 9.2) with three Hall sensors oriented orthogonally to each axis $\vec{x}$, $\vec{y}$, $\vec{z}$ in order to capture the magnetic induction $\mathbf{B}$ in

all directions. Each sensor is connected to an entry of a Gaussmeter (Figure 9.3d) which reads the signal and displays B_x, B_y and B_z.

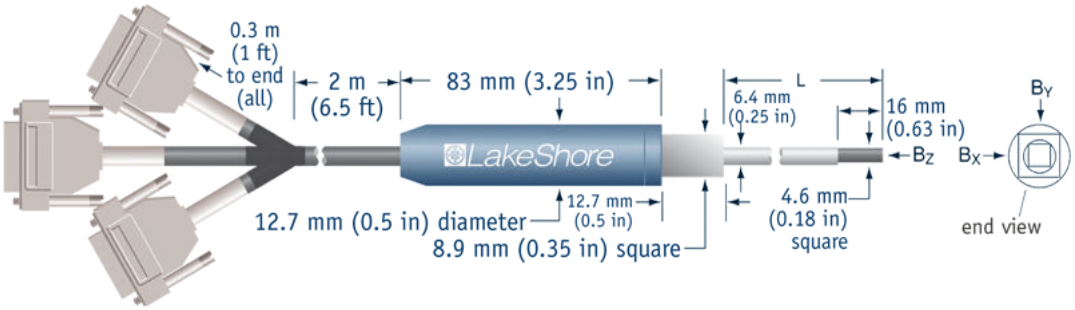

Figure 9.2 – Scheme of the HSE-1 tri-axis probe connectable to LakeShore Model 460 3-channels Gaussmeter (see Figure 9.3d)

Insertion into the magnet The Hall effect is inserted into the magnet thanks to a probe holder (Figure 9.3) which can be controlled by hand from the top of the magnet.

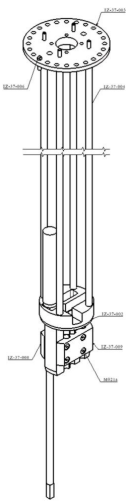

(a) Whole device

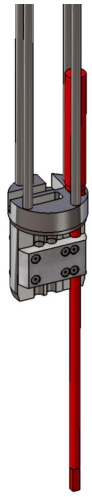

(b) Probe holder

(c) Hall probe in its holder

(d) LakeShore Model 460 3-channels Gaussmeter - display with zero current

Figure 9.3 – The probe holder has been tailored especially for the experiment. The disk at the top allows the probe to take various positions along a circle of constant radius.

We shall remark that the magnetic field measurements obtained with zero current (Figure 9.3d) are not the Earth's magnetic field. Indeed, the building in which the experiment is performed is composed of magnetic materials which slightly interfere with our measurements.

The probe holder has to be carefully inserted into the magnet, both to preserve Hall probe from damages and to avoid misalignment of the device. To this end, a camera placed at the bottom of the magnet hole allows to view the probe holder from the bottom of the magnet. Lighting the magnet hole with an optical fiber, we make sure that the probe holder is centered checking the remaining space between the holder and the magnet (Figure 9.4b).

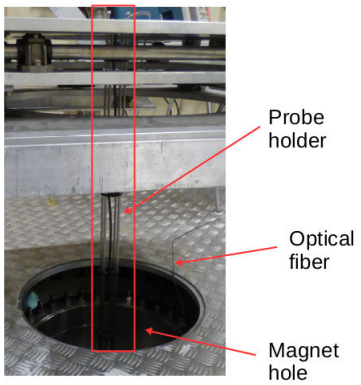

(a) Insertion of the probe holder into the magnet hole. Centering of the device is monitored with a camera.

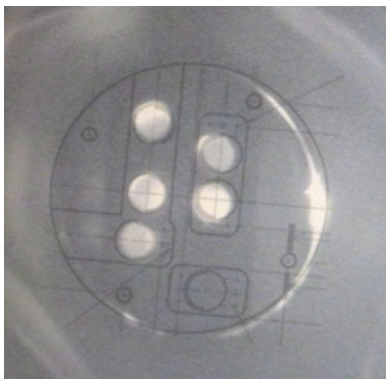

(b) Image captured by camera. Scheme of the probe holder has been projected on the camera picture to identify the position.

Figure 9.4 – Probe holder is carefully inserted into the magnet hole.

The top of the probe holder consists of a disk with uniform distributed holes (Figure 9.5) allowing to rotate the probe along a constant radius. The holes are equidistributed giving the possibility to have a measure point each 15 degrees (24 measure points per radius).

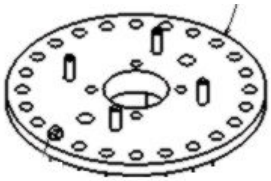

(a) CAD plan

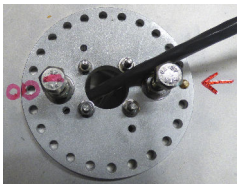

(b) Real use conditions

Figure 9.5 – The top of the device (figure 9.3a) consists in a holed disk allowing to position the probe at a given angle – each 15 degrees – along a circle of constant radius.

The probe holder has to maintain in place the Hall probe *(i)* to avoid contact with the magnet which could deteriorate the sensors and *(ii)* to ensure accuracy of the measurements by minimizing vibrations.

The bottom part of the probe holder (Figure 9.3) consists of a commutable box fitted with few holes giving different possibilities for the radius on which we want to record the magnetic field. We have two bottom pieces at our disposal for this experiment.

The first one with only a central hole –designed to make measurements on z axis ($r = 0\ mm$)– and the second one (figures 9.6a and 9.6b) with 6 radial positions from $r = 5\ mm$ to $r = 17.5\ mm$.

Finally, the position of the probe along z axis is then handled with an elevator (Figure 9.7a). The remote control (in yellow on Figure 9.7a) is used to move the elevator up and down. The elevator position is monitored with a graduated ruler.

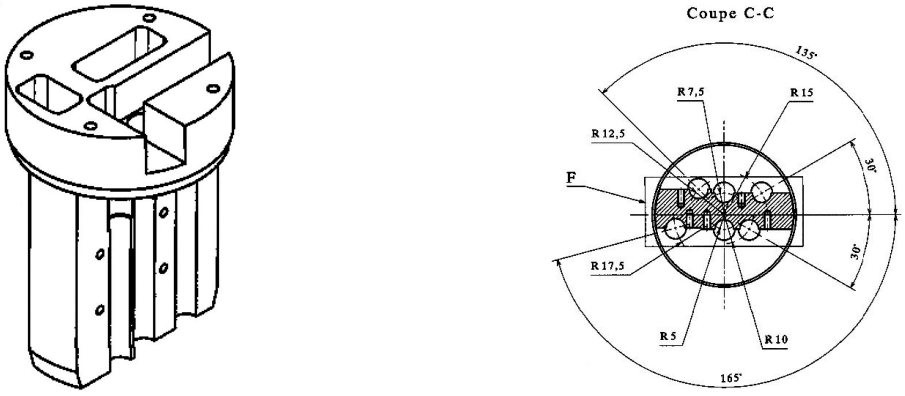

(a) Profile view (b) Top view

Figure 9.6 – The probe holder

Collecting measurements The Hall probe is fixed into the probe holder. The rotation given to the holed disk (Figure 9.5) makes the complete device rotate, leading to a rotation of the frame (x, y, z) of the probe at each measure.

The frame (x, y, z) rotates around the vertical axis along a circle of constant radius with x axis oriented outwards to the circle. Due to the positioning of the probe, B_x (resp. B_y) is close to B_r (resp. B_θ) with a constant shift angle of 15 degrees. This is due to mechanical constraints concerning the probe holder design.

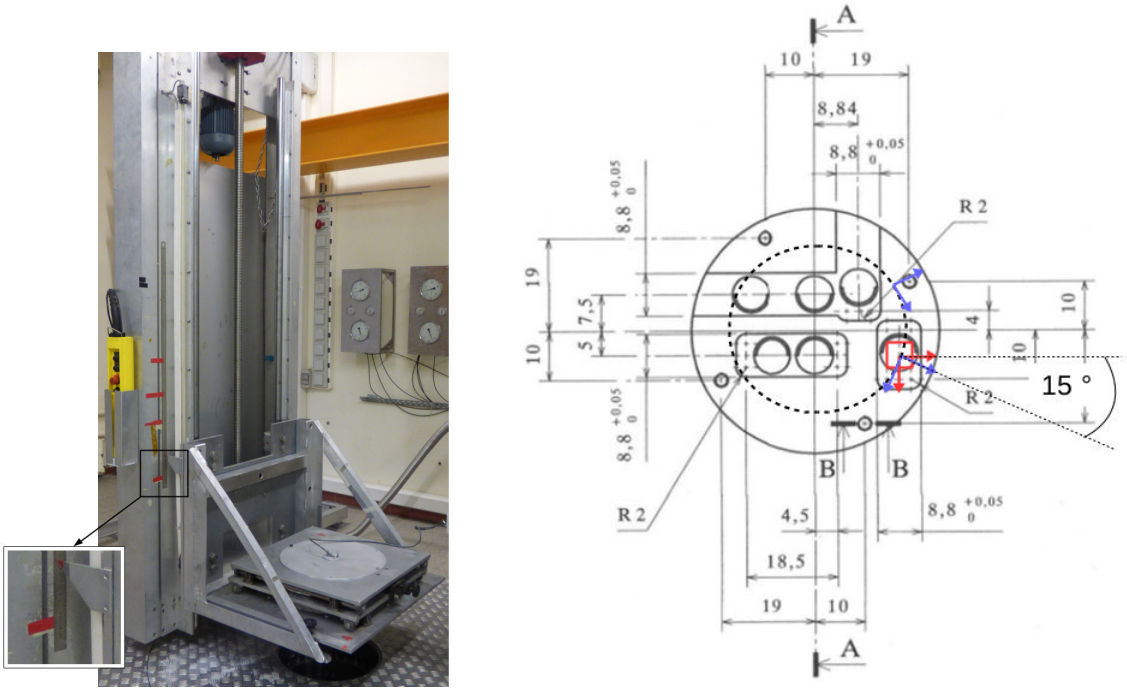

(a) (b)

Figure 9.7 – Overview of the elevator and zoom on the angular shift of the probe.

B_x, B_y and B_z relative to the Hall probe (in red on Figure 9.7b) are taken for 24 positions along a circle of constant radius and transcribed to B_r, B_θ and B_z (in blue on

Figure 9.7b) following

$$\begin{aligned} B_r &= cos(\theta)B_x - sin(\theta)B_y \\ B_\theta &= sin(\theta)B_x + cos(\theta)B_y \end{aligned} \tag{9.1}$$

We shall note that the Hall effect sensors are not all placed at the same position. The sensors measuring B_x and B_y are hence shifted of 2.08 mm to the center of the probe, as shown in Figure 9.8a. The sensor dedicated to B_z is at the center.

Figure 9.8b illustrates the rotation of the Hall effect probe along with the associated frame.

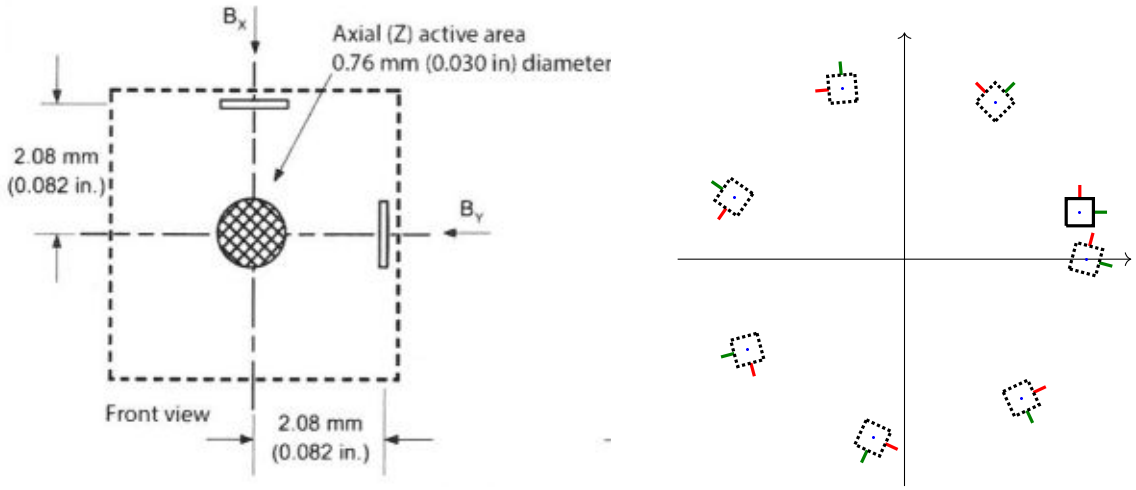

(a) Position of the sensors into the probe (b) Scheme of the probe rotation

Figure 9.8 – Position of the Hall effect sensors

As mentioned, the second part of this chapter is dedicated to the comparison between the experimental results obtained from the previously described process and the numerical ones coming from the 3D Biot & Savart's model introduced in section 3.3.

The geometry of the magnet on which the experiment has been performed comes directly from CAD. We remind that this conductor is composed of 12 helices. To compute the magnetic field inside the magnet hole, we introduce a cylindrical box of 40 mm in diameter and 400 mm long geometrically centered inside the 50 mm bore magnet.

Three meshes are considered for this geometry resulting from the union of the conductor and the box for which the mesh remains the same. The coarser one – denoted as mesh 1 in the following – consists of 1.5 millions of nodes for 7.6 millions of tetrahedrons. The second one – designated as mesh 2 – have about 2.2 millions of nodes for 13.3 millions of tetrahedrons. The last mesh – denoted as mesh 3 – is the finest one with 11.1 millions of nodes for 65.7 millions of tetrahedrons.

The figure 9.9 illustrates the magnetic field obtained with 500 A in the considered magnet. This simulation has been performed using the Biot & Savart's parallel algorithm with the finest mesh on the Curie supercomputer (TGCC, Paris). In the following, all

the simulations have been performed on the Curie supercomputer using 256 processors for the coarser mesh and 1024 for the other two.

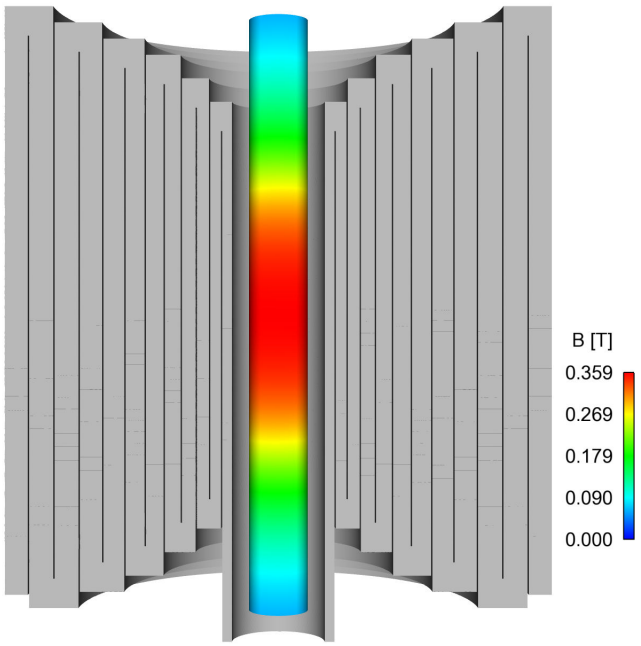

Figure 9.9 – Magnetic field computation through Biot & Savart's parallel algorithm

9.2 Preliminary measurements along z axis

We start the experiment by localizing the magnetic field center of the magnet, that is the point on which the vertical component of the magnetic induction is the highest. From theoretical considerations, the magnetic center of a symmetric solenoid is at center of the bore tube, halfway up the magnet.

The Hall effect probe is thus firstly placed at the geometric center of the magnet hole. Starting from this point, the objective is to determine the reference plan on which the maximal field value is reached, denoted as $z = 0$. To this end, we collect the magnetic induction components on various positions along the z axis steering the height from the elevator illustrated in Figure 9.7a.

As displayed in Figure 9.10a, the z-component of the magnetic field rises to 0.361 T defining the reference plan. Figure 9.10b plots the relative error between the experimental measurements of Figure 9.10a and the numerical results obtained both from the 3D Biot & Savart's law implementation and from the 2D axisymmetrical model. Figure 9.10b introduces the influence of the considered mesh.

Moreover, it shows that the 3D model allows to better evaluate the magnetic field at the helical cut extremities of the magnet.

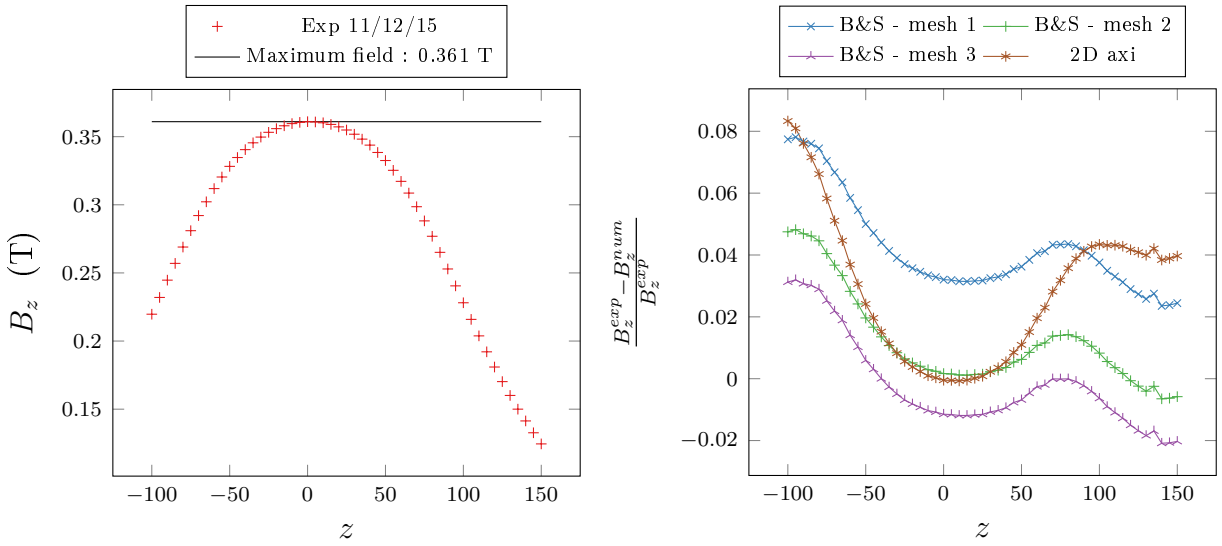

(a) Experimental (b) Comparison exp / num

Figure 9.10 – B_z along z axis

Figure 9.11a (resp. 9.12a) plots the experimental data obtained for B_x (resp. B_y) along z-axis. Figures 9.11b and 9.12b are their numerical equivalent, comparing the 2D axisymmetrical and the 3D model. The 3D model highlights a variation of these components along z, which confirms the asymmetry. Although the shape is coherent, the amplitude is highly different between the numerical model and the measurements.

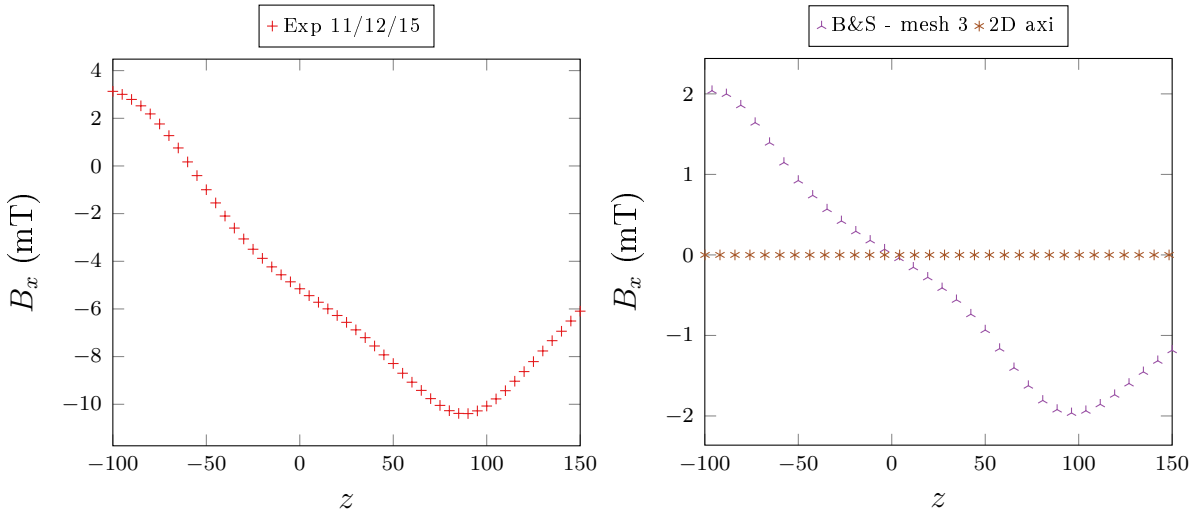

(a) Experimental (b) Numerical

Figure 9.11 – B_x along z axis

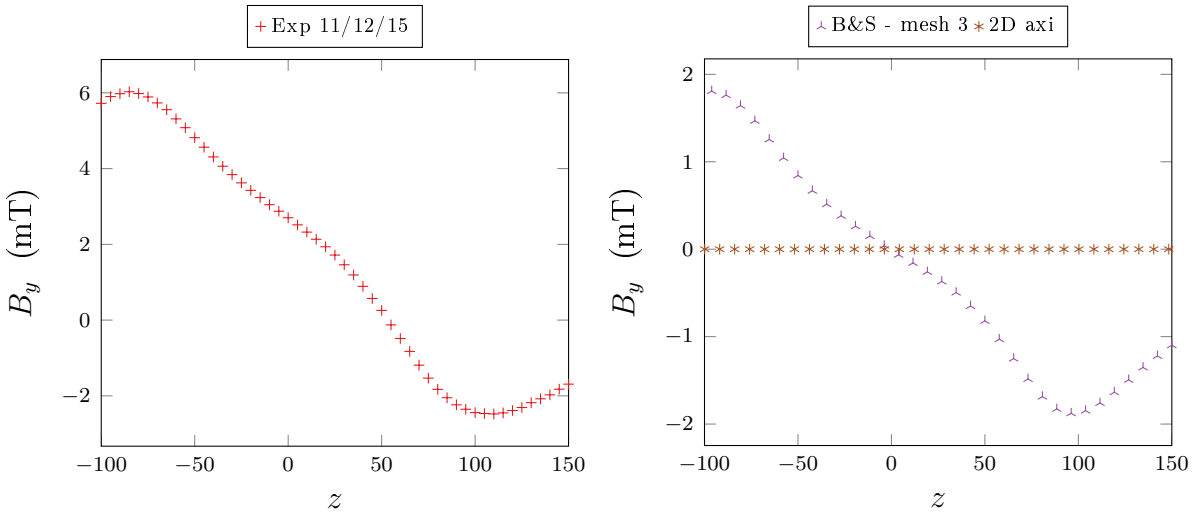

(a) Experimental (b) Numerical

Figure 9.12 – B_y along z axis

The results presented in figures 9.11 and 9.12 provide two main observations. First, the numerical results tend to prove that the considered magnet is not symmetrical and that the 2D axisymmetrical model is not adequate. Nevertheless, the amplitude of experimental values is widely different from one observed numerically in the 3D Biot & Savart model. This can be due to a misalignment of the probe into the magnet. A great attention has to be paid to the experimental set up especially to the probe older position.

From this considerations, two new measurement campaigns have been performed aiming to a better alignment of the probe holder. The agreement between the results obtained from both campaigns confirms their reproductibility.

The next sections focus on the magnetic field at off-axis position. In order to be easily interpreted, the results are displayed in cylindrical coordinates (9.1). We don't take into account the shift of the sensors within the probe (Figure 9.8a), which complicates the post-processing. Thus, we suppose that the sensors dedicated to B_x and B_y are located at the same point as the one measuring B_z.

9.3 Comparison at off-axis positions

9.3.1 Along a circle of radius $r = 17.5\ mm$ on plan $z = 0\ mm$

This section focus on the measurements of the magnetic field along the circle of radius $r = 17.5\ mm$ on the reference plan $z = 0\ mm$. If the magnet is symmetrical, the component B_r is supposed to be zero on the median plan.

The experimental results plotted in Figure 9.13a tends to show that B_r varies significantly along the circle. The numerical results obtained with 3D Biot & Savart's model (Figure 9.13b) confirm that the magnet is not symmetric.

Nevertheless, the order of magnitude of the experimental values collected seems abnormally high. A small inclination would be sufficient to reach such values for B_r, since the measurement would contain a part of the vertical component B_z. Moreover, the earth's magnetic field has not been taken into account during our experiment.

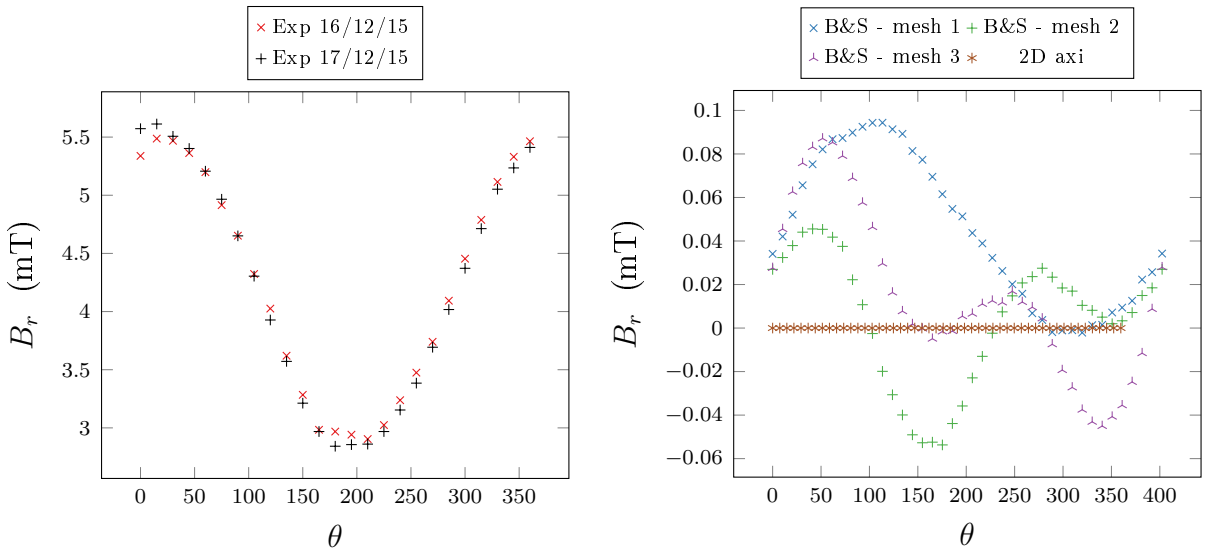

(a) Experimental (b) Numerical

Figure 9.13 – B_r along a circle of constant radius $r = 17.5\ mm$ at $z = 0\ mm$

As for the B_θ, the observations are similar to the previous ones for B_r. The experimental measurements (Figure 9.14a) as well as the 3D numerical results (Figure 9.14b) highlight a "3D effect". The order of magnitude and the amplitude of the experimental data could be due to an angular shift of the probe holder whose influence is wide on the median plan.

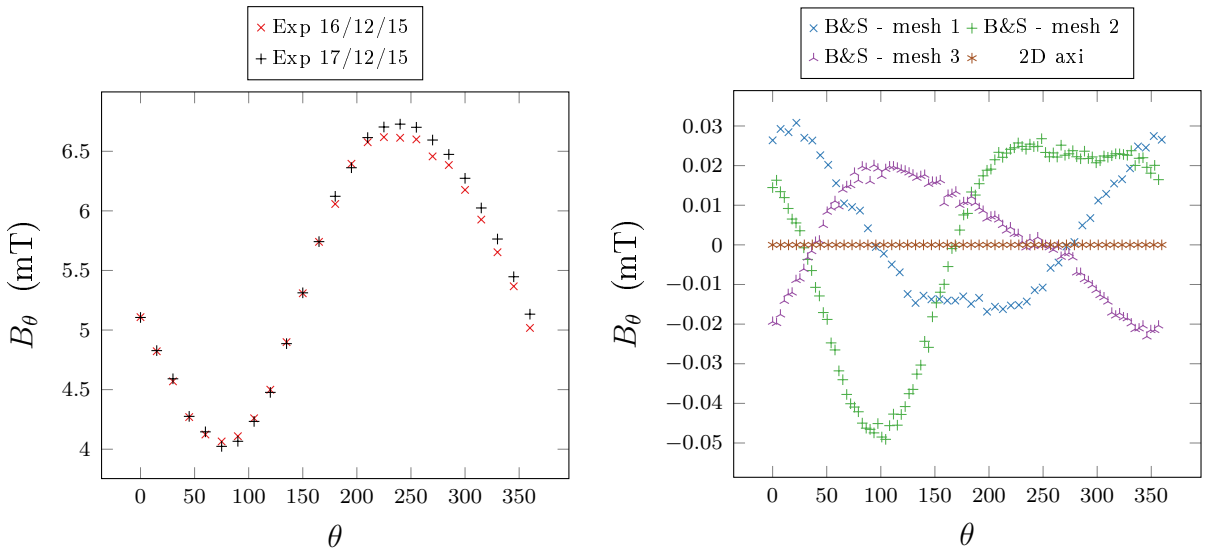

(a) Experimental (b) Numerical

Figure 9.14 – B_θ along a circle of constant radius $r = 17.5\ mm$ at $z = 0\ mm$

9.3.2 Along a circle of radius $r = 17.5\ mm$ on plan $z = 100\ mm$

This section focuses on the magnetic field obtained 100 mm above the median plan. Far from the magnetic center, the potential angular shift of the probe holder mentioned in the previous section would then have considerably less influence since the B_r and B_θ components of the magnetic field are supposed to be higher.

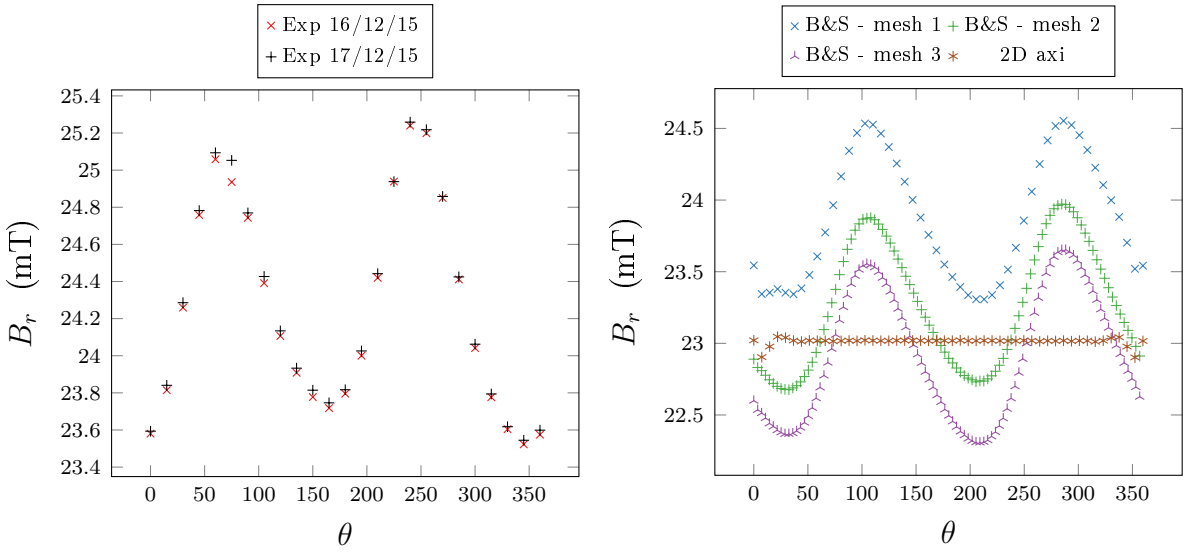

(a) Experimental (b) Numerical

Figure 9.15 – B_r along a circle of constant radius $r = 17.5\ mm$ at $z = 100\ mm$

Figures 9.15a and 9.15b display the B_r obtained experimentally and numerically along the circle of constant radius $r = 17.5\ mm$. At first, we can see that the order of magnitude and the shape of the graph are both consistent.

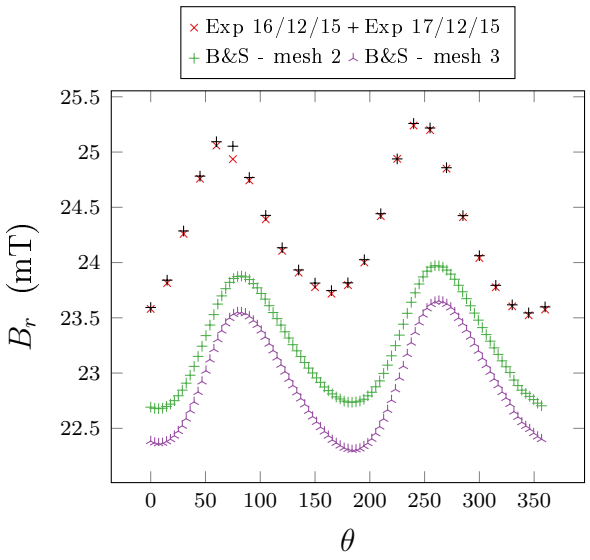

Figure 9.16 – Comparison of B_r along a circle of constant radius $r = 17.5\ mm$ at $z = 100\ mm$

To compare the previous experimental and numerical results, we have to take care

about the angular starting position of the Hall effect probe. The numerical results of Figure 9.16 whose starting position is known are shifted to fit with experimental ones at best. The corresponding offset is in coherence with the position indicated in the magnet assembly plans.

We remind that the Hall effect sensors are not exactly placed along the circle of radius $r = 17.5\ mm$ (Figure 9.8a). The shift of $2.08\ mm$ – which is not taken into account here – corresponds to a difference of about 10% in terms of radius.

In an axisymmetrical solenoid, the component B_r is proportional to the radius r. In that case, the difference of radius which is about 10% results in a difference of B_r of about 10%. This is what we observe on Figure 9.16 which fully stems from this radius offset. Moreover, the influence of the considered mesh is also highlighted in this comparison.

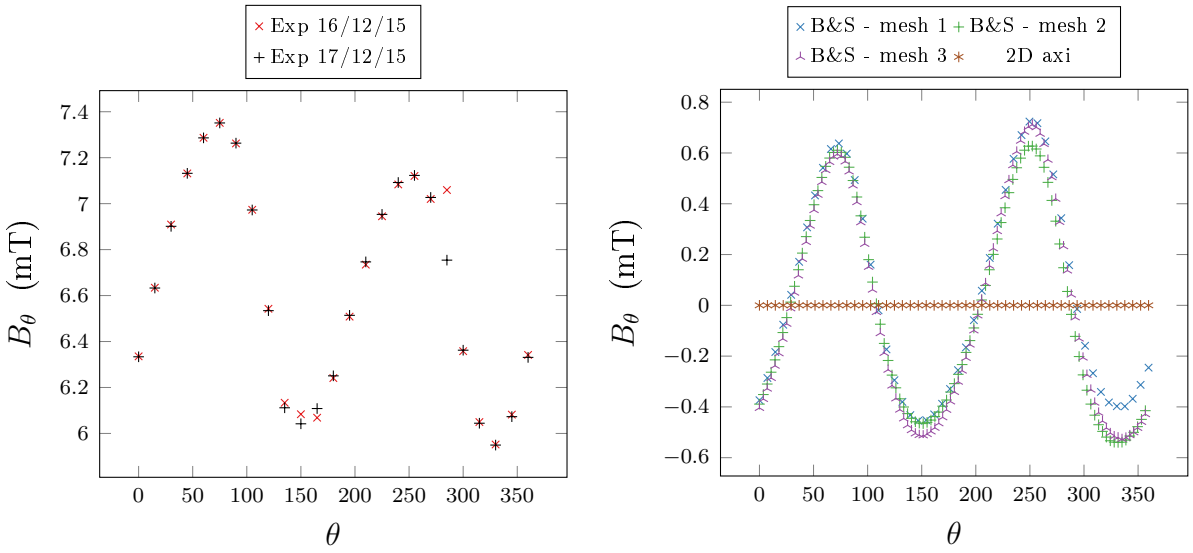

(a) Experimental (b) Numerical

Figure 9.17 – B_θ along a circle of constant radius $r = 17.5\ mm$ at $z = 100\ mm$

The Stokes theorem establishes a relation between the surface integral of a vectorial field and its line integral over the boundary of the surface. Let's denote C the closed circle on which the measurements are performed and S the surface it induces. The Stokes theorem applied to the magnetic field $\mathbf{B}$ gives

$$\oint_C \mathbf{B} \cdot d\mathbf{l} = \int_S \nabla \times \mathbf{B} \cdot d\mathbf{S} \tag{9.2}$$

In our case, the magnetic induction $\mathbf{B}$ is related to the magnetic field $\mathbf{H}$ by the constitutive law $\mathbf{B} = \mu_0 \mathbf{H}$ where μ_0 is the vacuum magnetic permeability. The Maxwell's equation gives $\nabla \times \mathbf{H} = \mathbf{j}$ with $\mathbf{j}$ the current density which is null over the surface S since S is out of the conductor.

Then, the line integral of B_θ along the circle C is expected to be null. Displayed in Figure 9.17b, the results obtained for B_θ with the 3D Biot & Savart's model tends to satisfy this theory. But this is not the case with the experimental data illustrated by Figure

9.17a. It seems that the measurements for B_θ contains also a part of the B_z component which could explain this difference in terms of order of magnitude. Nevertheless, we shall notice that both the shape and the amplitude are coherent between the two graphs.

9.3.3 Along a circle of radius $r = 17.5\ mm$ on plan $z = -100\ mm$

Finally, the last section presents the results obtained along the same circle of constant radius $r = 17.5\ mm$ but this time 100 mm below the magnetic center.

The results are expected to be symmetric with ones obtained at the same distance above the median plan $z = 0$. While this is true for numerical results displayed in Figure 9.18b, this is not the case for experimental results plotted in Figure 9.18a.

The difference in terms of magnitude can comes from the localization of the median plan (see Section 9.2) which could not be exact. But we don't explain the observed difference of shape for now.

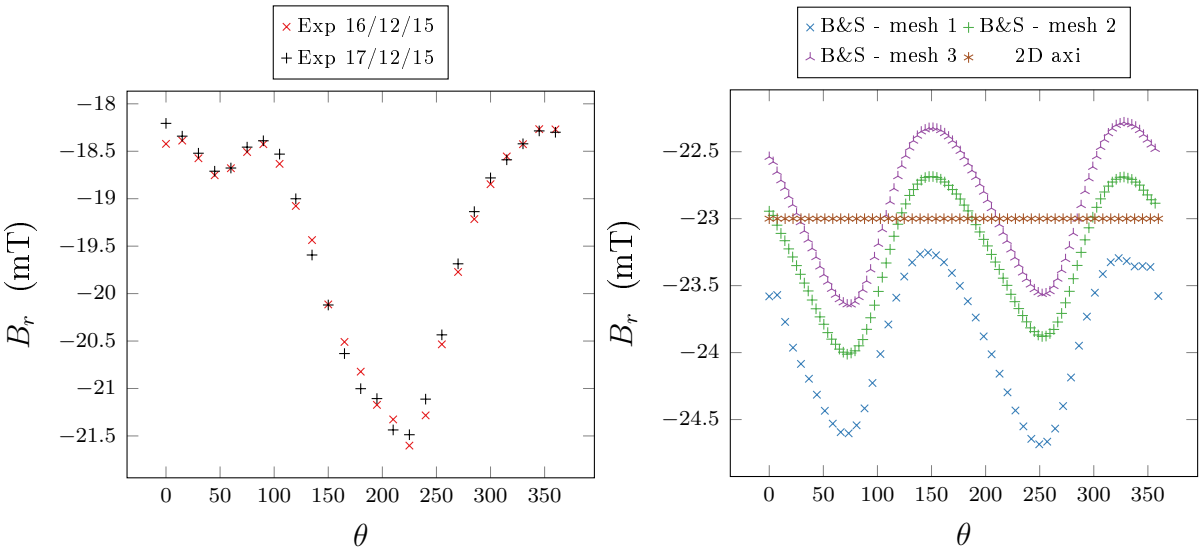

(a) Experimental (b) Numerical

Figure 9.18 – B_r along a circle of constant radius $r = 17.5\ mm$ at $z = -100\ mm$

Applying the same angular offset as previously, Figure 9.19 compares the previous experimental and numerical results.

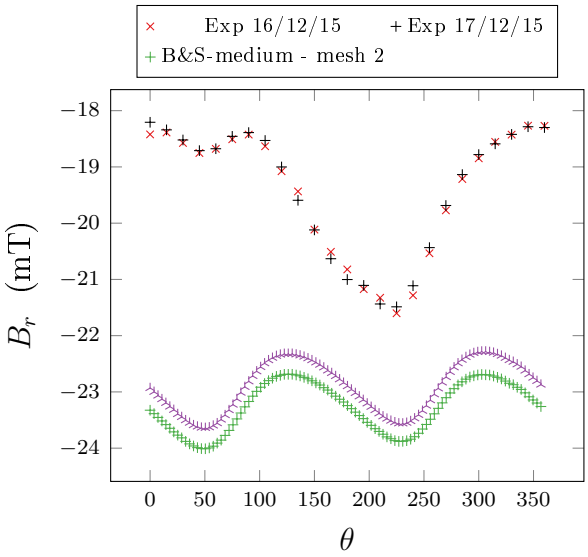

Figure 9.19 – Comparison of B_r along a circle of constant radius $r = 17.5\ mm$ at $z = -100\ mm$

Concerning B_θ, figures 9.20a and 9.20b show results whose amplitude is similar. Nevertheless, the shape of the graphs are not in coherence doubtless for the same reasons as for B_r (see Figure 9.19).

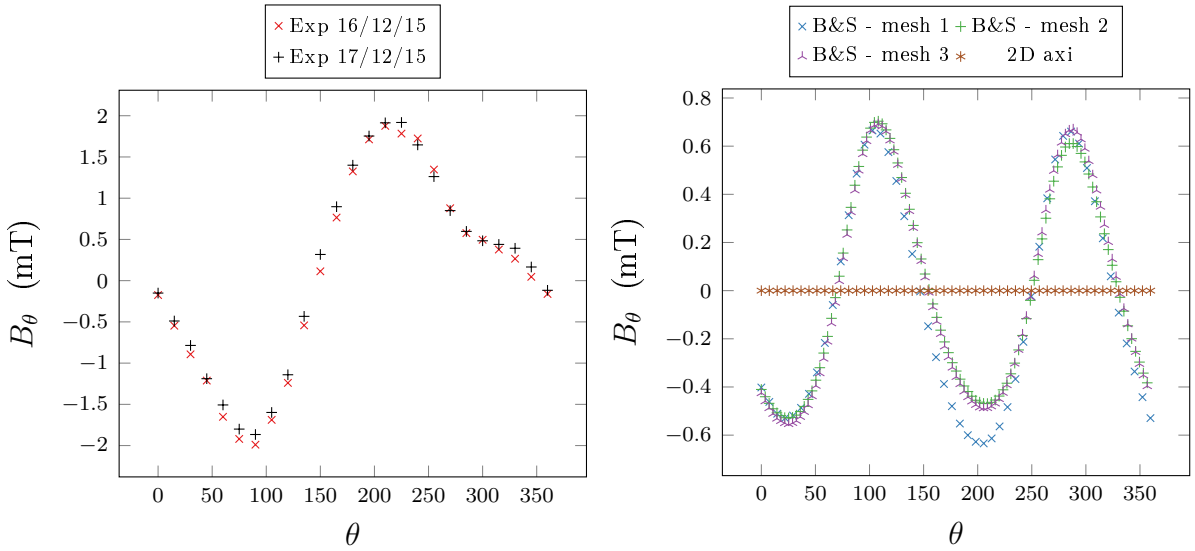

(a) Experimental (b) Numerical

Figure 9.20 – B_θ along a circle of constant radius $r = 17.5\ mm$ at $z = -100\ mm$

Conclusion

Several experiments undertaken at LNCMI have highlighted the asymmetry of the polyhelix magnets. This goes against the hypothesis considered in the existing 2D axisymmetrical models, and tends to reinforce the need of 3D modeling in this context.

The Biot & Savart's law introduced in Section 3.3 is used to endorse these observations.

Furthermore, the parallel implementation of this algorithm detailed in Chapter 6 allows to consider the whole magnet geometry within the model.

A dedicated experimental measurement campaign has been set up to validate the 3D numerical results and confirm experimentally the suspected effect of the asymmetry on the magnetic field. Starting with a detailed description of the experimental process, this chapter illustrates the comparison between the numerical and experimental results.

Both experimental measurements and 3D numerical results have allowed to confirm that the magnets are not axisymmetrical. Moreover, the periodicity of these variations observed along the circle of constant radius is related to the helical cut of the magnet. This is an important step in the understanding of the polyhelix magnets behavior. The impact of these observations on the mechanical stresses has not been investigated yet.

Although it validates our 3D model, this comparison is not fully satisfying especially in the lower part of the magnet, that is below the magnetic center. However, we shall note that the magnet on which the experiment has been performed has thousands hours of operation which could have altered its geometry. Aiming to better identify the factors that may have influenced these measurements, new experiments are currently in progress. They are performed on the two innermost helices of an recent insert, isolated from their standard operating environment in order to minimize the potential disruptions.

Finally, this study stresses the importance of the mesh size for such problems, which also confirms the relevance of a parallel implementation for this model.

Chapter 10

Validation of the elasticity model

Following the verification step based on the convergence study described in Section 3.4, this section focuses on the validation stage of the linear elasticity model. Dedicated to high field magnets simulation, the validation of this model should ideally be performed by comparison with experimental measurements obtained in real operating conditions. Nevertheless, the instrumentation of magnets in such condition is particularly difficult especially because of the cooling water flow and the high pressure environment, which makes the stress sensors difficult to install. In this context, the comparison of our model with Ansys commercial software applied on real magnet geometry consists in a first validation step. This work was made possible thanks to Julien Giraud, from the Laboratoire de Physique Subatomique et Cosmologie (LPSC).

This chapters describes this comparison at three levels. Starting by comparing the results in terms of temperature field – thus confirming the validity of the electro-thermal model –, we distinguish the displacements resulting from the thermal dilatation and from the Lorentz forces. In this context, the first section focuses on the displacements coming from the thermal dilatation only, while the second part deals with the displacements coming from the Lorentz forces only. The last part assesses the validity of the considered model considering both two forces.

Contents

For this comparison, we consider the inner helix of a real magnet insert on which we impose a current of 31000 A. In those kind of helix, the space between the turns is filled with glass marbles fastened using epoxy glue. Two materials have then to be considered, namely the copper alloy which forms the conductor and the glue. Since the glue contains a high proportion of glass marbles, we model the mechanical properties of the glue with the properties of glass as displayed in Table 10.1.

	Copper alloy	Glass
Electrical conductivity σ_0 $[S.m^{-1}]$	$55,6.10^6$	0
Thermal conductivity k_0 $[W.m^{-1}.K^{-1}]$	392	1.2
Temperature coefficient	$3,35.10^{-3}$	0
Lorentz number	$2,41.10^{-8}$	0
Young modulus $[MPa]$	120.10^3	69.10^3
Poisson coefficient	0.33	0.21
Dilatation coefficient $[K^{-1}]$	18.10^{-6}	9.10^{-6}

Table 10.1 – Physical parameters considered in elastic model validation

As to water cooling, we consider a constant heat transfer coefficient of 80000 $W.m^{-2}.K^{-1}$ and the water is set to 303 K.

As mentioned in Section 3.4, the forces induced by thermal dilatation are taken into account in the model. In our model, the temperature field is given by the non-linear electro-thermal model introduced in Section 3.1. The difference of electrical potential to impose as boundary condition is determined from the current intensity data, and the non-linearity is managed by a Picard algorithm. As to the reference models coming from Ansys software, the temperature field consists in an input data file obtained from an external code namely GetDP [Dular and Geuzaine, 1997] software.

The 3D magnetostatic model described in Section 3.2 was not available at the time when this study has been performed. For this reason, the magnetic field computation is given by the 2D axisymmetrical model in both cases. Although this study should be redone with the 3D magnetic field, it doesn't bias the validation since the two models are based on the same magnetic field data.

The following simulations are performed on 6 processors and based on a mesh composed of 39276 nodes distributed in 179428 tetrahedrons. Starting from the comparison on temperature field, the next section distinguish the forces coming from thermal dilatation only, Lorentz forces only, and finally both of them. In each case, we plot the difference between the results coming from Ansys software and from our model both over a vertical axis centered in helix width and over a radial axis going from internal to external radius.

10.1 Comparison on temperature

To ensure the coherence of the next comparisons, we start with the comparison on temperature field. Figure 10.1a (resp. Figure 10.1b) displays the relative difference between the temperature field given by our non-linear electro thermal and from the external code based on GetDP software over the vertical (resp. radial) direction. The comparison along the radius is located halfway up the helix which is about 200 mm heigh and 5 mm thick.

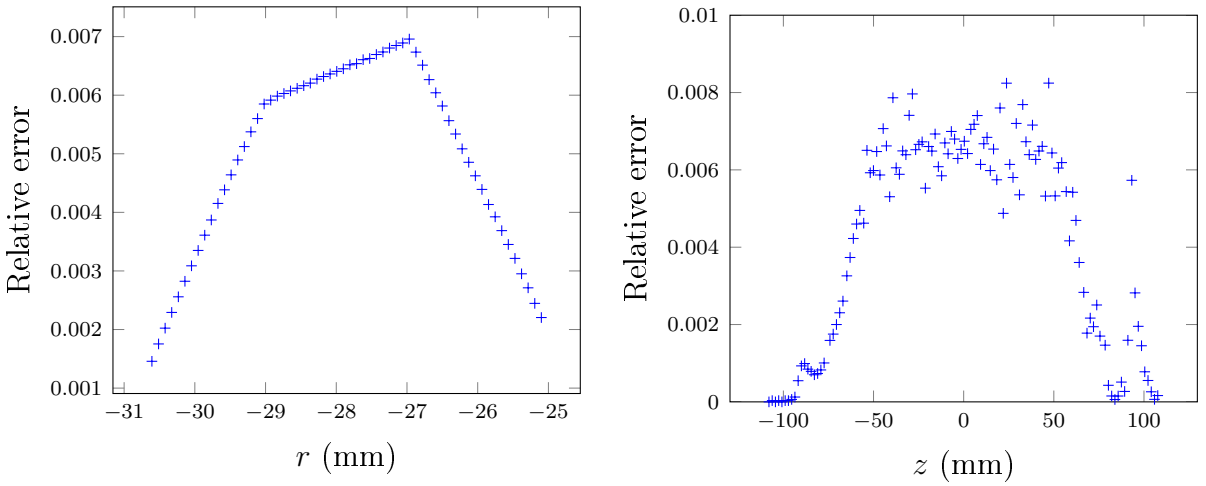

(a) Along helix radius

(b) Along vertical direction

Figure 10.1 – Difference on temperature between the two models along axial and radial directions

The relative difference observed in Figure 10.1 is lower than 1% which confirms that the temperature data input is coherent in both models. Moreover, this comparison sustains the validation of the electro-thermal model.

10.2 Thermal dilatation only

In this section, we consider the displacement and the stress coming only from the thermal dilatation, displayed in Figure 10.2. The Lorentz forces resulting from the magnetic field are not considered.

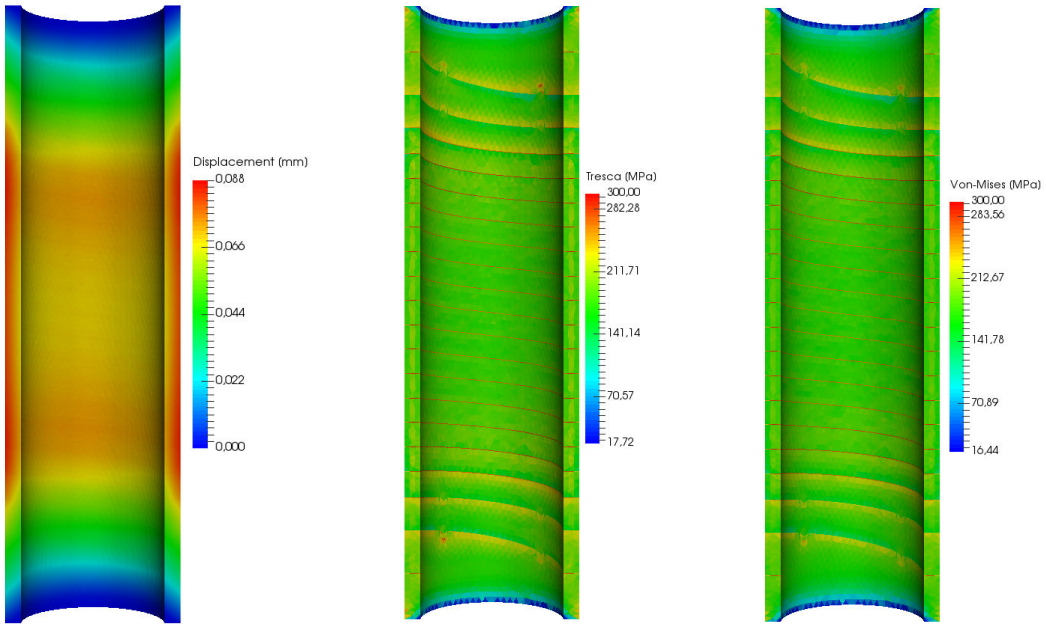

(a) Displacement

(b) Tresca

(c) Von-Mises

Figure 10.2 – Displacement and stress criterions with thermal dilatation only

Figure 10.3a (resp. 10.3b) illustrates the difference in terms of displacements over the radial (resp. vertical) direction. Due to the small order of magnitude for displacements, we consider absolute difference instead of relative one.

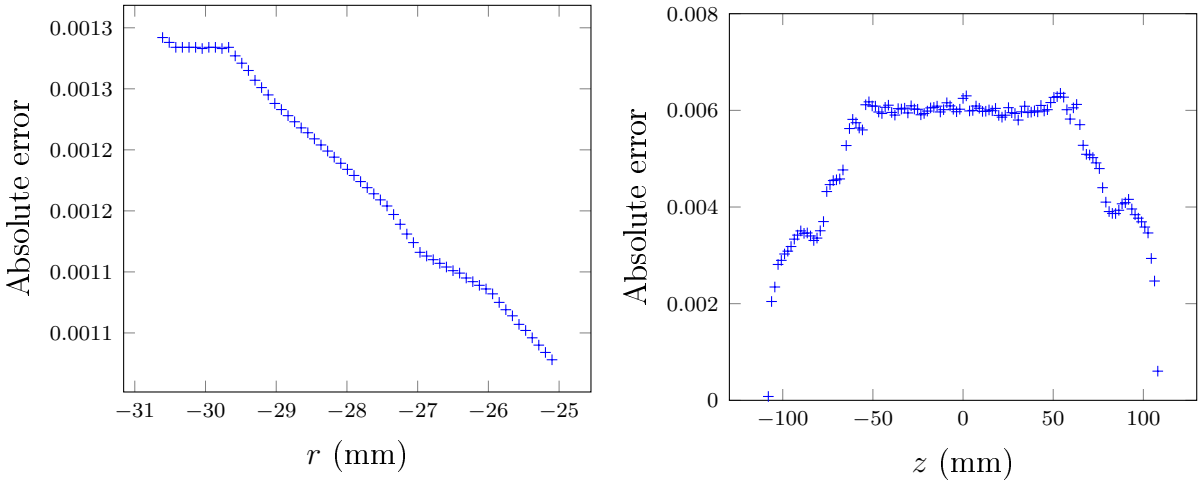

(a) Along helix radius

(b) Along vertical direction

Figure 10.3 – Difference on displacements between the two models along axial and radial directions with thermal dilatation only

Figure 10.3 shows an absolute difference less than a hundredth millimeter in both cases. This low difference can be due to the one observed for temperature field in the previous section.

As to the stress resulting from the thermal dilatation, the figures 10.4a and 10.4b (resp. 10.5a and 10.5b) focus on the Tresca (resp. Von-Mises) criterions values obtained on the same locations as previously.

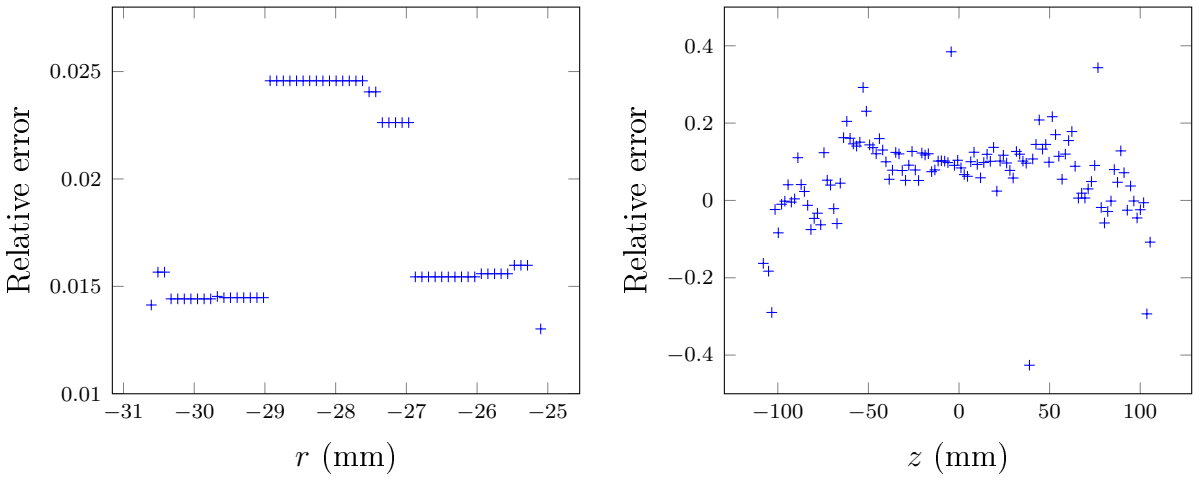

(a) Along helix radius

(b) Along vertical direction

Figure 10.4 – Difference on Tresca criterion between the two models along axial and radial directions with thermal dilatation only

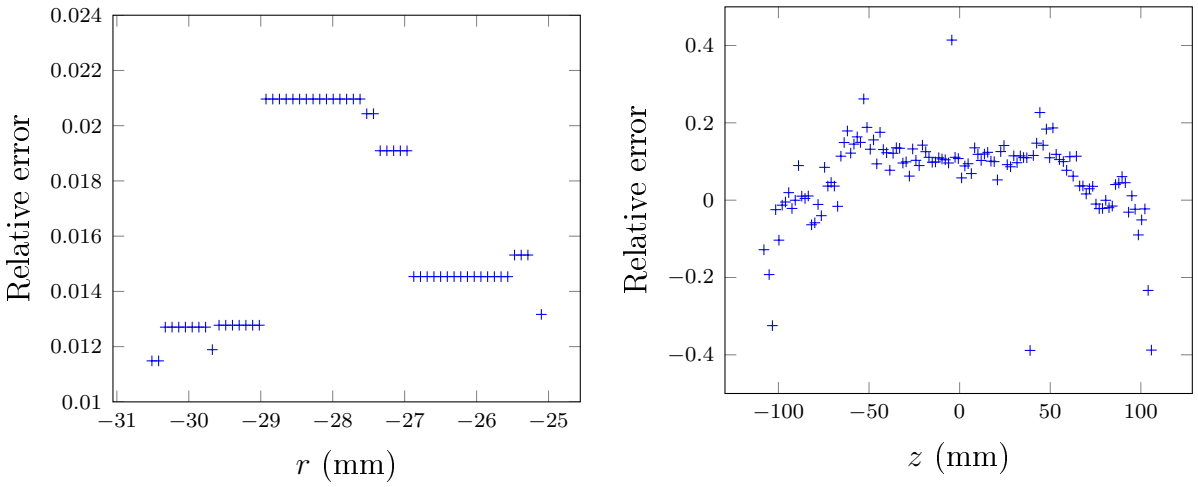

(a) Along helix radius

(b) Along vertical direction

Figure 10.5 – Difference on Von-Mises criterion between the two models along axial and radial directions with thermal dilatation only

If the order of magnitude is coherent between the models, our model tends to overestimate the stresses. As for displacement (Figure 10.3), this can be due to the overestimation of temperature illustrated in Figure 10.1.

10.3 Lorentz forces only

This section focuses on the displacement and stress coming from the Lorentz forces only. These corresponding fields are displayed in Figure 10.6.

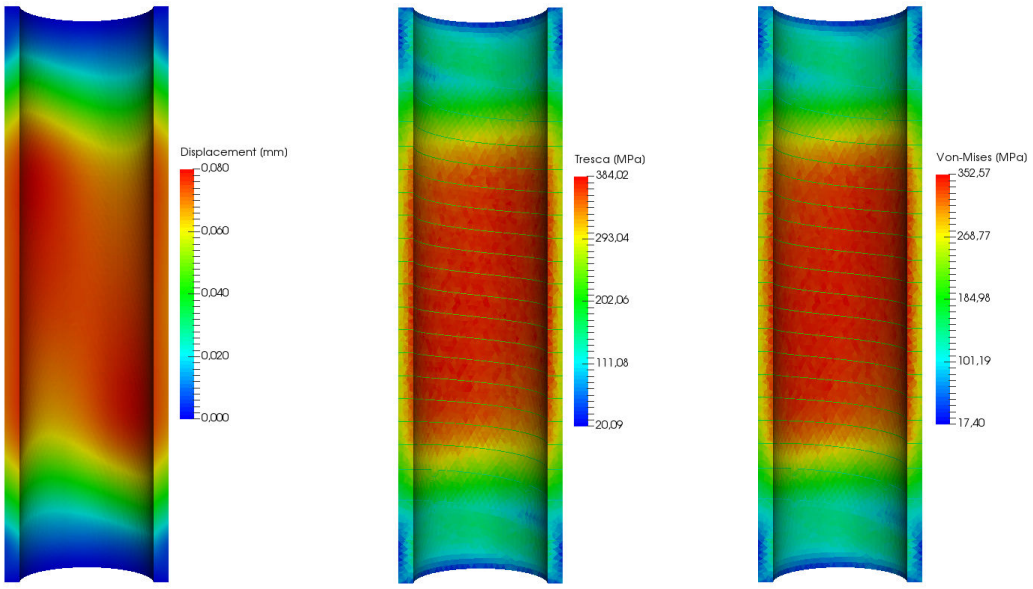

(a) Displacement

(b) Tresca

(c) Von-Mises

Figure 10.6 – Displacement and stress criterions with Lorentz forces only

The figures 10.7a and 10.7b illustrates the comparison of displacements resulting from magnetic forces over the radial and the vertical axis respectively.

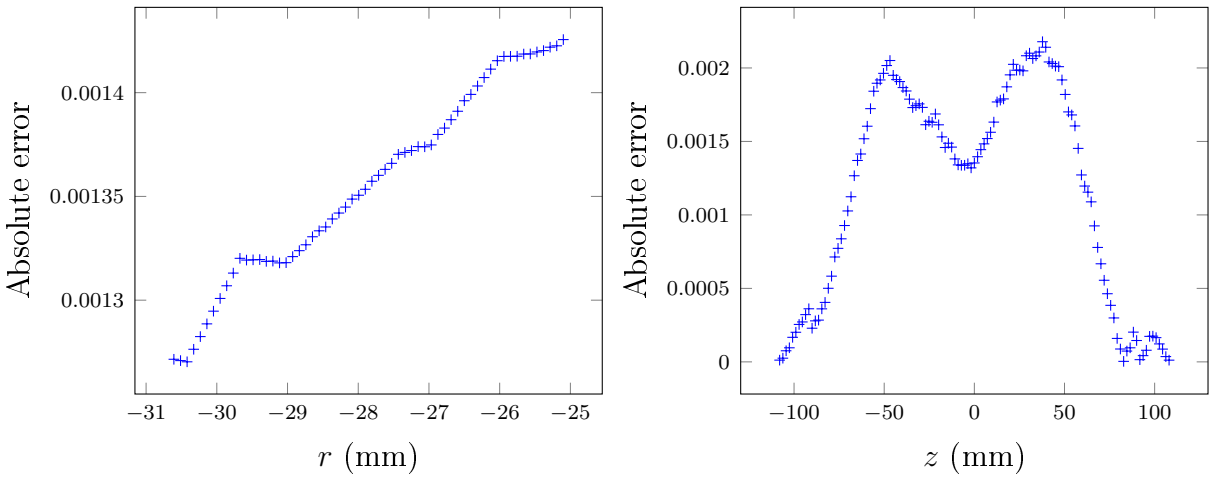

(a) Along helix radius (b) Along vertical direction

Figure 10.7 – Difference on displacements between the two models along axial and radial directions with Lorentz forces only

The results obtained along the radius (Figure 10.7a) are similar to ones obtained with thermal dilatation only, for which the absolute difference doesn't exceed $2 \cdot 10^{-3}$ mm. As to the values obtained along the vertical direction (Figure 10.7b), the models coincide more than in the previous case.

As previously, the comparison continues with the values of the stresses criterion. Figure 10.8a and 10.8b (resp. 10.9a and 10.9b) display them both along the vertical and the radial axis.

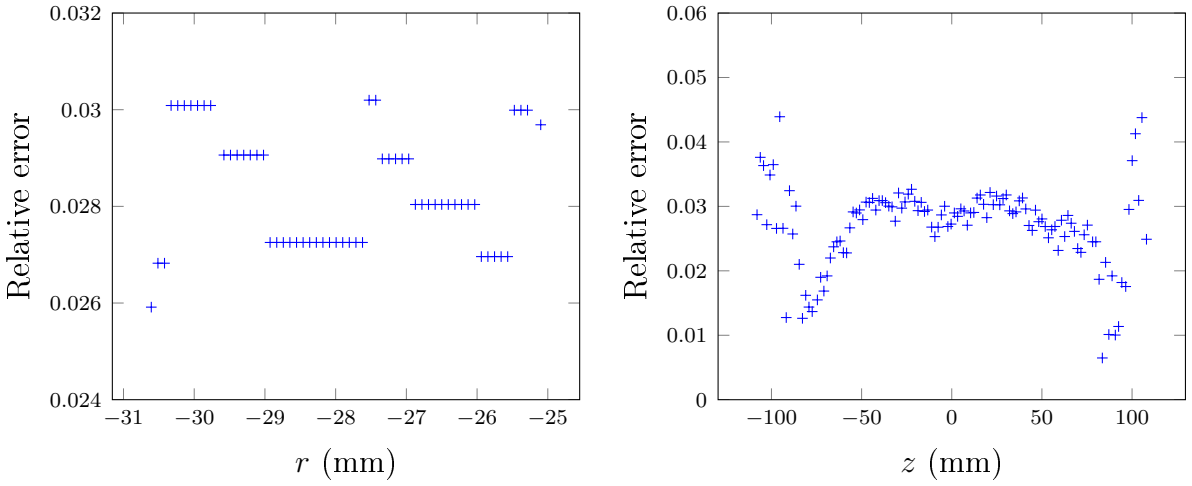

(a) Along helix radius (b) Along vertical direction

Figure 10.8 – Difference on Tresca criterion between the two models along axial and radial directions with Lorentz forces only

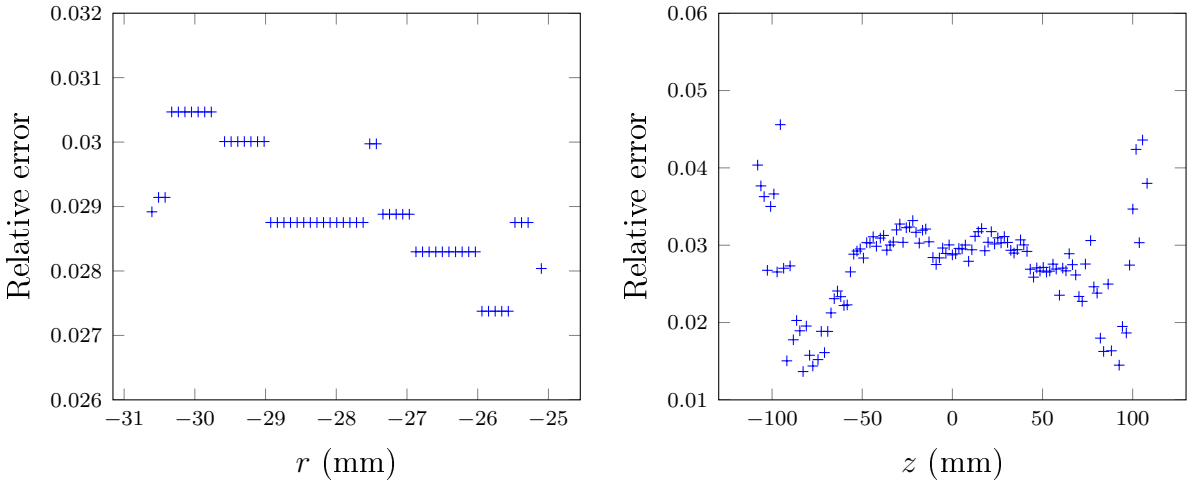

(a) Along helix radius (b) Along vertical direction

Figure 10.9 – Difference on Von-Mises criterion between the two models along axial and radial directions with Lorentz forces only

The relative difference between our model and Ansys software are similar with the one observed with thermal dilatation only, over the radial axis. Nevertheless, this difference is significantly lower than in figures 10.4b and 10.5b over the vertical axis. We remind that the magnetic field data comes from the same computation for both models.

10.4 Thermal dilatation and Lorentz forces

Finally, this last section illustrates the comparison with both Lorentz and thermal dilatation forces (Figure 10.10).

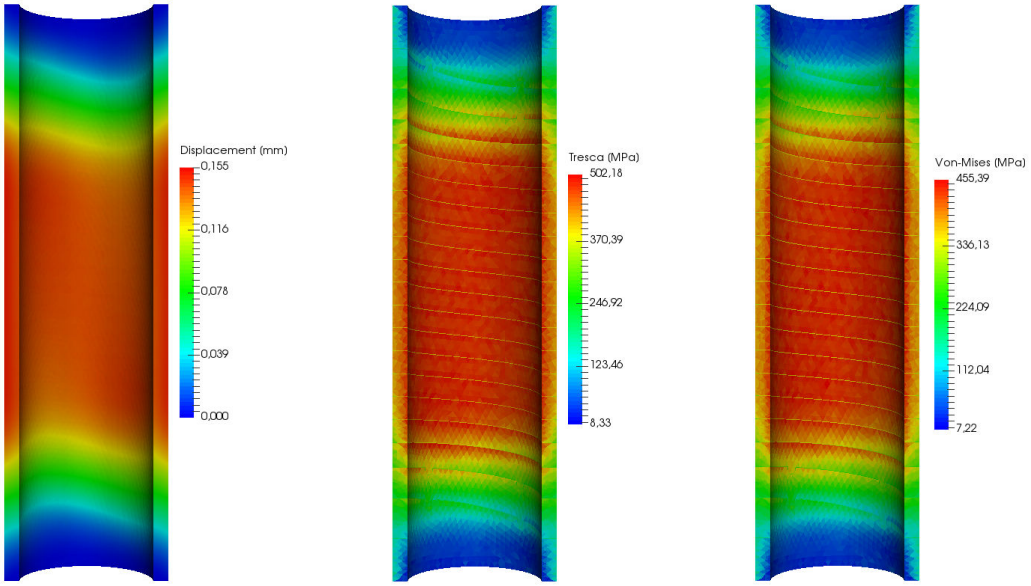

(a) Displacement (b) Tresca (c) Von-Mises

Figure 10.10 – Displacement and stress criterions with both Lorentz and thermal dilatation forces

The figures 10.11a and 10.11b display the differences between the two models along axial and vertical directions, in terms of displacements. The figures 10.12a and 10.12b focus on the Tresca yield strength, while Figure 10.13a and 10.13b concern the Von-Mises criterion. The resulting differences come close to the sum of the differences obtained with thermal dilatation only (Section 10.2) and Lorentz forces only (Section 10.3). We consider these values as sufficiently low to meet the objectives of our model.

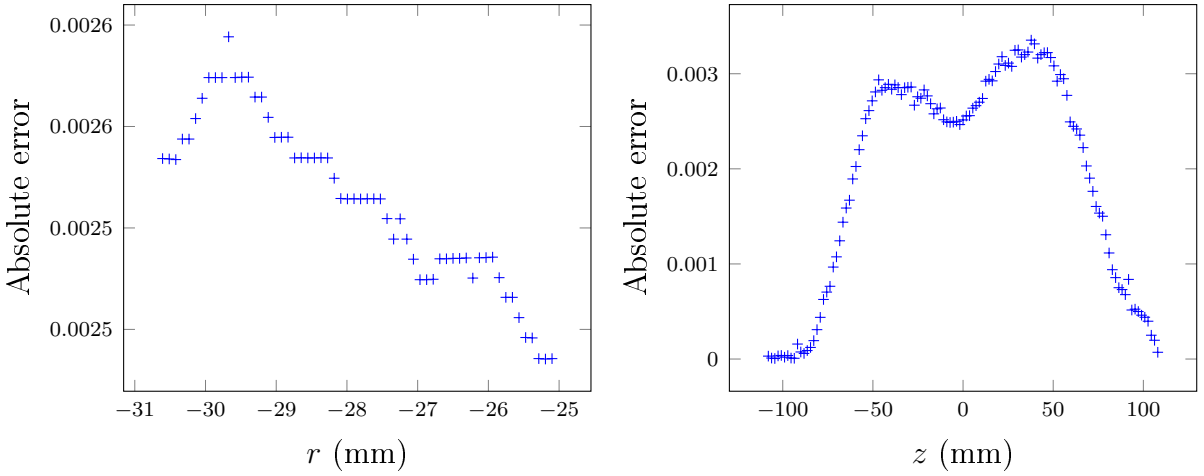

(a) Along helix radius

(b) Along vertical direction

Figure 10.11 – Difference on displacements between the two models along axial and radial directions with both Lorentz and thermal dilatation forces

We shall even note that the absolute difference obtained for displacements over the vertical axis are lower than previously, as if the two previous differences compensate.

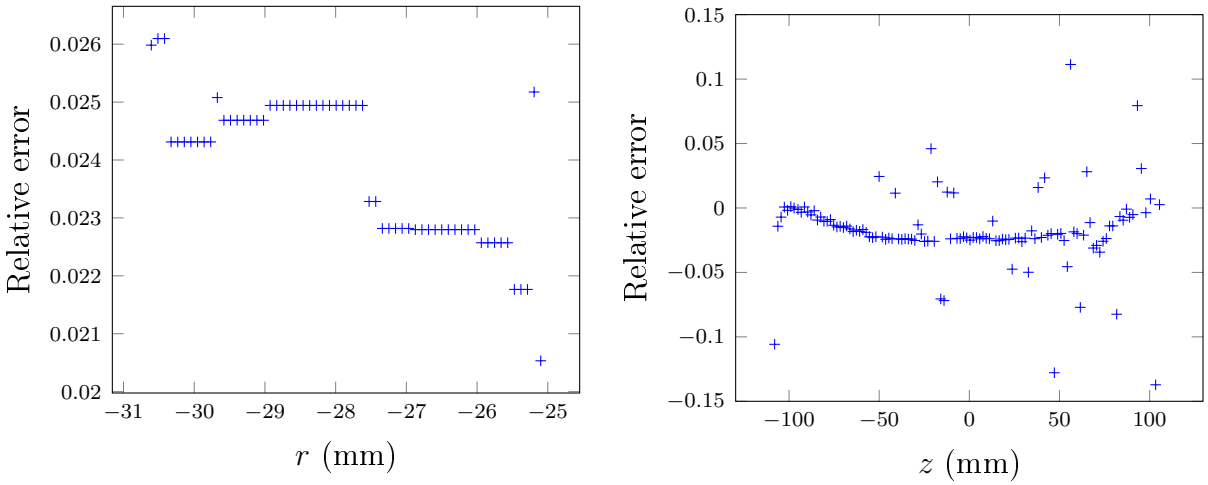

(a) Along helix radius

(b) Along vertical direction

Figure 10.12 – Difference on Tresca criterion between the two models along axial and radial directions with both Lorentz and thermal dilatation forces

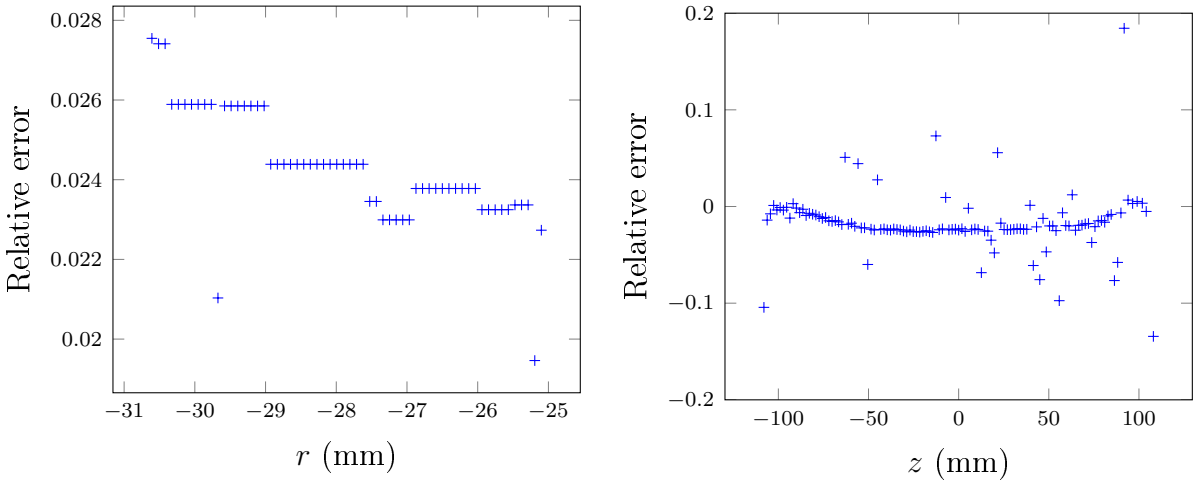

(a) Along helix radius

(b) Along vertical direction

Figure 10.13 – Difference on Von-Mises criterion between the two models along axial and radial directions with both Lorentz and thermal dilatation forces

Conclusion

In this chapter, we detail the validation of the linear elasticity model coupled with the electro-thermal and the magnetostatic ones. In the absence of experimental measurements, the validation is based on the comparison with dedicated commercial software. The coupling with the electro-thermal model through the thermal dilatation phenomenon and with the magnetostatic model to take into account the Lorentz forces are considered separately. In both cases, the comparison of the resulting displacements as well as the stress criterions proves the validity of our model.

Chapter 11

SER applied to the electro-thermal model

This section investigates the application of the SER method introduced in Section 2.3 on the reduced electro-thermal model detailled in Chapter 4. The objective is to assess the feasability and the relevance of this method in the context of high field magnets.

The first application focuses on the sector of Bitter magnet, already introduced in sections 8.2 and 8.3. As for the 2D benchmark, we compare the results obtained through the SER method and its variants with their equivalent coming from the standard reduced basis methodology. Moreover, this study investigates as well the impact of the training set size within the EIM building step.

The second part focuses on the computational time and especially on the gain offered by SER within the EIM Greedy algorithm. To this end, we apply SER on a larger problem, for which it has been initially designed. This application focuses on the radial helix introduced in Section 8.1.2.

Contents

11.1 Application to a Bitter magnet

The first application, aiming to highlight the feasibility of SER within the multi-physics electro-thermal model, is based on the geometry of the Bitter magnet's sector already used in the context of parametric studies. Apart from the previous numerical experiments of sections 8.2 and 8.3, all parameters vary into the ranges displayed in Table 11.1. In this section, we are interested both in the errors on the solution and on the output introduced in (2.38) and in the convergence study of the method. In addition to the maximal values of these errors, we investigate their average value over a set of parameters of size 1000 which remains the same throughout the study.

σ_0	$[40 \times 10^6, 60 \times 10^6]$ $MS.m^{-1}$
α	$[3.3 \times 10^{-3}, 3.5 \times 10^{-3}]$ K^-1
L	$[2.5 \times 10^{-8}, 2.9 \times 10^{-8}]$
$\mathbf{j}$	$[30 \times 10^6, 100 \times 10^6]$ $A.m^{-2}$
h	$[50000, 65000]$ $W.m^{-2}.K^{-1}$
T_w	$[293, 313]$ K

Table 11.1 – Input parameters

EIM trainset of size 100 We start by considering a trainset of size 100 in the EIM building step. Table 11.2 displays the behavior obtained applying the standard RB methodology.

N	M	$max(\epsilon^u_{M,N})$	$max(\epsilon^s_{M,N})$	$mean(\epsilon^u_{M,N})$	$mean(\epsilon^s_{M,N})$
5	5	1.64e+1	1.94e-1	1.51e+0	1.69e-2
10	10	6.84e+0	8.24e-2	4.90e-1	5.96e-3
15	15	6.30e-2	4.90e-4	5.33e-3	3.16e-5
20	20	1.31e-2	1.65e-4	1.28e-3	1.33e-5
25	25	9.80e-3	6.74e-5	6.88e-4	5.77e-6

Table 11.2 – Standard method - EIM trainset size = 100

To start with, Table 11.3 displays the maximum and average values of the errors resulting from the application of the initial SER method, within the reduced electro-thermal model. This numerical experiment relies on a random selection process for the RB approximation space building step, similar to the standard method illustrated in Table 11.2.

N	M	$max(\epsilon^u_{M,N})$	$max(\epsilon^s_{M,N})$	$mean(\epsilon^u_{M,N})$	$mean(\epsilon^s_{M,N})$
5	5	1.05e+1	2.09e-2	1.26e+0	3.27e-3
10	10	5.07e-1	3.42e-3	1.05e-1	4.69e-4
15	15	5.24e-1	1.05e-3	3.95e-2	1.18e-4
20	20	9.23e-2	1.89e-4	8.78e-3	2.79e-5
25	25	3.26e-2	1.90e-4	3.59e-3	2.72e-5
30	30	7.48e-3	6.62e-5	1.14e-3	8.02e-6
40	40	4.59e-3	5.10e-5	6.19e-4	5.12e-6
50	50	4.17e-3	5.03e-5	1.86e-4	1.47e-6
60	60	4.17e-3	5.04e-5	1.79e-4	1.59e-6

Table 11.3 – SER - Random - EIM trainset size = 100

The conclusion resulting from the comparison of the tables 11.3 and 11.2 are multiple. First of all, it allows to confirm the behavior observed with the 2D benchmark namely slightly higher errors for a same number of basis functions. The further study up to 60 basis functions also show that the errors obtained with the standard RB methodology are reachable through SER enriching the considered approximation spaces. Nevertheless, the resulting errors eventually reach a plateau.

Still considering the initial SER method, Figure 11.1 illustrates the convergence study performed for each considered EIM approximations. As expected, the observed behavior is similar to the preliminary studies performed in the context of the benchmark.

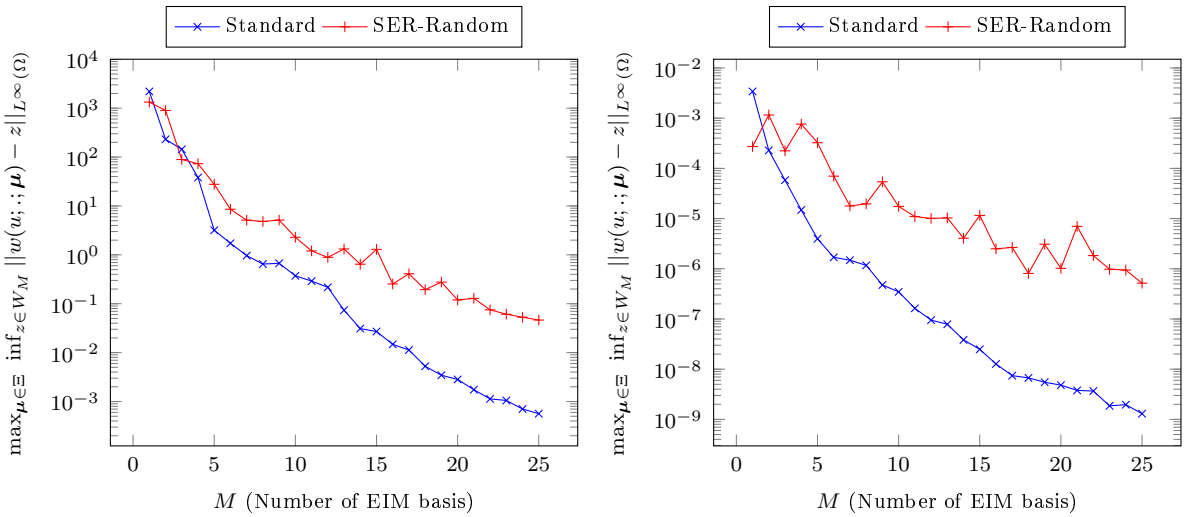

(a) EIM $\sigma(T)$ (b) EIM $k(T)$

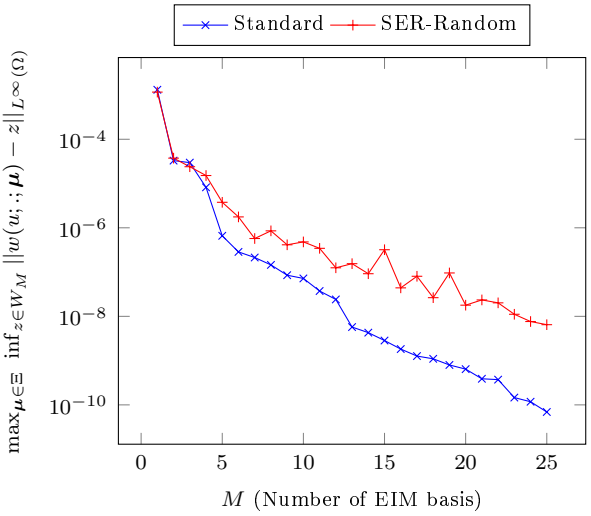

(c) EIM $\sigma(T)\nabla V \cdot \nabla T$

Figure 11.1 – EIM convergence study - Comparison of standard and SER random

Figures 11.2a and 11.2b concerns the convergence obtained from the reduced basis solution and output. Although the SER method tends to degrade the convergence of the solution, the convergence of the output seems not to be significantly impacted. These results especially support the relevance of SER in the context of parametric studies or uncertainty quantification.

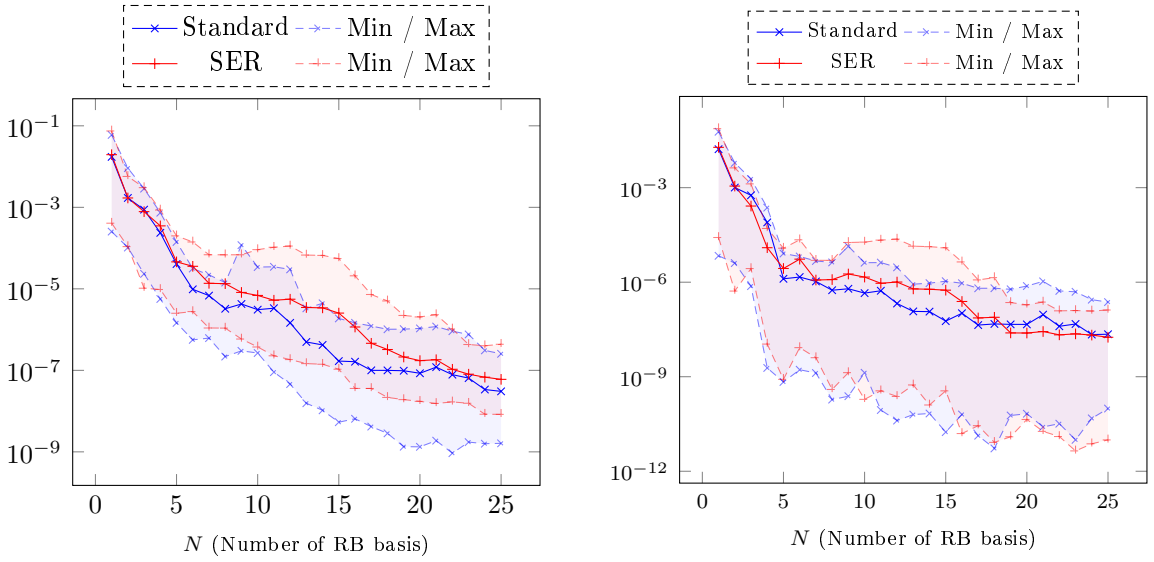

(a) RB solution

(b) RB output

Figure 11.2 – RB convergence study - Comparison of standard and SER random

Based on the same EIM trainset, the next study focuses on the error indicator introduced in Section 2.3.1. Table 11.4 illustrates its use through the parameter selection process during RB offline stage. This consists of the first variant investigated for SER. The Greedy algorithm displays little impact on the 2D benchmark (Table 2.2), however in this application it proves to have a significant influence.

N	M	$max(\epsilon^u_{M,N})$	$max(\epsilon^s_{M,N})$	$mean(\epsilon^u_{M,N})$	$mean(\epsilon^s_{M,N})$
5	5	7.66e+0	2.71e-2	1.25e+0	7.88e-3
10	10	3.37e-1	7.82e-4	1.49e-1	1.97e-4
15	15	4.85e-2	2.64e-4	1.75e-2	5.02e-5
20	20	2.93e-2	3.40e-4	3.48e-3	2.68e-5
25	25	5.23e-3	4.59e-5	1.21e-3	3.47e-6

Table 11.4 – SER - Greedy - EIM trainset size = 100

Lastly, Table 11.5 studies the effect of the $r-$adaptation variant on the considered application. Similarly with the results obtained on the 2D benchmark, this variant doesn't show any improvement compared with the previous one. By contrast, it even tends to deteriorate the reduced basis solution.

N	M	$max(\epsilon^u_{M,N})$	$max(\epsilon^s_{M,N})$	$mean(\epsilon^u_{M,N})$	$mean(\epsilon^s_{M,N})$
5	5	6.26e+0	2.00e-2	1.41e+0	6.26e-3
10	10	8.53e-1	8.34e-3	3.89e-1	1.23e-3
15	15	6.73e-1	7.34e-4	3.61e-1	2.56e-4
20	20	3.64e-1	3.57e-4	1.34e-1	4.22e-5
25	25	8.23e-2	2.49e-4	2.39e-2	2.41e-5

Table 11.5 – SER - Greedy - $r-$adaptation (EIM 20%, RB 20%)

Figure 11.3 compares the convergence of the EIM approximations, for the introduced

SER variants. It adds the results related with the use of the error indicator to the previous ones introduced in Figure 11.1. In coherence with the previous analysis based on the errors, these graphs highlight the influence of the smart parameter selection offered by the use of a Greedy algorithm in the RB approximation space building step. The low impact of the $r-$adaptation variant in this context is also visible through these convergence studies.

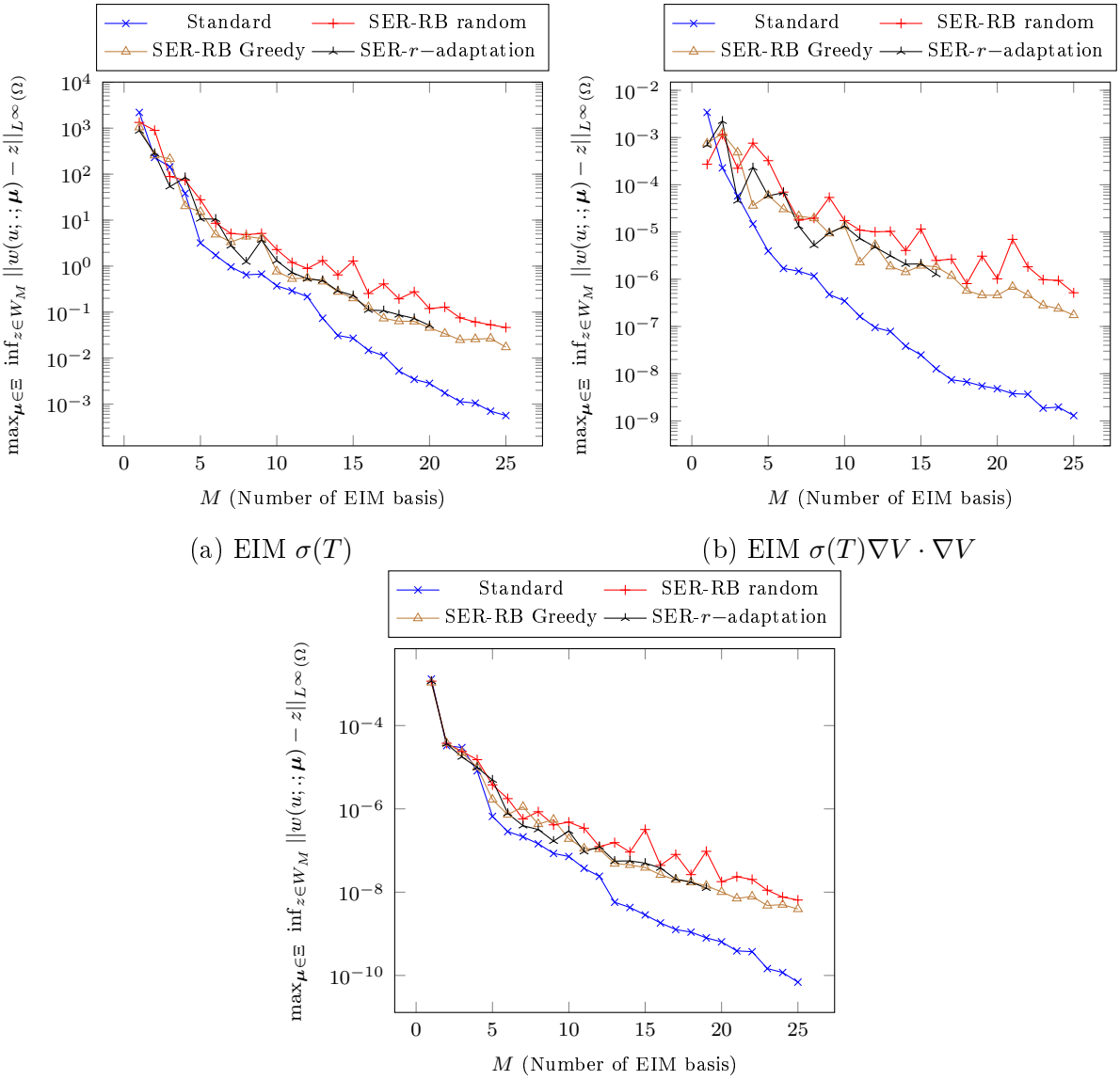

(a) EIM $\sigma(T)$

(b) EIM $\sigma(T)\nabla V \cdot \nabla V$

(c) EIM $k(T)$

Figure 11.3 – EIM convergence study - Comparison of standard and SER Greedy

We conclude this analysis by the study of the error indicator behavior used during the RB offline stage. Figure 11.4 plots the maximal values obtained in the parameter selection process at each step of the RB approximation space enrichment. This graph first allows to ensure that the expect behavior is obtained, namely the decrease of the error indicator with the size of the RB approximation space. It confirms also the previous remark concerning the $r-$adaptation method which does not improve the situation.

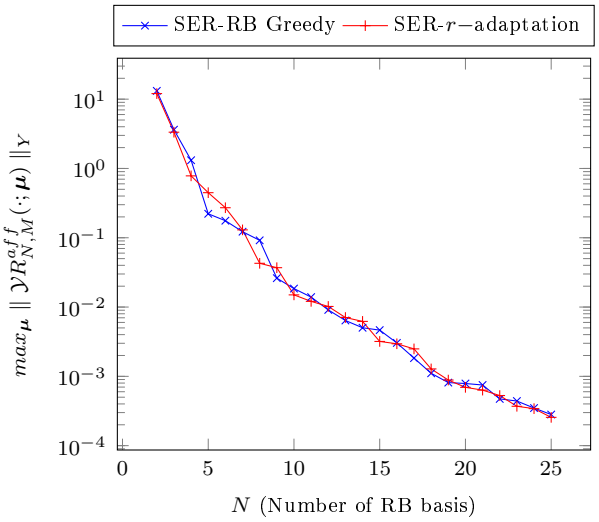

Figure 11.4 – Error indicator $\parallel \mathcal{Y}R^{aff}_{N,M}(\cdot;\boldsymbol{\mu}) \parallel_Y$ used in RB Greedy algorithm.

Regarding the SER multi-levels variant, the first results obtained on this application are illustrated in Figure 11.5. Like in the 2D benchmark, we observe an improvement of the EIM approximations convergence from the 2nd SER level. Although it doesn't allow to reach the behavior obtained with the standard RB methodology, these preliminary results tend to confirm the relevance of the multi-levels SER method.

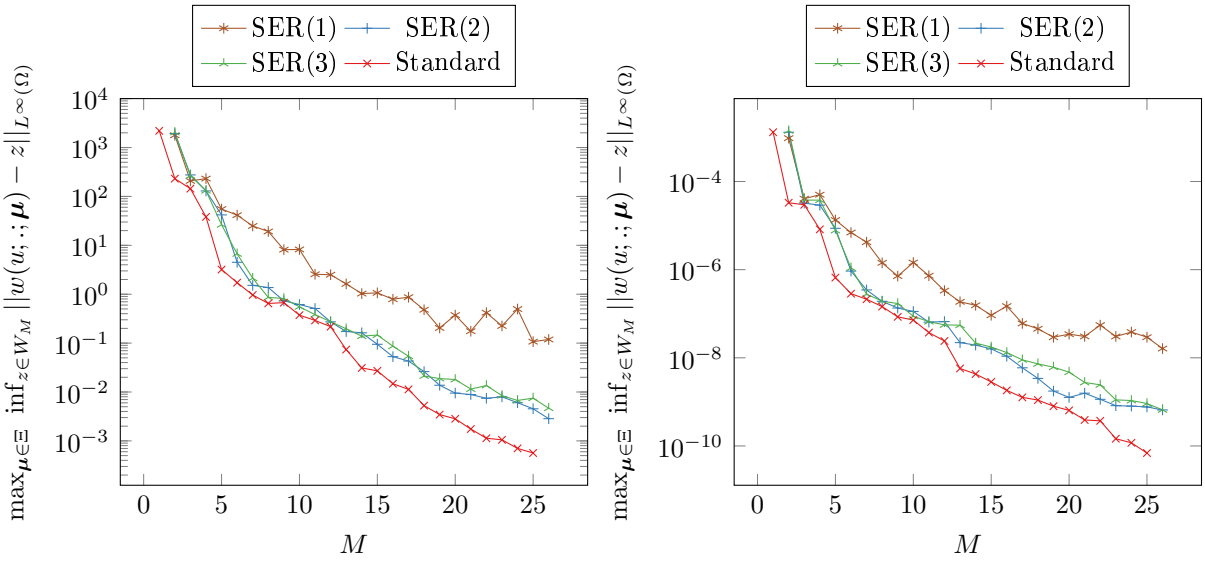

(a) EIM $\sigma(T)$ (b) EIM $k(T)$

Figure 11.5 – SER multilevel - Random - EIM convergence

We point out that the preliminar results presented in Figure 11.5 for the SER multi-levels variant need to be further developed. This variant gives promising results, but its implementation is recent. It still needs to be verified and validated for such multi-physics applications.

EIM trainset of size 1000 We continue this numerical experiment by investigating the influence of the EIM trainset size. To this end, we turn to a trainset of size 1000 which is thus ten times larger than the previous one. We note that there is no relations between this new trainset and the previous one. Table 11.6 displays the errors obtained with the SER method combined to the Greedy algorithm at the RB approximation space building step. Compared to its equivalent with the previous trainset illustrated by Table 11.4, the increase of the trainset set size does not seem to have a significant impact.

N	M	$max(\epsilon^u_{M,N})$	$max(\epsilon^s_{M,N})$	$mean(\epsilon^u_{M,N})$	$mean(\epsilon^s_{M,N})$
5	5	9.53e+0	3.57e-2	1.49e+0	5.59e-3
10	10	3.97e-1	1.74e-3	1.47e-1	7.85e-4
15	15	7.82e-2	1.93e-4	1.51e-2	4.51e-5
20	20	2.66e-2	8.03e-5	5.39e-3	2.22e-5
25	25	6.61e-3	4.84e-5	1.63e-3	1.07e-5

Table 11.6 – SER- RB Greedy - EIM trainset size = 1000

This consideration is supported by Figure 11.6 which compares the convergence of the EIM approximations in this context with the previous convergence studies.

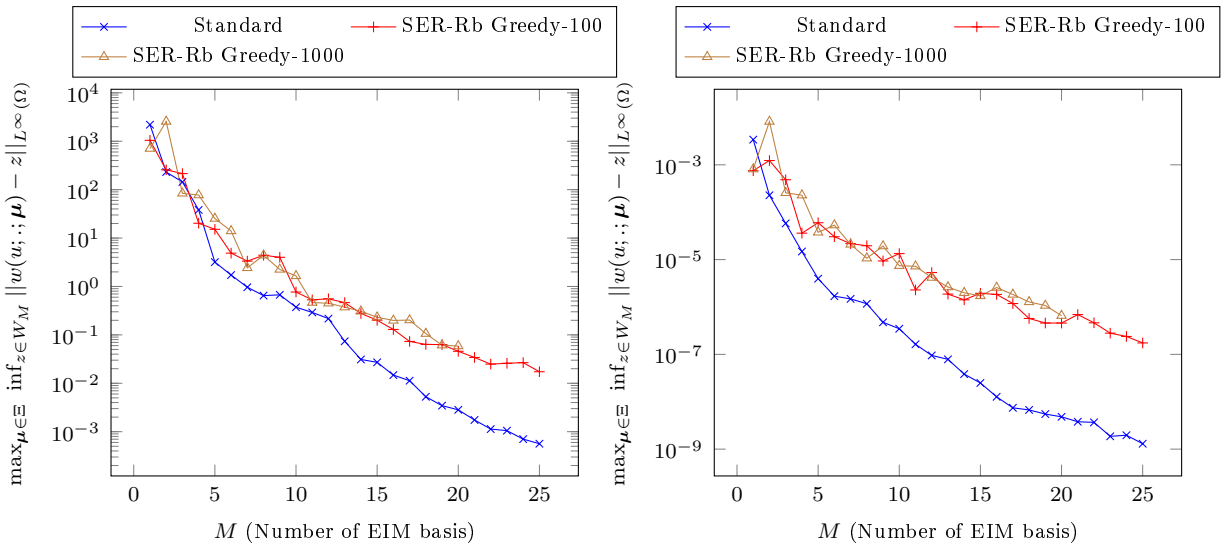

(a) EIM $\sigma(T)$

(b) EIM $\sigma(T)\nabla V \cdot \nabla V$

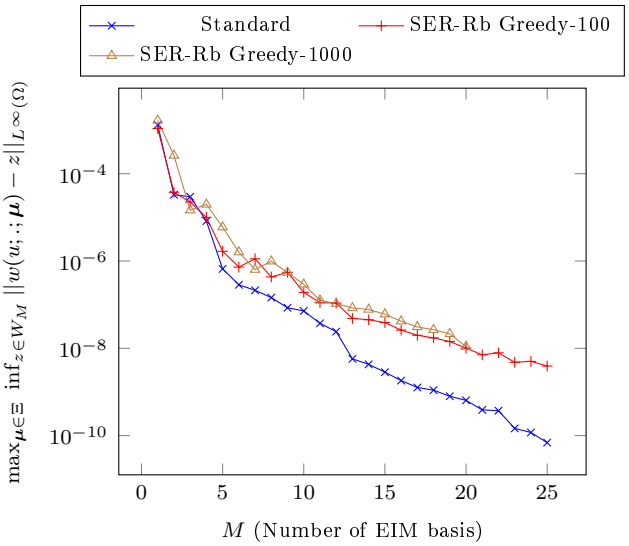

(c) EIM $k(T)$

Figure 11.6 – EIM convergence study - Eim training set of size 1000

11.2 Application to a polyhelix

Still based on the electro-thermal model, the second application focuses on the radially cooled helix introduced in Section 8.1.2. We now investigate the potential gain offered by the SER method for this larger problem. This numerical experiment compares the computational time required by the standard methodology and by SER on such a problem.

The mesh used in this study is composed of 2.2 millions of tetrahedrons, for approximately 500000 nodes (see Figure 8.1). The next simulations are performed on 12 processors, on a computer equipped with 2 multi-threaded 6 cores CPUs and 141 GB of shared memory. Like in Section 11.1 with the Bitter magnet, all input parameters vary. The ranges displayed in Table 11.7 are equivalent to the ones used in the sensitivity analysis of Section 8.1.2. The current density is replaced by the difference of potential V_D which directly gives the Dirichlet boundary condition on electrical potential.

σ_0	$[50 \times 10^6, 50.2 \times 10^6]$ $MS.m^{-1}$
α	$[3.3 \times 10^{-3}, 3.5 \times 10^{-3}]$ K^-1
L	$[2.5 \times 10^{-8}, 2.9 \times 10^{-8}]$
V_D	$[55, 65]$ V
h	$[70000, 90000]$ $W.m^{-2}.K^{-1}$
T_w	$[293, 313]$ K

Table 11.7 – Input parameters

The next study is based on EIM and RB approximation spaces of size 5. It aims to compare the computational time necessary to perform the EIM Greedy algorithm with the standard RB methodology and with the introduced SER method. To this end, we focus on the EIM approximation related with the electrical conductivity $\sigma(T)$ for which

the trainset is composed of 100 parameters.

Consisting of the same finite element solve in both cases, the computational time related with the initialization of the EIM building step is approximately 1760 seconds. From there, the SER method uses the reduced basis approximation which results from the first EIM basis function, while the standard methodology uses finite elements approximations. Regarding the first EIM Greedy algorithm for which the available reduced basis approximation relies on a single basis function, the mean time required to solve the reduced problem is 2.1 seconds compared with 2087 seconds for the corresponding finite element one. Regarding the whole set of resolutions performed within the EIM Greedy algorithm, this amounts to a factor close to 500 in terms of computational time.

Through each stage of the SER method, the EIM basis functions are built from a set of reduced basis approximations based on an enriched RB approximation space. In this context, Table 11.8 displays the mean time necessary for a single resolution and the resulting gain factor related with the whole EIM Greedy algorithm.

N	Mean time per online realization (s)	EIM Greedy algorithm gain factor
1	2.1	495
2	4.3	321
3	7.7	213
4	6.1	254

Table 11.8 – Performances of the SER method on a large scale multi-physics problem

The standard methodology with $N = M = 5$ results in an maximal output error of 4.5×10^{-2}, still considering the mean temperature over the domain as output. Only the SER method combined with the use of the error indicator (see Section 2.3.1) ensures the convergence of the online solver, which results in a maximal error of 2.1×10^{-1} compared with the finite element approximation.

The initial SER method using a random selection process regarding the building of the RB approximation space shows convergence problems on some inputs. This proves the relevance of a smart selection process in such a context.

Conclusion

As seen in the Chapter 8, the use of model order reduction is essential to perform efficiently parametric studies and sensitivity analysis in the context of high field magnet modeling. Nevertheless, the computational cost related with the EIM approximations carried out by the offline stage can remain prohibitive.

The SER method and its variants, introduced in Section 2.3, have been designed to address this issue. They are thus well suited for such applications. This section emphasizes on the feasability and the relevance of the SER method used within the reduced electro-thermal model, as a follow up of the results obtained with the 2D benchmark (see Chapter 2). The use of the error indicator (Section 2.3.1) proves essential in this appli-

cation. Especially, it is necessary to ensure the convergence of the method in the second example (Section 11.2). Like in the 2D benchmark, the multi-levels SER(l) is the most promising variant.

Moreover, this sections gives a first review in terms of computational cost of SER compared with standard RB methodology. This confirms the pertinence of this method on 3D industrial non-linear multi-physics application, and suggests that it opens various opportunities in such contexts.

We note that the implementation of the EIM method within the `Feel++` RB framework can be improved. Indeed, some of the operations still depend on the finite element dimension. We can hence expect to decrease the computational time, with an optimized implementation of the EIM algorithm which is currently in progress.

Chapter 12

Hybrid magnet design

As mentioned in introduction, two main technologies are involved to produce magnetic field from electrical current. On one hand, the superconducting magnets which conduct the current without electrical resistance but which are limited in terms of magnetic field intensity. On the other hand, the resistive magnets which are at the basis of high magnetic fields studied in this thesis.

The combination of these two technologies resulting in the so-called hybrid magnets intends to reach continuous field whose intensity exceeds 40 T. The only hybrid magnet currently in operation – located in the United States at the NHMFL, Tallahassee – reaches 45 T in 32 mm bore. In Grenoble, the development of an Hybrid magnet [Pugnat et al., 2016] aiming to reach 45 T is currently in progress.

As illustrated in Figure 12.1b, this magnetic field intensity is the sum of 27.3 T produced by a resistive magnet plus 9.2 T coming from a Bitter magnet and 8.5 T coming from the superconductor outsert.

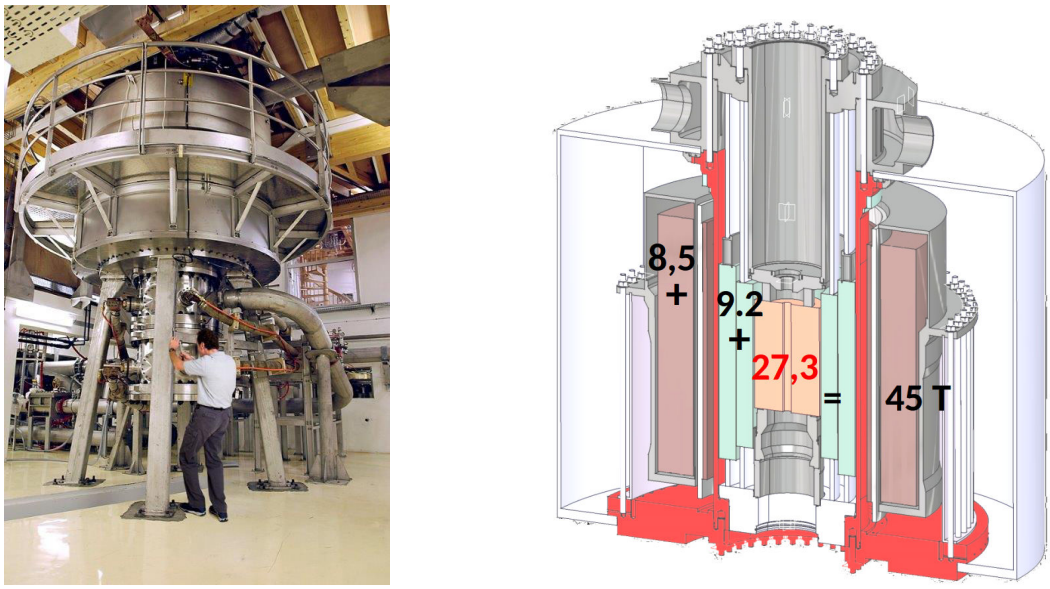

(a) Hybrid site (b) Outline

Figure 12.1 – Illustration of the LNCMI hybrid magnet

In this chapter, we focus on the resistive part based on the polyhelix technology developed at the LNCMI. The resistive insert (Figure 12.2) is composed of 14 longitudinally cooled helices. Its design is all the more challenging due to the background field generated by the superconductor.

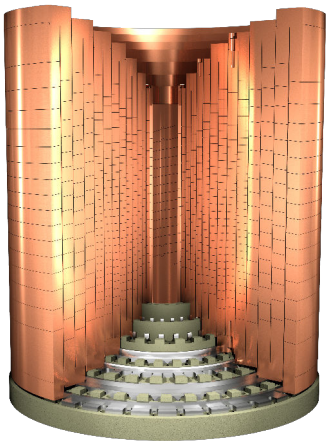

Figure 12.2 – Illustration of the hybrid resistive part

Based on the non-linear coupled multi-physics model introduced in Chapter 3, this study aims to anticipate the behavior of the resistive magnet within its operating environment. The first section focuses on the thermal behavior considering the maximum current intensity available. The second section deals with the resulting magnetic field, while the last one focuses on the mechanical quantities of interest, namely the displacements and stresses coming from the thermal dilatation and the Lorentz forces.

Contents

In each of these sections, we compare the behavior of two resistive magnet inserts. The first one denoted as standard is a polyhelix designed to be operated with only Bitter outsert. The second one is the resistive part of the hybrid magnet illustrated in Figure 12.2. The design of these two magnets composed both of 14 helices slightly differs due to the environment in which they operate.

The two inserts are made of the same copper alloy whose properties are given in Table 12.1. We shall note that such properties cannot be achieved from standard materials. This kind of alloy, which is still the focus of advanced research in the domain of materials, is specifically designed for this use. The cooling parameters are based on measurements obtained from other operating magnets. The helices of these magnets are hold in place by two plates at the top and at the bottom of the insert, while allowing a small vertical displacement. The plates are not considered in our geometry but are modeled by a homogeneous Dirichlet boundary condition at the bottom of the magnet.

σ_0	52.5 $MS.m^{-1}$	h	85000 $W.m^{-2}.K^{-1}$
k_0	380 $W.m^{-1}.K^{-1}$	T_w	292 K
α	3.6×10^{-3} $K^{-}1$	E	120 GPa
L	2.47×10^{-8}	ν	0.33
I	31000 A	α_T	18×10^{-6}

Table 12.1 – Input parameters

From a numerical point of view, the difficulty resides in the size of the problems related with these simulations. The meshes of the two inserts are made directly from the geometries coming from CAD, and indeed reach several millions of tetrahedrons. The number of degrees of freedom comes close to one million and the simulations takes about one hour on 32 processors.

12.1 Temperature

As already explained, the temperature is a critical variable in the context of high field magnets design. This first section introduces the comparison of the thermal behavior in the two resistive magnets. We remind that the design of these two inserts slightly differs, since they are intended to work under different conditions. Nevertheless, the current imposed is the same in both cases reaching an intensity of 31000 A.

Figure 12.3a (resp. 12.3b) illustrates the temperature map within the magnet in standard (resp. hybrid) environment. As expected, the maximum temperature is reached within the most internal helices due to the current density which is higher in this region. Moreover, the difference of design leads to a slightly higher temperature within the hybrid magnet resistive insert which limits all the more the choice in terms of material.

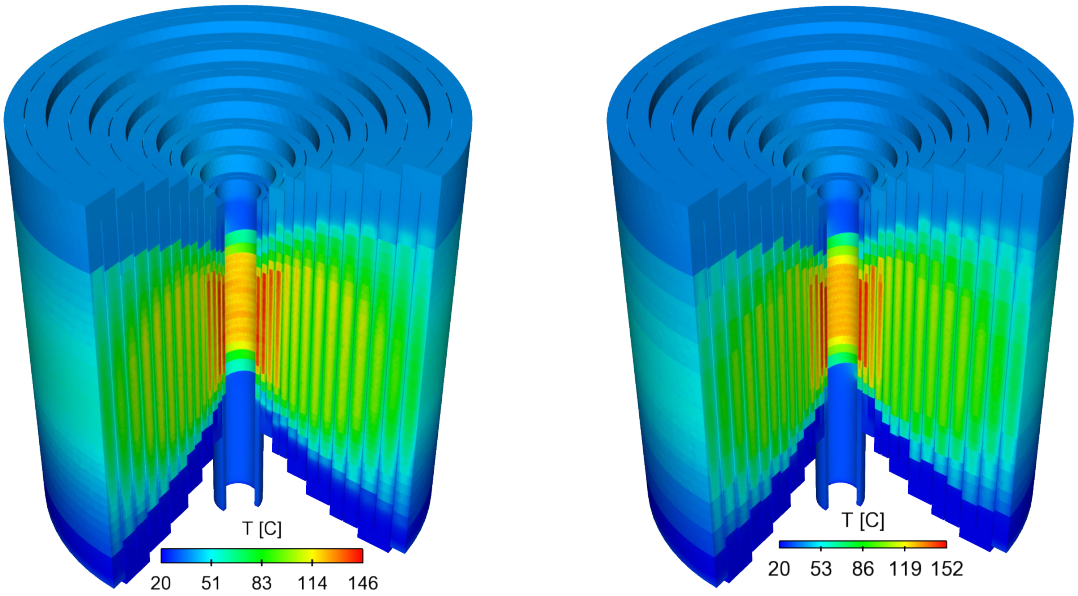

(a) Standard (37 T) (b) Hybrid (45 T)

Figure 12.3 – Temperature on 14 helices magnet insert

This analysis is confirmed by Figure 12.4 which displays the thermal behavior along x axis on the median plan. Besides the temperature values are similar within the external helices, this plot highlights the temperature increase in the most internal helices of the hybrid magnet resistive insert. Indeed, this polyhelix is designed to reach 27.3 T on its own which induces a higher current density on the innermost helices.

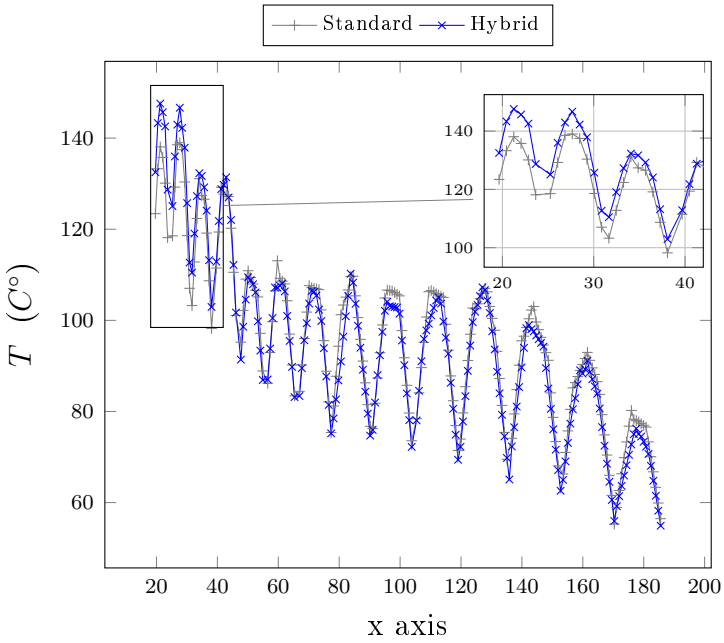

Figure 12.4 – Temperature along x axis on the median plan

12.2 Magnetic field

This second section focuses on the magnetic field computation for the two previous magnets. Although the 3D magnetostatic model has been introduced in Section 3.2 for this purpose, the following study is based on a 2D axisymmetrical analytical model.

Indeed, the add of a surrounding bounding box required to impose the infinity boundary conditions increase the complexity of the problem. For now, we don't succeed in building a mesh which could be appropriate to this 14 helices insert.

Figures 12.5a and 12.5b display the magnetic field map of the considered resistive magnet within their environment. The design optimization of these objects being performed from the employed 2D axisymmetrical model, the obtained magnetic values are in good agreement with the claimed performances. These magnets are indeed designed to reach 37 T and 45 T for a maximal current intensity of 31000 A.

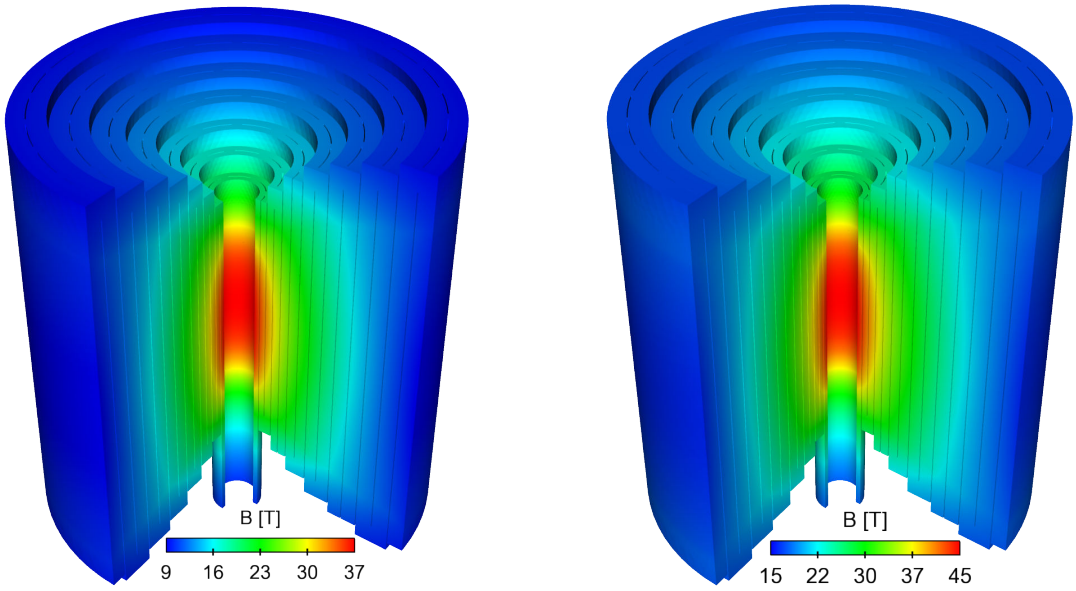

(a) Standard (b) Hybrid

Figure 12.5 – Magnetic field on 14 helices magnet insert

Nevertheless, 3D magnetic field computations have however been performed on a part of the hybrid magnet resistive insert to investigate the impact of its asymmetry, emphasized in Chapter 9. Figure 12.6 displays the magnetic field generated by the 8 innermost helices of this insert. The mesh used for this simulation is composed of 27 millions of tetrahedrons which amounts to 4.3×10^6 vertices and 31.6×10^6 edges on which the H_{curl}-conforming finite element degrees of freedom are located. Performed on 48 processors, the magnetic field computation on its own requires 1.3 hours.

On Figure 12.6, the conductor is colored by the current density imposed to the magnet while the arrows illustrating the 3D magnetic field are colored by its module. Some isosurfaces related with the magnetic field are represented as well.

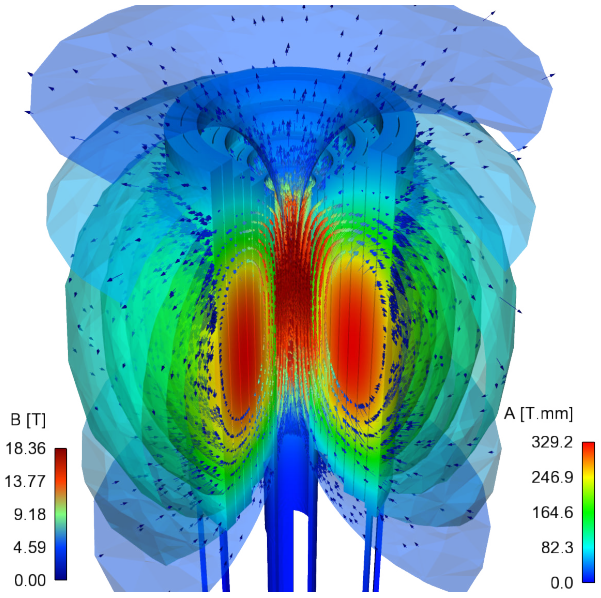

Figure 12.6 – 3D magnetic field

Figures 12.7 and 12.8 compare the 3D magnetic field with the 2D axisymmetrical results along the axis z and along a circle of constant radius $r = 20\ mm$. The maximum magnetic field values along z axis (Figure 12.7a) as well as the magnetic field homogeneity (Figure 12.7b) are in good agreement. This shows that the magnetic field profiles are coherent. In relation with the comparison with the dedicated measurement campaign introduced in Chapter 9, Figure 12.8 confirms the 3D effect previously highlighted.

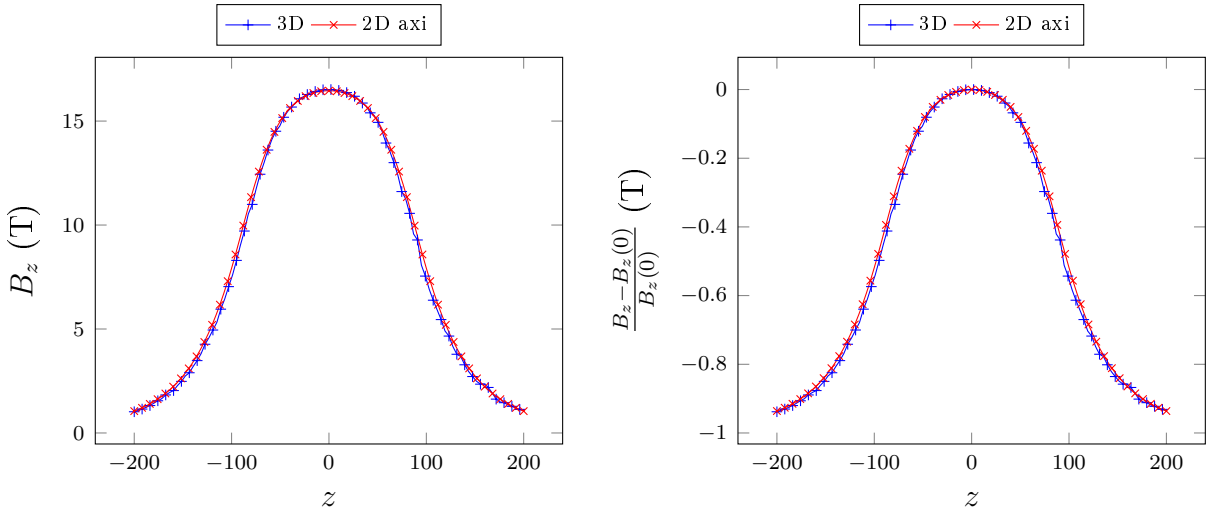

(a) B_z along z axis (b) Homogeneity along z axis

Figure 12.7 – Magnetic field profile along z axis

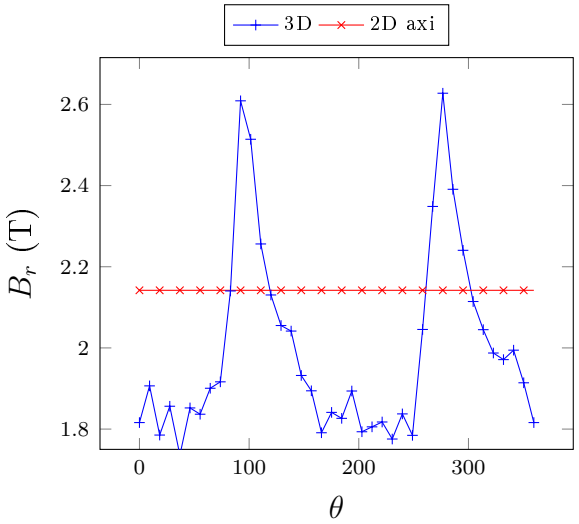

Figure 12.8 – B_r along circle of radius $r = 20\ mm$

12.3 Displacements and stresses

The displacements and the stresses caused both by the thermal dilatation phenomenon and the Lorentz forces is a key point of the high field magnet design as well. Especially, the choice of the material to be used in this context is guided by the estimation of the maximal stresses to support. The latter has to combine a sufficient mechanical resistance

with a suitable electrical conductivity.

To this end, the 3D linear elasticity model introduced in Section 3.4 is coupled with the temperature coming from the electro-thermal computations (see Section 12.1), and with the magnetic field obtained from the 2D axisymmetrical model (see Section 12.2), taking into account the whole magnetic environment.

At first, this model allows to compute the displacements resulting from the thermal dilatation and the magnetic forces as displayed in figures 12.9a and 12.9b. Although they not exceed one millimeter, these displacements remains important compared with the space between two copper tubes.

As described in Figure 12.9 on which the displacements are applied to the considered geometry multiplied by a factor 50, the resulting deformation makes the magnet take a barrel-like shape. This behavior is expected due to the compressive forces at the bottom and at the top caused by the plates allowing to hold the helices in place.

The displacements obtained within the hybrid environment are significantly higher due to the background field of the superconductor which increases the Lorentz forces.

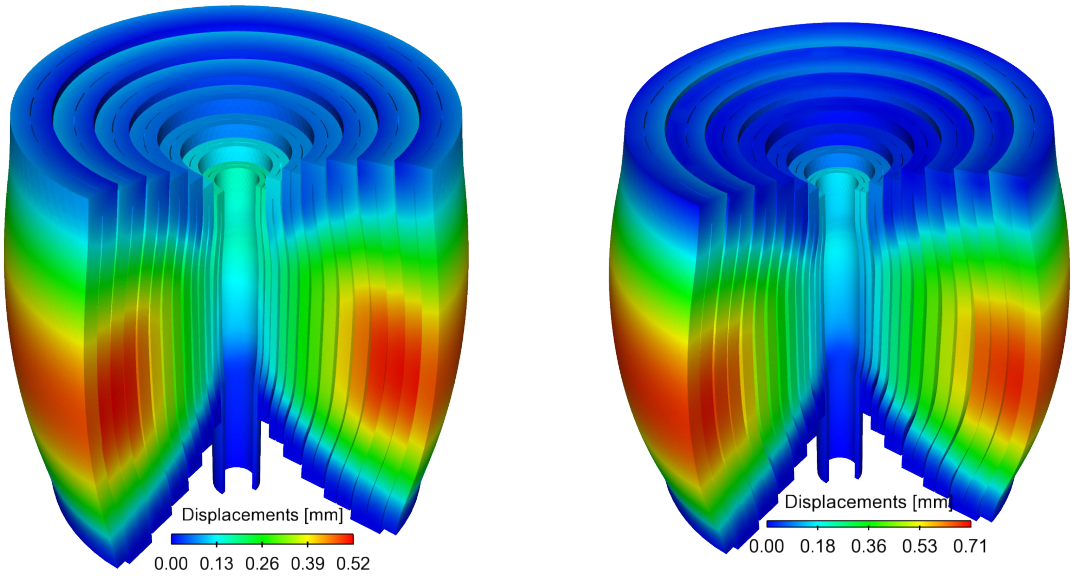

(a) Standard (37 T)

(b) Hybrid (45 T)

Figure 12.9 – Displacements on 14 helices magnet insert

From an engineering point of view, we refer instead to the relative displacement known as strain. The maximum displacement value in the standard case (Figure 12.9a) corresponds to a strain of 0.28% while the maximal displacements in the hybrid environment reaches 0.38%.

While the displacements are concentrated into the most external helices due to their size, this is not the case for the stresses whose repartition highly depends on the design.

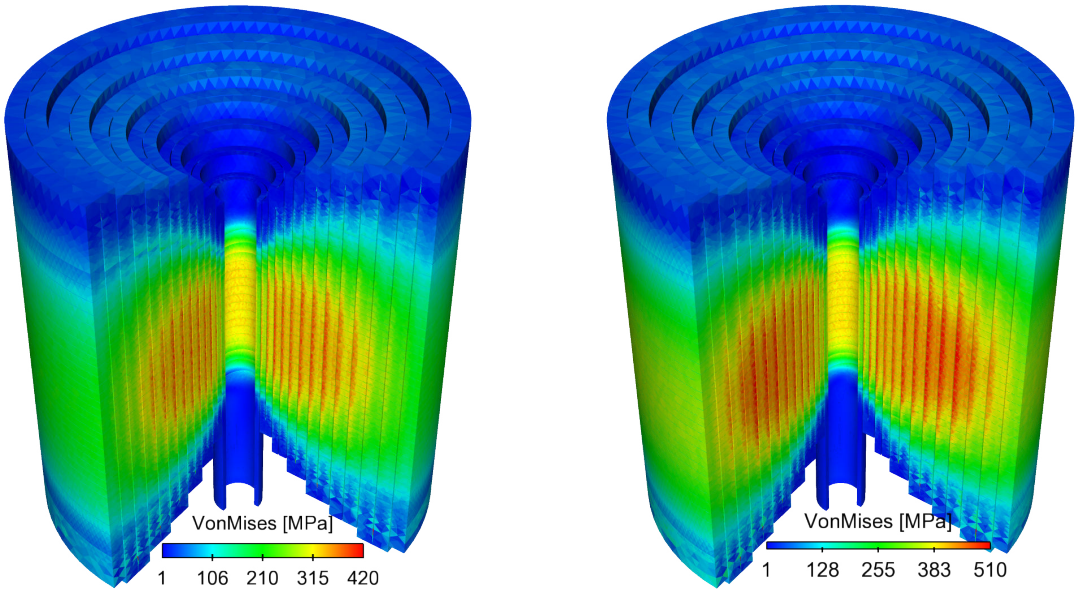

(a) Standard (37 T) (b) Hybrid (45 T)

Figure 12.10 – Von-Mises stress on 14 helices magnet insert

Figure 12.10a displays the Von-Mises stresses obtained within the standard environment which still reach more than 400 MPa. As to the hybrid magnet insert, Figure 12.10b illustrating the Von-Mises stresses emphasizes an important increase of the stresses which exceed 500 MPa.

Figure 12.11 compares the Von-Mises criterion computed along the x axis for the two inserts. The difference in terms of design is all the more marked through this graph showing that the highest stresses are not concentrated in the same helices. Besides the knowledge of the requested mechanical resistance, these results enable to anticipate the repartition of the stresses.

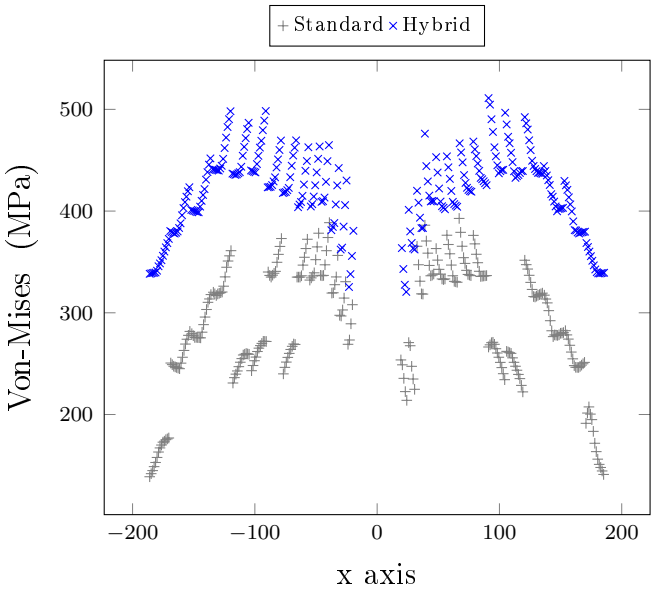

Figure 12.11 – Von-Mises stress along x axis

Turning back to the 3D magnetic field generated by the 8 innermost helices (Figure 12.6), we investigate the resulting stresses. In particular, the figures 12.12a and 12.12b compare the Von-Mises stress criterions computed from the Lorentz forces coming from the 2D axisymmetrical model and from the 3D one.

The two figures are on the same scale, and they show that the use of the 2D axisymmetrical model underestimates the stresses, which mean that they are even higher than expected. We also remind that the maximum magnetic field computed with the 3D model is higher than the one given by the 2D axisymmetrical model (Figure 12.7a). This can partly explain the difference in terms of stresses. Although this analysis doesn't allow a firm conclusion, it encourages to perform further studies in this sense.

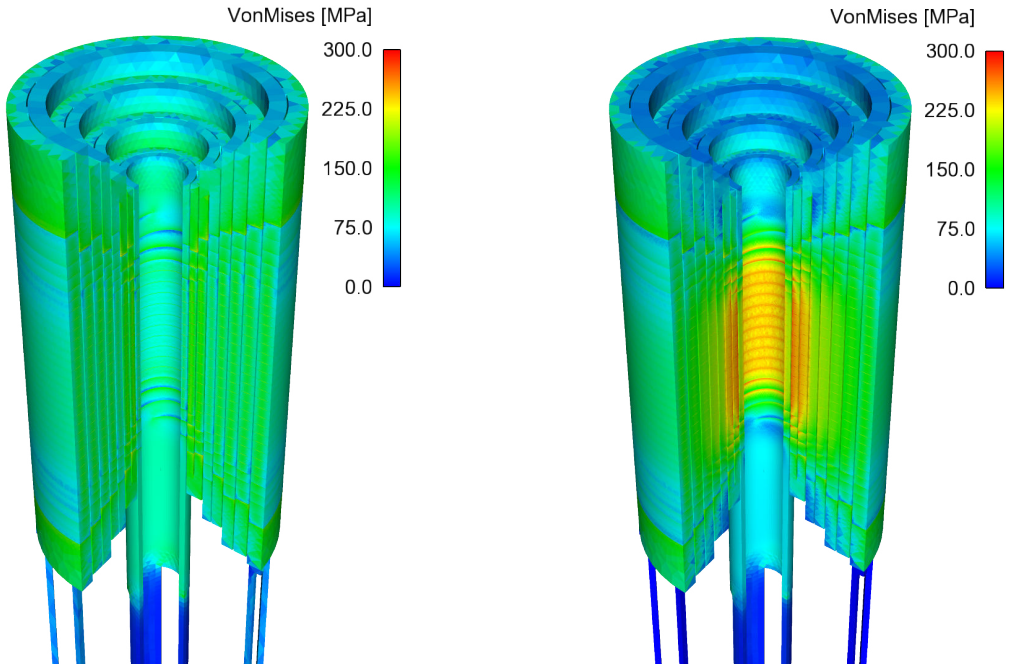

(a) Von-Mises (2D axi) (b) Von-Mises (3D)

Figure 12.12 – 3D stresses on the 8 most internal helices of the hybrid magnet resistive insert

Conclusion

In this chapter, we were interested in the predictive analysis of the behavior of the hybrid magnet resistive insert within its operating environment. To this end, we compare the temperature, the magnetic field and the resulting stresses of two resistive inserts. This allows both to get a better idea of the order of magnitude of the studied quantities in a standard environment, and to assess how the design of the hybrid magnet is challenging.

The magnetic field is computed using the 2D axisymmetrical model which serves to perform the design optimization. The 3D magnetostatic model is used on the 8 innermost helices only due to mesh complexity issues. The resulting magnetic field emphasizes the impact of the magnet asymmetry mentionned in the dedicated Chapter 9.

This study allows to predict the repartition of temperature and stresses within the whole resistive insert that was never before available. It bring insights for the specifications requested by the hybrid magnet, especially in terms of materials.

From a numerical point of view, this experiment proves the feasability of our multiphysics model on real and complex geometries. This study however needs to be pursued, in order to use the full 3D model on the whole 14 helices insert. The main difficulty comes from the application of the infinite boundary conditions related with the magnetostatic model. To overcome this issue, we investigate the use of the Biot & Savart model introduced in Chapter 3.3 on the boundaries of a smaller surrounding box.

Conclusions and outlook

Conclusion

Throughout this thesis, we have introduced a set of tools dedicated to high field magnets modeling. Various physics are involved in this context, leading to the development of a 3D non-linear multi-physics coupled model as our primary objective.

All these developments rely on the finite element method and its implementation within the `Feel++` library. In particular, they benefit from the high performance computing features of the library.

The 3D model come as a complement to the existing 2D axisymmetrical models, providing better insight for the high field resistive magnets developed at the Grenoble High Magnetic Field Laboratory. The core ingredients of this full 3D multi-physics model consist of a non-linear electro-thermal model, a magnetostatic model for which various formulations are considered, and a linear elasticity model resulting in the stresses computation. Chapter 3 precisely describes each of these models from the underlying equations, with the corresponding variational formulations. We illustrate their implementation with convergence studies, allowing to ensure that the expected mathematical properties are satisfied.

Regarding the magnetostatic model, the Maxwell's equations require to consider H_{div} and H_{curl} conforming finite elements instead of nodal ones. The Raviart-Thomas and Nédélec finite elements, detailed in Chapter 1, have been studied for this purpose. Their implementation within `Feel++` is an important contribution of this work. It is the focus of Chapter 5. Thanks to this development, the De Rham diagram is now fully supported in `Feel++`.

The magnetic field can also be computed from the Biot & Savart's law, coming from the Maxwell's equations as well. Its sequential implementation is trivial, but doesn't provide satisfactory performances for the large size problems we are interested in. However, the computation of the underlying integrals is not naturally parallel. To address this issue, we propose in Chapter 6 a parallel algorithm for the Biot & Savart's law which is original to our knowledge.

The validity of each developed model is illustrated through various numerical applications, choosen as meeting with the specific needs of the high magnetic field facilities. In particular, Chapter 9 presents a measurement campaign dedicated to magnet asymmetry. Indeed, some experiments (NMR and magnetic levitation) have shown that the magnetic field is 3D. However, up to this development the magnetic field was considered as 2D

axisymmetric for the magnet design. The parallel implementation of Biot & Savart's law especially enables to partly reproduce experimental measurements, considering the whole 3D geometry. This confirms the 3D nature of the magnetic field. It also justifies the importance of relying on a full 3D model for a better design optimization of high field magnets.

This multidisciplinary work has been presented in the international Magnet Technology conference in Seoul (Korea) [Daversin et al., 2015], along with a dedicated paper [Daversin et al., 2016b]. More recently, an overview of this project was the focus of a highlighted talk [Daversin et al., 2016a], at the 10th International Symposium on Electric and Magnetic Fields in Lyon (France).

To reach higher magnetic fields, the conception of magnets pushes the materials to their limit, making the reliability of these models all the more important. Nevertheless, the implementation of such a 3D model hides an important computational cost, due to the large size of the considered problems.

The uncertainties associated with the model inputs, namely the material properties as well as the operating conditions whose exact values are not known, must be taken into account within our model. In order to cater to the needs in terms of parametric studies and uncertainty quantification, the efficiency on our model requires a particular attention. The Reduced Basis (RB) method is well suited in such a many query context. It has thus been favored to circumvent the underlying complexity.

Its efficiency essentially relies on an offline/online strategy, which requires an affine decomposition of the problem. Chapter 2 describes the use of this method in the context of non-linear and non affinely parametrized problems. In particular, it introduces the Empirical Interpolation Method (EIM), widely used to recover the needed affine decomposition. Its application on the 3D electro-thermal model is presented in Chapter 4, illustrated by two concrete examples.

However, the use of EIM can imply a large number of finite element approximations, making its cost prohibitive. The Simultaneous Empirical interpolation and Reduced basis (SER) method has been proposed in this context. It aims to decrease the number of finite elements approximations, benefiting from the use of the reduced basis approximation within the EIM offline stage. To this end, the EIM and RB approximations spaces are built simultaneously.

Described in Chapter 2, SER is an original contribution of this thesis. We detail also numerous variants for this method, based on the development of an appropriate error indicator. All are backed by results on a 2D benchmark.

Turning back to the primary objective related with high field magnets modeling, Chapter 8 exhibits the use of the RB model to address some practical issues. The application of SER on this reduced electro-thermal model is the focus of Chapter 11. It proves to be relevant on such an application, opening new possibilities while ensuring a reasonable cost.

Firstly introduced in [Daversin and Prud'Homme, 2015a], the SER method has re-

cently been presented at MoRePaS (Model Reduction for Parametrized Systems) in Trieste (Italy) [Daversin and Prud'Homme, 2015b]. A paper [Daversin and Prud'Homme, 2016] detailing the last obtained results has just been submitted in this context.

Outlook

The follow up to be given to this project extends to multiple levels.

At first, the multi-physics model aiming to study the high field magnets can be enriched with more advanced models.

In particular, the account of water cooling process can be highly improved. The current cooling model relies on a constant heat transfer coefficient and an average coolant temperature. The hydraulic is far more complex and challenging especially for radially cooled helices. Indeed in this case, as the flow is not established, there is no valid correlation to estimate the heat transfer coefficient. An advanced turbulence model would then be of great interest.

The mechanical model introduced in Chapter 3 is based on the linear elasticity equation. This model is well suited as long as the deformations remain small. We have seen, for instance with the Hybrid magnet project detailed in Chapter 12, that the stresses can reach high values, approaching the elastic limits of the materials. Moreover, large deformations are observed on failing magnets. As soon as the elastic limit is exceeded, the linear model is no longer sufficient and the results coming from our model no longer make sense. Non-linear elasticity models should be investigated to study the potential plastic deformations.

Lastly, the models developed through this work are all limited to the steady case. Nevertheless, the power up of the magnets is not instant. The development of unsteady models could help to better understand what goes at this step. In addition, this kind of model would also be interesting to model the power failures. This is an important issue of the hybrid magnet project.

The improvement of our multi-physics model resides also in the underlying numerical methods. Chapter 5 describes the implementation of the Raviart-Thomas and Nédélec finite elements at lowest order. The implementation of the high order elements introduced in Chapter 1 is the next step. Other H_{div} and H_{curl} conforming finite elements could also be investigated, especially Brezzi-Douglas-Marini (BDM), and Nédélec of second type.

On the other hand, Hybrid Discontinuous Galerkin (HDG) methods [Egger and Schöberl, 2010] are investigated in various projects related with `Feel++`. It will be the focus of a talk at the workshop "advanced numerical methods: recent developments, analysis and applications", next October at IHP (Paris, France). These methods have the benefit of giving an optimal approximation of both the primal and flux variables. Regarding our multi-physics model, this kind of method could provide a better approximation of the current density, and of the current intensity which reads as its flux. In particular, it should help the convergence of the magnetostatic model whose preconditioning introduced in Chapter 3 requests a divergence-free current density. It should also improve the accuracy of magnetic field computations, and ease the account of conditions on current intensity

in the electro-thermal model.

Lastly, the sensitivity analysis described in Chapter 8 is currently limited to the first order Sobol indices. The computation of k^{th} order sensitivity indices should give further informations on the eventual interactions between the input parameters. Especially, the randomized orthogonal array-based method introduced in [Tissot and Prieur, 2014] could be used to evaluate the 2^{nd} order indices without depending on the parametric dimension.

The experimental results introduced in Chapter 9 have assessed the pertinence of our 3D model out of the magnetic center. It consists of a promising lead in the magnet behavior understanding. However, the measurement campaign aiming to validate the 3D magnetic field calculation – either using Biot and Savart's law or from the magnetostatic model – needs to be continued. More precision on the probe positioning system is essential for an efficient and reliable comparison between experiment and numerical computations. This is currently carried out on a small test bench.

Furthermore, the reduced electro-thermal model detailed in Chapter 4 proves reliable and efficient within uncertainty quantification context. The next step focuses on the extension of this reduced model to other physics, namely considering the magnetostatic and linear elasticity models introduced in Chapter 3. The potential difficulty in the multi-physics context resides in the coupling of the different physics.

The SER method introduced in this thesis consists in a significant breakthrough for the reduced basis methodology applied to non-linear and non affinely parametrized problems. The first investigated variants give encouraging results. However many others variants remain to be explored. The theoretical question of the a priori convergence of the method is still opened as well. The latest results for SER will be presented at the workshop "recent developments in numerical methods for model reduction", next November at IHP (Paris, France).

Finally, we have mentioned in Chapter 8 the use of `OpenTurns` library to perform uncertainty quantification studies. The embedding of uncertainty quantification tools, internally in the `Feel++` reduced basis framework, might be investigated to avoid the resort to an external library.

Bibliography

[A. Hervé, 1997] A. Hervé (1997). Integration of the magnetic components of circular thick coils and disk coils. *Proc. of fifteenth int. conf. on Magnet Technology*, Part two:1262–1270.

[Balay et al., 2012] Balay, S., Brown, J., Buschelman, K., Gropp, W. D., Kaushik, D., Knepley, M. G., Curfman McInnes, L., Smith, B. F., and Zhang, H. (2012). *PETSc Web page*.

[Barrault et al., 2004] Barrault, M., Maday, Y., Nguyen, N. C., and Patera, A. (2004). An empirical interpolation method: application to efficient reduced-basis discretization of partial differential equations. *Comptes Rendus Mathematique*, 339(9):667–672.

[Bebendorf and Ostrowski, 2009] Bebendorf, M. and Ostrowski, J. (2009). Parallel hierarchical matrix preconditioners for the curl-curl operator. *Journal of Computational Mathematics*, 27:624–641.

[Biro et al., 1996] Biro, O., Preis, K., and Richter, K. (1996). On the use of the magnetic vector potential in the nodal and edge finite element analysis of 3d magnetostatic problems. *IEEE Transactions on Magnetics*, 32:651 – 654.

[Boffi et al., 2013] Boffi, D., Brezzi, F., and Fortin, M. (2013). *Mixed Finite Element Methods and Applications*, volume 44. Springer Series in Computational Mathematics.

[Boost, 2008] Boost, C. (2008). Libraries. http://www.boost.org.

[Brezzi and Fortin, 1991] Brezzi, F. and Fortin, M. (1991). *Mixed and hybrid finite element methods*. Springer-Verlag.

[Brezzi et al., 1985] Brezzi, F., Jr., J. D., and Marini, L. D. (1985). Two families of mixed finite elements for second order elliptic problems. *Numerische Mathematik*, 47:217–235.

[Canuto et al., 2006] Canuto, C., Hussaini, M., Quarteroni, A., and Zang, T. (2006). *Spectral methods*. Springer.

[Canuto et al., 2009] Canuto, C., Tonn, T., and Urban, K. (2009). A posteriori error analysis of the reduced basis method for nonaffine parametrized nonlinear pdes. *SIAM Journal on Numerical Analysis*, 47(3):2001–2022.

[Chabannes, 2013] Chabannes, V. (2013). *Vers la simulation des écoulements sanguins*. PhD thesis, Université Joseph Fourier, Grenoble.

[Ciarlet, 1978] Ciarlet, P. (1978). The finite element method for elliptic problems, vol. 40 of classics in applied mathematics, society for industrial and applied mathematics (siam), philadelphia, pa, 2002. reprint of the 1978 original. *Reprint of the 1978 original*, 1(1):2–4.

[Colburn, 1933] Colburn, A. (1933). A method of correlating forced convection heat transfer data and a comparison with fluid friction. *Trans. AIChE*, 29:174–210.

[Conway, 2001] Conway, J. T. (2001). Exact solutions for the magnetic fields of axisymmetric solenoids and current distributions. *IEEE Transactions on Magnetics*, 37(4):2977–2988.

[Cotton, 1928] Cotton, A. (1928). Le grand électro-aimant de l'académie des sciences. *Recherches et Inventions*, 172.

[Daversin et al., 2016a] Daversin, C., Hild, R., Prud'Homme, C., and Trophime, C. (2016a). Full 3d non-linear multi-physics model for high field polyhelix magnets. *10th International Symposium on Electric and Magnetic Fields, Lyon, France*.

[Daversin and Prud'Homme, 2015a] Daversin, C. and Prud'Homme, C. (2015a). Simultaneous empirical interpolation and reduced basis method for non-linear problems. *C. R. Acad. Sci. Paris, Ser. I*, 353:1105–1109.

[Daversin and Prud'Homme, 2015b] Daversin, C. and Prud'Homme, C. (2015b). Simultaneous empirical interpolation and reduced basis method for non-linear problems. *Model Reduction of Parametrized Systems, Trieste, Italy*.

[Daversin and Prud'Homme, 2016] Daversin, C. and Prud'Homme, C. (2016). Simultaneous empirical interpolation and reduced basis method, application to non-linear multiphysics problem. Submitted.

[Daversin et al., 2015] Daversin, C., Prud'Homme, C., and Trophime, C. (2015). Full 3d multiphysics model of high field polyhelices magnets. *24th International Conference on Magnet Technology, Seoul, South Korea*.

[Daversin et al., 2016b] Daversin, C., Prudhomme, C., and Trophime, C. (2016b). Full three-dimensional multiphysics model of high-field polyhelices magnets. *IEEE transactions on applied superconductivity*, 26(4).

[Daversin et al., 2013] Daversin, C., Veys, S., Trophime, C., and Prud'Homme, C. (2013). A reduced basis framework: Application to large scale nonlinear multi-physics problems. *Esaim Proc.*, 43:225–254.

[Debray et al., 2012] Debray, F., Dumas, J., Trophime, C., and Vidal, N. (2012). Dc high field magnets at the lncmi. *IEEE transactions on applied superconductivity*, 22(3).

[Debray et al., 2002] Debray, F., Jongbloets, H., Joss, W., Martinez, G., Mossang, E., Petmezakis, P., Picoche, J., Plante, A., Rub, P., Sala, P., and Wyder, P. (2002). The grenoble high magnetic field laboratory as a user facility. *IEEE transactions on applied superconductivity,*, 12(1).

[D.H. Parkinson, 1967] D.H. Parkinson, B. M. (1967). *The generation of high magnetic fields*. Plenum Press.

[Dular and Geuzaine, 1997] Dular, P. and Geuzaine, C. (1997). Getdp: a general environment for the treatment of discrete problems. http://geuz.org/getdp.

[Dumitru, 2013] Dumitru, C. (2013). Numerical problems in 3d magnetostatic fem analysis. In *Advances in Automatic Control, Modelling & Simulation*. Proceeding of the 15th International Conference on Automatic Control, Modelling & Simulation.

[Dutfoy et al., 2009] Dutfoy, A., Dutka-Malen, I., Pasanisi, A., Lebrun, R., Mangeant, F., Gupta, J. S., Pendola, M., and Yalamas, T. (2009). OpenTURNS, an Open Source initiative to Treat Uncertainties, Risks'N Statistics in a structured industrial approach. In *41èmes Journées de Statistique, SFdS, Bordeaux (France)*.

[Egger and Schöberl, 2010] Egger, H. and Schöberl, J. (2010). A hybrid mixed discontinuous galerkin finite-element method for convection–diffusion problems. *IMA Journal of Numerical Analysis*, 30(4):1206–1234.

[Falgout et al., 2006] Falgout, R., Jones, J., and Yang, U. (2006). The design and implementation of hypre, a library of parallel high performance preconditioners. Hypre : High performance preconditioners, http://www.llnl.gov/CASC/hypre/.

[Geuzaine and Remacle, 2009] Geuzaine, C. and Remacle, J. F. (2009). Gmsh: a three-dimensional finite element mesh generator with built-in pre-and post-processing facilities. *International Journal for Numerical Methods in Engineering*, 79(11):1309–1331.

[Graglia, 1993] Graglia, R. D. (1993). On the numerical integration of the linear shape functions times the 3-d green's function or its gradient on a plane triangle. *IEEE Transactions on Antennas and Propagation*, 41(10):1448–1455.

[Greif and Schötzau, 2007] Greif, C. and Schötzau, D. (2007). Preconditioners for the discretized time-harmonic maxwell equations in mixed form. *Numerical Linear Algebra with Applications*, 14:281–297.

[Grepl et al., 2007] Grepl, M., Maday, Y., Nguyen, N. C., and Patera, A. (2007). Efficient reduced-basis treatment of nonaffine and nonlinear partial differential equations. *ESAIM: Mathematical Modelling and Numerical Analysis*, 41(03):575–605.

[Hiptmair and Xu, 2007] Hiptmair, R. and Xu, J. (2007). Nodal auxiliary space preconditioning in h(curl) and h(div) spaces. *SIAM Journal on Numerical Analysis*, 45:2483–2509.

[Huynh et al., 2007] Huynh, D., Rozza, G., Sen, S., and Patera, A. (2007). A successive constraint linear optimization method for lower bounds of parametric coercivity and inf–sup stability constants. *Comptes Rendus Mathematique*, 345(8):473–478.

[Janon et al., 2014a] Janon, A., Klein, T., Lagnoux-Renaudie, A., Nodet, M., and Prieur, C. (2014a). Asymptotic normality and efficiency of two Sobol index estimators. *ESAIM: Probability and Statistics*, 18:342–364.

[Janon et al., 2013] Janon, A., Nodet, M., and Prieur, C. (2013). Certified reduced-basis solutions of viscous Burgers equation parametrized by initial and boundary values. *ESAIM: Mathematical Modelling and Numerical Analysis*, 47(2):317–348.

[Janon et al., 2014b] Janon, A., Nodet, M., and Prieur, C. (2014b). Uncertainties assessment in global sensitivity indices estimation from metamodels. *International Journal for Uncertainty Quantification*, 4(1):21–36.

[Kolev and Vassilevski, 2009] Kolev, T. and Vassilevski, P. (2009). Parallel auxiliary space amg for h(curl) problems. *Journal of Computational Mathematics*, 27:604–623.

[Masserey et al., 2005] Masserey, A., Rappaz, J., Rozsnyo, R., and Swierkosz, M. (2005). Numerical integration of the three-dimensional green kernel for an electromagnetic problem. *Journal of Computational Physics*, 205(1):48–71.

[Maxwell, 1865] Maxwell, J. C. (1865). A dynamical theory of the electromagnetic field. *Philosophical Transactions of the Royal Society*.

[Montgomery, 1969] Montgomery, B. (1969). *Solenoid magnet design: The magnetic and mechanical aspects of resistive and superconducting systems*. Wiley-Interscience.

[Nédélec, 1980] Nédélec, J. (1980). Mixed finite elements in $\mathbb{R}^3$. *Numerische Mathematik*, 35:315–341.

[Nédélec, 1986] Nédélec, J. (1986). A new family of mixed finite elements in $\mathbb{R}^3$. *Numerische Mathematik*, 50:57–81.

[Patera and Rozza, 2007] Patera, A. and Rozza, G. (2007). Reduced basis approximation and a posteriori error estimation for parametrized partial differential equations. MIT Pappalardo Graduate Monographs in Mechanical Engineering. Copyright MIT 2006-2007.

[Pena, 2009] Pena, G. (2009). *Spectral element approximation of the incompressible Navier-Stokes equations evolving in a moving domain and applications*. PhD thesis, École Polytechnique Fédérale de Lausanne. n°4529.

[Prieur, 2014] Prieur, C. (2014). Analyse de sensibilité globale, approches stochastiques. *Ecole ASPEN*.

[Prud'homme, 2006] Prud'homme, C. (2006). A domain specific embedded language in C++ for automatic differentiation, projection, integration and variational formulations. *Scientific Programming*, 14(2):81–110.

[Prud'Homme et al., 2012] Prud'Homme, C., Chabannes, V., Doyeux, V., Ismail, M., Samake, A., and Pena, G. (2012). Feel++: A Computational Framework for Galerkin Methods and Advanced Numerical Methods. *ESAIM: Proc.*, 38:429 – 455.

[Prud'homme and Patera, 2004] Prud'homme, C. and Patera, A. (2004). Reduced-basis output bounds for approximately parameterized elliptic coercive partial differential equations. *Computing and Visualization in Science*, 6(2-3):147–162.

[Prud'homme et al., 2002] Prud'homme, C., Rovas, D. V., Veroy, K., Machiels, L., Maday, Y., Patera, A. T., and Turinici, G. (2002). Reliable real-time solution of parametrized partial differential equations: Reduced-basis output bound methods. *Journal of Fluids Engineering*, 124(1):70–80.

[Pugnat et al., 2016] Pugnat, P., Barbier, R., Berriaud, C., Berthier, R., Caplanne, G., Debray, F., Fazilleau, P., Hanoux, P., Hervieu, B., Manil, P., Molinié, F., Pes, C., Pfister, R., Queinec, Y., Pissard, M., Ronayette, L., Trophime, C., and Vincent, B. (2016). Status of the 43 t hybrid magnet of lncmi-grenoble. *IEEE transactions on applied superconductivity*.

[Quarteroni et al., 2011] Quarteroni, A., Rozza, G., and Manzoni, A. (2011). Certified reduced basis approximation for parametrized partial differential equations and applications. *Journal of Mathematics in Industry*, 1(1):1–49.

[Raviart and Thomas, 1977] Raviart, P.-A. and Thomas, J. M. (1977). Primal hybrid finite element methods for 2nd order elliptic equations. *Mathematics of computation*, 31(138):391–413.

[Rognes et al., 2009] Rognes, M., Kirby, R. C., and Logg, A. (2009). Efficient assembly of h(div) and h(curl) conforming finite elements. *SIAM Journal on Scientific Computing*, 31:4130–4151.

[Rozza et al., 2007] Rozza, G., Huynh, D., and Patera, A. (2007). Reduced basis approximation and a posteriori error estimation for affinely parametrized elliptic coercive partial differential equations. *Archives of Computational Methods in Engineering*, 15(3):1–47.

[Sabariego et al., 2006] Sabariego, R., Sergeant, P., Gyselinck, J., Dular, P., Dupré, L., and Melkebeek, J. (2006). Fast multipole accelerated finite element-boundary element analysis of shielded induction heaters. *IEEE Transactions on Magnetics*, 42(4):1407–1410.

[Schneebeli, 2003] Schneebeli, A. (2003). An $H(curl;\Omega)$-conforming fem : Nédélec's elements of first type.

[Sobol, 1993] Sobol, I. (1993). Sensitivity analysis for nonlinear mathematical models. *Mathematical Modeling and Computational Experiment*, 1:407—-414.

[Sudret, 2008] Sudret, B. (2008). Global sensitivity analysis using polynomial chaos expansion. *Reliability Engineering & System Safety*, 93(7):964–979.

[Tissot and Prieur, 2014] Tissot, J.-Y. and Prieur, C. (2014). A randomized Orthogonal Array-based procedure for the estimation of first- and second-order Sobol' indices. *Journal of Statistical Computation and Simulation*, pages 1–24.

[Trophime et al., 2002] Trophime, C., Egorov, K., Debray, F., Joss, W., and Aubert, G. (2002). Magnet calculations at the grenoble high magnetic field laboratory. *IEEE transactions on applied superconductivity,*, 12(1).

[Trophime et al., 2006] Trophime, C., Kramer, S., and Aubert, G. (2006). Magnetic field homogeneity optimization of the giga-nmr resistive insert. *IEEE Transactions on Applied Superconductivity*, 16(2):1509–1512.

[Veroy and Patera, 2005] Veroy, K. and Patera, A. (2005). Certified real-time solution of the parametrized steady incompressible navier-stokes equations: Rigorous reduced-basis a posteriori error bounds. *Int. J. Numer. Meth. Fluids*, 47:773–788.

[Veroy et al., 2003a] Veroy, K., Prud'homme, C., and Patera, A. (2003a). Reduced-basis approximation of the viscous Burgers equation: Rigorous *a posteriori* error bounds. *C. R. Acad. Sci. Paris, Série I*, 337(9):619–624.

[Veroy et al., 2003b] Veroy, K., Prud'homme, C., Rovas, D., and Patera, A. (2003b). A posteriori error bounds for reduced-basis approximation of parametrized noncoercive and nonlinear elliptic partial differential equations. *American Institute of Aeronautics and Astronautics Paper*, pages 2003–3847.

[Veroy et al., 2003c] Veroy, K., Prud'homme, C., Rovas, D. V., and Patera, A. (2003c). *A posteriori* error bounds for reduced-basis approximation of parametrized noncoercive and nonlinear elliptic partial differential equations (AIAA Paper 2003-3847). In *Proceedings of the 16th AIAA Computational Fluid Dynamics Conference*.

[Veys, 2014] Veys, S. (2014). *Un framework de calcul pour la méthode des bases réduites : applications à des problèmes non-linéaires multi-physiques*. PhD thesis, Université Joseph Fourier, Grenoble.

[White et al., 2006] White, D. A., Fasenfest, B. J., and Stowell, M. L. (2006). A parallel computer implementation of fast low-rankqr approximation of the biot-savart law. In *Proceedings of Progress In Electromagnetics Research Symposium*.

[Zaglmayr, 2006] Zaglmayr, S. (2006). *High order finite element methods for electromagnetic field computation*. PhD thesis, Johanned Kepler Universität.

[Zienkiewicz and Zhu, 1992] Zienkiewicz, O. C. and Zhu, J. Z. (1992). The superconvergent patch recovery and a posteriori error estimates. I. The recovery technique. *Internat. J. Numer. Methods Engrg.*, 33(7):1331–1364.

Perfectly characterized since more than 100 years, the magnetic field is present throughout our environment. Besides the numerous possibilities it opens, it constitutes a powerfull tool for researchers especially to probe and determine the properties of the matter. This kind of applications requires nevertheless magnetic fields of high intensity, namely higher than the one achievable by superconducting magnets. The "Laboratoire National des Champs Magnétiques Intenses" (LNCMI) develops water cooled resistive magnets providing such magnetic field to scientists. The design of these magnets represents a challenge in terms of design and materials. The numerical simulation proves essential to achieve such an optimization process. This thesis fits into a research collaboration between the Institut de Recherche Mathématique Avancée (IRMA) and the LNCMI whose goal is the development of a software toolchain for high field magnets modeling. Its primary objective resides in the development of a range of non-linear coupled models taking into account the whole involved physics, except the hydraulic related with the magnet cooling. Based on the finite element method, the resulting multi-physics model is implemented through the Feel++ library. The core ingredients necessary to implement this model are detailled together with its verification and its validation from experimental results when available. Designed for many query context, the reduced basis method applied to the multi-physics model aims to circumvent the complexity of the considered problem. The efficiency it offers especially allows to move towards parametric studies and sensitivity analysis in various concrete applications. Nevertheless, the necessary precomputations hide an important computational cost due to the non-linearity and the non-affine parametrization of the model. In order to reduce the latter, the Simultaneous Empirical interpolation and Reduced basis method is introduced through this thesis.

INSTITUT DE RECHERCHE MATHÉMATIQUE AVANCÉE
UMR 7501
Université de Strasbourg et CNRS
7 Rue René Descartes
67 084 STRASBOURG CEDEX

Tél. 03 68 85 01 29
Fax 03 68 85 03 28

www-irma.u-strasbg.fr
irma@math.unistra.fr

IRMA 2016/003
ISSN 0755-3390
http://tel.archives-ouvertes.fr/tel-01361722